Petrogenesis of the Panzhihua-type Gabbroic Layered Intrusions and Associated Fe-Ti-V Oxide Deposits: Insights from Mineral Chemistry and Numerical Modeling

by

Jian-Xiang Guan

B.Sc. Hons (China University of Geosciences)

University of Tasmania

Submitted in fulfilment of the requirements for the degree of
Doctor of Philosophy

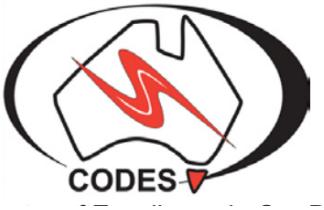

ARC Centre of Excellence in Ore Deposits

July, 2014

Declaration of Originality

This thesis contains no material which has been accepted for a degree or diploma by the University or any other institution and to the best of my knowledge and belief. This thesis contains no material previously published or written by another person, except where due references is made in the text of the thesis.

Jian-Xiang Guan

04/07/2014 July 2014

Authority of Access

This thesis may be made available for loan and limited copying in accordance with the Copyright Act, 1968.

Jian-Xiang Guan

04/07/2014 July 2014

Abstract

The Panzhihua-Xichang district, SW China, is located within the central part of the Emeishan Large Igneous Province (ELIP). The district hosts the world largest titanium resources and the third largest vanadium resources. Ti and V are hosted by magnetite and ilmenite, forming the unique Panzhihua-type deposits amounting to ~ 20 billion tonnes of Fe-Ti-V oxide in potential reserves. This project is mainly focused on understanding the formation mechanism of the Panzhihua gabbroic layered intrusion and associated Fe-Ti-V oxide deposit, and also on the neighbouring Taihe Intrusion.

Lithological and stratigraphic investigations by a wide range of researchers over the last 50 years have subdivided the Panzhihua Intrusion into a marginal zone (MGZ), lower zone (LZ), lower middle zone (MZa), upper middle zone (MZb) and upper zone (UZ). The Fe-Ti-V oxide ores are concentrated below the MZb, which is marked by the appearance of cumulus apatite. This study is centred on the rocks from the Lanshan and Zhujiabaobao sections of the Panzhihua intrusion. Samples were collected from the Lanshan and Zhujiabaobao open-pit mines, representing the lower ~ 700 of the 2000 meters of the total stratigraphy.

The rocks are composed of cumulus clinopyroxene (Cpx), plagioclase (Plag), magnetite (Mgt) and ilmenite (Ilm). Olivine (Ol) and apatite (Ap) occur as the main cumulus minerals below and above the ore bodies, respectively. Hornblende (Hbl) and Fe-rich sulfide (pyrrhotite-Po) are found throughout the intrusion. In general, the abundances of Fe-Ti oxides decrease up the section. Ilm becomes more abundant up the studied section. Fe-Ti oxides occur as massive and disseminated ores, as intercumulus minerals in a wide range of rocks, and as inclusions in silicate minerals in various rock types. Fe-Ti oxide inclusions are common in Ol and Cpx, also occasionally in Plag. Po occurs as discrete, inclusion and droplets, which arecharacterized by linear distribution of round-subround Po grains. Some discrete intercumulus Po grains coexist with Fe-Ti oxides in triple junction between silicate minerals. Po inclusions appear commonly in Cpx, Plag and Fe-Ti oxides, however, no Fe-Ti oxides are included in Po. Po droplets are only found in Cpx. Pentlandite (Pn), chalcopyrite (Cpy) and pyrite (Py) are subordinate minerals. Cpx and Mgt are characterised by extensive exsolution textures.

The whole-rock major element composition were obtained using XRF and solution ICP-MS at CODES, Univeristy of Tasmania. It may be well explained by a mixture of an ox-

ide end-member and a silicate end-member. The former consists of Mgt and Ilm in a constant ratio of approximately 4:1. The latter, consisting mainly of Cpx and Plag, is more variable due to large variations in modal proportions and occurrence of Ol, Hbl and Ap in some rocks. Trace element abundances also show strong correlations with the modal proportion of one or more minerals of either end-member. Rocks from the LZ and MZa contain less than 5% interstitial melt, which have little effect on the whole rock chemistry. Rocks from the MGZ have significant amounts of interstitial melt, which is likely the result of rapid cooling.

Mineral major and trace element compositions were analyzed using EMPA and LA-ICP-MS at the CSL and CODES respectively, University of Tasmania. The Panzhihua and Taihe Fe-Ti oxides are mostly depleted in Cr and Ni. Cr-rich Mgt and Ilm only appear in three wehrlite and one microgabbro from the MGZ. Re-equilibration with Mgt has resulted in an increase in Fo content of Ol. A significant difference in Fo content in Ol and $Mg\#_{Cpx}$ for coexisting Ol and Cpx indicates subsolidus re-equilibration. Temperatures calculated using a) an Ol-Cpx thermometer and b) an experimentally derived relationship between An content in Plag and temperature, indicate a small temperature difference (~20˚C) between gabbro located below and above the first and last massive ore, suggesting Fe-Ti oxides were deposited from compositionally similar magmas.

The whole rock and mineral compositions show little variation throughout the LZ and MZa, which is inconsistent with *in-situ* fractional crystallization. This strongly suggests that the parental magma for all rocks in the intrusion had a nearly constant composition. A major reversal is recorded in Plag An content in the lower MZa, however, this is not observed in other minerals (e.g. $Mg\#_{Cpx}$, Fo, Ni and V contents in Mgt and Ilm). Hence, it may not represent new primitive magma replenishment event as previously suggested. Instead, it is more likely a result of a localised increase in H_2O activity, which would significantly increase An content in Plag but would have little effect on other parameters.

Numerical modelings with the Petrolog3 algorithm are performed under various conditions. The highly consistency of mineral compositions and modal proportions between calculated and observed results reflect high quality of the modelings. We propose instead a new magma replenishment hypothesis. The MGZ rocks display large vertical variations in rock chemistry. Solidification at high cooling rates coupled with likely upward migration of residual melts, are responsible for compositional reversals within the MGZ. Later intrusion of less evolved crystal-laden magma formed dyke-like wehrlite, sometimes with porphyritic texture.

In the proposed model for the petrogenesis of the Panzhihua intrusion, the intrusion acted as an open plumbing system, where crystal-rich magmas with similar composition continuously flow through. In detail, the silicate minerals were crystallized in equilibrium during ascending and intrusion. These crystal-loaded parental magmas emplaced into a weakened zone of crustal dolomitic wall rocks. CO_2 released during reaction with wall rocks at the time of emplacement oxidized the parental magma, trigging Fe-Ti oxide fractional crystallization. Dense Mgt and Ilm accumulated on the floor by gravitational settling. Removal of Fe-Ti oxides from the magma also caused sulfide saturation (probably as a Fe-rich monosulfide liquid) due to the rapid decrease in melt Fe content. This immiscible sulfide liquid was segregated from the magma during Fe-Ti oxides fractionation, subsequently trapped and crystallized in the solidifying crystal piles. The density differences between minerals and melt may have resulted in different settling rates and formation of variety of rock types in the Panzhihua intrusion. Silicate minerals were accumulating at both the bottom and top of the chamber, forming layers with the intrusion, whereas Fe-Ti oxides were preferentially accumulated near the bottom. The magmatic system was closed after depositing approximately 1100m-thick cumulate at the bottom of the intrusion, and at least 800m-thick cumulate at the roof, leaving the entrapped liquid differentiated subsequently *in-situ*.

Acknowledgments

A PhD is never a sole work of any single person. Many people, besides the name on the cover of this thesis, have contributed to this project. I would like to take this opportunity to give my grateful acknowledgement to them, for their help and encouragement.

First and foremost, I am very much indebted to my supervisors, Prof. Leonid Danyushevsky and Prof. Anthony Crawford for initiating the research project. I owe my deepest gratitude to Leonid for his unstinting encouragement, inspiration and guidance, and his tolerance on my delay and terrible writing. I also very appreciate his understanding and willingness to help in my daily life. I always remember his asking on the first day when I came to CODES, "Are you happy here?". It is my fortune to meet and be supervised by him. I am particularly grateful to my co-supervisor Tony, whose door was always open and his available even after his retirement on last December.

I am grateful to Prof. Dave Green, Dr. Trevor Falloon, Dr. Paul Davidson, and Dr. Dave Hutchinson for their invaluable comments and suggestions on my one-day long mid-term review. Particularly, I thank Prof. Dave Green and Dr. Paul Davidson for their written feedbacks afterwards. Paul and Prof. Dima Kamenetsky also helped with my study on petrography.

I wish to express my thank to many staffs at CODES and Scholl of Earth Sciences for their contributions to this project: Professor Jocelyn McPhile, Simon Stephens, AI Cuison, Phil Robinson, Sarah Gilbert, Ian Little, Katie McGoldrick, Helen Scott, Karen Bradford, Deborah Macklin, June Pongratz, Peter Cornish, Keith Dobson. I thank Dr. Karsten Goemann and Dr Sandrin Feig for their support and advices druing my EMPA and MLA analyses at the CSL.

I would like to thank all my colleagues and friends who have made my stay at CODES and Hobart enjoyable. Special thanks are deserved for my past and present office mates: Dr. Nathan Fox, Dr. Anita Parbhakar-Fox, Dr. Olga Vasyukova, Mr. Daniele Redi, Mr. Jose Piquer, Mr Michael Musialike, Mr. Cesar Calderson-Tipiani. Thanks to those friends: Dr. Chun Kit Lai, Dr Lejun Zhang, Dr. Nic Jansen, Dr. Masoe Salam, Dr. Victor Hugo Halvan, Dr. Takayuki Manaka, Mr Alexey Lygin, Mr Jeffe Steadman, Mr. Wei Hong, Mr. Qiuyue Huang.

I am grateful to Dr. Huayong Chen and his wife Dr. Yuzhen Liu, and Dr. Zhaoshan Chang and his wife Mrs Hongzhen Hu, for being supportive with study and my family life.

My acknowledgements must also extend beyond the CODES community. Particular thanks must go to Prof. Xie-Yan Song and his research team at the Institute of Geochemistry,

Chinese Academy of Sciences. Xie-Yan has inspired me with interests on mafic-ultramafic magma evolution and mineralization. Without his encouragement and recommendation, I would not have such an opportunity to meet Leonid and Tony and study at CODES. His former and current PhD students, Lie-Meng Chen, Yu-Feng Deng, Wei Xie, Xiao-Qi Zhang, Yan Luan, Yu-wei She, are thanked for their help. Prof. Alexei Ariskin, Prof. Michael Lesher, Dr. Steve Barnes, Dr. Sarah Dare are thanked for their generous advices on many aspects of this project.

Finally, I sincerely thank my wonderful wife Fanghua and my two baby girls, who were born during this study, for sticking with me through this long process and their loving support. My heartfelt gratitude goes also to my parents and younger brother back in China, without their love and support, it would have been impossible to complete this thesis.

Table of Contents

CHAPTER 3 PETROGRAPHY

CHAPTER 4 WHOLE-ROCK AND MINERAL CHEMISTRY

List of Figures

List of Tables

List of Appendices

CHAPTER 1 INTRODUCTION

1.1 Magmatic Fe-Ti Oxide Ore Deposits

1.1.1 Distribution and Classification

Economic magmatic iron-titanium-phosphorus-vanadium (Fe-Ti-P-V) oxide ore deposits are mostly associated with two types of igneous bodies: anorthosite massifs and related mangerite, charnockite and (rapakivi-) granite (AMCG suite; Ashwal, 1993; Charlier, 2007; Duchesne, 1999; Emslie, 1978; Kolker, 1982; Owens & Dymek, 1992), and the mafic-ultramafic layered intrusions (Charlier *et al.*, 2008; Duchesne *et al.*, 2006; Eales & Cawthorn, 1996; Namur *et al.*, 2012; Ripley *et al.*, 1998; Wilson *et al.*, 1996; Zhou *et al.*, 2005). Another much less common type is alkaline igneous complexes (Jiang *et al.*, 2004; Ryabchikov & Kogarko, 2006). According to the differences in the host rocks, Fe-Ti-P-V oxide ore deposits may be divided into four types.

First, Fe-Ti±P±V oxide ore deposits in association with massif-type anorthosite. The host anorthositic plutons have generally been dated Mid-Proterozoic (Corrigan & Breemen, 1997; Higgins & van Breemen, 1996; Schärer *et al.*, 1996). Arndt (2012) described this period is an intermediate stage in the history of crustal formation, and this time constraint may relate to the distinct dome-and basin structure of Archean cratons (Choukroune *et al.*, 1995; Choukroune *et al.*, 1997). Crustal physicochemical conditions (e.g. temperature, density, viscosity, etc) at this stage were suitable for coupled diapiric uprising of anorthositic plutons and gravity-driven subsidence (Barnichon *et al.*, 1999; Bolle & Duchesne, 2007; Charlier *et al.*, 2006; Paludan *et al.*, 1994). Anorthosite massifs have two types of plagioclase, andesine (An23-48) and labradorite (An45-63) (Anderson & Morin, 1969). Important Fe-Ti±P±V resources are usually associated with andesine, whereas labradorite massifs may have no Fe-Ti deposits but giant Ni-Cu-Co deposits (e.g. the Voisey' Bay intrusion in the Nain Plutonic Complex in Labrador in Canada (Emslie *et al.*, 1994; Ryan, 2000). Ore rocks usually display massive lenses with sharp contacts with host rocks, or cross-cuttings. Ilmenite is the principal ore mineral, e.g, the Lac Tio mine and the Tellnes ilmenite deposit associated with massif anorthosites in the Grenville Province in Canada and the Rogaland Province in Norway, respectively (Charlier

et al., 2006, 2010). Magnetite may be as important as ilmenite in some cases, such as the Fe-Ti oxide deposit in the Suwalki Anorthosite, Northeastern Poland (Charlier *et al*., 2009). In some cases, apatite may be sufficiently abundant to form oxide-apatite gabbronorites (OAGN; Owens & Dymek, 1992), and even nelsonite (Chen *et al*., 2013; Dymek & Owens, 2001; Zhao *et al*., 2009), which contains Fe-Ti oxide and apatite in a proportion close to 2:1 (Kolker, 1982; Philpotts, 1967). Rutile and sapphirine have been found accompanying ilmenite in the Saint Urbain and Big island deposits of the Grenville Anorthosite Province, Quebec (Morisset *et al*., 2010). Except for some massive ores, most ore rocks contain variable amounts of plagioclase, ±orthopyroxene, ±olivine, ±clinopyroxene.

Second, Fe-Ti±P±V oxide ore deposits in association with mafic-ultramafic layered intrusions. The most typical representative is the magnetite deposit in the Upper Zone of the Bushveld Complex, South Africa (Cawthorn & Ashwal, 2009; Cawthorn & McCarthy, 1980; Eales & Cawthorn, 1996; Klemm *et al*., 1985; Reynolds, 1985a, 1985b; Tegner *et al*., 2006). Twenty-one layers of magnetite ore concentrate in the lower ~1000m thick cumulates of the Upper Zone, which is composed mainly of (ferro-)gabbronorite, olivine-gabbronorite, and apatite-ferrodiorite, with extreme examples of anorthosite, magnetitite and feldspathic pyroxenite. Magnetitite layers typically have sharp bases, but gradational tops into anorthosite. In the upper ~1000m of the Upper Zone, ilmenite and apatite have formed an alternative ore type for Ti and P resources (Von Gruenewaldt, 1993). The oxide ± apatite ores in the Bushveld Complex have obviously formed later than PGE mineralization in the Merensky Reef at the base of the Main Zone and UG2 Chromitite within the Critical Zone (Ballhaus & Sylvester, 2000; Barnes & Maier, 2002; Cawthorn, 2010; Eales & Cawthorn, 1996; Godel *et al*., 2007; Naldrett *et al*., 2009, 2012; Wilson & Chunnett, 2006). However, there are some Fe-Ti-P oxide deposits, although on a smaller scale, that are in close association with ultramafic rocks of mafic-ultramafic intrusions, with mineralized or un-mineralized sulphide mineralization, for instance, the Qareaghaj mafic-ultramafic intrusion, northwestern Iran (Mirmohammadi *et al*., 2007). Fe-Ti-P ores in these two examples crosscut the host rocks of troctolite, and dunite and wehrlite, respectively.

Third, Fe-Ti±P±V oxide ore deposits in association with mafic layered intrusions. This include: (1) the Panzhihua-type Fe-Ti-V oxide deposits hosted in gabbroic layered intrusions (Pang *et al*., 2010, Zhou *et al*., 2013), which are a part of the ~260 Ma Emeishan Large Igneous Province (ELIP), southwestern China. (2) and some Fe-Ti±P±V deposits in association

with mafic layered intrusions that occur within massif-type anorthosite provinces. Examples of this sub-type are: the Fe-Ti-P-V ore deposits in the Fedorivka olivine-gabbroic layered intrusion in the Korosten anorthosite-rapakivi granite Pluton, Ukraine (Duchesne *et al.*, 2006) and in the Bjerkreim-Sokndal Layered intrusion, Southwest Norway (Wilson *et al.*, 1996), the Fe-Ti-P deposits in the MCU II of the Sept Iles Layered intrusion (Namur et al., 2012) and the Grader Layered Intrusion in the Grenville Anorthosite Province, Quebec, Canada (Charlier *et al.*, 2008). The ore bodies occur as conformable, massive lenses or layers with sharp or gradational contacts against host rocks of gabbro, norite, anorthosite or troctolite. The ore types vary from Fe-Ti oxide ore (Magnetite- or ilmenite-dominated) without apatite in the lower part, to oxide-apatite rich ore in the upper part of mafic intrusions as apatite joins the liquidus assemblage at a lower temperature.

Fourth, Fe-Ti±P±V ore deposits in association with alkaline ultramafic complex. This type is rare, the only reported deposit is the magnetite-apatite deposit in Fanshan alkaline ultramfic complex, northern China (Jiang *et al.*, 2004). The ores occur within the oldest pyroxenite-dominated ultramafic rocks, which is the middle zone surrounded by alkaline rocks in both inner and outer zones.

The Fe-Ti-P oxide deposits are also present in volcanic-subvolcanic environments (e.g. Kiruna-type magnetite-apatite deposits in Sweden and Chile, Harlov *et al.*, 2002; Nystroem & Henriquez, 1994). Fe-Ti±P oxide-rich gabbros have also been reported in the oceanic crust (Dick *et al.*, 2000; Mitsis & Economou-Eliopoulos, 2001). However, these rocks have both magmatic and hydrothermal features and their origin is still controversial (Bookstrom, 1995; Cliff & Rickard, 1992; Frietsch, 1978; Frietsch & Perdahl, 1995; Hildebrand, 1986; Lundberg & Smellie, 1979; Müller *et al.*, 2003; Nystroem & Henriquez, 1994; Nystrom *et al.*, 2008; Nystrom & Henriquez, 1995; Parak, 1975).

1.1.2 Petrogenetic Models

Several mechanisms have been proposed for the genesis of magmatic Fe-Ti±P±V oxide deposits, i.e. liquid immiscibility, fractional crystallization and crystal settling and sorting, magma mixing, periodic fluctuations of fO_2, and pressure changes. At present, the first two mechanisms are widely suggested for the origin of Fe-Ti±P±V oxide deposits in various magmatic intrusions. Cawthorn and Ashwal (2009) suggested multiple processes may have occurred during magnetite accumulation in the Upper Zone of the Bushveld Complex, and the latter three may occur along with crystal settling and sorting.

1.1.2.1 Liquid immiscibility

Immiscible liquids are commonly observed from natural lunar rocks (Jolliff *et al.*, 1999; Roedder & Weiblen, 1970; Shearer *et al.*, 2001), mesostasis of terrestrial tholeiitic basalts (De, 1974; Philpotts, 1979, 1982; Sensarma & Palme, 2013), melt inclusions in cumulates of large layered intrusions (e.g. Skaergaard, Jakobsen *et al.*, 2005, 2011); Bushveld (VanTongeren & Mathez, 2012), Sept Iles (Charlier *et al.*, 2011), and in many experimental studies of natural or synthetic materials (Bogaerts & Schmidt, 2006; Charlier & Grove, 2012; Lester *et al.*, 2013; Longhi, 1990; Mcbirney, 1975; Philpotts & Doyle, 1983; Veksler *et al.*, 2007). Oxygen isotope composition (Bindeman *et al.*, 2008), microstructures (Holness *et al.*, 2011), composition of plagioclase (Humphreys, 2011), and large-scale outcrop-sized melanogranophyre from the Upper Zone (Jakobsen *et al.*, 2005; McBirney, 1996), are suggested as evidence for liquid immiscibility in the Skaergaard intrusion. Ultramafic pegmatites in the Bushveld Complex (Scoon & Mitchell, 1994) and Duluth Complex (Ripley *et al.*, 1998) are also considered as products of immiscibility. Liquid immiscibility has also been postulated in anorthosite complexes (Darling & Florence, 1995) and mid-ocean ridge magma chambers (Dixon & Rutherford, 1979).

Experimental studies have shown that immiscibility usually develops at very late stage of tholeiitic magma differentiation (Bogaerts & Schmidt, 2006; Charlier & Grove, 2012; Lester *et al.*, 2013; Philpotts & Doyle, 1983). High temperature immiscibility has also been reported (e.g. Veksler *et al.*, 2007), however, it invoked a strong debate (McBirney, 2008; Morse, 2008; Philpotts, 2008; Veksler *et al.*, 2008). The immiscibility gap is strongly affected by melt structure and composition, H_2O and other volatile contents, and intensive parameters (oxygen fugacity, temperature and to a lesser extent pressure and cooling rate) (Charlier *et al.*, 2013, Lester *et al.*, 2013). The two immiscible liquids may preferentially accommodate certain major and trace elements (Bogaerts & Schmidt, 2006; Hurai *et al.*, 1998; Schmidt *et al.*, 2006; Veksler *et al.*, 2006; Watson, 1976).

Liquid immiscibility has been proposed for the genetic mechanism for some Fe-Ti±P±V oxide deposits in various magmatic intrusions, including the Upper Zone of the Bushveld Complex (Reynolds, 1985a, 1985b; VanTongeren & Mathez, 2012; Von Gruenewaldt, 1993), Duluth Complex (Ripley *et al.*, 1998), Sept Iles layered intrusion (Charlier *et al.*, 2011; Namur *et al.*, 2012), Panzhihua-type layered intrusions (Wang & Zhou, 2013; Zhou *et al.*, 2005, 2008, 2013), and many others (Kolker, 1982).

1.1.2.2 Crystal settling and sorting

Gravity settling and sorting of early crystallized minerals was first proposed by Wager and Brown (1968) for the formation mechanism of the Skaergaard Intrusion, and later it has inspired a great number of subsequent followers and also many critics studying igneous differentiation (Campbell, 1977, 1978; Cawthorn, 1996, and references therein). A strong indication of crystal settling and sorting is the development of gradational layers and graded modal relationships observed in large layered intrusions (Cawthorn *et al.*, 2005; Eales & Cawthorn, 1996; McBirney, 1996). On the other hand, *in-situ* crystallization was proposed as a mechanism against standard crystal settling theory (Campbell, 1978; Cawthorn & McCarthy, 1980, 1981; McCarthy & Cawthorn, 1983).

In contrast to the liquid immiscibility hypothesis, many workers have suggested magmatic Fe-Ti±P±V oxide deposits and their host rocks have crystallized from Fe-Ti rich mafic magmas (Bai *et al.*, 2012; Charlier *et al.*, 2007, 2009; Duchesne, 1999; Dymek & Owens, 2001; Lee, 1996; Morisset, 2008; Namur *et al.*, 2010, 2012; Pang *et al.*, 2008a, 2008b, 2009; Song *et al.*, 2013; Tollari *et al.*, 2008). Based on their occurrence in the intrusions, Fe-Ti oxides may have appeared at a later stage, for example, the magnetite layers appear in the Upper Zone of the Bushveld Complex (Eales & Cawthorn, 1996); or as early liquidus phases, such as the Panzhihua layered intrusion (Pang *et al.*, 2008a), the Grader layered intrusion (Charlier *et al.*, 2008), the Bjerkreim-Sokndal layered intrusion (Wilson *et al.*, 1996), the Tellness (Charlier *et al.*, 2007) and the Allard Lake ilmenite deposit (Charlier *et al.*, 2010). Many experiments on basaltic compositions have shown magnetite saturates early at high fO_2 condition (Botcharnikov *et al.*, 2008; Toplis & Carroll, 1995). Crystallization modeling with the MELTs program (Ghiorso & Sack, 1995) has shown magnetite crystallization at high temperature (Pang *et al.*, 2008a). It is noteworthy that apatite arrives on the liquidus much later than Fe-Ti oxides, as indicated by its higher stratigraphic position in many layered intrusions (Namur *et al.*, 2010; Pang *et al.*, 2008b; Von Gruenewaldt, 1993), results from MELTs modeling (Pang *et al.*, 2008a; Shellnutt & Jahn, 2010; Song *et al.*, 2013) and crystallization experiments (Snyder *et al.*, 1993; Tollari *et al.*, 2006; Toplis *et al.*, 1994; Watson, 1979).

1.1.2.3 Magma mixing and changes in intensive parameters (fO_2 and pressure)

Magma mixing events may occur during ascent and/or emplacement, where a less evolved magma mixes with a residual evolved magma, or magma contaminated by country rocks. Harney *et al.* (1990) observed two contrasting platinum-group element (PGE) dis-

tribution patterns in rocks below and above the Main magnetite layer in the Upper Zone of the Bushveld Complex. They interpreted the magnetite accumulation as a result of a magma mixing event. Tegner *et al*. (2006) suggested that crystallization of the magnetite ore and the above nelsonite may relate to a mixing event of a stratified magma caused by periodic density inversion. Clark and Kontak (2004) have suggested that mixing of mafic and felsic magmas may produce Fe-Ti-P oxide melts, which have formed nelsonite in the Antauta Subvolcanic Center in Peru. Charlier *et al*. (2010) suggested that the ilmenite enrichment in the Allard Lake deposit (Canada) has resulted from two magmas mixing, enhanced by multiple injections and plagioclase flotation. Song *et al*. (2013) attributed the cyclic units in the Panzhihua Intrusion to periodic replenishment and mixing of more primitive magmas with evolved residual magmas on the floor of the magma chamber.

As magnetite saturation is strongly dependent on fO_2 of the magma (Botcharnikov et al., 2008; Toplis & Carroll, 1995), periodic fluctuations of fO_2 have been suggested as a mechanism for the formation of magnetite layers in the Upper Zone of the Bushveld Complex (Klemm *et al*., 1985). By analogy with the origin of chromitite layers (Cawthorn, 2005), an increase in pressure has also been proposed as the trigger of magnetite crystallization in the Upper Zone of Bushveld Complex (Cawthorn & McCarthy, 1980), and the origin of disseminated randomly-distributed plagioclase in the magnetitite layers (McCarthy & Cawthorn, 1983). The effect of changing pressure on Fe-Ti oxide formation was also highlighted in the Panzhihua-type gabbroic layered intrusion (Pang *et al*., 2008b; Song *et al*., 2013; Zhong *et al*., 2003) and Suwalki anorthosite (NE Poland) (Charlier *et al*., 2009).

1.2 Previous Work on the Panzhihua-type Fe-Ti-V Oxide Ore Deposit

The term "*Panzhihua-type Fe-Ti-V oxide deposits*" refers to the deposits associated with four large gabbroic layered intrusions within the central zone of the ~260 Ma Emeishan Large Igneous Province (ELIP), SW China. It is named after the most representative example - the Panzhihua Fe-Ti-V oxide deposit, which was discovered (~ late 1930s) and mined (from ~ early 1970s) first, and is the largest V-Ti bearing magnetite and ilmenite deposit in China. The Panzhihua deposit, along with Hongge, Baima, Taihe and Xinjie in the Panzhihua-Xichang (Panxi) district, account for 1333 Mt Fe-Ti-V ore reserves (Ma *et al*., 2003; Yao *et al*., 1993). Recent data have shown this area to contain ~10 billion tones proven ores and potentially the double amount of ore resources[1]. Reviews of mineralization in the ELIP were given by Song

1. Online data from the Ministry of Land and Resources of the People's Republic of China:

et al. (2005), Hu *et al*. (2005), Zhong *et al*. (2005), Zhou *et al*. (2008) and Pang *et al*. (2010). Pang *et al*. (2010) classified the Fe-Ti-V oxide deposits in the Panxi district as a new type based on comparison with worldwide important Fe-Ti oxide deposits in massif-type anorthosite, and layered intrusions.

Detail geological and petrological features of the Panzhihua-type deposits and host rocks were described in 1980s to early 1990s (Li & Mao, 1982; Li, 1992; Lu *et al*., 1989; PXGT, 1981; SBGMR, 1991; Song *et al*., 1994; Wang, 1982). During late 1990s and early 2000s, many attempts were made on explaining the formation of layering in the Panzhihua gabbroic intrusion (Luo, 2003; Ou & Jin, 2000; Sang & Jin, 2001; Song *et al*., 1997, 1999).

Zhong *et al*. (2002, 2003) first published their results of geochemical studies on the PGE-bearing Hongge Fe-Ti-V deposits in the international journals. Geochronological data have shown that these gabbroic layered intrusions and associated mineralization are contemporaneous with the ELIP (Shellnutt et al., 2009; Zhong & Zhu, 2006; Zhong et al., 2009; Zhou et al., 2002, 2005, 2008), and are genetically related to the high-Ti type of Emeishan basalts and picrites, which were likely derived from a garnet-bearing mantle source and undergone weak crustal contamination (Song *et al*., 2006; Wang *et al*., 2007; Xiao *et al*., 2004; Xu *et al*., 2001; Zhang *et al*., 2006). Geochemistry and isotope studies on more evolved rocks in the vicinity of the gabbroic layered intrusions have suggested a common temporal and spatial relationship (Shellnutt & Jahn, 2010; Shellnutt & Zhou, 2007; Zhong *et al*., 2007, 2009).

The parental magma is believed to be enriched in Fe and Ti (ferrobasalt), as inferred from a weighted average composition of 32 rocks from the Lanshan cross-section of the Panzhihua intrusion (Wang, 1982), or mass balance calculations (Zhang *et al*., 2009; Zhou *et al*., 2005). The bulk composition (Mg#=0.46) calculated by Zhou *et al*. (2005) is comparable to microgabbro from the marginal zone of Panzhihua intrusion (Pang, 2008). This liquid was suggested to be in equilibrium with Ol (Fo82) and had a Mg# of 0.56 (Pang *et al*., 2009). Fe-Ti rich basaltic or picritic magma has been accepted as parental magma to the Panzhihua-type deposits and host rocks.

Zhou *et al*. (2005) suggested the Fe-Ti rich liquid was formed by extreme fractionation of basaltic magma beneath or adjacent to the Panzhihua magma chamber. Pang *et al*. (2008b) compared the bulk composition of Zhou *et al*. (2005) with experimental results of Whitaker *et al*. (2007), and suggested Fe-Ti-rich liquid may have formed at a depth of ~10 Kbar, and emplaced at 5 Kbar. In contrast, more recent studies have advocated much shallower polyba-

http://www.mlr.gov.cn/tdzt/dzgz/dzzkgg1/gzdt/200907/t20090707_692580.htm

ric fractionation processes (e.g. 0.7-5 Kbar, Bai *et al.*, 2012; Ganino *et al.*, 2008; Hou *et al.*, 2012a; Howarth *et al.*, 2013a; Shellnutt & Jahn, 2010; Shellnutt & Pang, 2012; Song *et al.*, 2013; Zhang *et al.*, 2012).

According to geochemical and isotopic data (Pang, 2008; Song *et al.*, 2013; Zhang *et al.*, 2009; Zhou *et al.*, 2005), the Panzhihua-type parental magma had undergone little crustal contamination before emplacement, consistent with that of genetically related high-Ti basalts (Qi & Zhou, 2008; Song *et al.*, 2008; Xiao *et al.*, 2004; Xu *et al.*, 2001).

Crystallization modeling studies of the Panzhihua-type parental magma differentiation have resulted in a range of suggested fractionating mineral assemblages prior to magnetite saturation: olivine alone (Hou *et al.*, 2012b; Pang *et al.*, 2008a), olivine+clinopyroxene+Cr-spinel (Bai *et al.*, 2012), Cr-spinel+olivine+clinopyroxene+plagioclase (Song *et al.*, 2013), oliv ine+clinopyroxene+plagioclase (Ganino *et al.*, 2008; Shellnutt & Pang, 2012), and olivine+ch romite+orthopyroxene+clinopyroxene+plagioclase (Zhang *et al.*, 2012).

The Panzhihua-type gabbroic intrusions are generally accepted as open magmatic systems (Hou *et al.*, 2012b; Pang *et al.*, 2008b, 2009; Shellnutt & Jahn, 2010; Shellnutt & Pang, 2012; Song *et al.*, 2013; Zhong *et al.*, 2003; Zhou *et al.*, 2005). Pang *et al.* (2009) observed two major reversals in compositions of silicate minerals, and suggested they reflect replenishment events by a new primitive magma during accumulation of the Panzhihua intrusion. Zhang *et al.* (2011) and Song *et al.* (2013) interpreted several cyclic units as a response to periodic replenishments of less evolved magmas along the floor. Zhang *et al.* (2012) also attributed reversals across cyclic units in the Baima gabbroic layered intrusion to magma replenishments. Zhong *et al.* (2003, 2005) and Bai *et al.* (2012) have also explained compositional reversals across cyclic units with new primitive magma injections. Low Zr concentration in the Panzhihua has lead Pang *et al.* (2009) to speculate a significant loss of residual liquid to form coeval more evolved peralkaline granites. The Panzhihua gabbroic intrusion was suggested to be a part of a more complex magmatic system, which also includes spatially and temporally associated syenite and peralkaline A-type granitic pluton (Shellnutt & Jahn, 2010; Zhou *et al.*, 2013). Similarly, Shellnutt and Pang (2012) suggested the gabbroic unit, together with syenite of the Baima Igneous Complex, represent a closed magmatic system.

Two contrasting models have been proposed for the origin of Panzhihua-type Fe-Ti-V oxide ores. Liquid immiscibility hypothesis was first applied to the Panzhihua deposit by Zhou *et al.* (2005), and later to the Baima and Hongge deposits (Zhou *et al.*, 2008; Wang & Zhou,

2013), and economically less important Anyi and Mianhuadi deposits (Zhou *et al*., 2013). On the basis of mainly textural observations, these authors suggested magnetite crystallized from Fe-Ti rich melt that segregated from extremely evolved silicate magma. Hou *et al*. (2012b) proposed that various cumulates in the Panzhihua intrusions represent solidified liquids which had been stratified at depths due to olivine fractionation and double-convective diffusion.

On the other hand, according to petrographic observations, geochemistry data, and crystallization modeling, many other workers preferred an alternative genetic model for the Panzhihua-type Fe-Ti-V oxide deposits (Bai *et al*., 2012; Ganino *et al*., 2008, 2013; Howarth & Prevec, 2013b; Howarth *et al*., 2013a, Pang *et al*., 2008a, 2008b; Shellnutt & Jahn, 2010; Shellnutt & Pang, 2012; Song *et al*., 2013; Zhang *et al*., 2011, 2012). This model, magnetite and ilmenite were early fractionated phases during the Panzhihua-type magma differentiation. Fractional crystallisation followed by crystal settling and sorting, has been suggested as the mechanisms for ore formation. The trigger for the onset of Fe-Ti oxide crystallisation is commonly thought to be an increase in fO_2 due to assimilation by dolomitic wall-rocks.

1.3 Aims of the Project

This project is focused on the Panzhihua Intrusion and Taihe Intrusion with an aim of better understanding the petrogenesis of the Panzhihua-type Fe-Ti-V oxide mineralization, given the current controversy described in the previous section. Specific aims of the project include:

(1) To assess the nature of the Panzhihua magmatic system. Although it is commonly considered to be a system which is subject of fluctuations in oxygen fugacity during magma emplacement, the processes that resulted in the formation of the layered intrusion are poorly understood.

(2) To assess the origin of Fe-Ti rich parental magma. It has been commonly accepted that the parental magma of Panzhihua-type Fe-Ti oxide ores is enriched in Fe and Ti. However, the genesis of this magma is controversial. Convincing evidence is largely lacking for common conclusions that several new pulses of magma with more primitive compositions have been emplaced during the formation of the layered intrusion.

(3) To better understand magma emplacement and differentiation. It is well accepted that all Panzhihua-type intrusions were not formed by a single pulse of magma. However, the nature and origin of several cryptic compositional reversals observed in the Lower Zone and

Middle Zone A of the Panzhihua Intrusion, and their significance in the formation of Fe-Ti oxide ores requires further evaluation.

(4) To constrain the mechanism of the formation of Fe-Ti oxide ores, either fractional crystallization or liquid immiscibility. More evidence is needed to better constrain the genesis of Panzhihua-type Fe-Ti oxide ores.

(5) To understand the link between magnetite and sulphide saturation. Multi-stage segregations of immiscible sulphide liquids have been advocated for the depletion of PGE in sulphides which appear throughout the Panzhihua Intrusion. Previous studies have shown magnetite crystallization may have trigger sulfide saturation (Jenner *et al.*, 2010; Maier *et al.*, 2003). However, if this is the case in Panzhihua, needs to be assessed.

(6) Detailed textural investigations on rocks and ores from the Panzhihua and Taihe gabbroic layered intrusions, and new high-quality whole rock and mineral compositions obtained in this study significantly expand the existing set of data on Panzhihua-type Intrusions. Trace elements in Fe-Ti oxides and pyrrhotite from both intrusions measured in-situ using LA-ICP-MS technique have not been reported previously. The data obtained are used to better constrain the origin of ferro-basaltic magma, its emplacement and differentiation in a shallow magma chamber, and saturation of magnetite and sulphide in the Fe-Ti rich silicate magma.

1.4 Research Methods

The aims of this study are addressed on the basis of chemical compositions measured using state-of-the-art analytical facilities at CODES and Central Sciences Laboratory (CSL) at the University of Tasmania. Data generated during this study are integrated with previous published and unpublished data, with the purpose of providing internally consistent interpretation of the geochemical data, and developing a new model for the origin of the parental magma, its differentiation, saturation of oxides and sulphides, and ore formation.

Laboratory work include (1) sample preparation; (2) petrographic investigation using optical microscopy; (3) measurement of mineral modal proportions in selected samples using Mineral Liberation Analysis (MLA); (4) whole-rock major and trace element compositions analysed by XRF and solution ICP-MS, respectively; (4) mineral major and trace element composition determined using the EMPA and LA-ICP-MS techniques, respectively. Except for MLA and EMPA, which are operated by the Central Sciences Laboratory, the other analyses were performed using CODES analytical facilities. Sample preparation procedures and

analytical techniques used in this study are described in Appendix I.

1.5 Thesis Structure

This thesis consists of seven chapters.

Chapter 2 provides an overview of regional geology and mineralization in the Panxi area, and the local geology and litho-stratigraphy of the Panzhihua and Taihe gabbroic layered intrusions.

Chapter 3 describes key petrographic features of the samples from both intrusions, with a special emphasis on ore textures.

Chapter 4 presents the results of geochemical studies, including whole-rock and mineral major and trace element compositions.

Chapter 5 presents geochemical variations as a function of stratigraphic height. These variations bear important information on differentiation processes operating in mafic magma chambers.

Chapter 6 describes numerical modelling of mafic magma differentiation with Petrolog3 software.

Chapter 7 discusses several aspects of magma chamber processes, Fe-Ti oxide ore formation mechanism, and sulfide saturation history. A new petrogenesis model is developed for the Panzhihua-type Fe-Ti-V oxide deposits.

Chapter 8 summarizes the main findings of this work and its contribution to the understanding of the origin of parental magma, its evolution and metallogenesis. Possible future research directions are also discussed.

CHAPTER 2

GEOLOGICAL BACKGROUND

2.1 Introduction

This chapter starts with the introduction of the tectonic framework of China, with a special emphasis on the western margin of the Yangtze Block and the eastern part of the Tibetan Plateau, where the Emeishan large igneous province (ELIP) is located. This is followed by a general introduction to the ELIP. Finally, local geology of the Panzhihua and Taihe intrusions, which are the interests of this study, is described.

2.2 Tectonic Setting

From the global view of plate tectonics, the most of China belongs to the Eurasian plate; with only a small part in the Himalayas and the Coastal Range of Taiwan belonging to the peripheral portions of the Indian plate and the western margin of the Philippine Sea plate, respectively (Zhang *et al.*, 1984). Fig. 2.1 shows main Precambrian cratons and accretionary fold belts, which constitute the tectonic framework in China.

The South China Block is composed of the Yangtze Block in the northwest and the Cathaysian Block in the southeast. It is annealed to the North China Craton by the Qinling-Dabie orogenic belt to the north and borders the Tibetan Plateau by the Longmenshan thrust fault to the west. The boundary between the Yangtze Block and the Cathaysian Block is approximately along the southern margin of the Banxi Group. The geology of the western margin of the Yangtze Block and the eastern part of the Tibetan Plateau are introduced briefly below.

2.2.1 The Western Margin of the Yangtze Block

The Yangtze Block consists of the 3.8 Ga old Yangtze Craton which is overlaid by Mesoproterozoic to Cenozoic sedimentary rocks (e.g. Zhang *et al.*, 2006). Exposures of most basement rocks occur at the periphery only (Zhang *et al.*, 1984). Current understanding of the evolution of the Yangtze Craton is derived mainly from the studies of the periphery rocks. The Yangtze continental nucleus was formed by multi-stage reworking of the Archean crustal

material in Paleoproterozoic to Mesoproterozoic (Zhang *et al.*, 2006; Zhang & Zheng, 2007).

The overlying cover consists of Mesopoterozoic meta-sedimentary rocks of low-grade green-schist facies, and Neoproterozoic igneous rocks including granites and associated calc-alkaline basalts, andesites and rhyolites. A series of metamorphic complexes that are spatially associated with the Neoproterozoic granites occur as tectonic domains over a distance of more than 700 km in the north-south direction. They are regarded as the basement of the Yangtze Block and known as the Kangdian Grey gneisses (He *et al.*, 1988). The major complexes in the study area include, from north to south, the Kangdian complex, Miyi complex, and Yuanmou complex.

A number of Neoproterozoic intrusions in the northernmost and western Yangtze Block have been dated at 840-750 Ma (Huang *et al.*, 2008; Munteanu *et al.*, 2010; Zhou *et al.*, 2002; Zhu *et al.*, 2006, 2007). The extensive Neoproterozoic magmatism in SW China has been ascribed either to the activity of a mantle plume associated with the breakup of Rodinia (Li *et al.*, 1999, 2003), or to continental crust subduction (Zhou *et al.*, 2006a, 2006b), or anorogenic intra-continental rift setting (Huang *et al.*, 2008). In addition, the presence of ~ 1000 Ma ophiolites and 900 Ma granodiorites along the southeastern margin of the Yangtze Block suggests a Neoproterozoic collision between the Yangtze and Cathasia Blocks (Chen *et al.*, 1991). Thus, the Yangtze Block was surrounded by subduction zones and active continental margins in the Neoproterozoic.

Studies on the paleomagnetism have shown that, from Cryogenian period in Neoproterozoic to Fransnian age in the Devonian (around 750-380 Ma), the South China block was connected to Gondwana (Enkin *et al.*, 1992; Lin *et al.*, 1985; Yang *et al.*, 2004). The South China block rifted from Gondwana and moved toward the North China block during late Devonian time. The collision event of the South China block and North China block might have lasted for a very long period from the middle Paleozoic to the Early Permian and the Middle Jurassic (Roger *et al.*, 2010). By the time of Late Triassic, the South China block subducted northward under the North China block, inducing the closure of Songpan-Ganze Ocean. The Tertiary orogeny caused by the India-Asia collision led to the Songpan-Ganze prism thrust onto the South China passive margin and hence a significant shortening and crustal thickening of the blocks involved (Roger *et al.*, 2010).

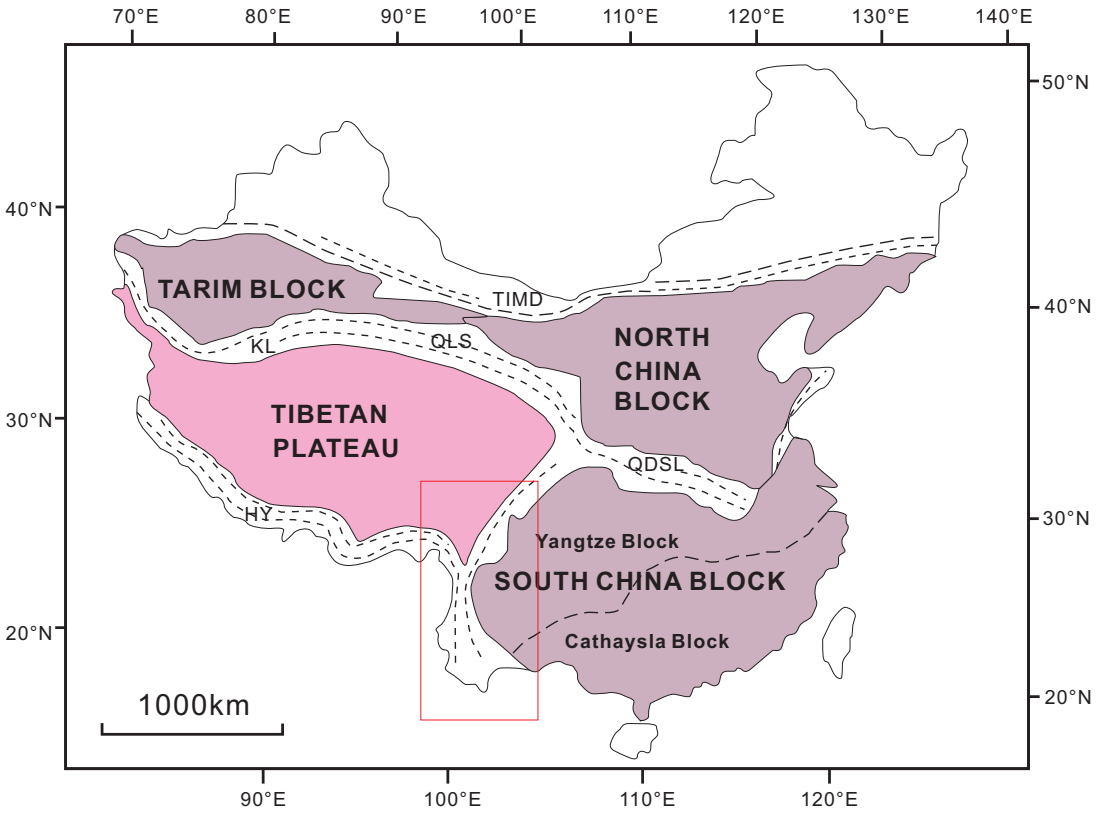

Fig. 2.1 Simplified tectonic map of China showing major tectonic blocks (modified after (Pang, 2008). HY=Himalaya fold belt, KL=Kunlun fold belt, QDSL=Qinlin-Dabie-Su-Lu fold belt, QLS=Qilianshan fold belt, TIMD=Tianshan-Inner Mongolia-Daxinganling fold belt. The rectangle shows the general scope of ELIP (see Fig. 2.2).

2.2.2 The eastern Tibetan Plateau (Songpan-Ganze terrane)

The Tibetan Plateau is composed of the Lhasa, Qiangtang, Yidun, and Songpan-Ganze terranes (Yin & Harrison, 2000). The Songpan-Ganze terrane is located in the easternmost part of the Tibetan Plateau and the west of the Sichuan basin. It is bounded by three subduction zones which were active synchronously during the Late-Permian to Early Jurassic: on the north by the Kunlun-Animaqing suture from the Kunlun orogenic belt (Yang *et al.*, 1996), on the east by the Longmenshan thrust belt from the South China Block (Burchfiel *et al.*, 1995), and on the west and SW by the Jinsha suture from the Qiangtang terrane (Zhang *et al.*, 1984). It undergone subsequent convergence between the North China, South China and the Qiangtang blocks, which induced the closure of the Songpan-Ganze oceanic basin (Roger *et al.*, 2010). The existence of the oceanic basin is supported by a thick sequence (up to more than 10km) of the late Triassic sedimentary strata of deep marine origin (Enkelmann *et al.*, 2007; Yin *et al.*, 1998). The Neoproterozoic and Paleozoic rock assemblages in the Songpan-Ganze terrane are comparable with those at the western margin of the Yangtze Block (Song *et*

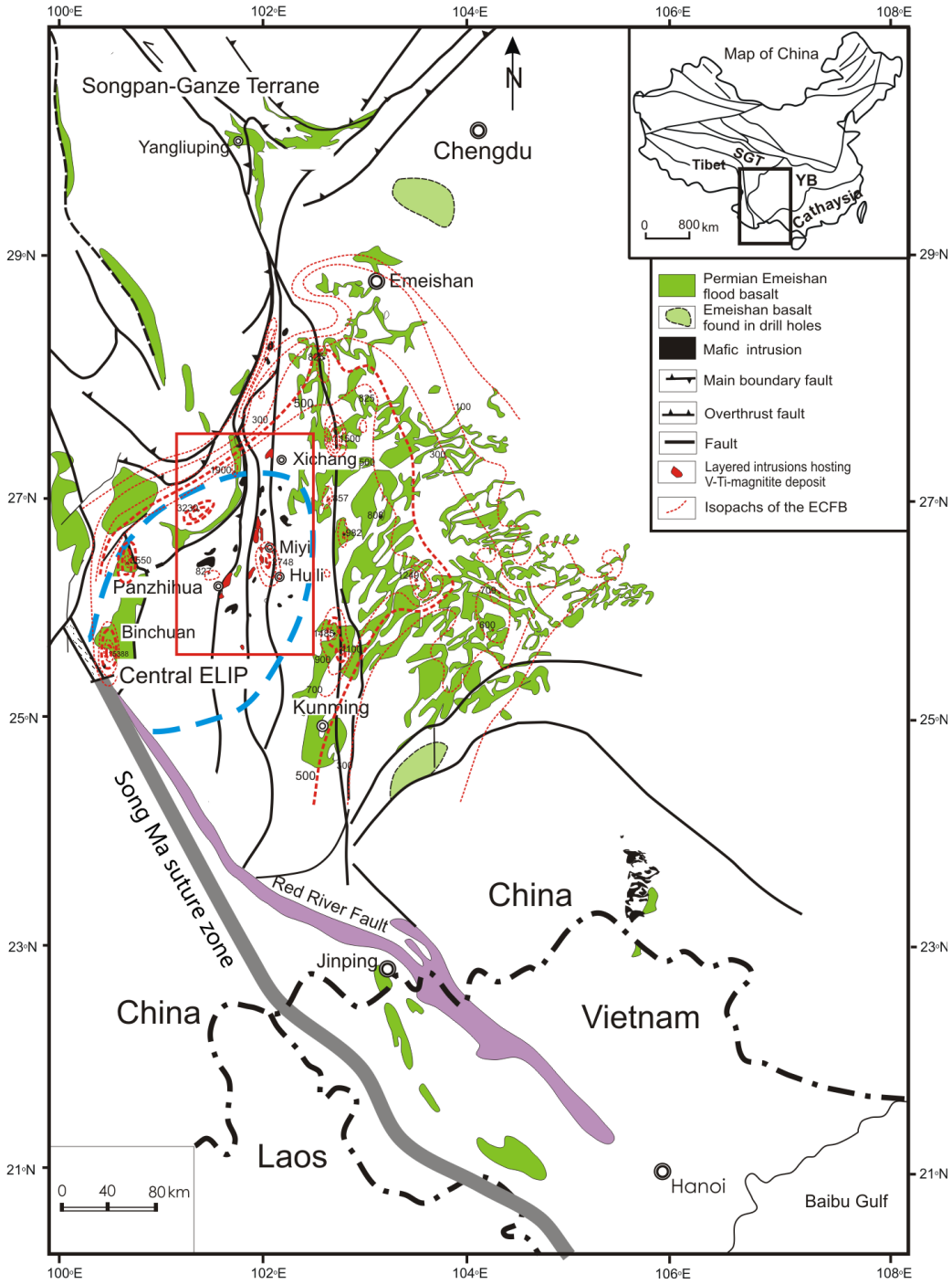

Fig. 2.2 Generalized geological map showing the distribution of basaltic rocks and associated mafic-ultramafic intrusions in the ELIP, SW China (SBGMR, 1991; Song *et al.*, 2008a).

al., 2004) .

2.3 Emeishan Large Igneous Province (ELIP)

The Emeishan large igneous province (ELIP), occupies the western part of the Yangtze Block and the eastern margin of the Tibetan Plateau, is generally referred to a rhomboidal in

shaped magmatic province in SW China and northern Vietnam (Fig. 2.2). It is defined by the distribution of massive late Permian continental flood basalts and spatially and temporally closely correlated sub-volcanic intrusions. The province has attracted extensive research and economic interests over the past decade. It is widely related to the ~260 Ma Emeishan mantle plume (Chung and Jahn, 1995; Xu *et al.*, 2001; Ali *et al.*, 2005). Below is a description of the general features of the ELIP, including continental flood basalts, spatially and temporally related mafic-ultramafic intrusion, and associated mineralization.

2.3.1 Continental Flood Basalts

The Emeishan Continental Flood Basalts (ECFB) covers an area in excess of ~2.5 $\times 10^5$ km^2 (Chung & Jahn, 1995; Zhang *et al.*, 1988). The original size has been speculated to exceed 5×10^5 km^2, including the eastern part of the Songpan-Ganze terrane in the west (Song *et al.*, 2004; Xiao *et al.*, 2004b), Jinping-Song Da district in the south (Wang *et al.*, 2007; Xiao *et al.*, 2003b), and Funing area in the northeast (Zhou *et al.*, 2006c).

The underlying Maokou Formation, which is a main constituent of the Permian carbonate platform widespread in south China, consists mainly of 250 to 600 m thick medium-bedded to massive limestones with abundant fossils, including foraminifera, algae, brachiopods, ostracods, echinoderms, gastropods, bivalves and corals (Ali *et al.*, 2005; He *et al.*, 2003). It was deposited across most of a largely submerged South China platform. Biostratigraphic and sedimentologic investigations of the Maokou Formation have revealed the existence of pre-eruption uplift and hence the dome structure of the ELIP (He *et al.*, 2003). Based on the extent of erosion or thinning of the Maokou Formation, the ELIP has been divided into three zones: the inner zone, the intermediate zone, and the outer zone (Xu *et al.*, 2004). The inner zone has the strongest erosion and is bounded by the Xiaojiang fault to the east, the Xichang-Qianjia fault to the northeast, and the Jinhe fault to the northwest. The extent of erosion decreases outwards and is generally minor in the outer zone. The inner zone and the outer zone are considered to correspond to the plume head and the peripheries of the mantle plume, respectively (Xiao *et al.*, 2004a; Xu *et al.*, 2001).

The Emeishan volcanic succession is predominantly basaltic flows and pyroclastics, with minor amounts of picrites and basaltic andesites (Chung & Jahn, 1995; Hanski *et al.*, 2004; Qi & Zhou, 2008; Song *et al.*, 2001; Wang *et al.*, 2007; Xiao *et al.*, 2003a, 2004a; Xu *et al.*, 2001; Zhang *et al.*, 2006b). The volcanic rocks overlie the Early Permian Maokou Formation of limestone, and is overlain by the Late-Permian Xuanwei formation of sandstone and mud-

stone with inter-bedded coal seams. The thickness of the entire volcanic succession decreases from over 5 km in the west (e.g. Binchuan, 5384m; Daju, 5500m), to a few hundred meters in the eastern part of the province (e.g. Qinyin, 270m; Ertan, 1009m) (Xu *et al.*, 2001, 2004; Zhang *et al.*, 2006b).

The Emeishan continental flood basalts have been divided into high- and low-Ti groups on the basis of Ti/Y ratios and TiO_2 contents of the Bingchuan and Ertan basalts (HT, Ti/Y>500, TiO_2>2.5 wt%; LT, Ti/Y<500, TiO_2<2.5 wt%) (Xu *et al.*, 2001). These rocks are different in spatial distribution and petrographic characteristics. For example, High-Ti basalts and alkaline lavas mainly occur on the periphery of the ELIP, whereas the low-Ti basalts and picrites are more abundant in the inner zone. At a given location, the low-Ti basalt is overlain by the high-Ti basalt (Xiao *et al.*, 2003a; Xu *et al.*, 2004). High-Ti basalts usually contain clinopyroxene and/or plagioclase phenocrysts, whereas low-Ti basalts are mostly aphyric (Xiao *et al.*, 2003a; Xu *et al.*, 2001). High- and low-Ti basalts have distinct mantle sources and variable degrees of crustal contaminations (Song *et al.*, 2008a; Wang *et al.*, 2007; Xiao *et al.*, 2004a; Xu *et al.*, 2001).

However, recently published data have cast doubt on the validity of the original subdivition into two separate groups (Hao *et al.*, 2004; He *et al.*, 2010; Hou *et al.*, 2011; Shellnutt & Jahn, 2011). For example, basalts with intermediate TiO_2 contents have been reported in Lijiang area, which could not be grouped into either high-Ti or low-Ti group (Hao *et al.*, 2004). Moreover, high-Ti basalts have also been reported form the inner zone, whereas low-Ti basalts are also found in the outer zone (Hou *et al.*, 2011; Shellnutt & Jahn, 2011). The spatial separation of the two groups is not as rigorous as suggested previously. Finally, differences in geochemistry between the two types of basalts may result from fractional crystallization process (Hou *et al.*, 2011), or various degrees of partial melting of the same mantle source (Shellnutt & Jahn, 2011).

2.3.2 Picrites

High magnesium picrites have been reported in many places, such as Lijiang, Dali, Jinping-Song Da, Panzhihua, Yiyang, and Muli area, most of which concentrated in the western and southern parts of the ELIP (Fig. 2.2) (Chung & Jahn, 1995; Hanski *et al.*, 2004, 2010; Kamenetsky *et al.*, 2012; Li *et al.*, 2012; Song *et al.*, 2001; Wang *et al.*, 2007; Xu *et al.*, 2001; Zhang *et al.*, 2006b, 2008).

Picrite flows occur intercalated with basaltic lavas at different stratigraphic positions of

volcanic successions (Xiao *et al.*, 2004a; Xu *et al.*, 2004; Zhang *et al.*, 2006b). For example, in the Binchuan section, picrite flows occur both within the High-Ti basalts, and the underlying Low-Ti basalts. Picrites occur at the lowermost, middle, and upper part of the Daju section, which is about 5500 m thick and is by far the thickest volcanic succession, which occurs near the city of Lijiang. The thickness of individual picrite flows varies from several meters up to 50m in some areas.

Picrites from different locations show similar petrographic features. Most of the picritic flows are highly porphyritic. Magnesium-rich olivine is the most abundant phenocryst (7~15 vol%), with minor diopsidic clinopyroxene. Olivine forsterite content usually ranging from Fo80 to Fo90, with some up to Fo93 (Hanski *et al.*, 2010). Olivine phenocrysts are usually altered to serpentine, with rare fresh cores. The groundmass is most often holocrystalline, consisting mainly of very fine grained anhedral clinopyroxene and plagioclase crystals. In some samples, it is composed of devitrified glass with needles of clinopyroxene (Hanski *et al.*, 2004; Wang *et al.*, 2007).

2.3.3 Mafic-ultramafic Intrusions and Related Mineralization

Hundreds of mafic-ultramafic intrusions are exposed along a N-S trending fault in the ELIP, especially within the Panzhihua-Xichang (Panxi) district (Fig. 2.3). This area was a focus of intensive research over the past decades due to common occurrence of two important magmatic ore deposit types: Cu-Ni-(PGE) sulphide deposits and Fe-Ti-V oxide deposits. The former is genetically associated with small ultramafic-mafic intrusions (e.g. Yangliuping, Jinbaoshan, Baimazhai, etc), and the latter is found within large layered mafic intrusions (e.g. Panzhihua, Baima, Honghe, Taihe, etc). Xinjie layered intrusion is regarded as a transitional type and hosts both types of mineralization.

Geochemical studies have shown that the small ultramafic-mafic intrusions and related magmatic sulphide deposits are genetically associated with the low-Ti basalts, whereas the large layered intrusions hosting Fe-Ti-V oxide deposits are associated with the high-Ti basalts (Hu *et al.*, 2005; Pang *et al.*, 2010; Song *et al.*, 2005; Zhou *et al.*, 2008). Geochronological studies have confirmed that the intrusions are contemporaneous with the Emeishan basalts, which were erupted ca. 260 Ma (Tao *et al.*, 2009; Zhong & Zhu, 2006; Zhong *et al.*, 2009; Zhou *et al.*, 2002, 2008).

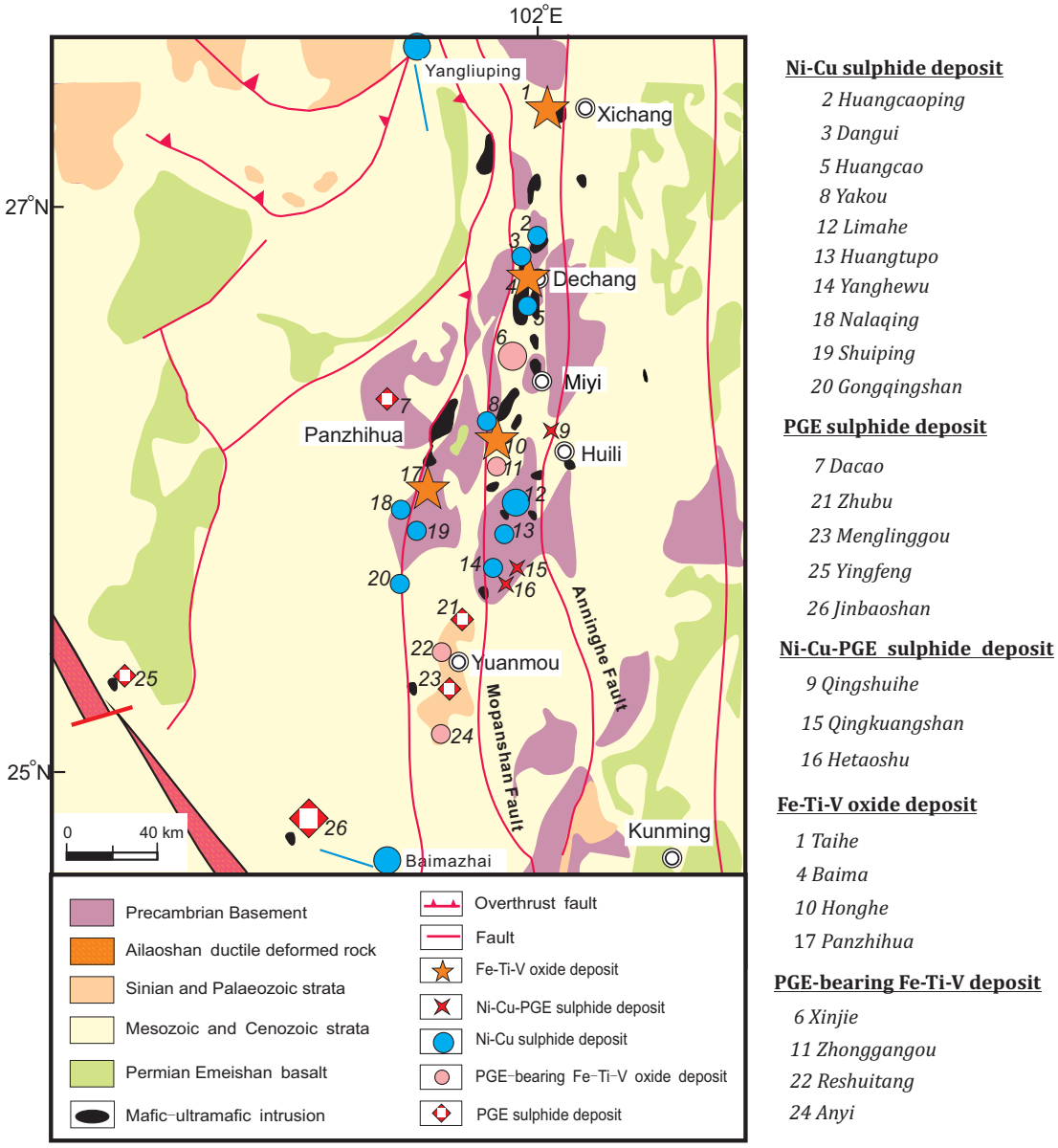

Fig. 2.3 Generalized geological map of the Panxi area, showing the distribution of mafic-ultramafic intrusions and associated various types of mineralization. (Modified after Song *et al.*, 2001).

2.3.3.1 Magmatic Ni-Cu-(PGE) sulphide deposits

Over 40 small ultramafic-mafic intrusions have been found to host magmatic Ni-Cu-(PGE) sulphide deposits or contain disseminated sulphides (Song *et al.*, 2005). Among them, Jinbaoshan, Yangliuping, Baimazhai, Limahe, and Zhubu are economically important and hence well-studied (Song *et al.*, 2003, 2008b; Tao *et al.*, 2007, 2008, 2009; Wang & Zhou, 2006; Wang *et al.*, 2008; Zhou *et al.*, 2008). These intrusions are found in both the central and outer zones of the ELIP. For instance, Jinbaoshan and Limahe are in the central zone, whereas Yangliuping in the north and Baimazhai in the south are in the outer zone (Fig 2.3).

The intrusions are hosted in Precambrian basement, Sinian and Palaeozoic strata. These intrusions are commonly small, generally reaching no more than several square km. The Baimazhai, Limahe, and Zhubu intrusions are concentric bodies, and the Jinbaoshan and Yangliuping intrusions are sill-like bodies. Sulphide deposits occur in the core part of the concentric-shaped intrusions, whereas in the sill-like intrusions, sulphide ores occur at the base or in the lower part of the intrusions. In each case, sulphide mineralization is associated with the ultramafic phases (Song *et al*., 2003; Tao *et al*., 2007, 2008; Wang & Zhou, 2006; Wang *et al*., 2008; Zhou *et al*., 2008). For instance, Pt-Pd ore layers occur within wehrlite of Jinbaoshan, Ni-Cu ores appear within orthopyroxenite of Baimazhai, and Ni-Cu-PGE ores lie within serpentinite in Yangliuping. The overlying mafic phases, mainly gabbro, are usually barren.

Based on the chalcophile and siderophile metal contents, the magmatic sulphide deposits in the ELIP have been divided into PGE, Ni-Cu-PGE and Ni-Cu types (Song *et al*., 2008b). Jinbaoshan and Zhubu are two deposits with significant PGE contents and small amounts of sulphides (1-2 vol %). The on-going exploration has revealed approximately 45 tons of Pt + Pd, with a grade range from 1 to 5 ppm and rarely up to 17 ppm (Tao *et al*., 2007). Typical Ni-Cu-PGE deposits are Yangliuping and Qingkuangshan, whereas Baimazhai and Limahe are the two Ni-Cu deposits. These PGE-poor deposits contain relatively high amounts of sulphides (10 vol %). The Ni, Cu and PGE resources, measured from Yangliuping and Zhenziyanwo mines of the Yangliuping deposit, are approximately 0.455 million tons, 0.148 Mt, and 56.7 ton (Song *et al*., 2005, and references therein). The average Ni and Cu grades of the Baimazhai deposit are 1.03 wt% and 0.81 wt%, respectively. The Ni metal in massive ores, which comprizes 60% of the total resource, reaches 50,000 tons (Wang *et al*., 2006, and references therein).

Different types of sulphide deposits have likely underwent various sulphide saturation histories and various degrees of sulphide segregation.

It is generally accepted that Ni-Cu-(PGE) sulphide ore deposits in the ELIP were formed by segregation of immiscible sulphide liquid from parental magmas with compositions similar to low-Ti Emeishan basalts (Song *et al*., 2003; Tao *et al*., 2007, 2008; Wang & Zhou, 2006; Zhou *et al*., 2008). Crustal contamination has been suggested as the primary trigger for immiscibility. Small mafic-ultramafic intrusions with Cu-Ni-(PGE) sulphide mineralization are believed to have acted as magma conduits for the low-Ti basalts.

2.3.3.2 Giant magmatic Fe-Ti-V oxide deposits

In contrast with the widespread distribution of sulphide deposits, all known Fe-Ti-V oxide deposits occur within the central zone of the ELIP (Fig 2.3). According to a recent report (http://www.xinhuanet.com/chinanews/2009-07/09/content_17050044.htm), a total of 1.94×10^{10} tons Fe-Ti oxide ore reserve in the Panxi region has been estimated. Among which, over 1×10^{10} tons is concentrated in the four large layered gabbroic intrusions (Panzhihua, Baima, Hongge, and Taihe) (Table 2.1). Titanium and vanadium resources are estimated at about 1.73×10^{9} tons and 4×10^{7} tons, being the first and third largest reserves in the world, respectively (Ma *et al.*, 2003).

Panzhihua, Baima and Taihe are gabbroic, with minor ultramafic phases intercalated in the stratigraphy; whereas Hongge and Xinjie are mafic-ultramafic, with the majority of wehrlite, olivine-clinopyroxenite , clinopyroxenite and overlying less abundant gabbro (Fig 2.4).

The gabbroic intrusions are mostly sill-like in shape. They are hosted mainly by Neoproterozoic metamorphic rocks and also Paleozoic strata. The intrusions are up to 20 km long and 2 km thick. They consist mainly of gabbro and diorite with small amounts of clinopyroxenite, wehrlite, troctolite. The rocks consist mainly of cumulus Ti-rich clinopyroxene, plagioclase,

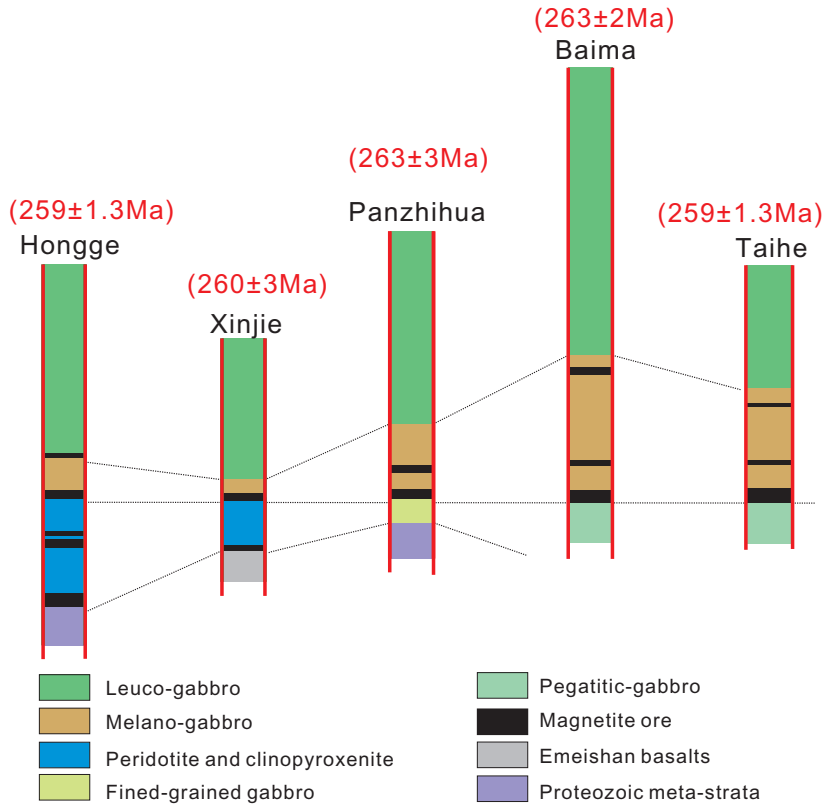

Fig. 2.4 Simplified stratigraphy of the Panzhihua, Hongge, Baima, Taihe, and Xinjie layered intrusions, also shown are geochronology data from (Luo *et al.*, 2006; Zhong & Zhu, 2006; Zhong *et al.*, 2009; Zhou *et al.*, 2002a, 2005, 2008).

Fe-Ti oxides, and in some cases olivine. Interstitial minerals also include hornblende and sulphides in addition to those listed above. Orthopyroxene is rare in these intrusions.

Table 2.1 Geological and geochemical characteristics of giant Fe-Ti-V deposits in the Pan-Xi Area (from Zhong *et al.*, 2005)

Deposit	Host rock	Area, thickness	Reserve(t); Mean grade (%)			Grade of byproduct (%)					Ore minerals	Gangue minerals	Sulfide minerals
			TFe	TiO_2	V_2O_5	Cr_2O_3	Co	Ni	Cu	PGE			
Panzhihua	Gabbro	38 km^2, 712-2570m	2.05×10^9; 33.23	2.37×10^8; 11.68	6.01×10^6; 0.30	0.13	0.02		0.04		V-Ti magnetite, ilmenite	Titanaugite, labradorfeldspar	pyrrhotite, chalcopyrite, pyrite, pentlandite
Hongge	Gabbro, clinopyroxenite, olivine clinopyroxenite	60 km^2, >1700m	1.83×10^9; 27.04	1.96×10^8; 10.57	1.45×10^7, 0.24	0.31		0.06	0.03	0.354 (@0.533 ppm)	V-Ti magnetite, ilmenite	titanoaugite, diopside, olivine, titanohornblende, basic plagioclase	Pyrrhotite, pentlandite, pyrite, chalcopyrite, cubanite
Taihe	Gabbro	13 km^2, 1213-1913m	1.78×10^9; 30.31	2.00×10^8; 11.76	5.18×10^6, 0.27		0.011		0.02		Ti-magnetite, ilmenite	titanaugite, basic plagioclase	Pyrrhotite, pyrite
Baima	Plagioclase peridotite, plagioclase-bearing olivine clinopyroxenite, troctolite, olivine gabbro	50km^2, up to 3989m	1.15×10^9, 25.51	4.48×10^7; 6.55	2.85×10^6; 0.21		0.015	0.023	0.033		Ti-magnetite, ilmenite	titanaugite, basic plagioclase, olivine, hornblende, biotite	Pyrrhotite, chalcopyrite, pyrite, cobalt pyrite, pentlandite, cubanite

Fe-Ti oxide ores occur mainly at the lower parts of the gabbroic intrusions (Ma *et al.*, 2003; PXGT, 1981, 1987; SBGMR, 1991). In the Xinjie intrusion, where both sulphide and oxide mineralization occur, magnetite ore horizon occurs in the upper parts of cycles I (peridotitic, clinopyroxenitic and gabbroic cumulates) and II (clinopyroxenitic and gabbroic cumulates) (Zhong *et al.*, 2004).

Two main petrogenetic models have been proposed for the Fe-Ti oxide ore deposits in the Panxi area. One is the liquid immiscibility hypothesis, which has magnetite and ilmenite crystallized from Fe-Ti oxide melt that segregated immiscibly from extremely differentiated silicate magmas (Wang & Zhou, 2013; Zhou *et al.*, 2005, 2008, 2013). The other, which currently receives more support, is fractional crystallization followed by crystal settling and sorting (Bai et al., 2012; Ganino et al., 2008, 2013; Hou et al., 2012; Pang et al., 2008a, 2008b, 2009, 2010, 2013; Shellnutt & Jahn, 2010; Shellnutt & Pang, 2012; Song et al., 2013; Wang et al., 2008; Zhang et al., 2011, 2012). These authors suggested magnetite crystallized from less differentiated silicate magma at an early stage. Dolomitic wall rock contamination is generally thought to be the trigger of magnetite saturation.

2.4 Local Geology of the Panzhihua and Taihe Layered Intrusions

Wang (1982) described the petrology of the Panzhihua layered intrusion, whereas Li and Mao (1982) described the Taihe, Hongge and Xinjie layered intrusions. Descriptions are also found in several industry reports (PXGT, 1981, 1987; SBGMR, 1991). The Panzhihua intrusion was first described in the international literature by Zhou *et al.* (2005), followed by Pang *et al.* (2008a, 2008b, 2009), Song *et al.* (2013), and Zhang *et al.* (2009). In contrast, much less is published on the Taihe intrusion (Hou *et al.*, 2012, Pang *et al.*, 2010).

2.4.1 Geology of the Panzhihua Layered Intrusion

2.4.1.1 General geology

The Panzhihua layered intrusion, dated at 263±3 Ma (Zhou *et al.*, 2005), is a gabbroic sill-like body with an exposed area of approximately 19 km × 2 km, and a maximum known thickness of 3 km. It dips to the northwest at 40-60˚, striking northeast (NE) to southwest (SW) (Fig. 2.5). The intrusion concordantly intruded in the Late Neoproterozoic Dengying Formation of dolomitic limestones, and covered by Late Permian syenites and Triassic con-

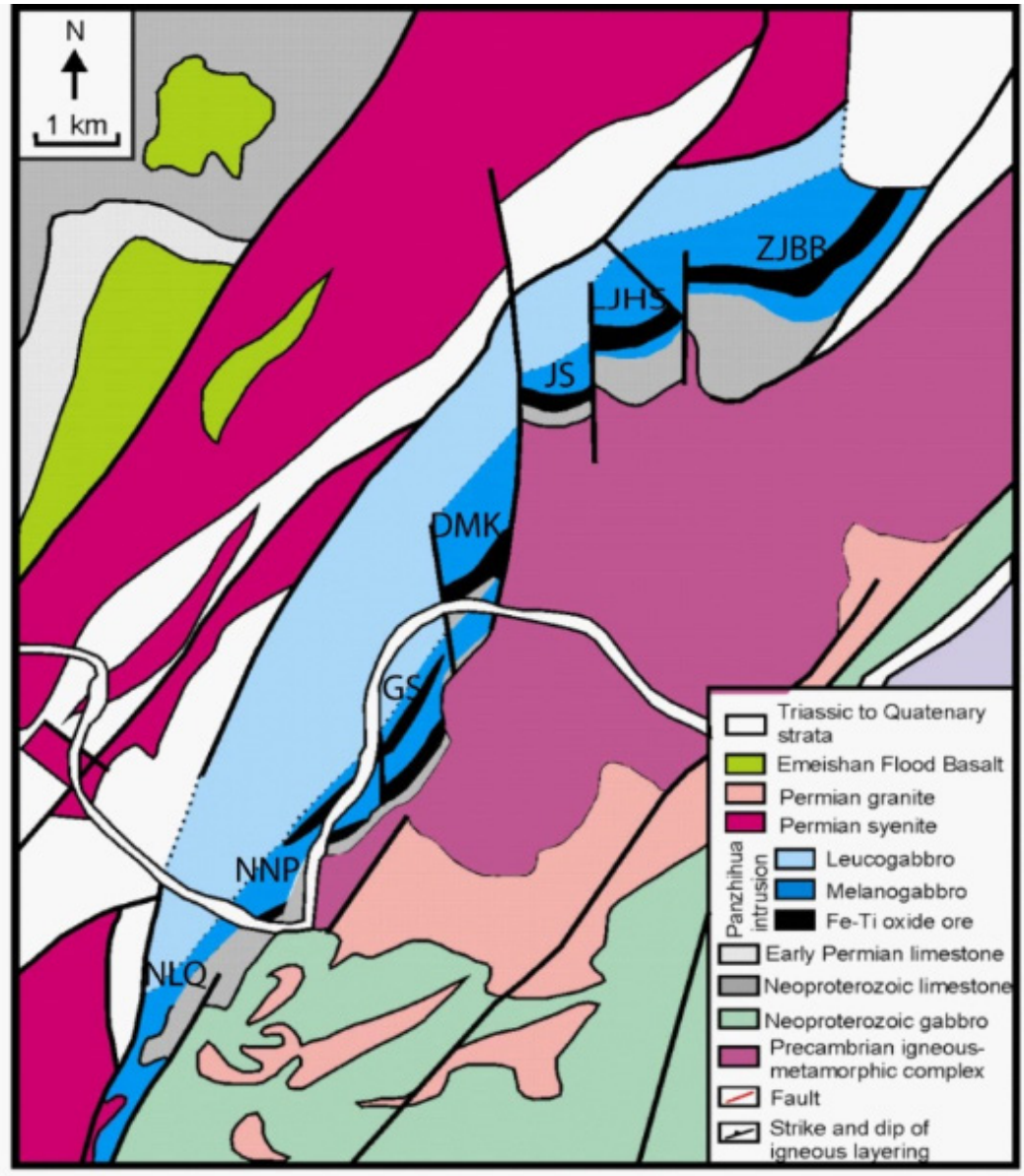

Fig. 2.5 Geological map of the Panzhihua district, showing the local geology of the Panzhihua gabbroic layered intrusion and related intermediate to felsic rocks. (Modified after Zhou *et al.*, 2005)

glomerate, shales and coal seams. Currently there is no age data of the Panzhihua syenites, however, the Baima syenites were intruded in 262 ± 2 Ma (Zhou *et al.*, 2008).

The footwall limestone that lies near the contacts had been metamorphosed to fosterite and diopside marbles. The hanging-wall syenites and conglomerates comprise discontinuous covers at different parts of the intrusion (Fig. 2.5). To the west of the syenites, granites with similar orientation intrude into the overlying Emeishan basalt, which is volumetrically much smaller in the Pan-Xi region compared with the other areas in the ELIP. The syenite and granite are considered by some as genetically related to the underlying layered gabbroic rocks, representing a continuous compositional evolution trend from mafic to intermediate to felsic

Table 2.2 Lithology, subdivisions, and sampling of the Panzhihua layered intrusion. Column 1-5 and 6-8 are extracted from unpublished reports SBGMR (1991), and Zhou et al. (2005) and Pang et al. (2008b), respectively. Column 9 lists samples collected from Zhujiabaobao and Lanshan.

1.Rhythmic Layer	2.Petrology	3.Ore body	4.Ore type	5.Ore layer thickness	6.Discriminative features	7.Zone	8.Thickness (m)	9. Zone This study	10.Sample
III	Coarse-grained leucogabbro, interbedding a few plag-pyroxenite	-	Un-mineralized	N/A	Leucogabbro, coarse-grained, layered	UZ	500~1500	UZ	N/A
	Oxide hosted in the lower melanogabbro	1	Sparse disseminated	~10 m; decrease in thickness from SW to NE	Apatite > 5 %	MZb	~400	MZb	PZ-45, PZ-44
	Oxide hosted in the plag-pyroxenite, less in melanogabbro	2	Sparse disseminated	10~20 m; decrease in thickness from SW to NE					
II	Layered melanogabbro, gradually contact with IV ore body	3	Sparse disseminated	2~3 m	Layered	MZa	~400	SMZ	N/A
	Layered melanogabbro, locally interlaying fine-grained wehrlite	4	Disseminated	Increasing in thickness from SW to NE, e.g Nalaqing 60 m, Lanshan 70, Zhujiabaobao 230 m.	Layered				PZ-43, PZ-42 PZ-41,PZ-40 PZ-39
	Layered melanogabbro	5	Disseminated, dense disseminated	Increase in thickness from SW to NE, 110 m in Zhujiabaobao, only 26 m in Nalaqing	Layered				PZ-23, PZ-38 PZ-37, PZ-36 PZ-22, PZ-35, PZ-21
	Coarse-grained olivine gabbro and layered gabbro, interbedding with wehrlite, pyroxenite. Discriminate from overlying V and underlying VII with a layer of coarse-grained dense disseminated ore	6	Dense disseminated, and massive	30- 50 m; decrease from SW to NE. Absent in Gongshan and Nalaqing	Layered			MMZ	PZ-33, PZ-32, PZ-20, PZ-31, PZ-19, PZ-18 PZ-17, PZ-16
I	Medium-coarse grained gabbro, interlaying with disseminated ore	7	Banded/layered	20 m, centimeter to meter-scale of single ore layer. Becoming thinner from Jianshan section to both SW and NE direction	Layered, Sulphide up to 10-20 %, usually 5-10 %				N/A
	Medium-coarse grained gabbro, interlayered with wehrlite, and medium-coarse grained anorthosite. Anorsosite on top	8	Dense disseminated, massive	Getting thicken and richer from SW to NE. Over 40 m thick in Zhujiabaobao section, and extends for 850 m without obvious change in thickness	Layered, as shown by oriented Plag				PZ-15, PZ-14, PZ-30, PZ-29, PZ-13, PZ-28 PZ-27, PZ-12
Marginal Zone	Isotropic coarse-grained gabbro	9	Sparse disseminated	Unknown, varies largely, relatively thick in Zhujiabaobao, Lanshan, and Nalaqing, gradually getting thinner along trend and strike.	Isotropic, locally sulphide up to 10%. Hb-enriched.	LZ	0~110		PZ-11, PZ-10 PZ-26, PZ-25 PZ-24, PZ-9
	Fine-grained gabbro interplaying with coarse-grained gabbro/wehrlite apophasis/ /lens of massive ore	-	Un-mineralized	Decimeter-scale lens of massive ore	Fine-grained, holnblende-rich, sulphide-rich, Marble inclusions	MGZ	0~40	MGZ	PZ-8, PZ-7 PZ-6, PZ-5 PZ-4, PZ-3 PZ-2, PZ-1
Wall rock	Marble, skarn	-	-	-	-	-	-		-

Abbreviations: MGZ-marginal zone; LZ-lower zone, MZa-lower middle zone; MZb-upper middle zone; UZ-upper zone; MMZ-main mineralization zone; SMZ-subordinate mineralization zone.

rocks (Shellnutt & Jahn, 2010).

Near N-S trending and steeply dipping late-stage tectonic faults have cut the Panzhihua intrusion into six sections (Fig. 2.5). From NE to SW, they are Zhujiabaobao, Lanshan, Jianshan, Daomakan, Gongshan, and Nalaqing. The first three sections contain the thickest ore bodies, and have been the primary mining targets for over forty years, and now provide excellent exposure. Most of the previous studies of the Panzhihua gabbroic layered intrusion and associated Fe-Ti-V oxide deposit sampled these economically significant mines.

2.4.1.2 Stratigraphic subdivision

The Panzhihua intrusion was well-preserved during the extensive regional tectonic activity associated with the Cenozoic Indian-Eurasian collision. Deformation and metamorphism are only found in local shear zones and are minor.

The Panzhihua layered intrusion consists mainly of gabbroic rocks with various amount of Fe-Ti oxides, and volumetrically subordinate micro-gabbro, ultramafic (peridotite, wehrlite and pyroxenite), and intermediate to felsic rocks (syenite, granophyre, and anorthosite). Massive titanomagnetite and ilmenite-dominated oxide ores concentrate in the lower part of the intrusion.

The initial four-zone subdivision of the layered stratigraphy, the Marginal Zone, the rhythmic I, II and III, was proposed and used by the local geologists, based on the extent of layering, disappearance and appearance of certain minerals (apatite, olivine), variations in mineral composition (plagioclase and olivine) and mode (Ol/(Ol+Aug), Mgt/(Mgt+Ilm), and petrographic features (Ma *et al.*, 2003; SBGMR, 1991; Wang, 1982). For the purposes of exploration, nine ore bodies were identified based on their location within the intrusion, host rocks and ore types. This classification adequately reflects some features of the intrusion, such as the dominance of more evolved rocks in the upper part of the intrusion and Fe-Ti oxides in the lower part.

However, it does not accurately reflect variations in the cumulus and inter-cumulus minerals. Zhou *et al.*, (2005) divided the stratigraphy into the Marginal Zone (MGZ), the Lower Zone (LZ), the Middle Zone (MZ), and the Upper Zone (UZ). The MZ was further separated into the lower MZa and higher MZb marked by the appearance of cumulus apatite (Pang *et al.*, 2008b). In this study, we have combined the LZ and lower MZa as subordinate mineralization zone (SMZ), and the rest of MZa is the main mineralization zone (MMZ). The MGZ, MZb and UZ follows previous classifications. Table 2.2 compares different classifica-

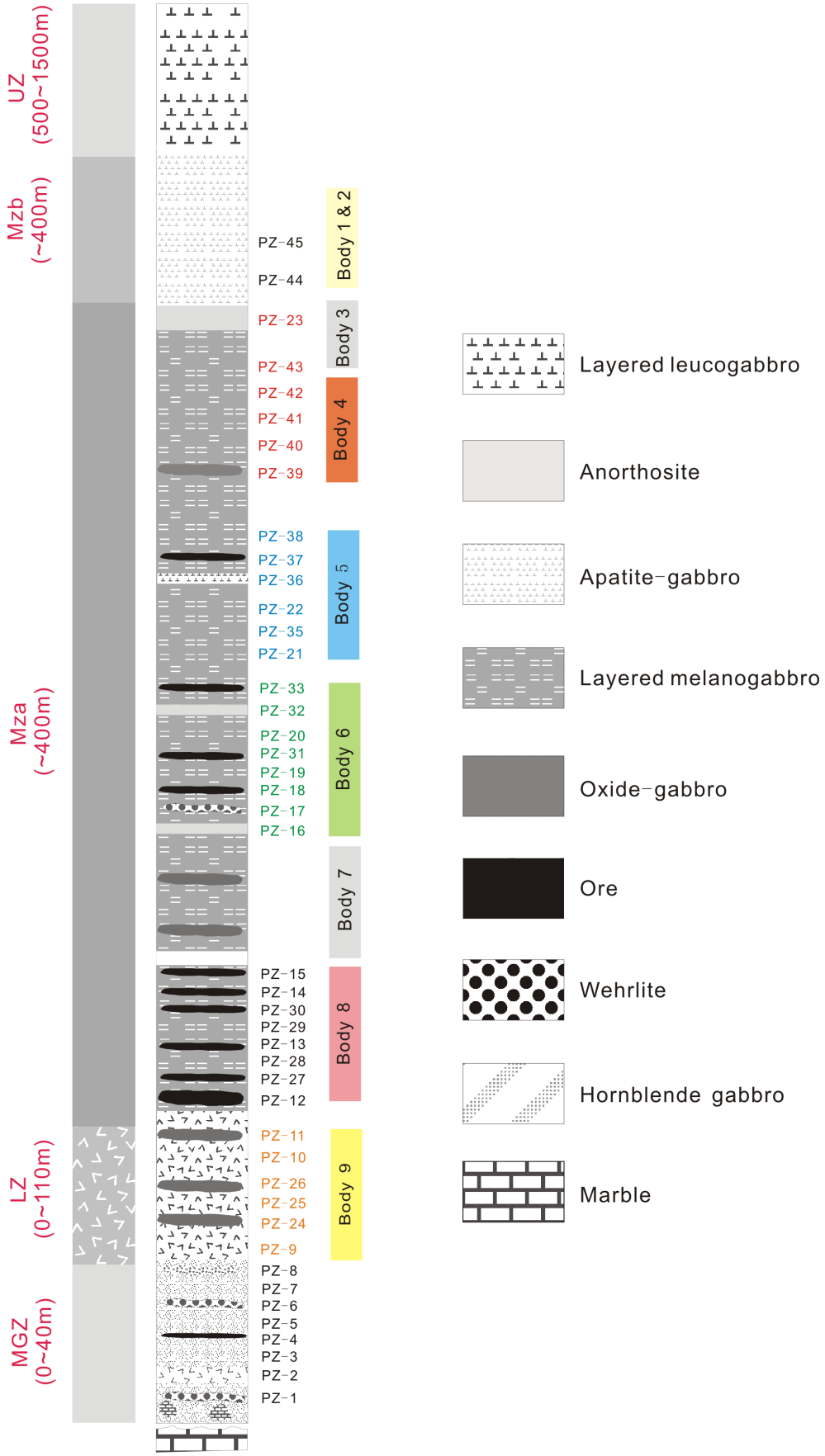

Fig. 2.6 Generalized stratigraphic column of the lower part of the Panzhihua gabbroic layered intrusion.

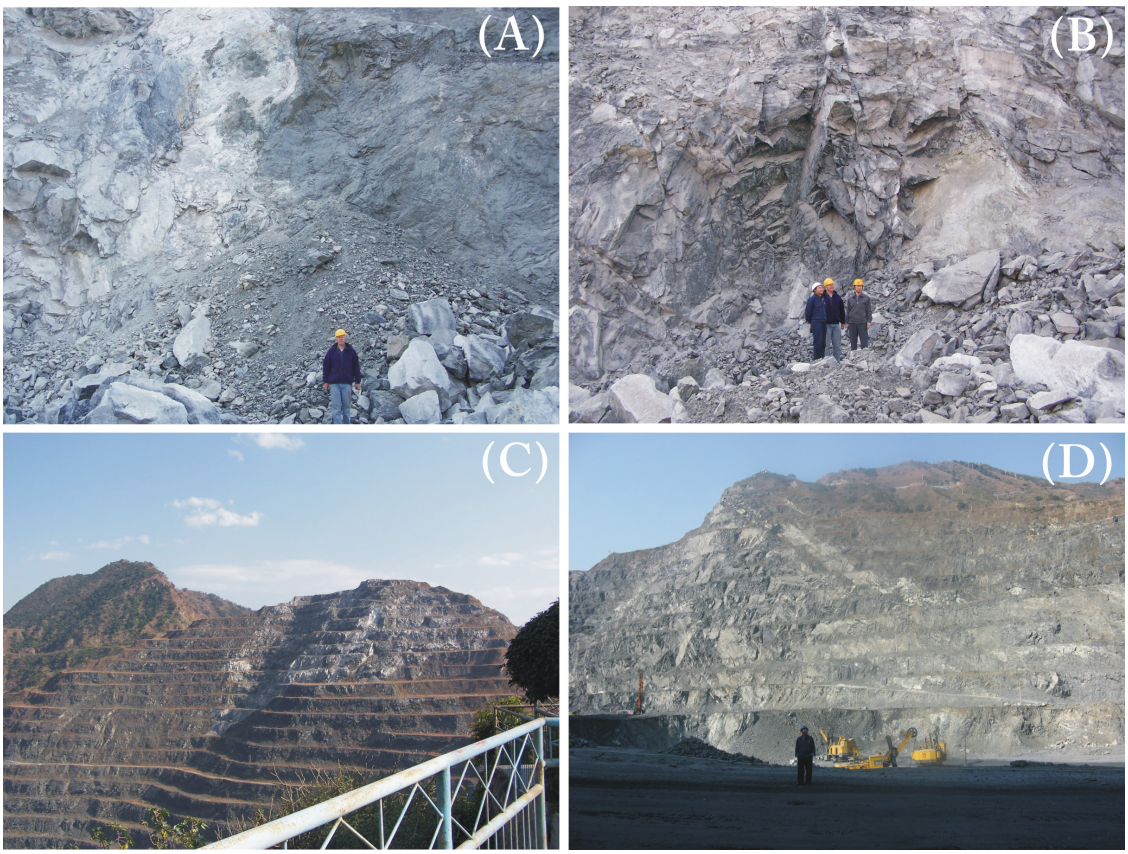

Fig. 2.7 Field photographs of the marginal zone of the Panzhihua layered intrusion, showing the great heterogeneity. (A) Highly irregular contact between the MGZ and footwall marble. (B) Dark melonogabbro block included in the footwall marble, forming a dome-shaped structure. (C) Large marble block occurs discordantly within the lower part of the intrusion. (D) A meter-scale syenite dyke intruded in the MZ/UZ of the intrusion.

tion schemes and also shows the relative locations of samples collected from the Lanshan and Zhujiabaobao section of the Panzhihua Intrusion for this study. It is clear that all samples were collected from the lower and middle part of the intrusion (~700 m). This sampling covers all ore bodies occurring in the Panzhihua, except for ore body 7 and ore body 3, which are absent in these two sections (Fig 2.5).

2.4.1.3 Main features of each zone

The major characteristics of each zone are listed in Table 2.2 and shown on Fig 2.6.

The Marginal Zone is 0-40 m thick; it is characterized by a wide range and uneven distribution of rock types. It consists mainly of fine-grained gabbro and olivine gabbro with abundant marble xenoliths derived from the footwall (Fig 2.7). Fine-grained gabbros contain abundant brown hornblende/amphibole and some Fe-Ti oxides. Coarse-grained gabbro contains more Fe-Ti oxides, forming the first disseminated ore body (Ma *et al.*, 2003; SBGMR, 1991). New sampling has showed that first massive ore lens occur in the MGZ, and fine-

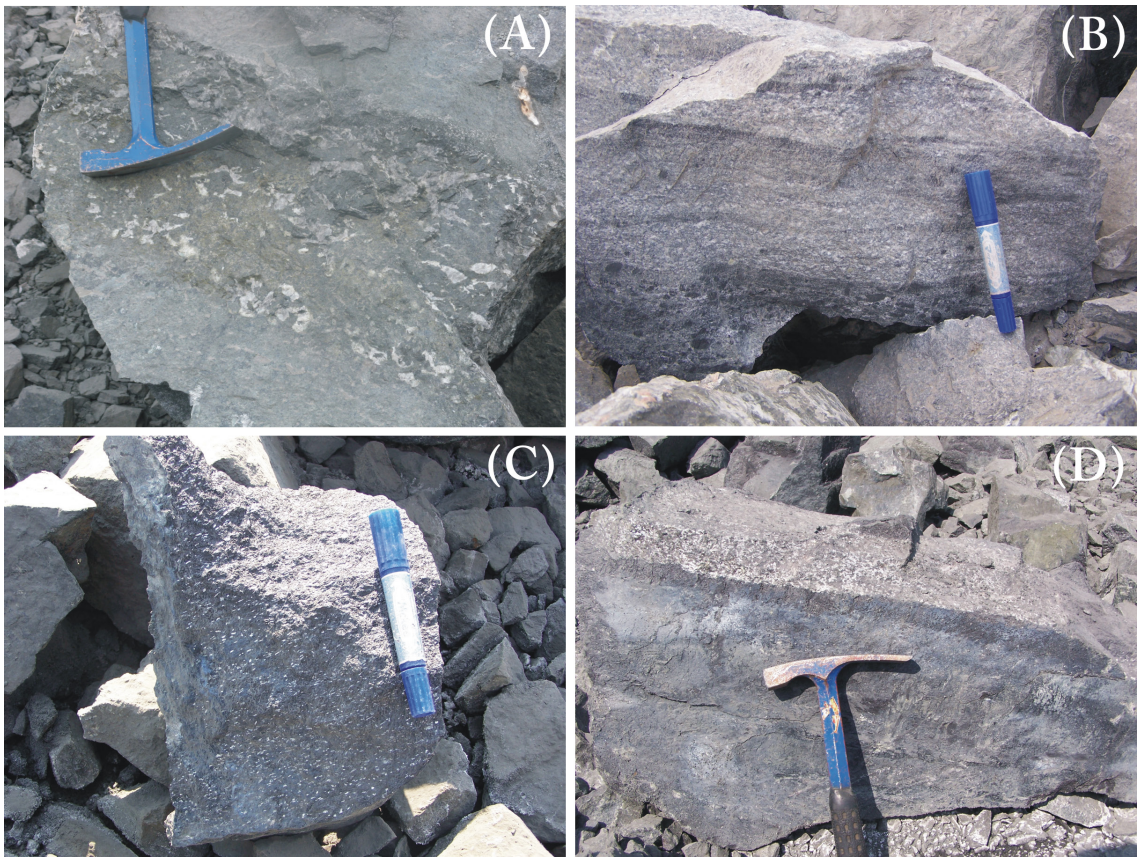

Fig. 2.8 Field photographs of layered structures in the Panzhihua Intrusion. (A) Coarse-grained gabbro in sharp contact with fine-grained gabbro in the MGZ/LZ, LS. (B) Layered structure of a leucogabbro in sharp contact with melonogabbro, MZa. (C) Igneous lamination as shown by light-color plagioclase in a melonogabbro, MZa. (D) Layered leucogabbro in sharp contact with massive Fe-Ti oxide ore, MZa.

grained plagioclase-bearing wehrlite is in contact with the footwall marble. The MGZ rocks are also enriched in sulphide, which can reach up to 10 vol % in total (SBGMR, 1991).

The Lower Zone is 0 to 110 m thick, and is distinct from the others by the isotropic coarse gabbro with local pegmatitic facies (Fig.2.8 A). Disseminated ore body 9 occurs in the Lower Zone, interlaying within gabbros. The thickness of ore body 9 varies greatly, generally decreases along trend and strike.

The Middle Zone is about 800 m thick, and is separated into MZa and MZb according to the appearance of cumulus apatite. This zone is characterized by widespread occurrence of layered medium-grained melano-gabbro, with small amounts of leucogabbro and anorthosite (Fig. 2.8 B-D).

The MZa contains significant ore bodies 1 to 8. Among these, ore body 6 is massive, up to 60 m thick in the Daomakan section in the south, but is usually 30-50 m in thickness in other sections. The other ore bodies are either dense disseminated or disseminated,

inter-bedding with layered melano-gabbro. Generally, the amount of Fe-Ti oxides decreases upwards whereas the amounts of felsic minerals increase. Clinopyroxene-bearing anorthosite occurs at the top of ore body 8, which is up to 60 m thick and hence the main ore body in the Panzhihua deposit. Ore body 7 is sulphide enriched, locally up to 10-20 %, generally 5-10 %. Anorthosite, up to 3 m thick, also occurs at the top of ore body 3. Above this anorthosite, MZb starts where apatite first occurs in the cumulus (up to 5 %). Small disseminated ore body 1 and 2 occur at the lowest part of the MZb, but disappear rapidly up the section.

The Upper Zone (UZ) consists mainly of coarse-grained layered leucogabbro with a thickness ranging from 500 to 1500 m. Olivine gabbro, olivine-clinopyroxenite, and anorthosite are present in places. No Fe-Ti oxide mineralization was found in the Upper Zone.

In summary, the Panzhihua intrusion is dominantly gabbroic, with several minor ultramafic rock layers found at various heights. The rocks become more evolved upwards, mainly due to changing mineral proportions, as indicated by the lighter color. Massive Fe-Ti oxide ores concentrate in the lower part of the layered intrusion. Disseminated ores are present up to the top of the MZa.

2.4.2 Geology of the Taihe Layered Intrusion

2.4.2.1 General geology

The Taihe Layered Intrusion is located ~ 12 km to the west of the Xichang City, and lies between the N-S trending Anninghe and Mopanshan Faults (Fig 2.3). It extends NE diping

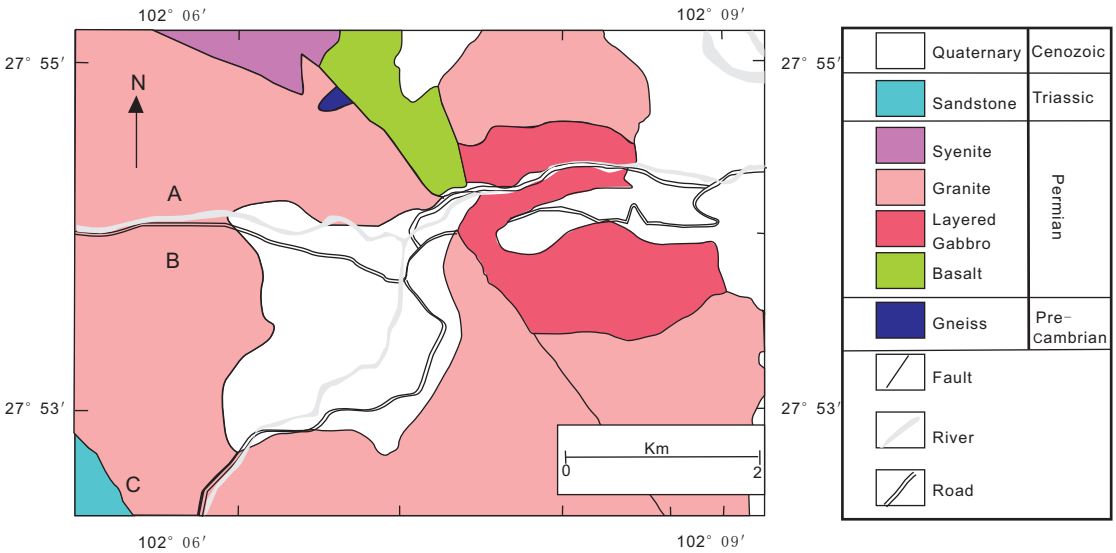

Fig. 2.9 Simiplified geological map of the Taihe gabbroic layered intrusion and associated syenite and granitic rocks (After Shellnutt & Zhou., 2007).

to SE at 50° to 60°. The outcroping area is over 13 km^2, and the documented thickness is over 2000 m (SBGMR, 1991).

The eastern part of the Taihe Intrusion is covered by Quaternary Anning River alluvial deposits, and the western part is in a fault contact with Triassic sandstone (Fig 2.9). The rest of the intrusion is surrounded by late-stage granite, syenite, and alkali-syenite, which intrude the gabbroic body. Basalts are constrained by the NW and NNW faults and partly in contact with the layered gabbros in the northwest (Fig 2.9). The Taihe granite was dated at ~ 260 Ma (Luo *et al*., 2006), while the gabbroic intrusion was 264 ± 3 Ma (JGS, unpublished data, in Pang *et al*, 2010), indicating their likely genetic relationship with the Emeishan LIP.

The Taihe Intrusion is characterised by rhythmic layering and igneous lamination. The layering is parallel to the strike directions. Xenoliths of marbles, diopside-skarns or garnet-skarns are found along the contact. Late-stage faults cutting the intrusion are mostly N-S trending. There is a number of late-stage diabase, gabbroic aplite and alkaline syenite dyke cutting the intrusion.

2.4.2.2 Stratigraphic subdivision

Based on rock textures and occurrence of Fe-Ti oxide ores, the Taihe gabbroic intrusion was subdivided into five petrological zones: from bottom to top, the Lower Gabbro zone, the Layered Ore-Bearing Gabbro zone, the Layered Leucogabbro zone, the Massive Gabbro zone, and the Uppermost Contaminated zone (Li & Mao, 1982). The main characteristics of each zone are summarized as below based on the descriptions in the literature cited above.

The Uppermost Contaminated zone is about 70 m thick, and was speculated to be close to the upper contact which is not preserved. The main rocks are melanogabbro, some of which contain olivine. It is characterized by taxitic structure that the consituting minerals are uneven and extremely irregular in composition and textures. Anorthite content of plagioclase increases from An35 in the leucogabbro below the Uppermost zone to An42 in the melanogabbro. A few mafic xenoliths occur within this zone. The plagioclase in the xenoliths is An42 - An40.

The Massive Gabbro zone is similar in rock types and mineralogy to the Lower Gabbro zone. It is about 260 m thick, consisting mainly of apatite-bearing massive leucogabbro and some olivine-gabbro and apatite-olivine-gabbro. No layering is observed in this zone. Anorthite content of the plagioclase decreases upwards from An59 to An35.

The Layered Leucogabbro zone is over 260 m thick. Pyroxenite occurs interlayered with the layered medium-grained leucogabbro. Disseminated ores occur in the pyroxenite from the

lower part of this zone. This mineralized pyroxenite contains apatite up to 10 % and plagioclase with higher anorthite content (An56-An70).

The Layered Ore-bearing Gabbro zone is about 1200m in thickness. Layered melanogabbro and Fe-Ti oxide ores compose the majority of this zone. Pyroxenite is found interbedding within the sequence. Small amounts of troctolite and wehrlite occur at the bottom of this zone. Based on the hosting rock types, the Fe-Ti oxide ores are divided into three units (I, II, III). Massive and dense disseminated Fe-Ti oxide ores occur in the lower part of the zone. The hosting rocks are mainly gabbro, with some anorthosite and pyroxenite at different stratigraphic heights (Fig 2.10). Apatite occurs in the upper part of this zone, where the Fe-Ti oxide is less abundant. Olivine is occasionally found in the unmineralized upper part. Plagioclase becomes more evolved upwards, from An72 to An 57.

The Lower Gabbro zone is over 265m thick (the bottom contact is not exposed), consisting mainly of apatite-bearing leucogabbro (Fig 2.10). The gabbro is coarse-grained to pegmatitic without prominent layering features. Apatite occurs as euhedral crystals while olivine

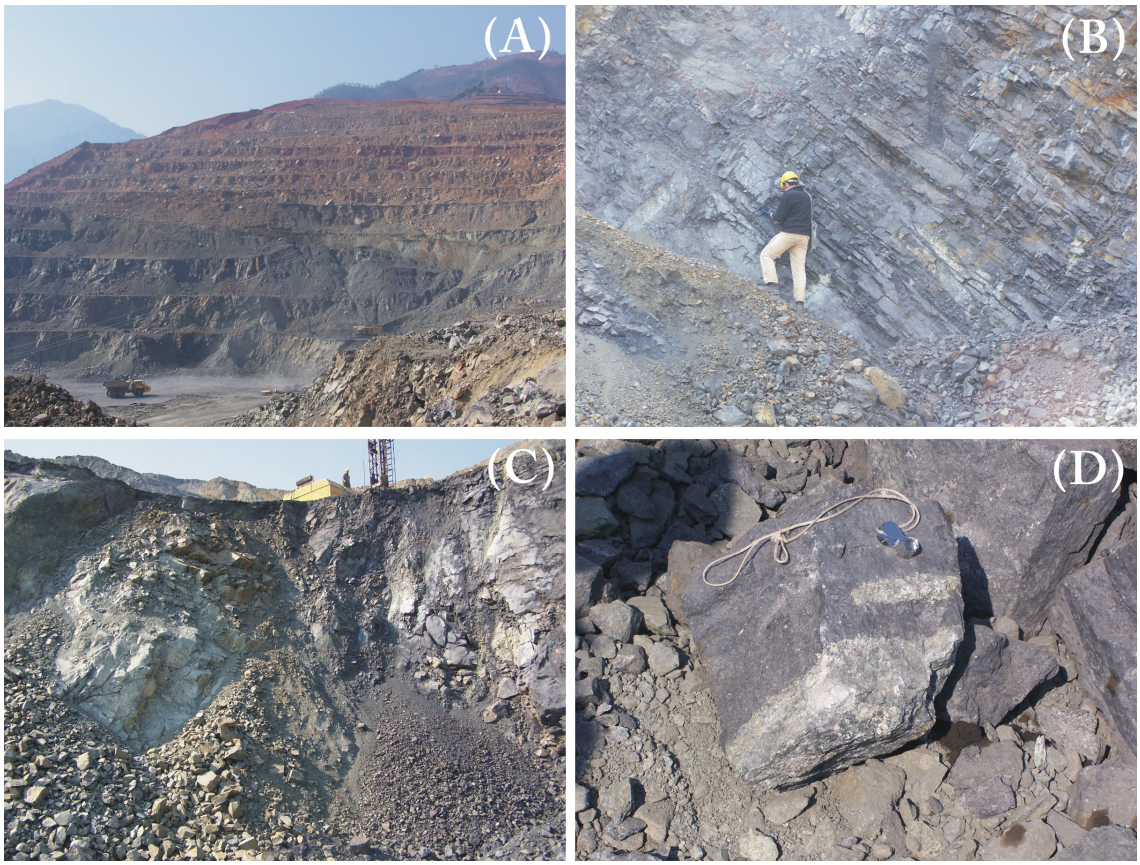

Fig. 2.10 Field photographs of the layered Taihe intrusion. (A) The Taihe open-pit mine. (B) Layered structure of the Fe-Ti oxide ore-bearing melonogabbro zone. (C) Anorthosite blocks in the layered melonogabbro. (D) Massive Fe-Ti oxide ore rock with anorthosite inclusion.

is absent in this zone. The plagioclase is uniform in composition (An57 - An58).

In summary, the Upper taxitic Gabbroic zone and the Lower Gabbroic zone of the Taihe intrusion are both massive un-mineralised gabbroic rocks. The massive Fe-Ti oxide ores concentrate in the lower part of the intrusion. Disseminated ores occur at various stratigraphic heights within the intrusion, but mainly associated with the layered gabbro. Apatite occurs in considerable amounts above the Upper Layered Ore-bearing zone, where Fe-Ti oxide minerals are much less abundant.

2.4.3 Similarity Between the Panzhihua and Taihe Intrusions

The Panzhihua and Taihe layered intrusions are both dated at around 260 Ma (260 ± 3 Ma vs 260 Ma, Zhou *et al.*, 2005; Luo *et al.*, 2006), and generally regarded as intrusive equivalents of the Emeishan flood basalts. They are similar with regards to rock types, mineralogy, internal structure, and the occurrence of the Fe-Ti oxides.

The Panzhihua and Taihe intrusions are both composed of gabbro with various Fe-Ti oxides, massive ore, and subordinate amount of anorthosite, clinopyroxenite, and wehrlite. The gabbro is more evolved upwards as indicated by the increasing amount of light-colored plagioclase and its decreasing anorthite content. Apatite-gabbro occurs only in the upper barren portion. Anorthosite and ultramafic rocks occur as interbedding layers at various heights of the gabbroic sequences. Olivine occurs throughout the Panzhihua intrusion, and especially in the apatite-rich MZb, where olivine occur as one of the cumulus minerals (Pang *et al.*, 2008; SBGMR, 1991). Olivin-bearing gabbro is also common in the Taihe intrusion, however, it disappears in the Lower Massive Gabbroic zone.

Rhythmic layering is another common feature of the Panzhihua and Taihe intrusions (Fig 2.8; Fig 2.10B). Modal-layering and grain-size layering both occur, but the former is the dominant type. The modal layering, centimeter to decimeter in scale, is formed by alternating layers enriched in either light-coloured plagioclase or dark-coloured Fe-Ti oxides and/or mafic minerals. Igneous lamination is shown as linear arrayed plagioclase and/or brown holnblende. The directional lineation is defined mainly by plagioclase, while most hornblende grains are not parallel, instead, they have small angle in contract. Gabbro with layered structure account for large proportions of both inclusions. For example, the thickness of layered gabbro is about 1450 m out of the total of 2000 m in the Taihe intrusion, and this proportion is even greater in the Panzhihua intrusion.

Taking into account that the roof contact is not exposed in both intrusions, and the

bottom contact is only known in the Panzhihua intrusion, it is likely that the complete stratigraphy of this type of gabbroic layered intrusions include: (1) the marginal zone consisting of fine-grained gabbro, (2) the lower zone of massive coarse-to pegmatic gabbro, (3) the lower zone of ore-bearing layered melanogabbro, (4) the middle zone consisting of a lower layered melanogabbro and upper apatite-rich melanogabbro, (5) the upper layered leucogabbro, (6) the upper massive leucogabbro, (7) and the uppermost taxitic gabbro. Zones 5 and 6 are not found in the Panzhihua intrusion, likely due to the tectonic erosion. Zone 1 is not observed in the Taihe intrusion, likely due to poor exposure of the intrusion.

The massive Fe-Ti oxide ores concentrate mainly in the layered melanogabbro without cumulus apatite (e.g. zone 3, 4). The abundance of the Fe-Ti oxide decreases upwards. Appearance of large amounts of apatite coincides with fast disappearance of Fe-Ti oxides. In the Taihe Intrusion, Fe-Ti oxide ore also occurs within anorthosite (Fig 2.10D).

In summary, the Panzhihua and Taihe intrusions were emplaced into the present location during the Late Permian mantle plume activity at around 260 Ma. The similarities in their petrology, layering structure, and occurrence of the Fe-Ti oxides, imply that they may have common parental magmas, magmatic processes and ore genesis.

CHAPTER 3 PETROGRAPHY

This chapter presents the petrography of the Panzhihua and Taihe Layered Intrusions. The first section is a brief introduction of the sample locations, methods and an overview of the petrology of the Panzhihua layered intrusion. It is followed by a detail study of the petrography, including mineralogy and textural characteristics, with an emphasis on the microtextures of Fe-Ti oxide ore minerals and Fe-Ni-Cu-S sulphide minerals. The next section is a brief description of Taihe rocks.

The terminology used is inherited from studies of the Skaergaard Intrusion (Wager *et al.*, 1960; Irvine, 1982), and earlier studies of the Panzhihua intrusion (Pang *et al.*, 2008b; Zhou *et al.*, 2005; SBGMR, 1991; PXGT, 1981, 1987). The terminology is summarized in Table 3.1.

Table 3.1 Cumulus names and abbreviations, and the corresponding rock names for the Panzhihua and Taihe Intrusions (modified after Irvine,1982). Note there is no cumulus orthopyroxene in the two intrusions.

Cumulates	Cumulus minerals	Abbreviation	Rock name
Peridotitic	Olivine-augitic clinopyroxene	oc-C	Wehrlite
	Clinopyroxene	c-C	Clinopyroxenite
Pyroxenitic	Clinopyroxene-olivine	co-C	Olivine clinopyroxenite
	Clinopyroxene-magnetite-ilmenite	cmi-C	Oxide clinopyroxenite
	Plagioclase	p-C	Anorthosite
	Plagioclase- clinopyroxene	pc-C	Gabbro/microgabbro
Gabbroic	Plagioclase-clinopyroxene-olivine	pco-C	Olivine gabbro
	Plagioclase-clinopyroxene-magnetite-ilmenite	pcmi-C	Fe-Ti oxide gabbro
	Plagioclase-clinopyroxene-apatite	pca-C	Apatite gabbro
	Plagioclase-clinopyroxene-hornblende	pch-C	Hornblende gabbro
Oxide	Magnetite-Ilmenite	mi-C	Fe-Ti oxide ore

3.1 Petrography of the Panzhihua Intrusion

3.1.1 Introduction

A set of 44 samples was collected from the lower part of the Panzhihua Layered Intrusion in two open-pits. Samples were labeled as “PZ-n”, where “n” denotes sample number. Samples with number between 1 and 23 were collected from the Lanshan section (LS), and 24-45 from the Zhujiabaobao section (ZJBB).

These samples represent the lower ~ 700 m of the cumulus stratigraphy of the Panzhi-

hua Intrusion, where all significant Fe-Ti oxide ore layers are concentrated. This section corresponds to the Marginal Zone (MGZ), Lower Zone (LZ), Middle Zone a (MZa), and the lower part of the Middle Zone b (MZb), following the stratigraphy suggested by (Pang *et al.*, 2008; Zhou *et al.*, 2005). Samples from two open-pits are combined together according to their stratigraphic position in relation to the ore bodies 1 to 9 (from top to bottom)[1]. The position of the samples relative to ore is used for comparison of rock mineralogy and compositions between this study and previous work (Pang *et al.*, 2008; SBGMR, 1991; Zhou *et al.*, 2005).

Mineral Liberation Analysis (MLA) was used on selected 24 samples to identify accessory minerals, and to obtain accurate mineral modes. No cumulus orthopyroxene is found in studied samples. The details of this technique are presented the Appendix I, and the result of MLA measurements are shown in Figure 3.1 and Table 3.2, together with an generalised cumulus stratigraphy of the Panzhihua Intrusion.

A number of rock types have been recognized in the Panzhihua gabbroic intrusion (Table 3.1): gabbro, Fe-Ti oxide ore, ultramafic rocks (wehrlite, pyroxenite), anorthosite (or an-

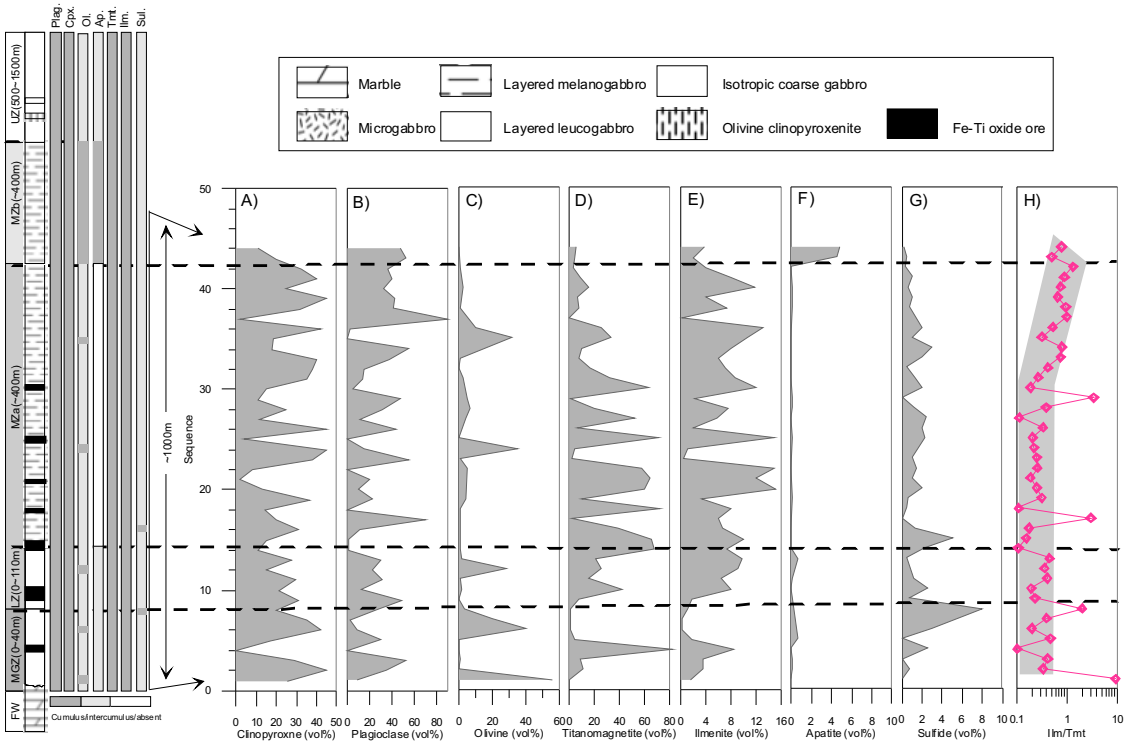

Fig. 3.1 Stratigraphy of cumulus (dark grey) and intercumulus (grey) phases in the Panzhihua Intrusion (modified after Pang, 2008), and the mineral modes of (A) clinopyroxene, (B) plagioclase, (C) olivine, (D) magnetite, (E) ilmenite, (F) apatite, (G) sulphide, and (H) Ilm/Mgt ratio. Dashed lines indicate the boundaries between subzones.

[1] Local geologists have subdivided the Panzhihua Fe-Ti-V oxide deposit into 9 ore bodies, among which the VIII and VI ore bodies are the largest.

Table 3.2 Representative MLA results for mineral modal proportions in samples from the Panzhihua Intrusion.

Zone[1]	MGZ				LZ						MZa						MZb
Sample	PZ-1	PZ-2	PZ-4	PZ-5	PZ-24	PZ-10	PZ-11	PZ-27	PZ-15	PZ-18	PZ-31	PZ-20	PZ-21	PZ-37	PZ-41	PZ-43	PZ-45
Rock[2]	Wehr	Gb	Ore	Hb-bi-gb	Ore	Ox-gb	Ore	Ox-gb	Ol-pyx-ore	Ore	Ore	Ol-ox-gb	Ox-gb	Pyx-ore	Ox-gb	Hb-gb	Ap-gb
Cumulate[3]	oc-C	pc-C	mi-C	pch-C	mi-C	pcmi-C	mi-C	mcpi-C	mico-C	mi-C	mpci-C	pcmio-C	cmpi-C	mi-C	pcmi-C	pc-C	pca-C
Sequence[4]	1	2	4	5	10	13	14	16	22	25	27	28	31	35	40	42	44
Cpx[5]	25.43	44.65	0	16.92	21.23	27.29	10.99	31.26	8.24	4.06	11.5	24.89	34.99	18.57	24.83	32.31	10.55
Plag	9.3	35.47	0	30.13	11.96	29.67	1.56	11.61	0.47	0.1	10.66	31.02	14.24	0.13	32.74	36.75	47.18
Ol	55.72	0.13	0.16	0.16	1.81	1.64	1.11	0.85	5.16	0.41	3.91	6.55	2.72	31.46	2.57	1.14	0.27
Hbl	4.96	2.82	0.01	29.72	8.49	2.69	4.12	3.38	4.46	1.52	3.28	4.5	4.09	2.31	4.84	6.85	15.63
Mgt	0.15	10.84	82.11	3.78	41.72	21.31	68	38.33	57.44	71.38	52.04	19.53	32.05	33.24	15.79	2.98	4.82
Ilm	1.43	3.64	8.52	1.79	8.07	9.68	7.39	6.69	14.83	14.83	5.82	7.58	8.68	10.67	11.84	4.01	3.79
Spl	0.01	0.05	4.34	0.01	0.52	0.02	1.2	0.33	0.86	2.45	1.39	0.72	0.23	0.24	0.09	0.01	0.02
Chl	1.7	0.53	1.54	5.64	1.62	5.7	2.99	4.1	6.19	2.38	5.91	3.33	1	2.13	3.1	10.38	6.39
Sul	0	0.72	2.56	0	2.52	0.46	2.23	1.27	1.51	2.29	2.47	1.24	1.26	1.07	0.59	0.28	0.22
Ap	0.02	0.05	0.01	0.7	0.01	0.58	0.02	0	0	0.03	0.01	0.03	0	0.01	0.06	0.01	4.76
Bi	0.09	1.05	0.01	10.65	0.03	0.27	0	0.67	0.02	0.01	0.05	0.26	0.02	0.03	0.04	0.12	2.98
Ttn	0	0	0	0.04	0	0	0	0.03	0	0	0.09	0	0	0	0.01	0.03	0.02
Zeo	0	0	0	0	1.88	0	0	0	0	0	0	0	0	0.01	3.43	3.09	3.17
Unknown	0.24	0.04	0.47	0.46	0.01	0.65	0.14	1.29	0.5	0.34	2.48	0.34	0.59	0.01	0.04	1.98	0.05
Total	99.04	99.99	99.73	99.99	99.88	99.94	99.74	99.81	99.68	99.81	99.6	99.97	99.87	99.89	100	99.99	100

1: Zone divisions after Zhou *et al.* (2005) and Pang *et al.* (2008).
2 & 3: Rock and cumulus names of the studied rocks.
4. Sequence of samples from two different sections is obtained according to the field record.
5. Cpx-clinopyroxene, Plag-plagioclase, Ol-olivine, Hbl-hornblende, Mgt-magnetite, Ilm-ilmenite, Spl-spinel, Chl-chlorite, Sul-sulphide, Ap-apatite, Bi-biotite, Ttn-titanite, Zeo-zeolite.

orthositic gabbro), and late-stage dykes of granophyric and felsic compositions (SBGMR, 1991; Zhou *et al.*, 2005). A subdivision is made for gabbroic rocks, based on the abundance of Fe-Ti oxides, and the abundance of some other cumulus minerals. First, gabbroic rocks with less than 15 vol%, and 15-40 vol% Fe-Ti oxides, are referred to as gabbro (microgabbro if fine-grained) and oxide gabbro, respectively. A rock with >40 vol% Fe-Ti oxides is called Fe-Ti oxide ore, including disseminated and massive ores. Second, olivine-, apatite-, and hornblende- have been used to denote gabbro where the amount of these minerals is >5 vol%.

Gabbroic rocks comprise most of the Panzhihua intrusion. Except for the isotropic coarse-grained gabbro in the uppermost and lower zones of the Panzhihua Intrusion, most of the gabbroic rocks have prominent layered texture. Fe-Ti oxide ores occur as tabular and lens-shaped layers generally concentrated in the lower part of the Panzhihua Intrusion within gabbros. Pyroxenite-hosted Fe-Ti oxide ore layers are rare. The ultramafic and anorthositic rocks occur conformably within the gabbroic sequence at different stratigraphic heights. Olivine pyroxenite layers are found in the MZ of the Zhujiabaobao open-pit, and also in the Upper Zone of the Panzhihua Intrusion (Pang, 2008; SBGMR, 1991). Anorthosite layers (up to 3 m thick) are found concordantly on top of the ore body VIII and ore body III (SBGMR, 1991), which represent the start and end of significant Fe-Ti oxide mineralization, respectively. Dykes of mafic to felsic compositions cut the Panzhihua intrusion at different heights. In the lower part of the mineralized gabbro part of the intrusion, pegmatitic gabbroic dykes and less abundant syenitic dykes occur. In the Middle and Upper part of the intrusion, the dykes are mainly of anorthositic composition. A few dioritic dykes occur cutting through the entire intrusion, but their genetic relationship to the intrusion is not demonstrated (Zhou *et al.*, 2005).

3.1.2 Gabbroic Rocks

Gabbro (Gb): These are mainly melano-gabbro comprising the majority of the Panzhihua Intrusion (Fig.3.2). These gabbros are medium- to coarse-grained consisting of 20-40% plagioclase, 30-45% clinopyroxene, 0-15% Fe-Ti oxides, 0-7% olivine, 0-8% hornblende, and 0-5% apatite. In general, the plagioclase mode increases upwards, whereas the abundance of the mafic minerals decreases. Relative proportions of plagioclase and clinopyroxene vary significantly; however the combined amount of these two minerals is relatively constant at 70-85 vol% (Table 3.2).

Plagioclase normally forms ca. 0.5-2 mm subhedral grains with lobate boundaries, interlocking with adjacent mineral aggregates, especially when in contact with Fe-Ti oxides (Fig

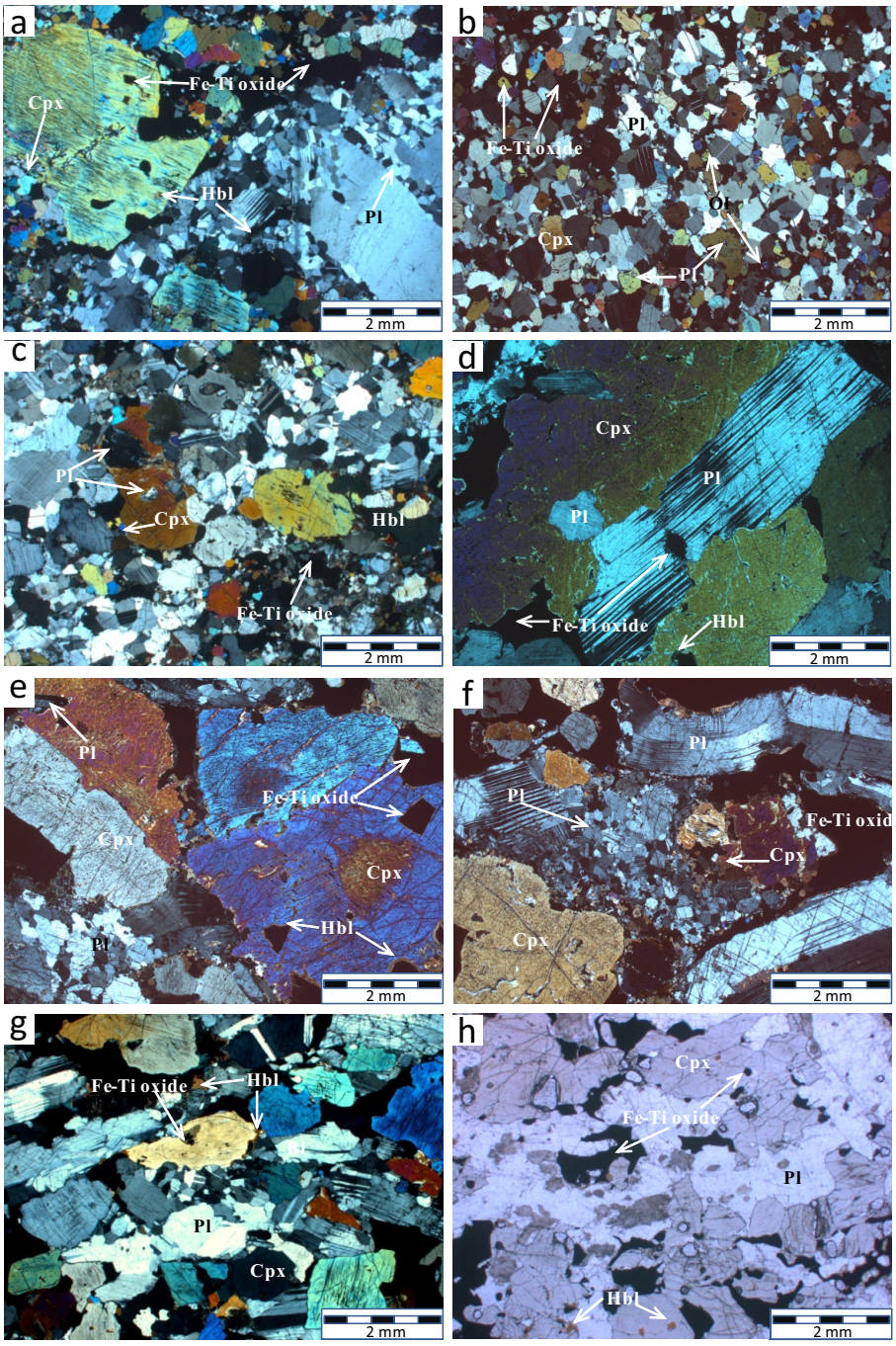

Fig. 3.2 Photomicrographs of representative melanogabbro from the Lanshan (a-d) and Zhujiabaobao (e-h) open-pits, Panzhihua Intrusion. (a) Typical recrystalized gabbro from the MGZ, showing characteristic features of two size populations of both Plag and Cpx. Note extensive exsolution of Fe-Ti oxides around Cpx. Hbl rimming Plag and Cpx when in contact with Fe-Ti oxides (PZ-2, pc-C, MGZ). (b) Typical fine-grained equigranular texture gabbro (PZ-3, pc-C, MGZ). (c) Medium-grained non-equigranular textured gabbro (PZ-9, pc-C, LZ). (d) atypical coarse-grained gabbro, showing interlocking feature of Plag and Cpx. Note a grain of Plag enclosed in Cpx (PZ-19, pc-C, MZa). (e) and (f) gabbro from the ZJBB showing non-equigranular coarse-grained texture and recrystallization of Plag (PZ-25, pc-C, LZ), and deformed twin of Plag (PZ-27, pc-C, MZa). (g) typical medium-grained gabbro from ZJBB section, showing orientated Cpx and recrystallization of Plag (PZ-39, pc-C, MZa). (h) medium-grained gabbro from the MZa (PZ-40, pc-C, MZa).

3.2). In some MGZ and LZ gabbro, two populations of plagioclase with distinct crystal sizes (0.1 mm vs >5 mm) are recognized. Plagioclase laths may be slightly deformed, displaying bent, kinked twinning, oscillatory extinction, granulation (primary crystals are replaced by smaller recrystallized grains), possibly caused by compaction. Single plagioclase grains with high aspect ratio and larger dimensions (up to 5 mm) occur occasionally in these rocks. Plagioclase may occur as a host mineral for small subhedral to anhedral Fe-Ti oxides, less commonly pyrrhotite, and occasionally clinopyroxene.

Clinopyroxene is subhedral to anhedral with a long dimension ranging from 1 mm to 1 cm. Generally, the morphology becomes more irregular and in some cases has curved boundaries when in contact with Fe-Ti oxides or plagioclase. The crystal size may be as small as 100 μm in some MGZ and LZ rocks where two populations of clinopyroxene and plagioclase are developed. Clinopyroxene shows broadly developed Schiller texture, which is characterized by exsolution of numerous small and regularly oriented plates of ilmenite. This texture is also developed in larger clinopyroxene inclusions in other phases, but is rare in the small recrystallized grains. The lamellae usually become coarser in the center, and gradually taper out towards the margins. In some cases, the lamellae develop unevenly. In the Panzhihua Intrusion gabbros, clinopyroxene may occur as the dominant mineral phase, containing inclusions of other minerals, opaque minerals (Fe-Ti oxides and sulphide), apatite and plagioclase, in the order of decreasing frequency. Fe-Ti oxide inclusions in clinopyroxene are very common throughout the intrusion. Clinopyroxene with apatite inclusions occurs only in the MZb apatite-gabbro which occurs above the zone of Fe-Ti oxide accumulation. Plagioclase in clinopyroxene is only found in samples from the MGZ and the upper MZa. It is noteworthy that below and above this interval, no significant Fe-Ti oxide accumulation is found.

Ca-poor pyroxene is rare in the Panzhihua rocks, and only appears in the microgabbro in the MGZ (Pang, 2008). It displays fine- to medium-grained texture and subhedral to anhedral shape. The amount of orthopyroxene (Opx) is less than 1 vol %.

Microgabbro (Mic-gb): This type of gabbro only occurs in the MGZ of the Panzhihua intrusion. It consists of ~52% plagioclase and ~30% clinopyroxene, 12% Fe-Ti oxides, 3% hornblende, and less than 1% olivine, trace amount of sulphide and apatite (<0.1%) (Table 3.2).

Plagioclase and clinopyroxene show nearly equigranular texture with fine-grained (<500μm) interlocking anhedral to subhedral grains, forming a dense cumulate texture (Fig

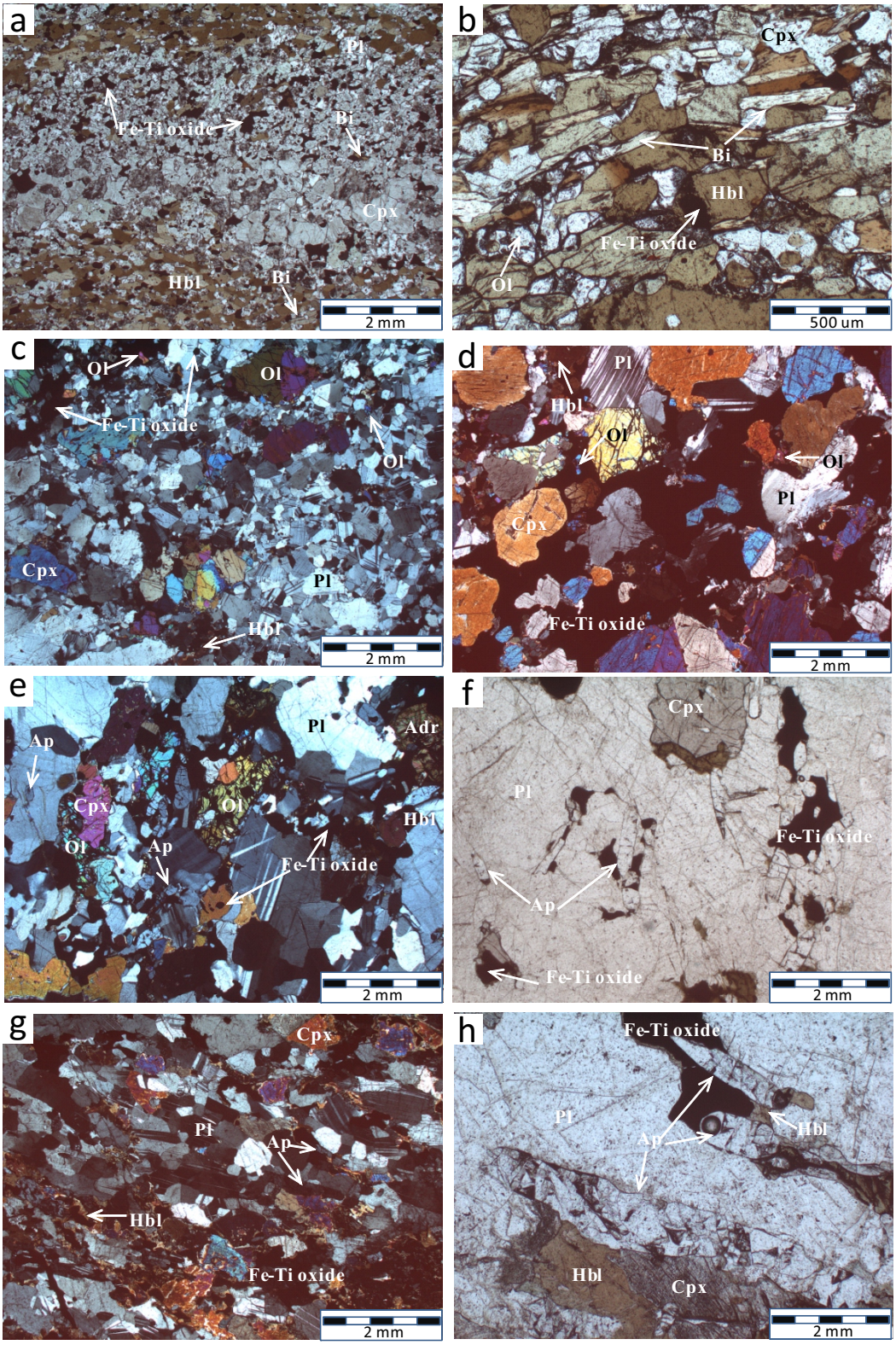

Fig. 3.3 Photomicrographs of representative Hbl-rich rock (a-b), Ol-gabbro (c-d), and Ap-gabbro (e-h) from the Panzhihua Intrusion. (a) Banded Hbl-rich rock consists of alternative layers of gabbroic (Cpx + Plag) and brown-colored Hbl-dominated zone (PZ-5, pchb-C, MGZ). (b) a less layered but strongly orientated Hbl-rich rock (PZ-7, pch-C, MGZ). (c) and (d) Ol-gabbro (PZ-20, pcmi-C, MZa) and oxide-rich Ol-gabbro (PZ-41, pco-C, MZa). (e) and (f) Ap-Ol-gabbro (PZ-44, pcoa-C, MZb). (g) and (h) Ap-gabbro (PZ-45, pca-C, MZb).

3.2b). A few plagioclase laths display polysynthetic twins. Tiny-grained inclusions of plagioclase and Fe-Ti oxides are common in clinopyroxene. Olivine occurs as ~100-200 μm anhedral grains attached to plagioclase in contact with Fe-Ti oxides, or isolated in the Fe-Ti oxides.

Hornblende-rich gabbro (Hbl-gb): These are found in the MGZ of the Lanshan open-pit and show fine-grained texture and are often transitional to hornblende-rich wehrlite (Fig 3.3). They are composed of ~30% hornblende, 10% Bi, 30% qlagioclase, 17% clinopyroxene, 5% Fe-Ti oxides, trace amount of olivine, sulfide. It is characterized by alternating layers of Hornblende-rich and gabbroic compositions (Fig 3.3a), or strongly orientated but less banded texture (Fig 3.3b). Hornblende is commonly anhedral to subhedral with grain size ranging from 0.5 to 1 mm.

The orientation of hornblende defines the foliation texture of the rocks. Bi laths are ~ 200-400 μm in the long direction. Clinopyroxene grains are anhedral, occurring as aggregates or interstitial to hornblende. Plagioclase occurs as anhedral, partly altered, interstitial to clinopyroxene and hornblende. Olivine, when present, displays anhedral or occasionally subround shapes in between hornblende.

Olivine-gabbro (Ol-gb): These rocks are present mainly in the MZa of the Panzhihua Intrusion. Olivine occurs as two groups of population sizes: the larger size (>1 mm) group occurs as anhedral grains with indented or straight boundaries adjacent to clinopyroxene or plagioclase, whereas the smaller size (0~100 μm) group occurs as irregular-shaped discrete grains between other silicate minerals, or included in Fe-Ti oxides (Fig 3.3c & d). These different appearances may reflect distinct genesis, cumulus or intercumulus, respectively.

Apatite-gabbro (Ap-gb): The appearance of abundant cumulus apatite marks the base of the MZb. apatite gabbro contains ~ 5% apatite, 40-50% plagioclase, 10-30% clinopyroxene, 0-8% olivine, 5-8% Fe-Ti oxides, 0-1% sulfide, and 15% hornblende and trace amount of andradite in one sample (Fig 3.3e-h). Plagioclase is more abundant than clinopyroxene. Plagioclase and clinopyroxene show similar textural relationship to other gabbro. Apatite is usually associated with plagioclase aggregates (Fig 3.3f & h). Apatite is recognized as colourless, commonly elongated or stubby elongated or stubby hexagonal crystals, or tabular plate. The size of apatite crystal varies from 0.3 μm to >2 mm (Fig 3.e-h). Olivine occurs as interstitial. It is noteworthy that olivine is always occurring between Fe-Ti oxides and either plagioclase or clinopyroxene. Some andradite grains occur attached to plagioclase in contact with Fe-Ti oxides.

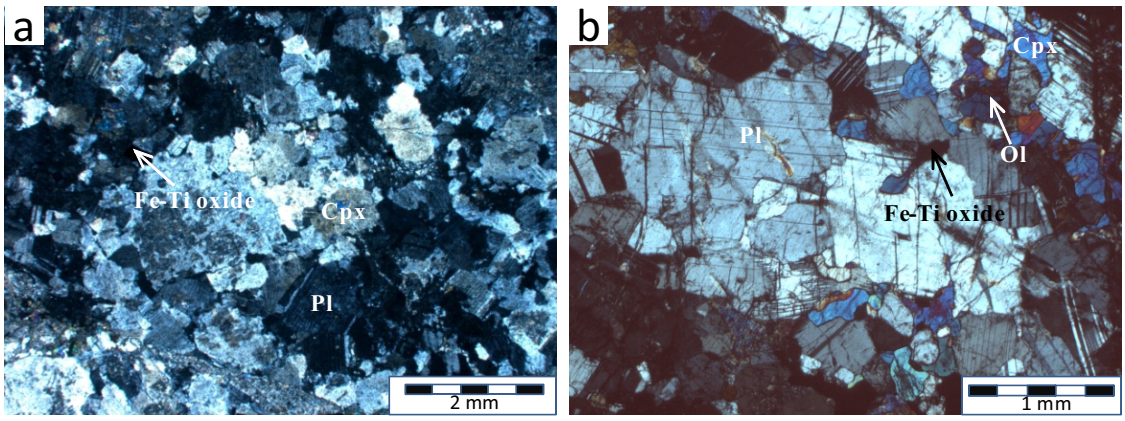

Fig. 3.4 Photomicrographs of representative appearance of anorthositic rocks from the MZa in the Panzhihua Intrusion. (a) an altered anorthosite from the Lanshan section (PZ-23, p-C, MZa). (b) anorthositic gabbro shows cumulus Plag and interstitial Cpx (PZ-32, pc-C, MZa).

Anorthositic gabbro (Anorth-gb): These are found in both Lanshan and Zhujiabaobao sections. These rocks contain 70-90% plagioclase, 2-10 % clinopyroxene, 0-4% olivine, 1-4% hornblende, 1-3% Fe-Ti oxides (Table 3.2). Plagioclase occurs mostly as 1-2 mm irregular laths or grain aggregates. In some places plagioclase is moderately altered (Fig 3.4a & b). Fe-Ti oxide, clinopyroxene and olivine occur as interstitial to plagioclase. Hornblende usually rims the plagioclase in contact with Fe-Ti oxide, similar to other gabbro.

Fe-Ti oxides, mainly magnetite and ilmenite, display multiple occurrences in gabbroic rocks: interstitial, discrete, and as inclusions (Fig 3.5a-d). Interstitial Fe-Ti oxides have irregular shapes. It may appear as a single phase either of magnetite or ilmenite, or as magnetite-ilmenite aggregates which are interstitial to silicate minerals but have straight and flat boundaries with adjacent oxide minerals (Fig 3.5a & b). Within polycrystalline aggregates, straight boundaries, which are similar to those in the cumulus phases, are interpreted as an indication of co-crystallisation of magnetite and ilmenite from the intercumulus liquid, rather than intrusive or replacement relationships. Fe-Ti oxides inclusions in clinopyroxene are very common in gabbroic rocks, where they have variable sizes and shapes (Fig 3.5c). Olivine and plagioclase also host Fe-Ti oxides. Exsolution of ilmenite is commonly seen in clinopyroxene (Fig 3.5d).

Sulphide minerals in the gabbro from the Panzhihua intrusion include mainly pyrrhotite (Po), subordinate chalcopyrite (Ccp), pentlandite (Pn), and occasionally pyrite (Py) (Fig 3.5e-h). Pyrrhotite occurs as discrete setting between silicates or coexisting with Fe-Ti oxides. Chalcopyrite and pentlandite usually coexist with pyrrhotite almost without exception. Only few individual phases of chalcopyrite and pentlandite are found in the studied samples, which

probably due to a 2D sectioning effect on a polymineralic sulfide aggregate (Fig 3.5e). Pentlandite are explained as exsolution from the pyrrhotite, while chalcopyrite is unlikely to be exsolved from po and probably forms from separate high emperature intermediate solid solution (ISS) phase (Naldrett, 2004). Pyrite aggregate consisting of euhedral pyrite is only found in moderately altered gabbro, which may be a product of secondary alteration (Fig 3.5g). It is also common that pyrrhotite occur as inclusion in clinopyroxene, few in plagioclase, and as droplets in clinopyroxene (Fig 3.5h).

3.1.3 Ultramafic Rocks

The ultramafic rocks in the Panzhihua Intrusion include wehrlite and olivine-pyroxenite. In this study, wehrlite were collected from the MGZ and MZa in the Lanshan section. olivine-pyroxenite contains abundant Fe-Ti oxides and hence has been grouped into ore rocks which will be described in the Section on Fe-Ti oxide ores.

The wehrlite consists of 35-55% olivine, 25-50% clinopyroxene, 0-15 % plagioclase, 1-4% Fe-Ti oxides, 0-6 % sulfide, and 2-5% hornblende. In general, wehrlites in the MGZ have more olivine, sulfide and hornblende and less clinopyroxene, plagioclase and Fe-Ti oxides, compared with wehrlites from the MZa.

Wehrlites from different stratigraphic levels also show distinct textural features. In the MGZ wehrlite from near the bottom contact, some of olivine and clinopyroxene are fractured, forming a net-like pattern surrounding larger olivine and clinopyroxene (Fig 3.6a & b). In another MGZ wehrlite from a higher level, cumulus large olivine is set in a matrix of small grains of clinopyroxene (Fig 3.6d & e). In the MZa wehrlite, olivine aggregates form a network surrounding large clinopyroxene (Fig 3.6f-h).

Olivine inclusions in clinopyroxene are found in both the contact and MZa wehrlite (Fig 3.6c & f). Zoned-pattern exsolution in clinopyroxene is also seen in these rocks (Fig 3.6b, f-h). In the MZa wehrlite, olivine occurs also as inclusions in the plagioclase (Fig 3.6f).

In all wehrlites, Fe-Ti oxides are minor, accounting for <5%, but the ratio of Ilm/magnetite vary significantly, from 0 to ~10 (Fig 3.1). For example, in the contact wehrlite, the total amount of magnetite and ilmenite is 1.5%, whereas the ratio of ilmenite to magnetite is 9.3 (Table 3.2).

Oxide minerals are found as disseminated grains and also inclusions in olivine fragments (Fig 3.7a-f). Similar textures occur in the primary clinopyroxene, in which random and/or zoned distribution of Fe-Ti oxides are common (Fig 3.7a, c, f).

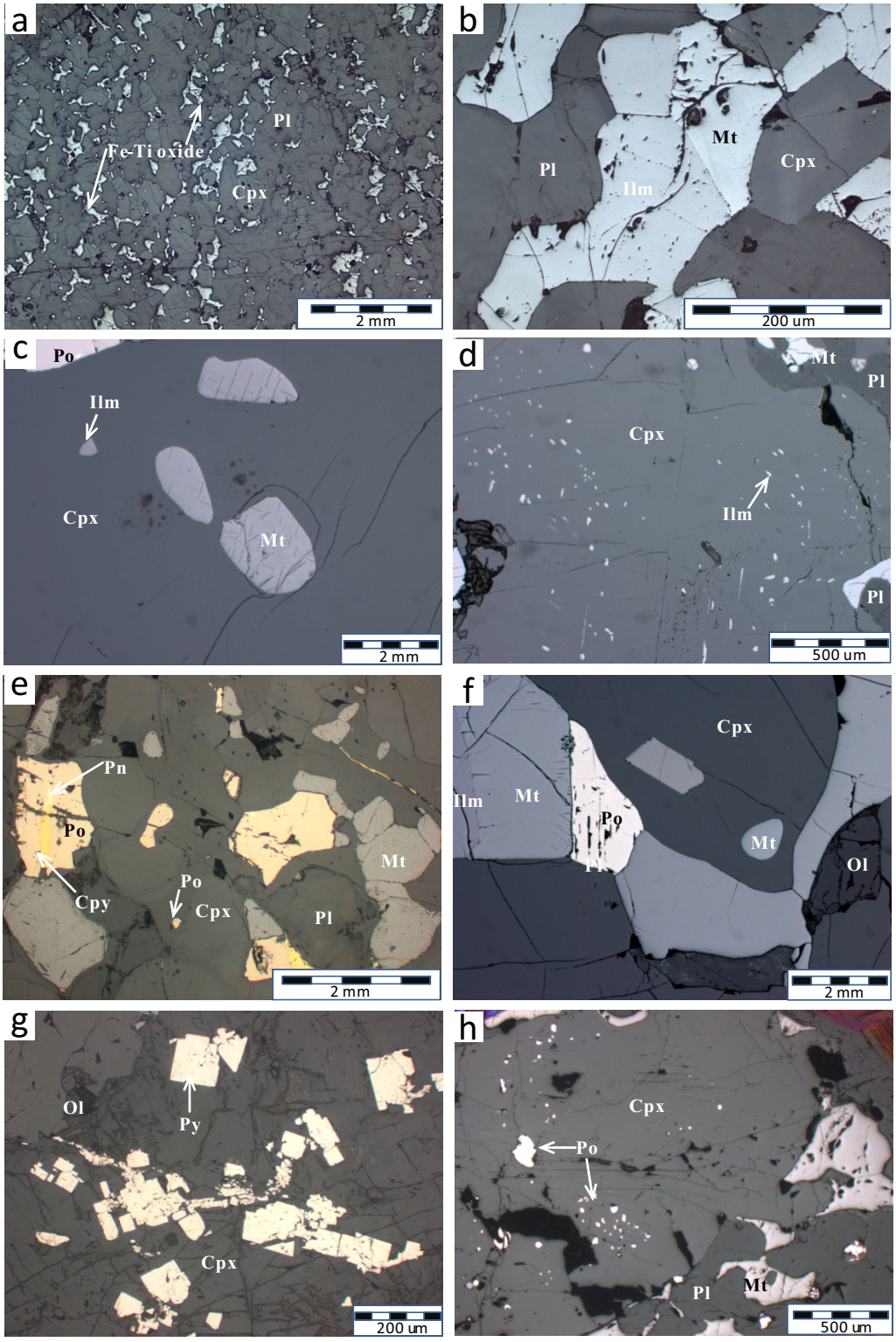

Fig. 3.5 Photomicrographs of representative appearance of Fe-Ti oxides (a-d) and sulphides (e-h) in the gabbroic rocks from the Panzhihua Intrusion. (a) and (b) Interstitial Fe-Ti oxide (a) and intergrowth of Mgt and Ilm (b) (PZ-3, pc-C, MGZ). (c) Fe-Ti oxide inclusion in Cpx (PZ-29, pcmi-C, MZa). (d) Exsolution of Ilm in Cpx (PZ-20, pcmi-C, MZa). (e) Sulphides in gabbro (PZ-2, pc-C, MGZ). (f) Sulphide coexisting with Fe-Ti oxides in gabbro (PZ-40, pc-C, MZa). (g) Sulphide aggregates in moderately altered gabbro (PZ-43, pc-C, MZa). (h) Droplets of sulphide in Cpx (PZ-42, pc-C, MZa).

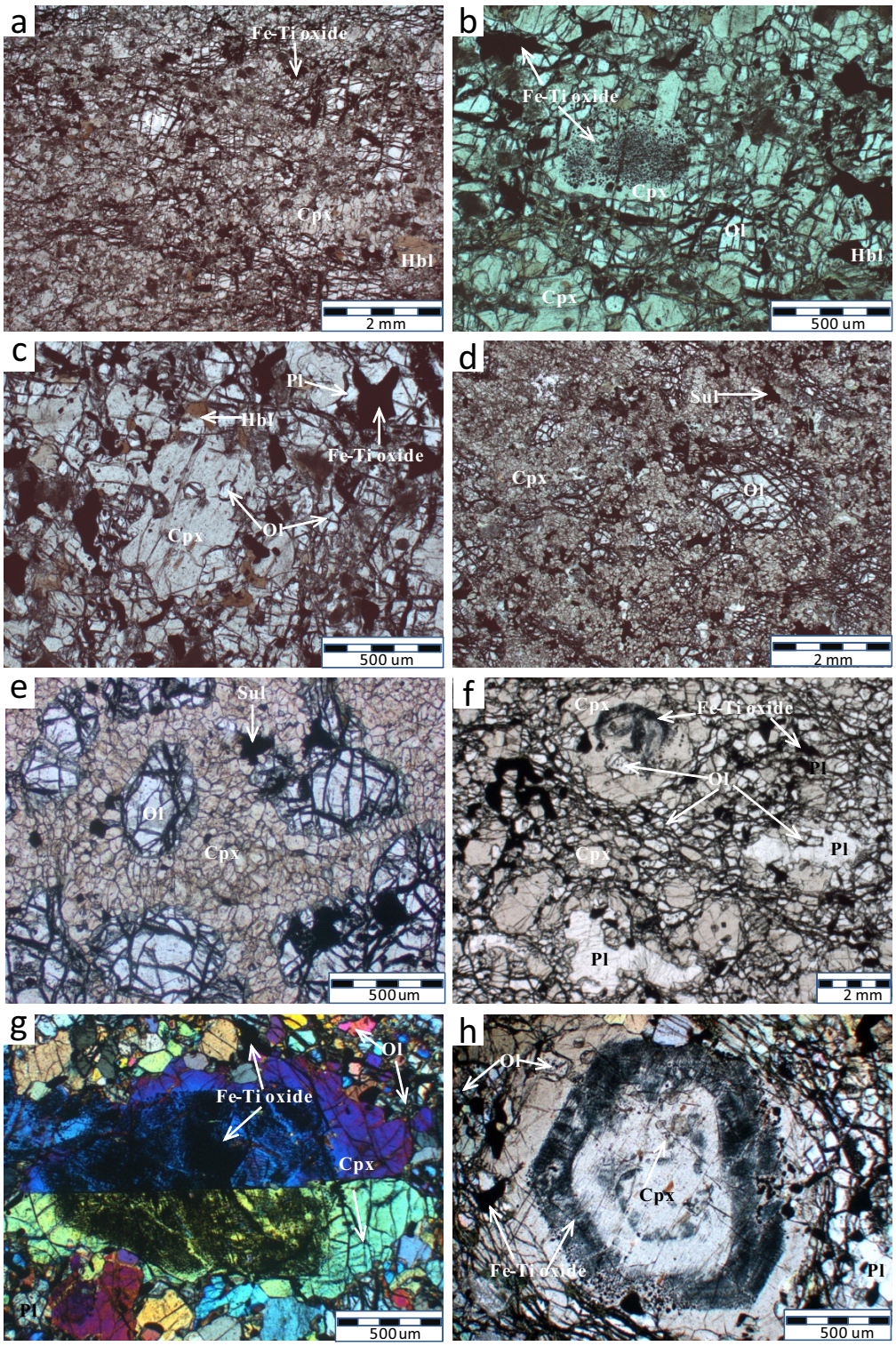

Fig. 3.6 Photomicrographs of representative werhrlites from the Lanshan open-pit , Panzhihua Intrusion. (a-c) a plag-bearing wehrlite from the MGZ near the contact with footwall marble , showing an extensively fractured Ol and Cpx texture (a), zoned-pattern exsolution in Cpx (b), and olivine inclusion in Cpx (c) (PZ-1, oc-C, MGZ). (d) and (e) another contact wehrlite shows porphyry-like texture consisting of porphyry Ol surrounded by small tight connected Cpx aggregates (PZ-6, oc-C, MGZ). (f) - (h) plag-rich wehrlite from the MZa, showing net-like Ol surrounding large Cpx and as inclusion in both Cpx and plag (f), and different exsolution patterns in Cpx (g-h).

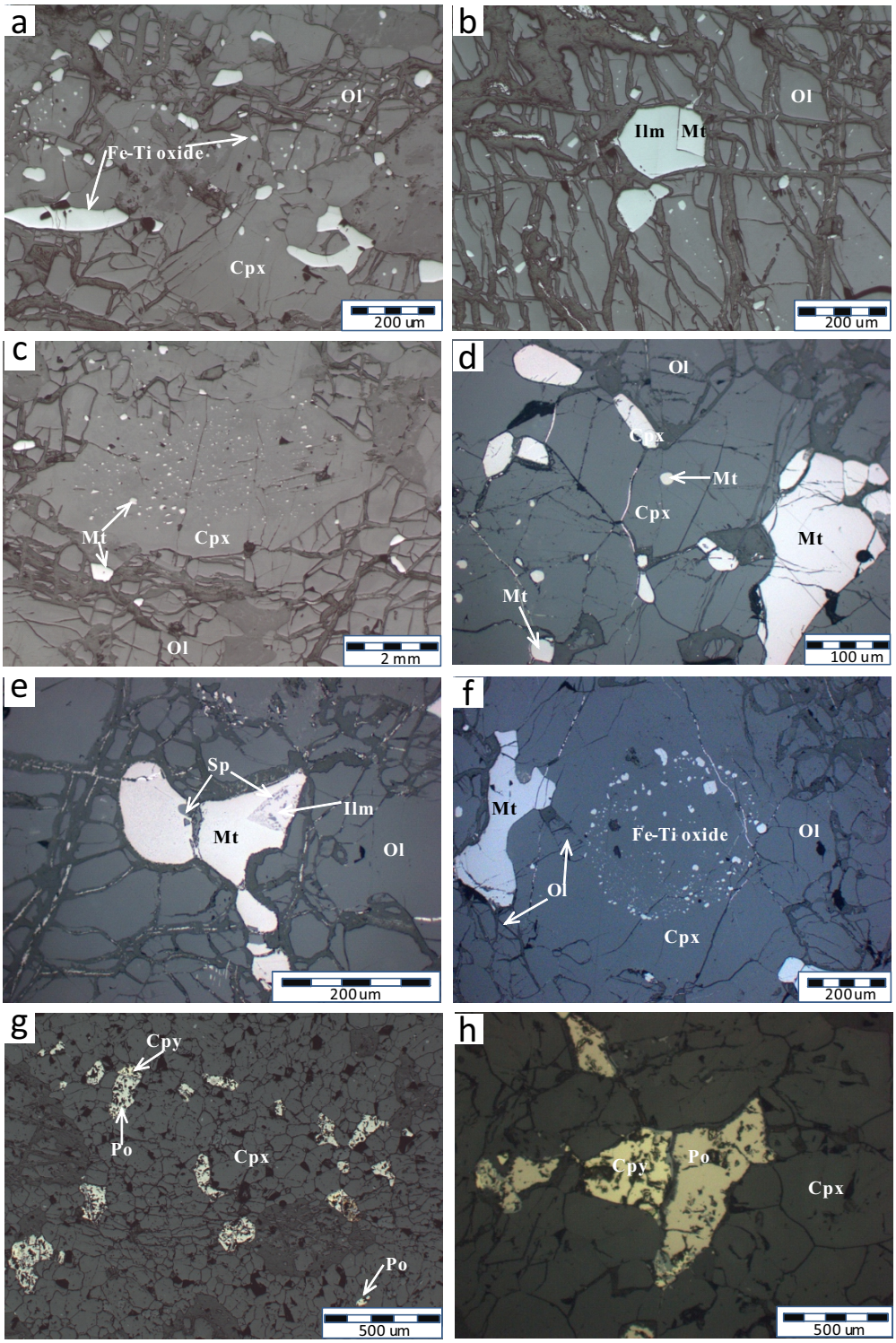

Fig. 3.7 Photomicrographs of Fe-Ti oxides (a-f) and sulphides (g-h) in the wehrlite rocks from the Panzhihua intrusion. (a-c) Fe-Ti oxide occurrence in the MGZ wehrlite near the contact (PZ-1, oc-C, MGZ), showing an overview of the Fe-Ti oxide occurrence in the contact wehrlite, two-phase Fe-Ti oxide inclusion in Ol (b), and exsolution of Fe-Ti oxide in Cpx (c). (d-f) Fe-Ti oxide occurrence in the MZa wehrlite (PZ-17, oc-C, MZa), showing discrete grains and inclusions of Fe-Ti oxides (d), coexisting Ilm and Mgt with Spl exsolutions (e), and exsolution of Fe-Ti oxide in Cpx (f). (g) and (h) sulphides in wehrlite from the MGZ, showing disseminated sulphide (g), and coexisting Cpx and Po.

Fe-Ti oxides show subhedral to anhedral morphologies in most cases, with grain sizes ranging from barely visible up to 500 μm. Magnetite and ilmenite may occur as single phases, or as two-phase intergrowths (Fig.3.7b). Granular spinel grains are found along the single-phase magnetite boundaries, or along the sharp boundaries between a composite magnetite and ilmenite (Fig 3.7e).

Sulphides are more abundant (up to ~ 5%) in the wehrlite from the MGZ, than in the MZa. The abundance, occurrence, and mineral assemblage of sulphides in wehrlite are similar to those in gabbroic rocks. Disseminated sulfide is mainly pyrrhotite (Fig 3.7g & h). Pentlandite is also quite common, with the textural relationships suggesting crystallisation from a sulfide liquid.

3.1.4 Fe-Ti Oxide-rich Rocks (magnetite+ilmenite > 15%)

Fe-Ti oxide-rich rocks include the oxide ore (also called massive ore in this study) and oxide-rich gabbro (often referred to as disseminated ore in the literature).

The massive ores consist of up to 90% magnetite and ilmenite (ilmenite/magnetite<0.3), with the amounts ranging from 33 to 82%, and 6 to 15%, respectively. Silicate minerals include: 0-21% clinopyroxene, 0-12% plagioclase, 0.1-4% olivine, and 0-9% hornblende. The wide range of silicate mineral contents reflects differences in the host rocks: gabbro- or olivine-pyroxenite-hosted ore.

The oxide-rich rocks are intermediate between gabbro and Fe-Ti oxide ore. They consist of 15-38 % magnetite, 6-12 % ilmenite (ilmenite/magnetite: 0.3-0.8), 24-38 % clinopyroxene, 12-33 % plagioclase, 1-3 % olivine, and 2-7 % hornblende (Table. 3.2). The silicate mineral have comparable textures with those in oxide ore rocks.

3.1.4.1 Silicate minerals

Silicate mineral assemblages in the oxide-rich rocks are clinopyroxne + plagioclase ± olivine or clinopyroxene + olivine ± plagioclase. The oxide-rich rocks show cumulus textures (pcmi-C or pcomi-C) with silicate mineral(s) isolated by Fe-Ti oxides (Fig 3.8). The crystals show common resorption features, unlike in the gabbroic rocks (Fig 3.8a & b).

Clinopyroxene are generally medium to coarse-grained, but in some cases in the LZ of the ZJBB section, clinopyroxene grains (>2cm) are found surrounded by recrystallized olivine aggregates, which consist of ~100 um sized olivine grains (Fig 3.8c). Plagioclase and biotite patches, and tiny magnetite inclusions occasionally occur within the clinopyroxene host (Fig

3.8d). Clinopyroxene in contact with Fe-Ti oxides are usually rimmed by hornblende and/or olivine (Fig 3.8e-g). Olivine rims consist of a few small olivine grains with various extinctions (Fig 3.8g). In addition, olivine may occur as subrounded cumulus grains coexisting with clinopyroxene or isolated grains in the Fe-Ti oxide matrix (Fig 3.8b-f). Sometimes, olivine is elongated (Fig 3.8f). Plagioclase occur as >1 cm long laths with an aspect ratio of ~ 5 (Fig 3.8h). Plagioclase is often rimmed by hornblende, whenever it is in contact with Fe-Ti oxides. Plagioclase usually defines the foliation of the rock (Fig 3.8h).

Inclusions of Fe-Ti oxides and sulphides are common in clinopyroxene and plagioclase in the ore rocks. Some Fe-Ti oxide inclusions show similar hornblende rims to those around the host minerals (Fig 3.8a & h). It is not as common to find Fe-Ti oxides in fractures in olivine in these rocks as it is in wehrlite and gabbroic rocks.

of the rock (Fig 3.8h).

3.1.4.2 Micro-textures of Fe-Ti oxides (oxy-exsolution and boundaries)

The magnetite and ilmenite crystals generally have sizes ranging from 0.5-2 mm, correlating with the modal proportion of Fe-Ti oxides. They usually have equilibrium boundaries with other magnetite or ilmenite grains, characterized by triple junctions with ~ 120° (Fig 3.9a-d). Silicate remnants, mostly olivine, are common in the Panzhihua ore rocks (Fig 3.9a, b, d).

The magnetite, a solid solution of magnetite and ulvospinel (abbreviated as ulvospinel-magnetite$_{ss}$), in massive ore rocks are characterized by various degrees of ilmenite intergrowths (ilmenite$_{ss}$) and granular or lense-shaped hercynite ($FeAl_2O_4$)(Fig 3.9e-h).

According to the classification of Buddington and Lindsley (1964), the ilmenite$_{ss}$ intergrowths in magnetite may be divided into: (1) trellis type, (2) composite (granular) types, and (3) sandwich types. The intensity of the oxidation is characterised by 7 stages, from primary homogeneous ulvospinel-rich magnetite solid solution (C1) to the most advanced stage (C7) represented by an assemblage of pseudobrookite $_{ss}$ and hematite $_{ss}$ (Haggerty, 1991).

Trellis type. This type of ilmenite$_{ss}$ is characterized by orientation of fine spindles of ilmenite along 1-3 sets of the spinel planes (equal to stage of C1 to C2), usually with granular exsolution of hercynite (Fig 3.9e, g, h), which is rare in magnetite in wehrlite and oxide-poor gabbro. The hercynite exsolution is irregular to lensoidal with size ranging from barely visible to ~40 μm. It is usually distributed randomly, but occasionally forms linear arrays (Fig 3.9f & h). ilmenite lamellae are concentrated mostly along magnetite boundaries, and progressively

develop towards the centre of the magnetite grains. They display sharp contacts with magnetite host, and usually taper out at the intersection of two or more sets of lamellae and towards the boundaries. Lamellae that parallel to any one set of octahedral planes are in optical continuity. The ilmenite$_{ss}$ is formed by partial oxidation of ulvospinel in ulvospinel-magnetite$_{ss}$, and can be expressed as follows:

$$6\ Fe_2TiO_4\ (uvospinel) + O_2 = 6\ FeTiO_3\ (ilmenite) + 2\ Fe_3O_4\ (magnetite) \quad (1)$$

At a higher state of oxidation, when ulvospinel is completely oxidized, the expression is:

$$4\ Fe_2TiO_4\ (ulvospinel) + O_2 = 4\ FeTiO_3\ (ilmenite) + 2\ Fe_2O_3\ (hematite) \quad (2)$$

Sandwich types. This type is characterized by thick (20-50 μm) laths of ilmenite along a single plane in magnetite (Fig 3.10a-d). Ilmenite forms long, continuous laths with sharp straight contact with the host magnetite. There are abundant hercynite inclusions of various sizes, forms and orientation within the ilmenite laths (Fig 3.10 b-d). The fact that all hercynite exsolutions are confined within the ilmenite laths indicates their genetic relationship with ilmenite. The sandwich type ilmenite laths in magnetite may originate from either oxidation exsolution or primary crystallization from the melt.

Composite types. This types refers to euhedral to anhedral ilmenite inclusions within or on the borders of a magnetite host. This type of ilmenite has been recognized in both wehrlite (Fig 3.7e) and massive ore rocks (Fig 3.10e-f). Ilmenite have sharp, either irregular or straight boundaries with the magnetite host. The ilmenite inclusions usually have hercynite exsolution with irregular to granular forms, and become coarse from the boundary to the centre (Fig 3.7e; Fig 3.10e-f). The genesis of these composite ilmenite inclusion is controversial, either primary precipitation or oxidation-caused exsolution (Haggerty, 1976).

Compared to the extensive oxy-exsolution features in cumulus magnetite described above, cumulus ilmenite show much less exsolution texture, even when coexisting with trellis textured magnetite (Fig 3.9c; Fig 3.11a). However, laths of rutile in the ilmenite host are observed in some cases (Fig. 3.11b). These rutile-rich laths are long, straight, and have sharp contact with host ilmenite. The width of the lath is ranging from 10 to 80 μm, usually parallel to each other.

The boundaries between magnetite and ilmenite are variable. In some cases, it is a sharp contact, but in many cases it is a reaction boundary with abundant hercynite exsolutions (Fig 3.11). The reaction zone is usually <50 μm wide (Fig 3.11a, c, e). The hercynite exsolutions are irregular to granular, and the sizes vary from barely visible to 40 μm, which is within the

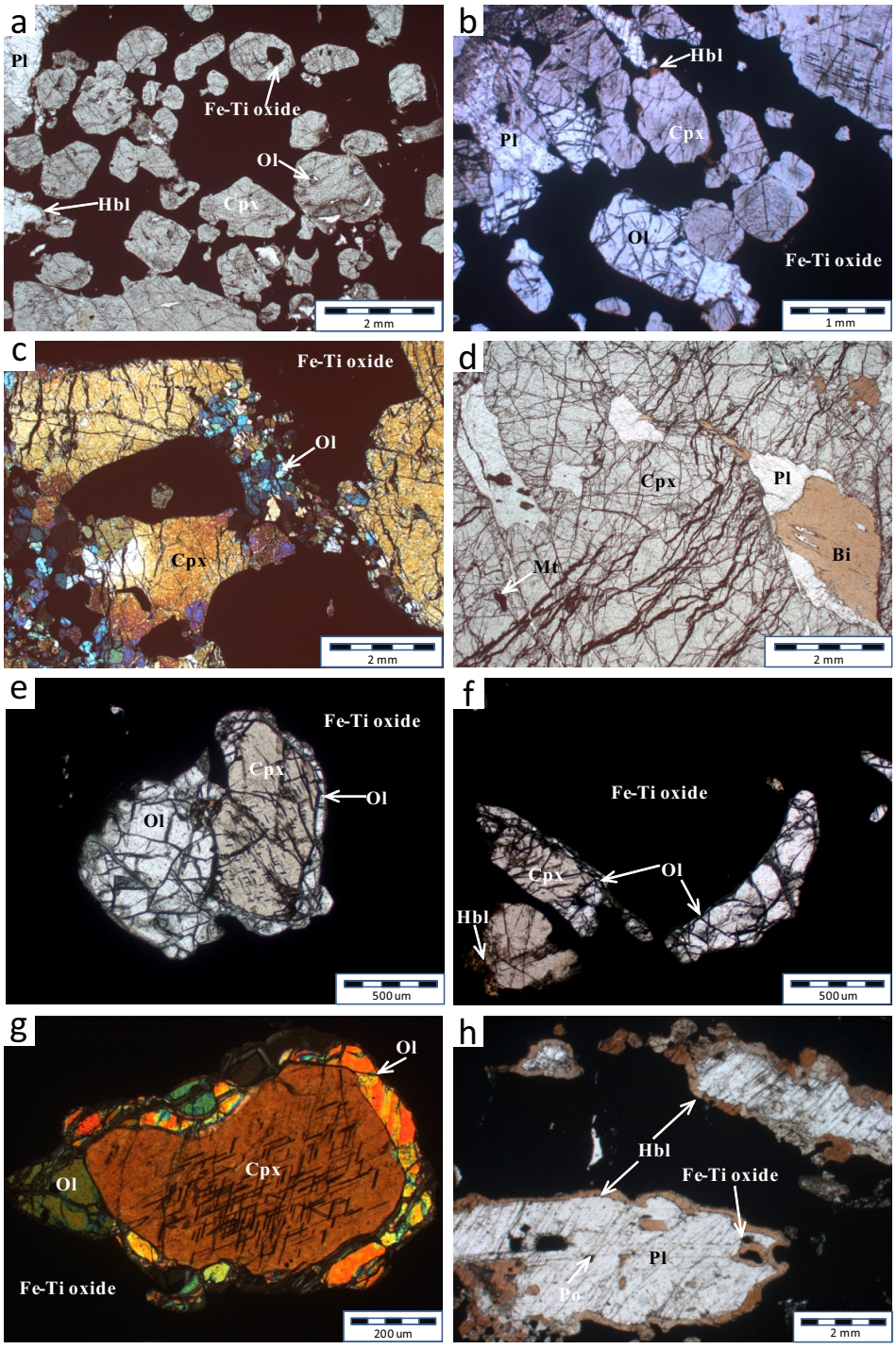

Fig. 3.8 Photomicrographs show occurrences of silicate minerals in the Fe-Ti oxide-rich rocks from the Panzhihua Intrusion. (a) Subrounded Cpx in a Plag-bearing pyroxenite-host ore (PZ-27, mi-C, MZa) from the ZJBB. (b) a Plag-bearing Ol-pyroxenite ore (PZ-38, pcmi-C, MZa) from the MZa, ZJBB. (c) & (d) a pegmatitic Ol-pyroxenite ore (PZ-26, ocmi-C, LZ) in ZJBB showing a part of a Cpx megacryst and numerous small recrystallized Ol (c), and poikilitic Plag and Bi in the Cpx megacryst (d). (e) & (f) a massive ore (PZ-11, mi-C, LZ) from the LS section, showing coexisting Cpx and Ol (e), and elongated Ol and Cpx (f). Note Cpx are rimmed by Ol. (g) a Cpx crystal rimmed by Ol aggregate in a massive ore (PZ-13) from the MZa, LZS (h) Oriented Plag rimmed by Hbl in a massive ore (PZ-14, mi-C, MZa). Note inclusions of Mgt and Po in the Plag.

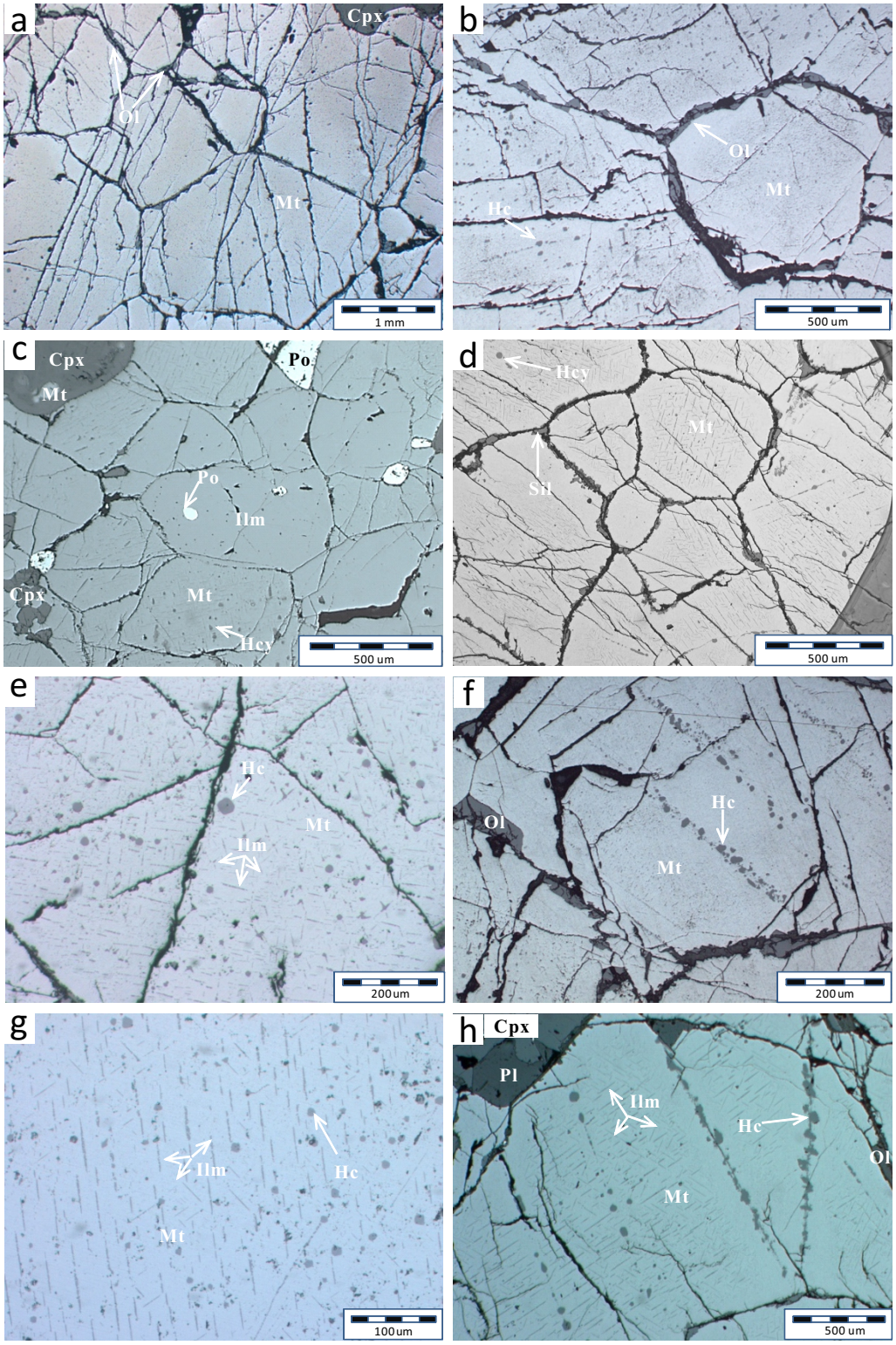

Fig. 3.9 Photomicrographs show occurrences of massive ore and oxy-exsolution in Mgt from the Panzhihua Intrusion. (a) & (b) massive ore from the Lanshan section (PZ-13, 14, mi-C, MZa). Note silicate remnants in the triple junctions. (c) & (d) massive ore from the ZJBB section (PZ-27, PZ-31, mi-C, MZa). (e) Coexisting Ilm_{ss} and granular Hc exsolution (PZ-11, mi-C, LZ). (f) Oriented granular Hc in Mgt host (PZ-14, mi-C, MZa). (g) Coexisting Ilm_{ss} and Hc exsolution in Mgt host (PZ-27, mi-C, MZa) from ZJBB section. (h) linear Hc exsolution in Mgt host (PZ-31, mi-C, MZa) from the ZJBB.

range of those in magnetite or in the sandwich type ilmenite$_{ss}$. Note that magnetite is usually free of granular hercynite exsolutions, where sandwich-type ilmenite occurs within magnetite (Fig 3.10a), or the ilmenite-magnetite boundaries develop (Fig 3.11a, c, e).

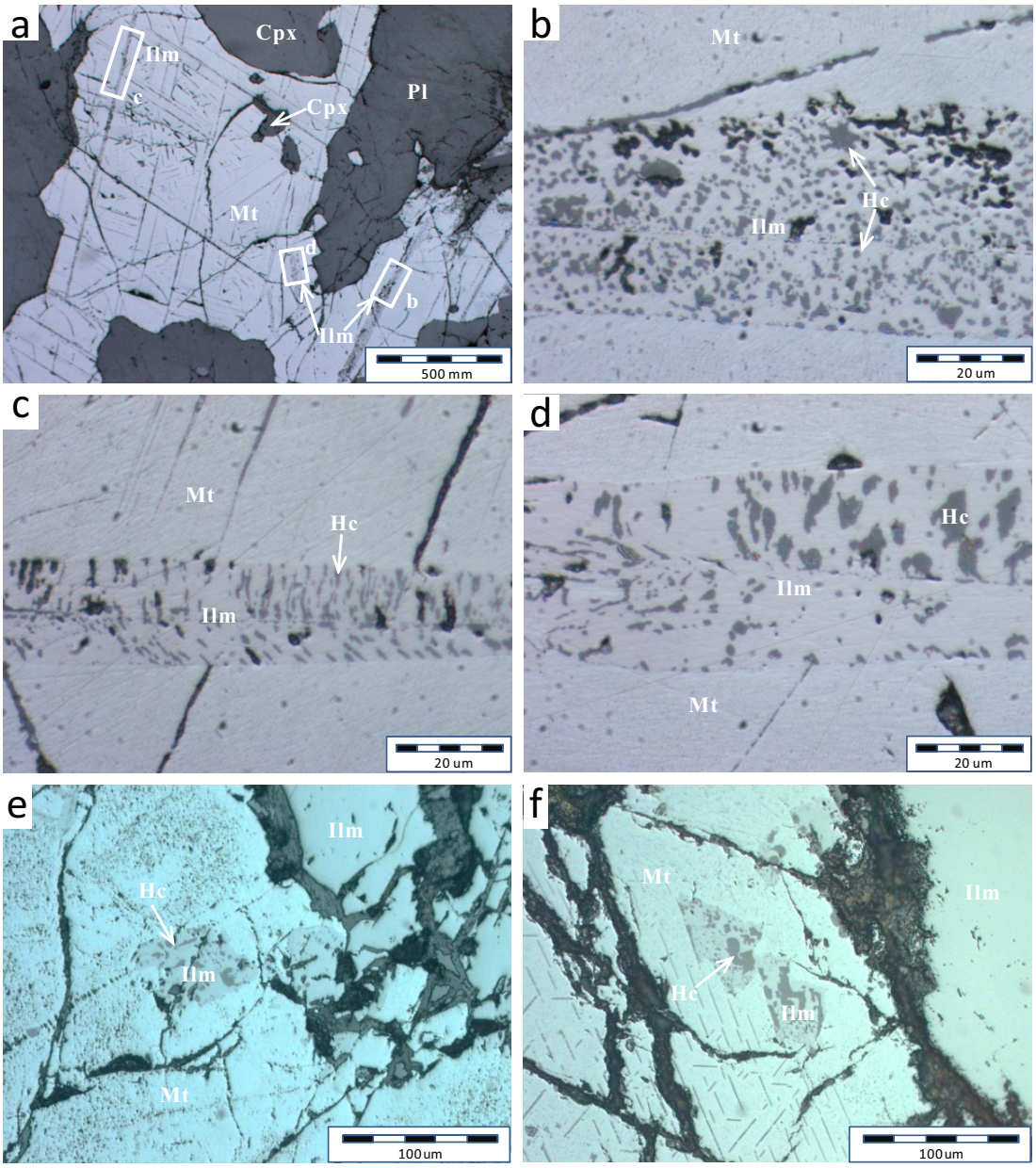

Fig. 3.10 Photomicrographs show sandwich-type Ilm$_{ss}$ in Mgt (PZ-10, pcmi-C, LZ) from the LS section of the Panzhihua Intrusion. (a) An overview of the host Mgt. (b-d) different types of Ilm$_{ss}$ laths on basis of the distribution patterns of the Hc exsolutions: dense & random (b), oriented (c), and coarsen and random (d). Note Ilm$_{ss}$ are constrained well by flat and straight boundaries with Mgt, and all Hc exsolution are confined within the Ilm$_{ss}$, indicating its genesis relationship with the Ilm$_{ss}$. (e) & (f) composite Ilm$_{ss}$ in Mgt from the ZJBB section (PZ-30, 31, mi-C, MZa). Note the irregular shape of Ilm and various sizes of Hc exsolutions.

3.1.4.3 Micro-textures of Fe-Ni-Cu-S sulphides

Sulphide assemblage (pyrrhotite ± pentlandite ± chalcopyrite ± pyrite) is similar to that in the oxide-poor gabbro and wehrlite. Pyrrhotite is the most common sulphide mineral, whereas others account for a very small amount of the total sulphide, which is up to 8 vol% in the studied samples. The amount of sulphide generally decreases from the bottom of the intrusion up the section (Fig 3.2G).

Pyrrhotite occurs mainly as subhedral to anhedral dessiminated grains in Panzhihua oxide-rich rocks (massive ore and oxide-rich gabbro) (Fig 3.12). It usually has straight boundaries with magnetite and/or ilmenite, in some cases with ~120˚ triple junctions (Fig 3.12a-c). Pyrrhotite and silicate minerals have either straight or curved or rugged contact (Fig 3.12b-d). The size of sulphides varies from several microns to ~ 1 mm, mostly <500 um (Fig 3.12). Generally, sulphides are coarser in oxide-rich rocks (Fig 3.12e & f). Some large pyrrhotite grains may have inclusions of pentlandite (Fig 3.12d & g) or occasionally pyrite (Fig 3.12h). Flame-like pentlandite exsolutions are also observed (Fig 3.12c & h). In addition, tiny to small grains of pentlandite commonly found next to pyrrhotite (Fig 3.12b-e). The variations of the morphology and grain size likely reflect subsolidus recrystallisation. In some cases, especially when in contact with magnetite, pyrrhotite may be replaced by magnetite, probably due to oxidation (Fig 3.12b, h).

Pyrrhotite in oxide-rich rocks may occur enclosed in silicate and oxide minerals, similarly to oxide-poor rocks (Fig 3.13; Fig 3.14). clinopyroxene is the most common host mineral for pyrrhotite (Fig 3.13a-c; Fig 3.14a-b), followed by plagioclase (Fig 3.13d; Fig 3.14c) and olivine (Fig 3.14d). Only one pyrrhotite with triangular shape is found in hornblende occurring among slightly altered plagioclase (Fig 3.13e). Pyrrhotite in magnetite and ilmenite are also common (Fig 3.13f-h; Fig 3.14f-h).

Pyrrhotite enclosed in silicate minerals may be rounded, or irregular, or even triangular. The grain sizes range to several hundreds of μm, mostly 40-150 μm (Fig 3.13a-e; Fig 3.14a-e). It may occur as a single phase, or a composite of pyrrhotite, pentlandite, and occasionally magnetite or ilmenite, regardless of the type of the host mineral or abundance of Fe-Ti oxides (Fig 3.13a-e, Fig 3.14a-e). However, small round-shaped sulphide droplets are only observed in clinopyroxene (Fig 3.13b; Fig 3.14e). Silicate minerals hosting pyrrhotite usually lack hornblende rims, except one case of clinopyroxene (Fig 3.13c). However, this may be a result of post-magmatic alteration.

Pyrrhotite enclosed in ilmenite exclusively shows sharp contacts with the host and round shapes, with a size of 100-200 μm (Fig 3.13f; Fig 3.14f). In contrast, magnetite-hosted pyrrhotite grains are extremely variable in grain sizes, varying from barely visible up to ~ 200μm (Fig 3.13g-h; Fig 3.14g-h). They are characterised by a corona of hercynite (Fig 3.13g-h; Fig 3.14g), even when the host magnetite is itself an inclusion in clinopyroxene (Fig 3.14h). Hercynite surrounding pyrrhotite, and the granular hercynite occurring along the boundaries of magnetite inclusions, have compositions similar to those occurring within magnetite, and to those at the boundaries of magnetite and ilmenite. It may suggest that (1) pyrrhotite in magnetite and ilmenite are both primary rather than exsolution, as sulfur solubility in spinel is negligible; (2) hercynite, either granular within the magnetite or at the boundaries, or as a rim around pyrrhotite, were exsolved from magnetite, rather than from ilmenite or clinopyroxene.

Pentlandite and chalcopyrite occur mainly as intergrowths in pyrrhotite. They seldomly form separated grains. Cobalt-rich pentlandite is found in the first massive ore in the Marginal Zone. Aggregates of euhedral pyrite are only found in moderately altered gabbro, and are likely product of secondary alteration.

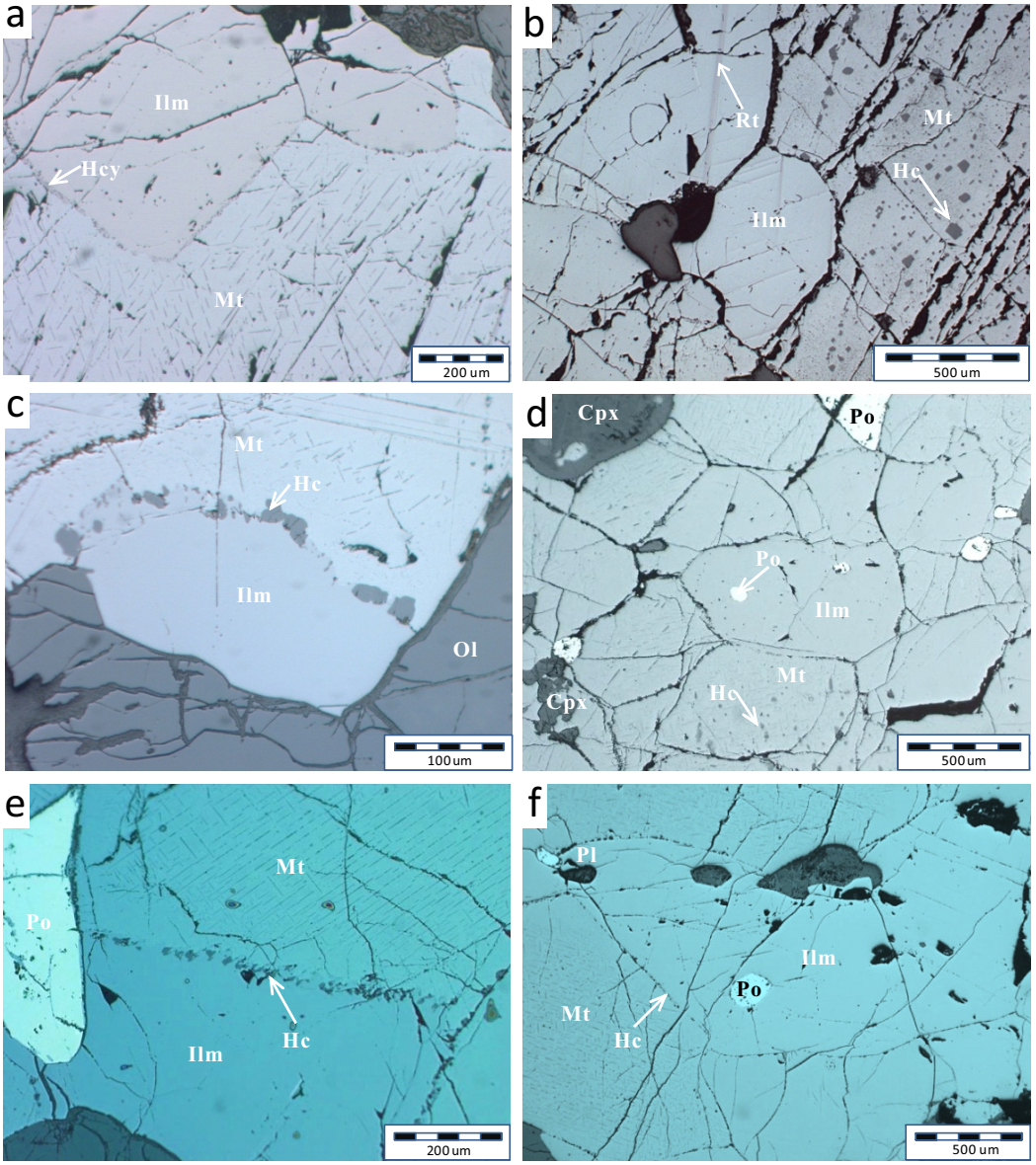

Fig. 3.11 Photomicrographs show occurrences of Ilm, and its boundaries with Mgt in oxide-rich rocks from the Panzhihua Intrusion. (a) Cumulus Ilm with straight boundaries with coexisting Mgt at a triple junction of ~ 120˚C (PZ-10, pcmi-C, LZ). Note the relatively clear surface of Ilm compared with trellis Ilm_{ss} in Mgt. (b) Cumulus Ilm coexisting with Mgt in a massive ore rock (PZ-14, mi-C, MZa). (c) Curved Ilm-Mgt boundary with granular Hc exsolution (PZ-20, pcomi-C, MZa). (d) Cumulus Ilm and Mgt in an ore rock from the LZ of ZJBB section (PZ-24, mi-C, LZ). (e) A straight Ilm-Mgt boundary with Hc exsolution (PZ-24). (f) Cumulus Ilm-Mgt in an ore rock from the MZa of the ZJBB (PZ-38, mi-C, LZ). Note the Po inclusion in Ilm (d & f).

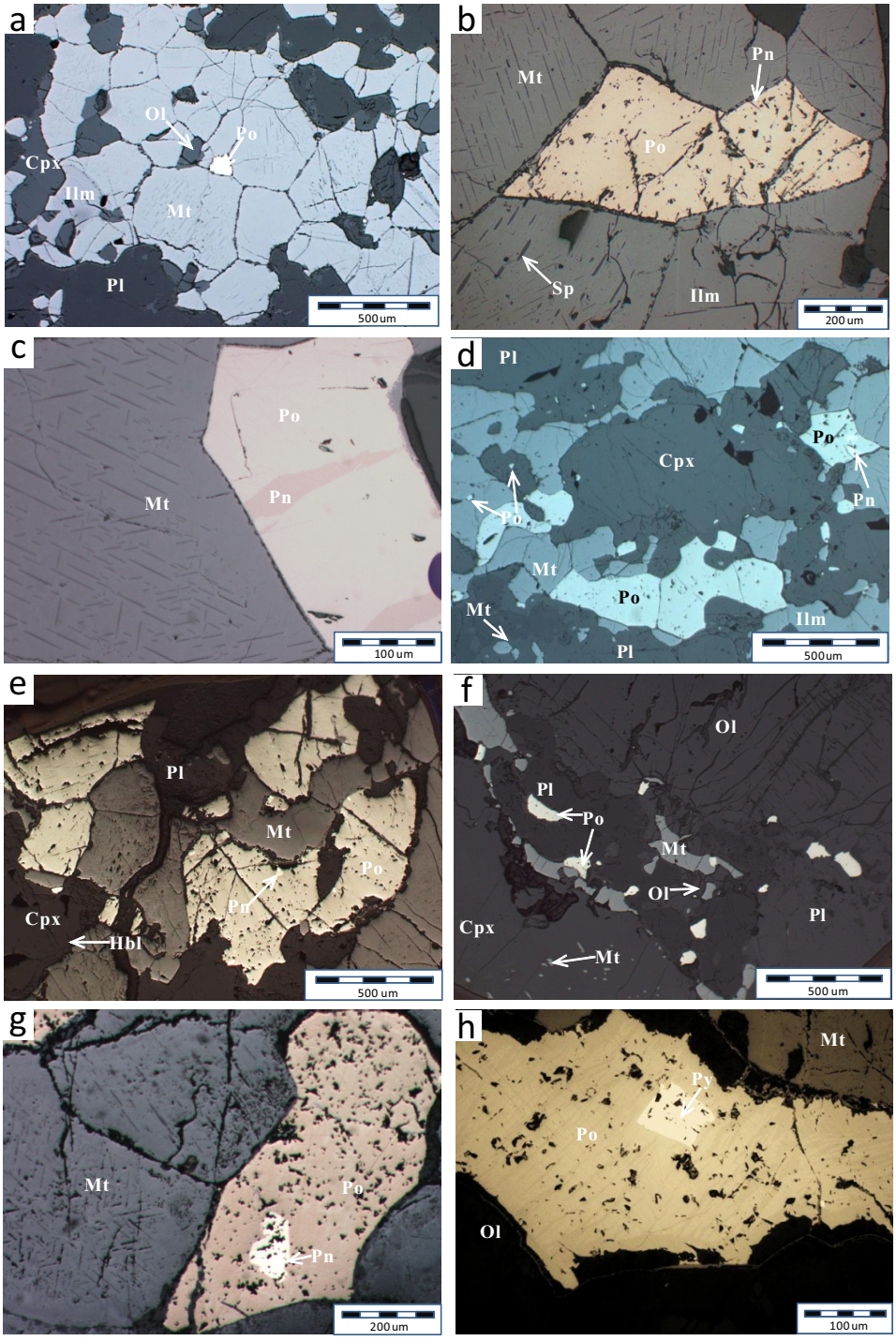

Fig. 3.12 Photomicrographs show occurrences of sulphide in oxide-rich rocks from the Panzhihua Intrusion. Figure (a), (c) (e), (g) show samples from LS, (b), (d), (f), (H) show samples from ZJBB. (a) A Po discrete show ~ 120° triple junction with Fe-Ti oxide grains (PZ-20, pcomi-C, MZa). (b) Intergrowth of Po and Mgt. Note Pn exsolution occur near the boundary of Po (PZ-10, pcmi-C, LZ). (c) Po with Pn exsolution coexisting with Mgt (PZ-40, pcmi-C, MZa) (d) An overview of appearances of sulphide minerals (PZ-24, pcmi-C, LZ). (e) Po and Fe-Ti oxide intergrowth. Note the rugged contact between Po and Cpx in the lower central part (PZ-31, mi-C, MZa). (f) An overview of appearance of sulphide in a silicate-rich area (PZ-20, pcomi-C, MZa). (g) A Pn inclusion in Po discrete (PZ-11, mi-C, LZ). (h) A Py inclusion in Po. Note the Po has abundant flame-like Pn exsolution (PZ-30, mi-C, MZa).

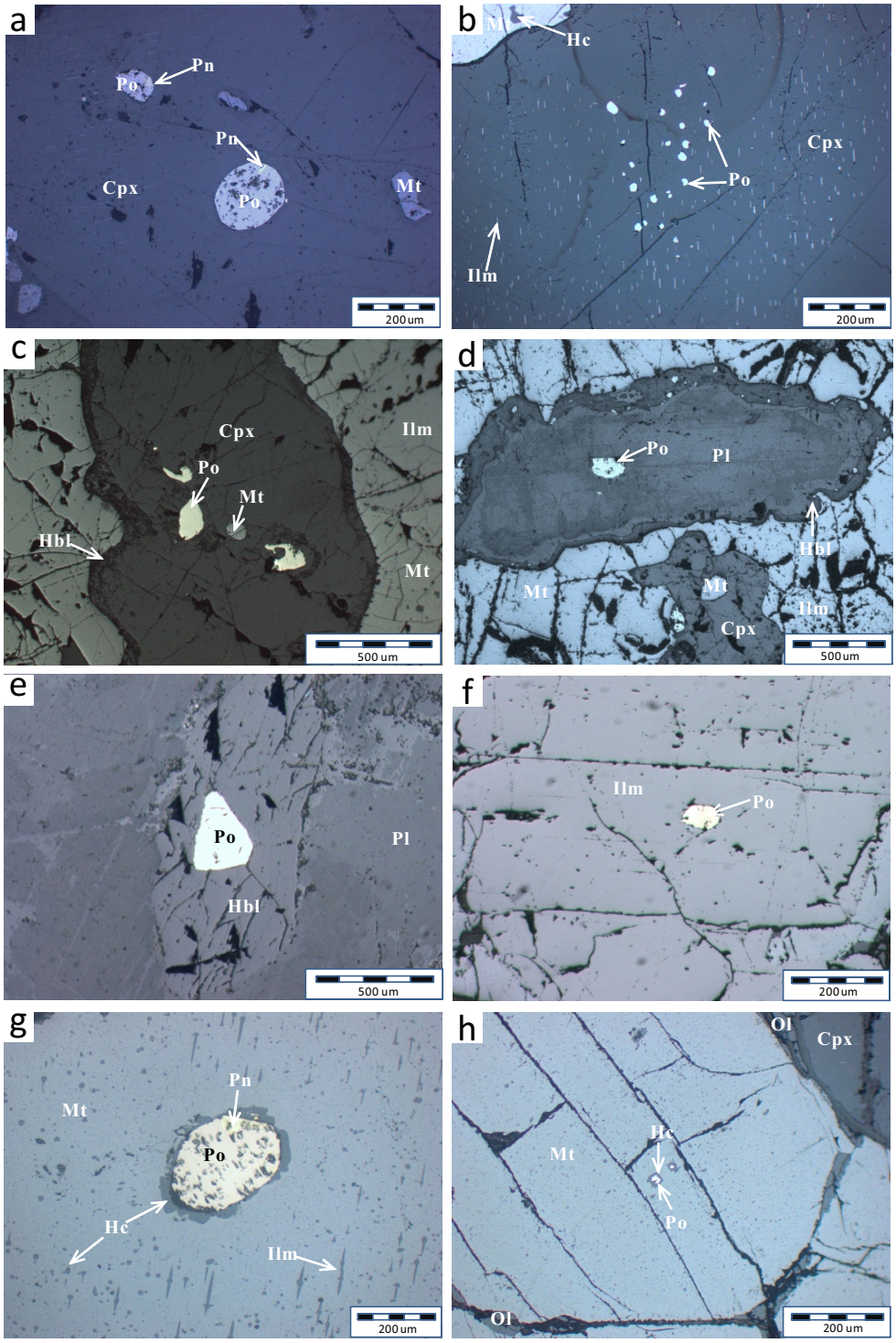

Fig. 3.13 Photomicrographs show occurrences of sulphide mineral(s) enclosed in silicate and oxide minerals in samples from the LS section of the Panzhihua Intrusion. (a) Round-shaped Po and Pn composite inclusion in Cpx crystal, also included are two irregular-shaped Mgt (PZ-21, pcmi-C, MZa). (b) A bunch of sulphide droplets in Cpx (PZ-13, mi-C, MZa). (c) Anhedral Po enclosed in Cpx with a round Mgt inclusion. Note the Hbl rim around Po (PZ-15, mi-C, MZa). (d) A subrounded Po inclusion in Plag (PZ-18, mi-C, MZa). (e) A triangle-shaped Po enclosed in Hbl (PZ-15, mi-C, MZa). (f) A round-shaped Po inclusion in Ilm (PZ-11, mi-C, LZ). (g) A round-shaped Po inclusion in Mgt. Note the Hc along the Po (PZ-14, mi-C, MZa). (h) A tiny Po surrounded by Hc in a Mgt crystal (PZ-13, mi-C, MZa).

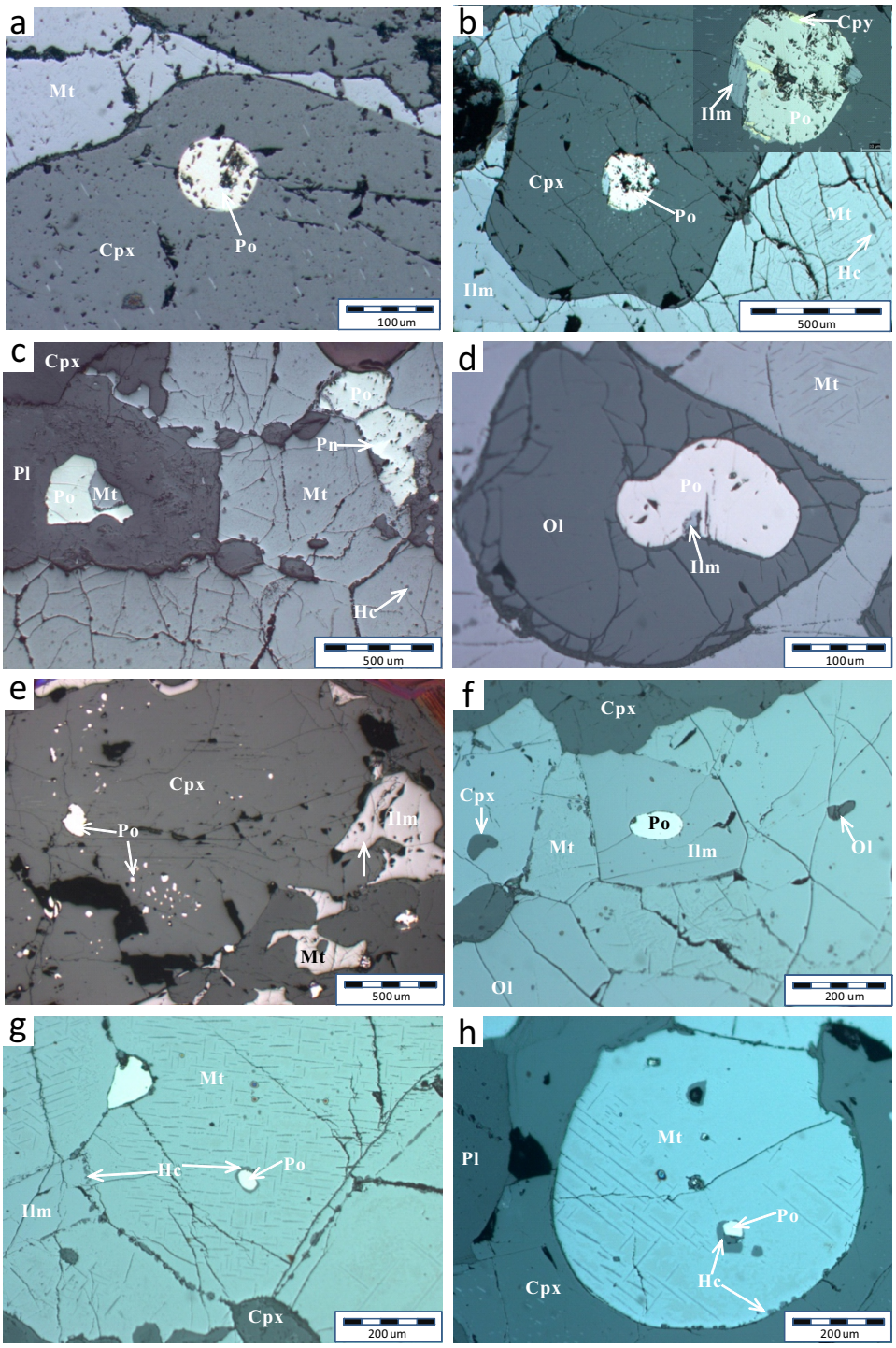

Fig. 3.14 Photomicrographs show occurrences of sulphide mineral(s) enclosed in silicate and oxide minerals in samples from the ZJBB section of the Panzhihua Intrusion. (a) A round-shaped Po droplet included in Cpx crystal (PZ-27, pcmi-C, LZ). (b) A round-shaped sulphide and oxide composite in Cpx (PZ-31, mi-C, MZa). (c) A Po and Mgt intergrowth included in Plag (PZ-33, mi-C, MZa). (d) A subrounded Po and Ilm composite in Ol (PZ-38, pcmi-C, MZa). (e) A bunch of sulphide droplets in Cpx (PZ-42, pcmi-C, MZa). (f) A round-shaped Po inclusion in Ilm (PZ-24, pcmi-C, LZ). (g) A round-shaped Po inclusion in Mgt. Note another triangle Po grain in triple junction (PZ-24, pcmi-C, LZ). (h) Po surrounded by Hc in a round-shaped Mgt partly enclosed in Cpx (PZ-24, pcmi-C, LZ).

3.2 Petrography of the Taihe Intrusion

3.2.1 Introduction

Taihe Intrusion exhibits similar stratigraphy to the Panzhihua Layered Intrusion. Layered medium-grained gabbro comprises the majority of the cumulate body. The mineralized layered gabbroic rocks overlie the lower coarse-pegmatic gabbro and are in turn covered by unmineralized layered medium-grained gabbro. In general, the abundance of plagioclase increases upwards. Apatite gabbro, with Ap between 5-10%, occurs first at the top of the mineralized layered gabbro. Its abundance increases upward with the unmineralized layered zone. Massive Fe-Ti oxide ores occur in the lower part of the layered gabbro. The amount of Fe-Ti oxide decreases upwards. Except for the gabbro, the host rocks for the ore include anorthosite and pyroxenite (SBGMR, 1991). Pyroxenite interlayers occur within the apatite gabbro zone and extend both up and down for ~200 m, whereas the anorthositic disseminated ore only appears below the apatite zone.

11 samples, including gabbro and Fe-Ti oxide ore, have been collected from the Taihe open-pit mine. Samples were collected in sequence from the lower stratigraphic height up the section (~300m), although the exact height of each sample is unknown.

Petrography of Taihe rocks is similar to Panzhihua. Details of the mineralogy and textural observations are as follows.

3.2.2 Gabbroic Rocks

Taihe melonogabbros consist of 35-45% plagioclase, 40-50% clinopyroxene, 5-10% Fe-Ti oxides, 0-2% olivine, 2-10% hornblende. Sulphides and apatite are rare.

Despite extensive alteration, Taihe gabbroic rocks show cumulus textures with cumulus clinopyroxene, plagioclase, and occasionally olivine and Fe-Ti oxides, and similar intercumulus minerals (Fig 3.15).

Hornblende usually occurs as a rim on silicate minerals surrounded by Fe-Ti oxides. It becomes more abundant in the gabbro from the lower stratigraphy; especially in more alterated samples (Fig 3.15a). Plagioclase occurs either as ~2 mm long laths, or more commonly as ~500 μm subhedral to anhedral short laths, both of which display polysynthetic twins and less commonly simple twins (Fig 3.15b-c). Clinopyroxene occurs as subhedral to anhedral grains in contact with plagioclase and/or Fe-Ti oxides (Fig 3.15b-d). The grain sizes range from 100

μm up to 2 mm. Lamellae due to exsolution of Fe-Ti oxides in clinopyroxene are similar to those in the Panzhihua (Fig 3.15b-c). Olivine occur as two populations, of which the first is large discrete grains associated with plagioclase aggregates (Fig 3.15b), and the second population is small granular olivine with hornblende rims within Fe-Ti oxides (Fig 3.15c). It may be inferred that the discrete olivine may have primary composition as it is surrounded by plagioclase and hence avoided possible reaction with oxide minerals. The latter population of olivine may be affected by late magmatic processes.

Similar to Panzhihua Fe-Ti oxides, magnetite and ilmenite are two major oxide minerals in the Taihe Intrusion. They occur as an intergrowth of both magnetite and ilmenite with flat boundaries or interstitial to silicate minerals (Fig 3.15e). Occasionally, magnetite and ilmenite occur as two-phase inclusions in silicate minerals (Fig 3.15f). The boundaries between magnetite and ilmenite are characterized by abundant exsolutions of hercynite (Fig 3.15g), which is also very common in the Panzhihua rocks. Apatite inclusions in ilmenite were not observed in Panzhihua (Fig 3.15h).

3.2.3 Massive Fe-Ti Oxide Ore

Taihe Fe-Ti oxide ores show cumulus textures of polygonal magnetite and ilmenite grains. The grain sizes mostly vary between 500 μm to 1 mm in diameter (Fig 3.16a & b). Compared with Panzhihua Fe-Ti oxides, magnetite is generally more oxidized in Taihe as shown by hematite lamellar (Fig 3.16c & d). Some of the hematite lamellae have been filled with sulphide (Fig 3.16d). Granular spinel is also observed in the Taihe magnetite (Fig.3.16c, e), which are also found at the boundaries of magnetite and ilmenite (Fig 3.16f). Granular pores in many magnetite crystals may be a trace for the spinel which have been removed probably due to late-stage alteration and/or weathering (Fig 3.16e).

Sulphide minerals include pyrrhotite, pyrite, chalcopyrite, pentlandite and its cobalt-rich variety. Pyrrhotite and pyrite are two main sulphide minerals in the Taihe ore rock. pyrrhotite occurs as subhedral to anhedral grains coexisting with Fe-Ti oxides and silicate minerals (Fig 3.16g). Pyrrhotite inclusions in silicate minerals are also observed, however, pyrrhotite in ilmenite is not as common as in Panzhihua rocks. The grain sizes of pyrrhotite vary greatly from several μm to 1 mm (Fig 3.16g). Pyrite in Taihe ore rocks usually forms a net-like texture in magnetite (Fig 3.16h). It occurs in the fractures and crystal boundaries of magnetite, and is likely related to late-stage alteration.

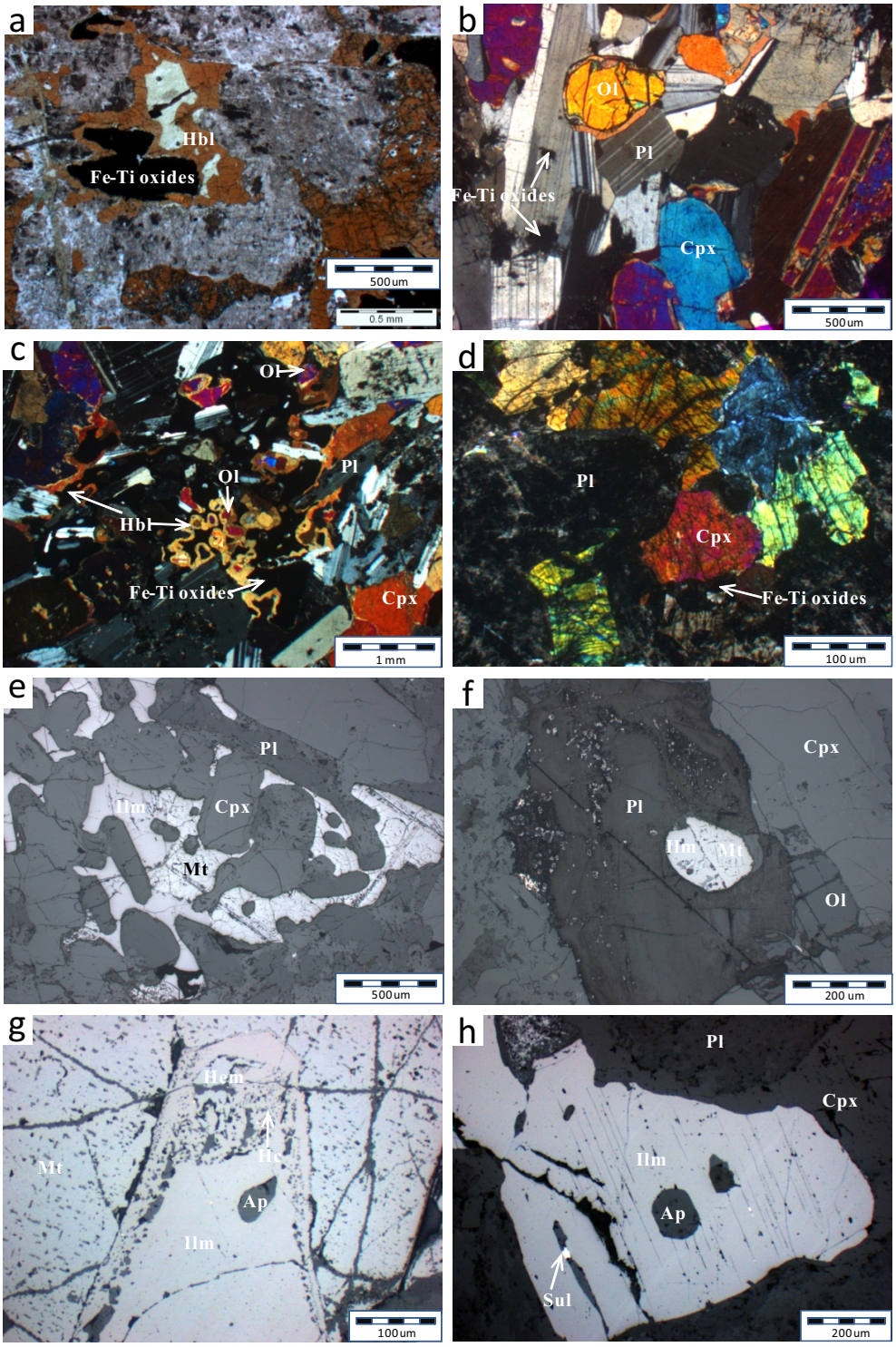

Fig. 3.15 Photomicrographs show occurrences of gabbroic rocks from the Taihe Layered Intrusion. (a) Altered Hbl-rich gabbro (TH-5, pch-C). (b) A fresh ol-gabbro shows a sub-rounded Ol crystal in a Plag aggregate (TH-9, pco-C). (c) Small Ol grains surrounded by Hbl in a Fe-Ti oxide rich area in the same sample as above (TH-9, pco-C). (d) a slightly altered cumulus gabbro (TH-11, pc-C). (e) Interstitial Fe-Ti oxides in gabbro (TH-9, pco-C). (f) Mgt-Ilm intergrowth in Plag (TH-10, pco-C). (g) Mgt-Ilm boundaries with abundant Hc exsolution. Note Ap inclusion in Ilm (TH-5, pc-C). (h) euhedral Ap inclusions in Ilm (TH-5, pc-C).

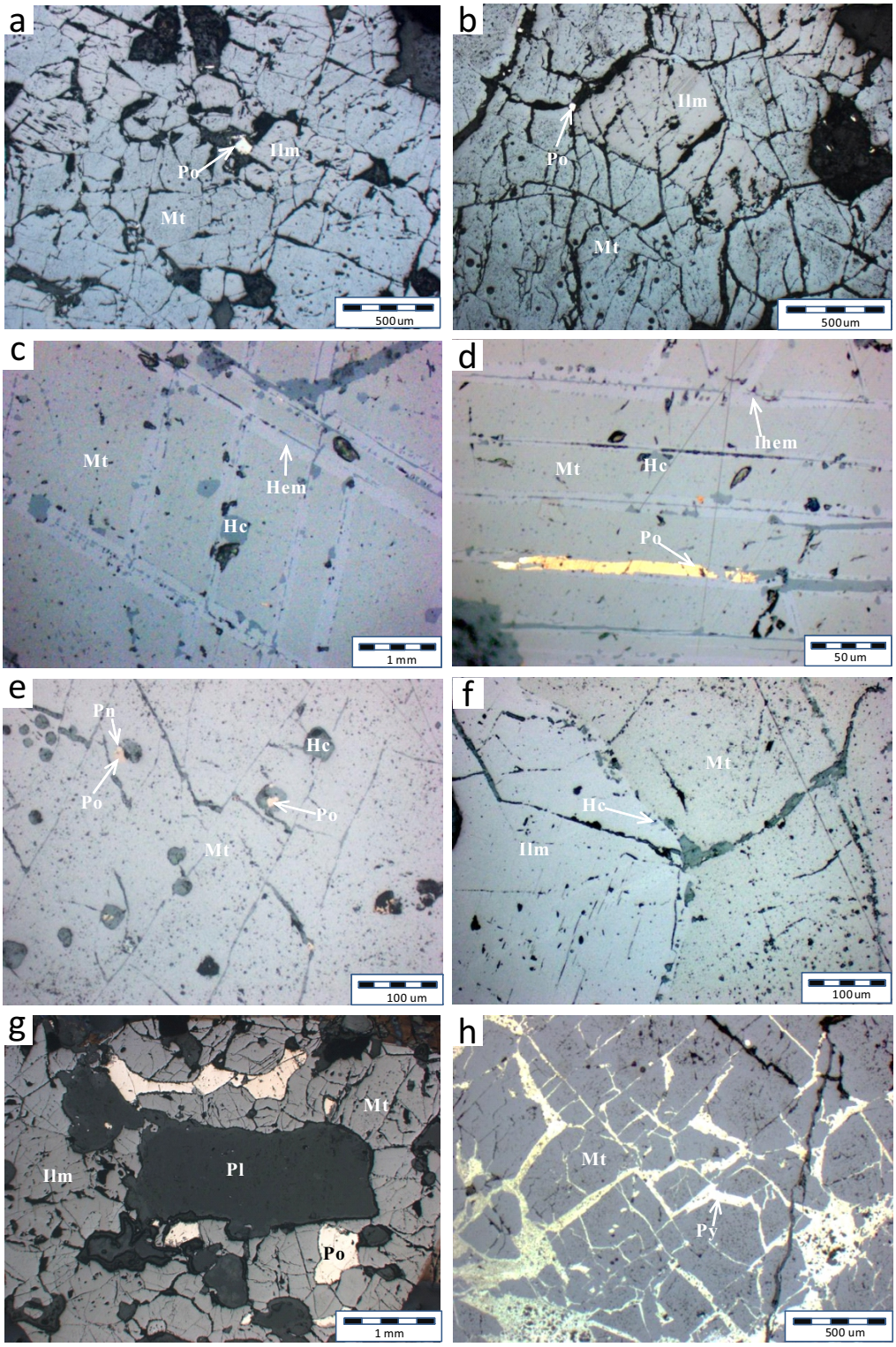

Fig. 3.16 Photomicrographs show occurrences of Fe-Ti oxides and sulphides in ore rocks from the Taihe Layered Intrusion. (a) & (b) Overviews of cumulus Fe-Ti oxides (TH-6, TH-9, mi-C). (c) Ilm lamellae, and Hc exsolution in Mgt (TH-1, mi-C). (d) Elongate sulphide filling Ilm lamellae in Mgt (TH-1, mi-C). (e) Granular Hc exsolution in Mgt. Note sulphide sometimes occur within Hc (TH-3, mi-C) (f) Ilm-Mgt boundaries with Hc exsolution (TH-4, mi-C). (g) Appearances of anhedral sulphides in massive ore (TH-4, mi-C). (h) Net-like Py filling alongside Mgt crystal boundaries and cracks (TH-6, mi-C).

3.3 Summary

The most important characteristics of the Panzhihua petrography described above are summarized as follows:

(1) Panzhihua and Taihe Intrusion were formed by accumulation of plagioclase, clinopyroxene, magnetite, ilmenite, and in some places olivine and apatite. The latter two only occur at certain crystallization stages. Hornblende and sulphide (mainly pyrrhotite) are more abundant in the lower part of the cumulate. Ilmenite becomes abundant relative to magnetite in the upper stratigraphy.

(2) Clinopyroxene may occur as host mineral for olivine, plagioclase, Fe-Ti oxides and sulphide, implying prolonged crystallization of clinopyroxene.

(3) Deformation recorded in plagioclase twins indicate that compaction may have played a role, and that the interstitial liquid was partly squeezed out.

(4) Fe-Ti oxide inclusions in olivine, plagioclase and clinopyroxene in more mafic wehrlite rock indicate early Fe-Ti oxide saturation in Panzhihua. However, it is unclear whether the Fe-Ti oxides hosted in gabbroic rocks were formed by early fractionation of Fe-Ti oxide.

(5) Sulphide inclusions in Fe-Ti oxides in gabbro and ore rocks are common, whereas Fe-Ti oxide inclusions in sulphide are rare. Moreover, sulphide inclusions are not found in wehrlite. It is thus inferred that segregation of sulphide liquid likely occurred at the same period as crystallization of Fe-Ti oxides.

(6) Crystallization sequence may be as follow: olivine ± plagioclase-clinopyroxene/magnetite/sulfide/ilmenite/-apatite.

(7) Clinopyroxene and magnetite display abundant exsolution textures; their compositions are thus not representative of the original magmatic compositions.

(8) the Taihe Intrusion has similar petrography, which in turn indicates it may have similar genesis to the Panzhihua Intrusion.

CHAPTER 4

WHOLE-ROCK AND MINERAL CHEMISTRY

This chapter describes whole-rock and mineral chemistry of the Panzhihua and Taihe gabbroic layered intrusions. First I describe the variations in whole-rock major and trace elements in the Panzhihua rocks in the context of published data. This is followed by whole-rock chemistry of samples from the Taihe intrusion. The factors controlling whole-rock chemistry will also be discussed. The second part is the chemistry of major minerals that occur in both layered intrusions. The major element compositions of silicate minerals (olivine, clinopyroxene and plagioclase) are described for the Panzhihua intrusion. The major and trace element compositions in magnetite and ilmenite are described for both intrusions, followed by the major and trace element compositions of pyrrhotite, the main sulphide mineral in these intrusions.

4.1 Whole-rock Geochemistry

4.1.1 Introduction

Forty four samples were collected from two open-pit mines in Panzhihua (Lanshan and Zhujiabaobao). These samples represent two separate sections, which are compiled to form a more complete profile representing the lower approximately 700 m of cumulates in Panzhihua.

A total of eleven rocks were collected from the exposed section of the open-pit mine in Taihe. The samples cover approximately 300 m of the Taihe cross-section, however the exact position of the samples within the intrusion are not constrained.

Major and trace element compositions of the samples were analysed by XRF and solution ICP-MS at CODES, University of Tasmania. Sample preparation procedures and analytical methods are described in the Appendix I.

4.1.2 Whole-rock Major Element Composition

Representative analysis of the whole rock major and trace element compositions for rocks from the Panzhihua and Taihe gabbroic layered intrusions are presented in Table 4.1 and Table 4.2, respectively. Only four of the 44 Panzhihua samples, and one of the 11 Taihe samples have loss on ignition (LOI) values larger than 3 wt%, which suggests that most of the

Table 4.1 Whole rock major and trace element compositions for samples from the Panzhihua Intrusion (PZ-1 to PZ-23 and PZ-24 to PZ-45 were from Lanshan and Zhujiabaobao open-pit mines, respectively).

Sample#	PZ-1	PZ-2	PZ-3	PZ-4	PZ-5	PZ-6	PZ-7	PZ-8	PZ-9	PZ-10	PZ-13	PZ-16	PZ-17	PZ-19
Rock	Wehr	Gb	Gb	Ore	Hb-gb	Wehr	Hb-gb	Hb-gb	Hb-gb	Ox-gb	Ore	Gb	Wehr	Gb
Height *	1	2	3	4	5	6	7	8	9	13	18	23	24	26
Zone	MGZ								LZ		MZa			
SiO_2	41.7	43.61	41.65	9.77	43.56	40.24	42.65	48.89	40.09	24.41	3.47	38.15	38.77	38.46
TiO_2	1.23	3.28	3.98	12.72	3.01	1.61	2.13	2.41	3.9	10.33	15.08	2.68	2.32	4.4
Al_2O_3	4.92	14	15.58	5.92	15.01	6.05	7.8	12.46	14.77	8.6	4.64	18.51	3.27	13.33
Fe_2O_3	13.9	17.61	18.6	61.27	14.5	10.6	13.57	11.03	19.92	40.78	70.84	12.3	20.26	20.82
MnO	0.2	0.18	0.18	0.33	0.23	0.14	0.17	0.17	0.17	0.32	0.36	0.1	0.23	0.17
MgO	26.76	5.85	5.91	6.3	7.5	21.88	19.01	7.95	6.15	6.41	5.4	5.22	22.22	7.27
CaO	8.32	10.88	12.15	3.72	11.17	14.44	9.48	8.26	12.05	7.67	1.24	15.31	10.23	12.84
Na_2O	0.26	2.93	2.29	0.1	2.3	0.16	1.62	3.02	1.97	1.08	<0.05	2	0.3	1.58
K2O	0.03	0.5	0.16	0.03	1.28	0.06	1.24	2.7	0.31	0.09	0.01	0.24	0.01	0.21
P_2O_5	0.08	0.03	0.03	0.01	0.4	0.01	0.18	0.3	0.04	0.1	0	0.03	0.01	0.03
V_2O_5	0.04	0.1	0.11	0.38	0.07	0.04	0.06	0.06	0.12	0.23	0.46	0.08	0.08	0.14
LOI+	2.46	0.55	-0.02	-1.14	1.32	4.43	1.64	2.55	0.55	-0.41	-1.53	5.35	1.54	0.21
Total	99.89	99.51	100.6	99.4	100.3	99.67	99.55	99.8	100.04	99.61	99.97	99.96	99.24	99.45
Mg#	80.91	42.24	41.16	18.46	53.24	81.96	75.51	61.34	40.47	25.71	14.37	48.30	70.71	43.46
						Trace Elements (ppm)								
Sc	27	28	28	23	34	24	29	30	31	26	18	24	38	35
V	211	489	577	2213	362	216	301	288	618	1361	2698	377	420	713
Cr	2428	18	46	327	164	1861	1773	185	4	4	104	1	1633	2
Co	130	108	104	268	71	99	116	65	120	163	284	116	158	125
Ni	1197	100	68	184	60	1022	856	56	66	59	173	21	723	65
Cu	44	288	29	399	80	198	138	107	160	51	200	52	23	134
Zn	109	113	115	325	130	73	87	84	111	247	347	73	125	100
Ga	10	22	24	39	22	11	15	16	22	29	40	18	10	21
Rb	0.92	9.26	1.73	0.22	26.24	2.32	34.45	83.15	6.84	1.45	0.05	6.5	0.29	3.03
Sr	190	591	658	61	847	85	208	977	794	370	6	769	53	540
Y	12	11	8	3	28	13	19	23	7	7	1	6	8	7
Zr	38	51	19	18	199	106	116	200	20	31	13	18	17	22
Nb	6.2	5.8	1.4	2.5	37.1	7.2	18.2	31.1	1.8	7.6	2.2	4.6	0.5	2.3
Ba	21	283	114	8	538	6	307	904	118	72	2	260	4	118
La	3.6	8.7	2.6	0.6	29.2	5.5	14.9	29.7	2.8	2.5	0.2	5.3	0.9	2.1
Ce	11.3	16.3	6.5	1.8	68.9	13.8	35.2	64.3	7.1	6.9	0.6	8.5	3.7	6.0
Pr	1.7	2.1	1.0	0.3	9.0	2.2	4.9	8.4	1.1	1.1	0.1	1.0	0.7	1.0
Nd	8.9	10.0	5.8	1.7	41.8	10.8	22.3	36.2	5.9	5.9	0.7	4.8	4.5	5.5
Sm	2.6	2.6	1.8	0.6	9.1	3.0	5.3	7.6	1.8	1.7	0.2	1.3	1.6	1.7
Eu	0.9	1.3	1.0	0.2	2.9	1.0	1.7	2.2	1.0	0.8	0.1	0.8	0.6	0.9
Gd	2.7	2.7	2.0	0.6	7.8	3.2	5.0	6.4	2.0	1.9	0.3	1.5	1.9	2.0
Tb	0.5	0.4	0.3	0.1	1.2	0.5	0.8	1.0	0.3	0.3	0.0	0.2	0.3	0.3
Dy	2.4	2.2	1.7	0.5	6.0	2.7	4.1	4.9	1.6	1.5	0.2	1.2	1.7	1.7
Ho	0.4	0.4	0.3	0.1	1.1	0.5	0.7	0.9	0.3	0.3	0.0	0.2	0.3	0.3
Er	1.2	1.1	0.7	0.2	2.9	1.3	1.9	2.4	0.7	0.7	0.1	0.5	0.8	0.7
Tm	0.2	0.1	0.1	0.0	0.4	0.2	0.3	0.3	0.1	0.1	0.0	0.1	0.1	0.1
Yb	0.9	0.9	0.5	0.2	2.3	1.0	1.5	2.0	0.5	0.5	0.1	0.4	0.5	0.5
Lu	0.1	0.1	0.1	0.0	0.3	0.2	0.2	0.3	0.1	0.1	0.0	0.1	0.1	0.1
Hf	1.2	1.5	0.8	0.6	5.0	2.7	3.3	5.0	0.7	1.1	0.5	0.6	0.8	0.8

Table 4.1 Whole rock major and trace element compositions for samples from the Panzhihua gabbroic Layered Intrusion (continued).

Sample	PZ-20	PZ-23	PZ-24	PZ-28	PZ-29	PZ-32	PZ-33	PZ-37	PZ-39	PZ-40	PZ-41	PZ-43	PZ-44	PZ-45
Rock	Ox-gb	Leuco	Ore	Leuco	Ox-gb	Gb	Ore	Ore	Gb	Gb	Ox-gb	Gb	Ap-gb	Ap-gb
Height	28	37	10	17	19	29	30	35	38	39	40	42	43	44
Zone	MZa		LZ	MZa									MZb	
SiO_2	31.89	58.58	14.82	41.43	32.06	45.24	3.39	19	38.07	41.69	27.49	40.94	41.86	40.18
TiO_2	6.88	0.18	13.15	3.35	5.69	1.55	18.09	12.17	6.61	5.03	12.03	4.41	3.94	3.54
Al_2O_3	11.3	19.78	6.2	20.89	13.37	25.73	4.37	2.7	13.93	11.26	9.84	13.43	16.89	15.82
Fe_2O_3	30.07	4.42	54.65	15.35	27.82	5.41	68.2	47.39	20.67	18.65	34.29	17.59	13.61	15.71
MnO	0.23	0.06	0.38	0.13	0.19	0.05	0.38	0.4	0.19	0.24	0.27	0.21	0.17	0.2
MgO	8.66	2.89	5.78	2.5	5.23	1.03	5.59	13.92	6.25	8.21	6.64	6.85	4.53	5.32
CaO	9.38	3.72	5.19	9.46	12.27	11.84	1.18	4.13	11.39	13.56	8.53	12.76	11.95	11.65
Na_2O	1.4	8.55	0.45	3.85	0.95	4.56	<0.05	0.08	2.1	1.79	1.3	1.95	3.11	3.12
K_2O	0.08	0.02	0.05	0.33	0.1	0.29	0.02	0.03	0.1	0.08	0.06	0.1	0.15	0.46
P_2O_5	0.03	0.11	0.01	0.09	0.03	0.06	0.01	0.03	0.03	0.03	0.01	0.03	2.35	2.19
V_2O_5	0.18	0.01	0.3	0.08	0.19	0.04	0.44	0.24	0.11	0.09	0.19	0.08	0.04	0.03
LOI	-0.5	2.27	-1.14	2.74	1.96	4.26	-1.41	-0.05	0.14	-0.31	-0.75	1.98	1.07	1.17
Total	99.59	100.58	99.84	100.2	99.86	100.05	100.26	100.03	99.58	100.32	99.91	100.32	99.66	99.39
Mg#	38.80	59.01	18.89	26.39	29.27	29.54	15.29	39.27	39.96	49.22	29.89	46.16	42.29	42.71
						Trace Elements (ppm)								
Sc	27	7	23	12	24	3	19	23	25	34	28	26	11	11
V	941	45	1761	416	918	173	2332	1239	555	442	993	399	193	166
Cr	29	41	3	<0.04	10	114	62	5	3	1	64	0	0	0
Co	180	55	231	89	148	52	255	210	114	105	158	84	75	72
Ni	62	12	74	28	10	13	58	13	6	2	22	1	1	1
Cu	121	1	180	57	46	28	113	29	24	14	39	16	7	10
Zn	162	41	339	102	124	22	325	240	102	91	166	88	79	69
Ga	23	19	32	24	21	19	36	20	18	17	22	17	19	19
Rb	1.26	0.19	0.37	5.48	1.75	3.27	0.2	0.15	0.96	0.69	0.63	1.2	1.19	6.89
Sr	398	459	137	1725	547	1638	14	18	630	487	427	670	979	1132
Y	6	10	4	6	5	3	1	4	6	10	6	8	23	23
Zr	19	94	21	31	23	16	20	22	22	20	28	16	14	11
Nb	2.5	2.9	3.5	4.6	2.9	1.9	4.6	7.8	6.9	2.8	7.9	3.0	4.2	2.7
Ba	53	36	19	352	96	196	6	4	77	61	56	85	121	192
La	1.9	21.4	0.8	5.3	2.4	3.6	0.5	0.6	1.7	1.9	1.3	2.0	17.0	16.5
Ce	5.0	36.2	2.4	11.5	5.9	7.7	1.3	2.2	4.7	6.2	3.7	5.6	45.5	43.5
Pr	0.8	4.0	0.4	1.5	0.9	1.0	0.2	0.4	0.8	1.2	0.6	1.0	7.3	7.0
Nd	4.5	14.4	2.5	7.1	4.4	4.1	1.1	2.5	4.5	7.1	3.7	5.8	38.8	37.5
Sm	1.4	2.4	0.8	1.7	1.3	0.9	0.3	0.9	1.5	2.5	1.3	2.0	9.6	9.1
Eu	0.7	1.4	0.4	1.2	0.8	0.8	0.1	0.4	0.9	1.2	0.7	1.2	3.5	3.4
Gd	1.6	2.0	0.9	1.7	1.4	0.8	0.4	1.0	1.7	2.9	1.5	2.2	9.3	8.9
Tb	0.3	0.3	0.1	0.3	0.2	0.1	0.1	0.2	0.3	0.5	0.2	0.4	1.2	1.1
Dy	1.3	1.7	0.8	1.3	1.2	0.6	0.3	0.9	1.4	2.4	1.3	1.9	5.6	5.3
Ho	0.2	0.3	0.1	0.2	0.2	0.1	0.1	0.2	0.3	0.4	0.2	0.3	0.9	0.9
Er	0.6	1.0	0.3	0.6	0.5	0.3	0.2	0.4	0.6	1.1	0.6	0.8	2.1	2.0
Tm	0.1	0.2	0.0	0.1	0.1	0.0	0.0	0.1	0.1	0.1	0.1	0.1	0.2	0.2
Yb	0.4	0.9	0.2	0.5	0.4	0.2	0.1	0.3	0.4	0.7	0.4	0.5	1.1	1.0
Lu	0.1	0.2	0.0	0.1	0.1	0.0	0.0	0.1	0.1	0.1	0.1	0.1	0.1	0.1
Hf	0.7	2.3	0.7	0.9	0.8	0.4	0.7	0.8	0.8	0.8	1.0	0.7	0.5	0.4

Height *- relative sequence from the contact up to the lower part of MZb. LOI+-includes the loss of sulfur. Minus values are caused by the incorporation of extra oxygen.

Table 4.2 Major and trace element composition of the samples from Taihe Intrusion.

Sample#	TH-1	TH-2	TH-3	TH-4	TH-5	TH-6	TH-7	TH-8	TH-9	TH-10	TH-11
Rock	Ore	Ore	Ore	Ore	Gb	Ore	Ore	Ore	Gb	Gb	Gb
Height	1	2	3	4	5	6	7	8	9	10	11
SiO_2	15.29	5.21	8.24	5.75	33.09	4.05	11.11	4.11	44.13	48.46	42.56
TiO_2	11.09	14.89	13.99	14.01	7.23	16.88	13.85	16.01	1.82	0.95	1.73
Al_2O_3	12.23	5.49	5.3	7.98	20.76	6.5	4.93	6.89	17.37	14.77	21.92
Fe_2O_3	47.91	64.03	62.21	63.67	20.68	64.05	59.06	64.83	9.05	10.44	7.28
MnO	0.26	0.34	0.34	0.31	0.13	0.33	0.4	0.33	0.12	0.17	0.09
MgO	5.31	7.22	7.47	5.84	2.91	5.86	6.7	6.12	8.31	8.19	5.49
CaO	5.04	0.71	1.2	0.88	9.31	0.04	3.7	0.09	16.08	12.62	15.4
Na_2O	0.29	<0.05	<0.05	<0.05	1.74	<0.05	0.07	<0.05	1.39	2.31	1.54
K_2O	0.2	0.01	0.01	0.01	1.36	0.01	0.02	0.01	0.13	0.41	0.81
P_2O_5	0.09	0.02	0.02	0.03	0.44	0.02	0.04	0.03	0.08	0.1	0.06
V_2O_5	0.31	0.42	0.41	0.42	0.14	0.38	0.35	0.41	0.05	0.05	0.06
LOI	1.71	1.53	0.66	0.74	2.59	1.96	-0.24	0.88	1.09	1.63	3.28
Total	99.71	99.88	99.84	99.63	100.4	100.1	99.98	99.72	99.62	100.1	100.2
Mg#	19.62	19.89	20.91	16.8	23.66	16.77	19.99	17.21	66.91	63.34	62.41
Trace element (ppm)											
Sc	10			10		12	21		29	42	20
V	1825			2389		2159	2074		251	253	250
Cr	6			43		9	9		245	218	164
Co	182			239		270	207		74	78	50
Ni	334			355		447	75		115	100	106
Cu	452			329		1328	161		68	126	122
Zn	216			298		281	307		41	68	34
Ga	31			36		31	31		15	15	17
Rb	5.88			0.11		0.1	0.45		4.83	15.84	36.29
Sr	1249			79		24	50		1328	408	1616
Y	2			1		0	4		7	17	4
Zr	13			10		12	18		14	58	10
Nb	3.1			2.5		4.7	3.2		1.0	7.5	1.0
Ba	97			10		10	10		81	158	277
La	1.9			0.7		0.4	1.3		3.3	9.0	2.7
Ce	4.5			1.6		0.8	4.3		9.3	18.5	7.0
Pr	0.6			0.2		0.1	0.8		1.6	2.3	1.1
Nd	3.2			1.1		0.6	4.7		9.3	9.8	6.2
Sm	0.7			0.2		0.2	1.5		2.7	2.5	1.7
Eu	0.5			0.2		0.1	0.6		1.5	0.9	1.0
Gd	0.6			0.2		0.2	1.5		2.7	2.8	1.7
Tb	0.1			0.0		0.0	0.2		0.4	0.5	0.2
Dy	0.4			0.1		0.1	1.1		1.8	3.1	1.1
Ho	0.1			0.0		0.0	0.2		0.3	0.6	0.2
Er	0.2			0.1		0.1	0.4		0.7	1.9	0.4
Tm	0.0			0.0		0.0	0.1		0.1	0.3	0.1
Yb	0.1			0.0		0.1	0.3		0.4	1.7	0.3
Lu	0.0			0.0		0.0	0.0		0.1	0.3	0.0
Hf	0.4			0.3		0.4	0.7		0.6	1.6	0.4

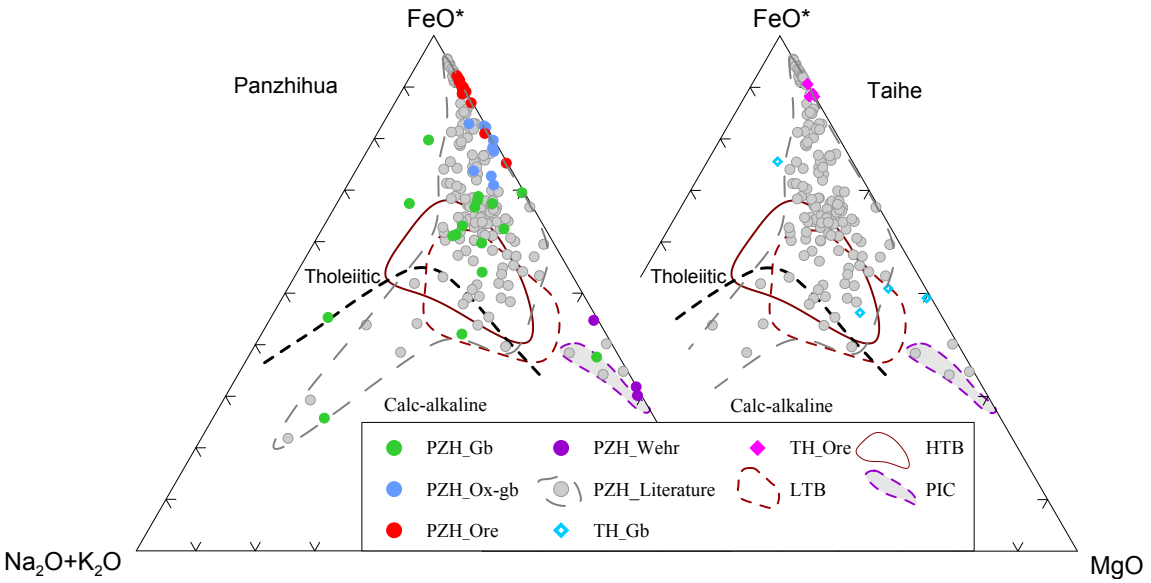

Fig. 4.1 AFM diagrams show the differentiation trend of Emeishan basalts, picrites, Panzhihua and Taihe Intrusion rocks. Published Panzhihua data are from Zhou *et al* (2005) and Pang (2008a). Emeishan basalt data are from Xu *et al* (2001), Xiao *et al* (2003, 2004), Song *et al* (2001, 2008), Wang *et al* (2007), Qi *et al* (2008).

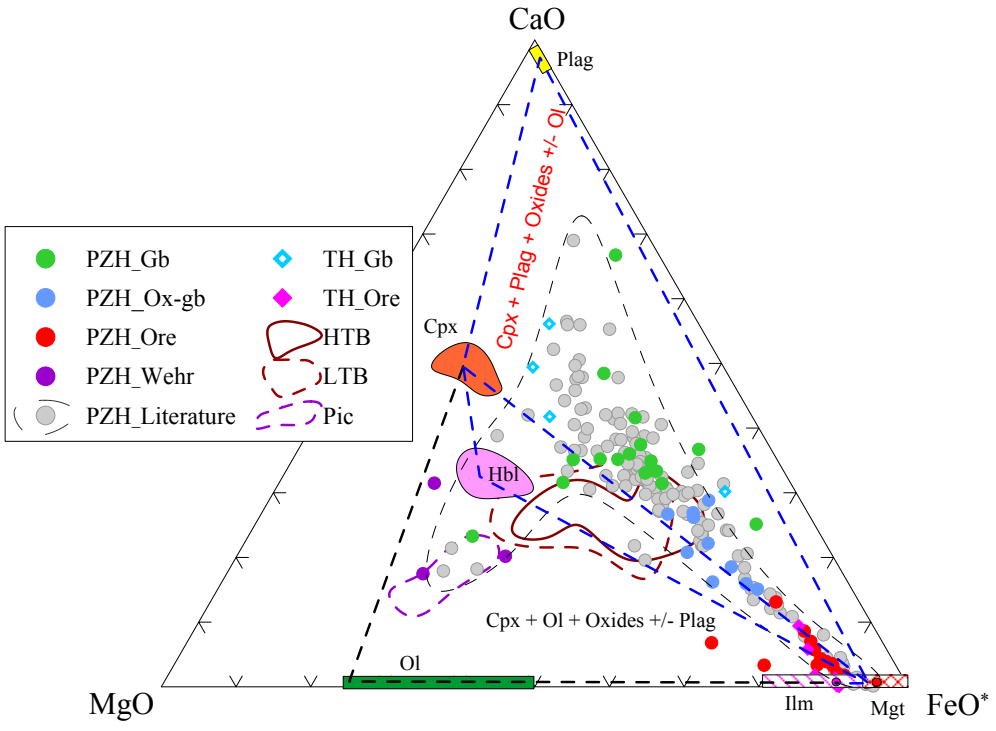

Fig. 4.2 A ternary diagram showing distribution of whole rock CaO-MgO-FeO* in the Panzhihua and Taihe rocks. Also shown are the compositional ranges of main rock forming minerals. Note that most rocks can be explained by accumulation of Cpx and Fe-Ti oxides, and/or Plag, and/or Ol. Mineral compositions are from this study and that of Pang *et al.* (2009). Emeishan basalt data are from Xu *et al* (2001), Xiao *et al* (2003, 2004), Song *et al* (2001, 2008), Wang *et al* (2007), Qi *et al* (2008).

rocks have not been strongly hydrated. This is in accordance with petrologic observations.

As the most abundant metamorphic mineral is chlorite (0.5-13.0 vol%), it indicates low-metamorphism in most rocks. Biotite is an index mineral for high-grade metamorphism, and only occurs in a substantial amount (up to 10.6 vol%) in strongly foliated hornblende-rich rocks in the MGZ of Panzhihua intrusion. The lack of obvious correlation between LOI and mobile elements (e.g. Cs, Rb, K, Ba, Sr, Na) suggests little effects of alteration on the whole-rock compositions. We thus consider the data as representative of the original igneous compositions.

Figure 4.1 shows the compositions of Panzhihua and Taihe rocks, and the Emeishan continental flood basalt (ECFB), on the AFM diagram. The ECFB follow a tholeiitic differentiation trend. Most of the intrusive rocks from the two intrusions display strong enrichment in FeO^* and CaO, falling out of the field defined by the high-Ti basalt series (HTB) of the ECFB (Fig. 4.1 and Fig. 4.2). Oxide-rich intrusive rocks are strongly depleted in total alkalies. Most of our data on Panzhihua are within the published data (Zhou *et al.*, 2005; Pang, 2008). However, three of our leucogabbro samples with the lowest content of MgO are outside the field of published data on Panzhihua. Taihe ore rocks are similar in composition to Panzhihua ores, but Taihe gabbros are somewhat higher in MgO (Fig. 4.1). Taihe leucogabbros are similar to the low-alkalies leucogabbro from Panzhihua. However, this Taihe sample is distinct in having abundant hornblende and a small amount of cumulus oxide minerals.

Figure 4.2 shows the distribution of the Panzhihua and Taihe rocks on a CaO-MgO-FeO^* diagram. Compositions of most rocks may be explained by accumulation of various amounts of Fe-Ti oxides into a typical basalt (gabbro). Two Fe-Ti oxide-rich rocks are depleted in plagioclase, consistent with oxide accumulation into wherlitic rocks. Panzhihua wherlites are characterised by extensive accumulation of olivine and clinopyroxene, and lack of Fe-Ti oxides and plagioclase. Note that all gabbros are displaced from the clinopyroxene–plagioclase joint line towards higher FeO^* contents, mostly due to the prevalent occurrences of Fe-Ti oxides and some may be caused by presences of hornblende in gabbroic rocks.

The Panzhihua gabbroic layered intrusion displays a large range of major element rock compositions (in wt%): 3.4 to 58.6 SiO_2, 0.2 to 18.1 TiO_2, 2.7 to 25.7 Al_2O_3, 4.4 to 70.8 $Fe_2O_3^*$, 1.0 to 26.8 MgO, 1.2 to 15.3 CaO, 0.1 to 0.4 MnO, 0.05 to 8.6 Na_2O, 0 to 2.7 K_2O, 0 to 2.3 P_2O_5, 0 to 0.5 V_2O_5. Similar range is observed in the Taihe intrusion: 4.1 to 48.5 SiO_2, 1.0 to 16.9 TiO_2, 4.9 to 21.4 Al_2O_3, 7.3 to 64.8 $Fe_2O_3^*$, 2.9 to 8.3 MgO, 0 to 16.1 CaO,

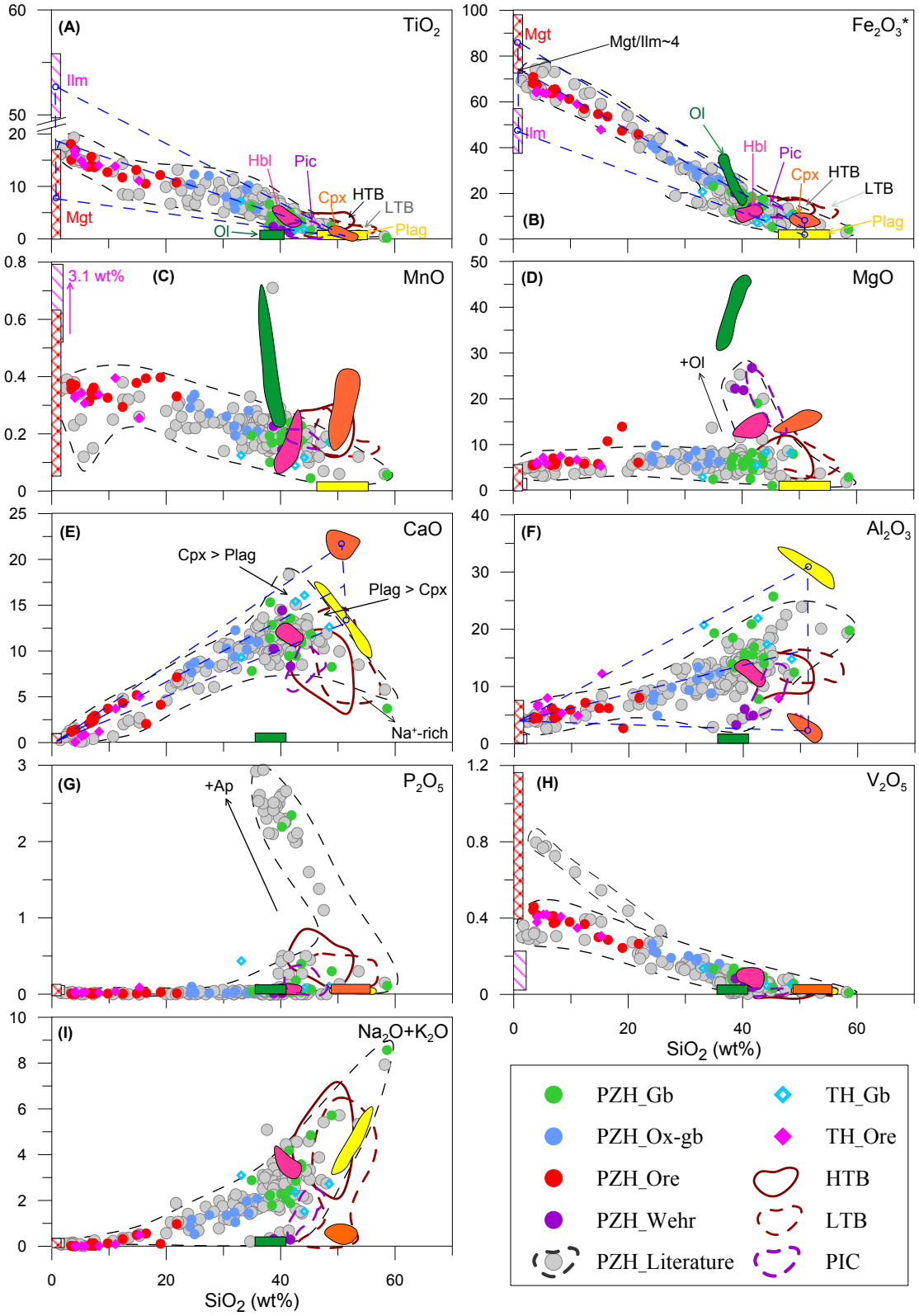

Fig. 4.3 Harker diagrams illustrating the geochemical characteristics of studied rocks from the Panzhihua and Taihe Intrusions. Also shown are published data on Panzhihua rocks (dashed line), Emeishan high-Ti basalt (darker grey area, HTB), low-Ti basalts (light grey area, LTB), and composition ranges of 6 major constituting minerals. Blue empty circles in A, B, E and F represent the average composition of minerals. The oxide pole is estimated to compose of Mgt and Ilm with a ratio of 4. See text for details.

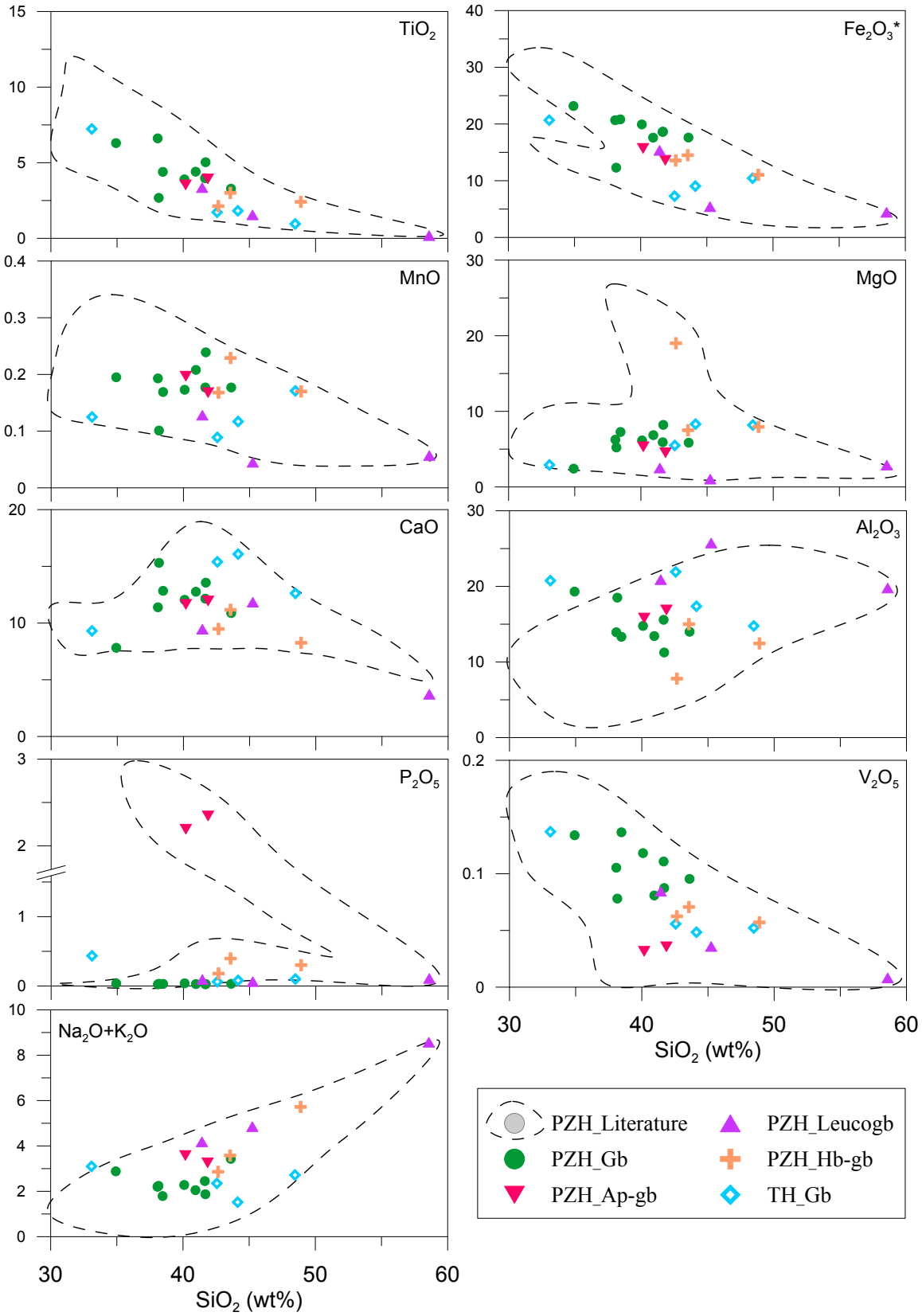

Fig. 4.4 Harker diagrams illustrating the whole-rock major element compositions of gabbroic rocks from the Panzhihua and Taihe Intrusions. Panzhihua literature data sources are as shown on Fig. 4.1.

0.1 to 0.4 MnO, 0.05 to 2.3 Na_2O, 0 to 1.4 K_2O, 0 to 0.4 P_2O_5, 0 to 0.4 V_2O_5.

The correlations between whole rock major element compositions are plotted on the Harker diagram (Fig. 4.3), also shown are published data on the Panzhihua intrusion and volcanic rocks from the Emeishan large igneous province (ELIP). It is clear that the new data in this study cover well the compositional range defined by previous data on the Panzhihua intrusion, regardless of the scanty of our data due to small sample population. The most distinct difference is found in V_2O_5 content, where a group of samples from Pang (2008) display a much sharper increase in V_2O_5 with decreasing SiO_2 contents than either our samples or the data of Zhou *et al*. (2005) and Song *et al*. (2013) (Fig. 4.3 H). As all rock samples from these studies were collected from the same section, we believe that these differences are analytical.

The whole rock major element compositions are distinct for different rock types, reflecting their cumulate nature. Generally, the oxide ore rocks in both intrusions are characterized by higher $Fe_2O_3^*$, TiO_2, V_2O_5, MnO, but lower CaO, Al_2O_3, Na_2O and K_2O, in comparison with gabbroic rocks. The oxide-rich gabbros lie in between the oxide ore and gabbroic rocks. No systematic correlations have been observed between whole rock MgO contents and other oxides. Instead, $Fe_2O_3^*$, TiO_2, V_2O_5 and MnO contents show a negative correlation with SiO_2, whereas CaO, Al_2O_3, Na_2O and K_2O contents shows a positive correlation with SiO_2 (Fig. 4.3). Elevated contents of MgO and P_2O_5 in some rocks are due to accumulation of olivine and apatite, respectively (Fig. 4.3 D, G).

The Panzhihua wehrlites are characterized by high MgO (21.9 to 26.8 wt%) and low Al_2O_3 (3.3 to 6.1 wt%) and total alkali contents (0.2 to 0.3 wt%). However, the other major elements are within the compositional range of gabbroic rocks (Table 4.1; Fig. 4.3). The averaged Mg# of wehrlites decreases from >80 (81 to 82) in the Marginal Zone (MGZ) to 71 in the Middle Zone A (MZa) (Table 4.1). The Mg# of typical Panzhihua melanogabbroic rocks vary between 40 and 49 (Table 4.1). In some cases, where abundant ferromagnesium minerals present (e.g. olivine, hornblende), the Mg# of gabbro may reach up to 76, while in other plagioclase-rich leucogabbro, this value may be as low as 19 (Table 4.1).

The major element composition of Taihe rocks fall within the range of Panzhihua samples, and show comparable element abundances between similar rock types (Table 4.2; Fig. 4.3, Fig. 4.4). However, there is one gabbro which shows slightly higher Al_2O_3 and P_2O_5 at a given $Fe_2O_3^*$ content, compared with Panzhihua gabbro (Fig. 4.4). Al_2O_3 enrichment is also seen in one Taihe ore rock (Fig. 4.3).

The Panzhihua whole-rock compositions may be considered as mixtures of Fe-Ti oxides and silicates in various proportions, as the "two-pole theory" proposed for Bjerkreim-Sokndal layered intrusion by Duchesne & Charlier (2005). As shown in the Figure 4.3, the Fe-Ti oxide pole, consisting of magnetite and ilmenite, has substantial concentrated compositional ranges, compared with the silicate pole that composed mainly of clinopyroxene and plagioclase. This is probably due to the relatively constant ratio of magnetite to ilmenite, but more variable in silicate minerals. By extrapolation of the trend lines in Figure 4.3 A and B, as well as the average composition of Fe-Ti oxides, the ratio of magnetite to ilmenite (Mgt/Ilm) is estimated to be approximately 4 in ore rocks. This value is almost the same as average values in MGZ and MZa ore rocks measured by the mineral liberation analysis (MLA) technique (3.9, not including leucogabbro and wehrlite). Measured leucogabbros are characterized by slightly lower value of Mgt/Ilm, indicating increases in ilmenite relative to magnetite. A extreme value of 9.7 is found for Mgt/Ilm in a contact wehrlite (PZ-1). It may result from small total amount of Fe-Ti oxide in these rocks, which makes it more difficult to estimate the Mgt/Ilm proportion from the whole rock compositions accurately. On the other hand, uneven distribution of Fe-Ti oxides within rocks may affect measurements of mineral modal proportions using thin sections.

The ratio of constituting minerals (e.g. Cpx/Plag) in the silicate pole is hard to estimate, because scattered data of CaO, Al_2O_3 and total alkaline are sufficient evidences for large compositional ranges and variable modal proportions of silicate minerals (Fig. 4.3 E, F and I). Also, addition of olivine and/or hornblende may further complicate interpretation of the silicate pole. For most melanogabbro, the ratio of Cpx/Plag approaches 1, as shown by extrapolation of compositional trend Figure 4.3 F.

To investigate the compositional differences exist between various types of gabbroic rocks, only gabbroic rocks are plotted in the same Harker diagram for clarification (Fig. 4.4). Overall, the Panzhihua melanogabbros have lower SiO_2, total alkalines and P_2O_5, but higher TiO_2, Fe_2O_3* and V_2O_5, in compared with other types of gabbros (Fig. 4.4 A-F). These compositions reflect more abundant Fe-Ti oxides present in melanogabbro than others. The Panzhihua apatite-gabbro are recognized by remarkably higher content of P_2O_5 than the other rocks (Fig. 4.4 G).

The relationships between mineral modal proportions and whole rock major element compositions are further examined on Figure 4.5. The most striking common feature on these

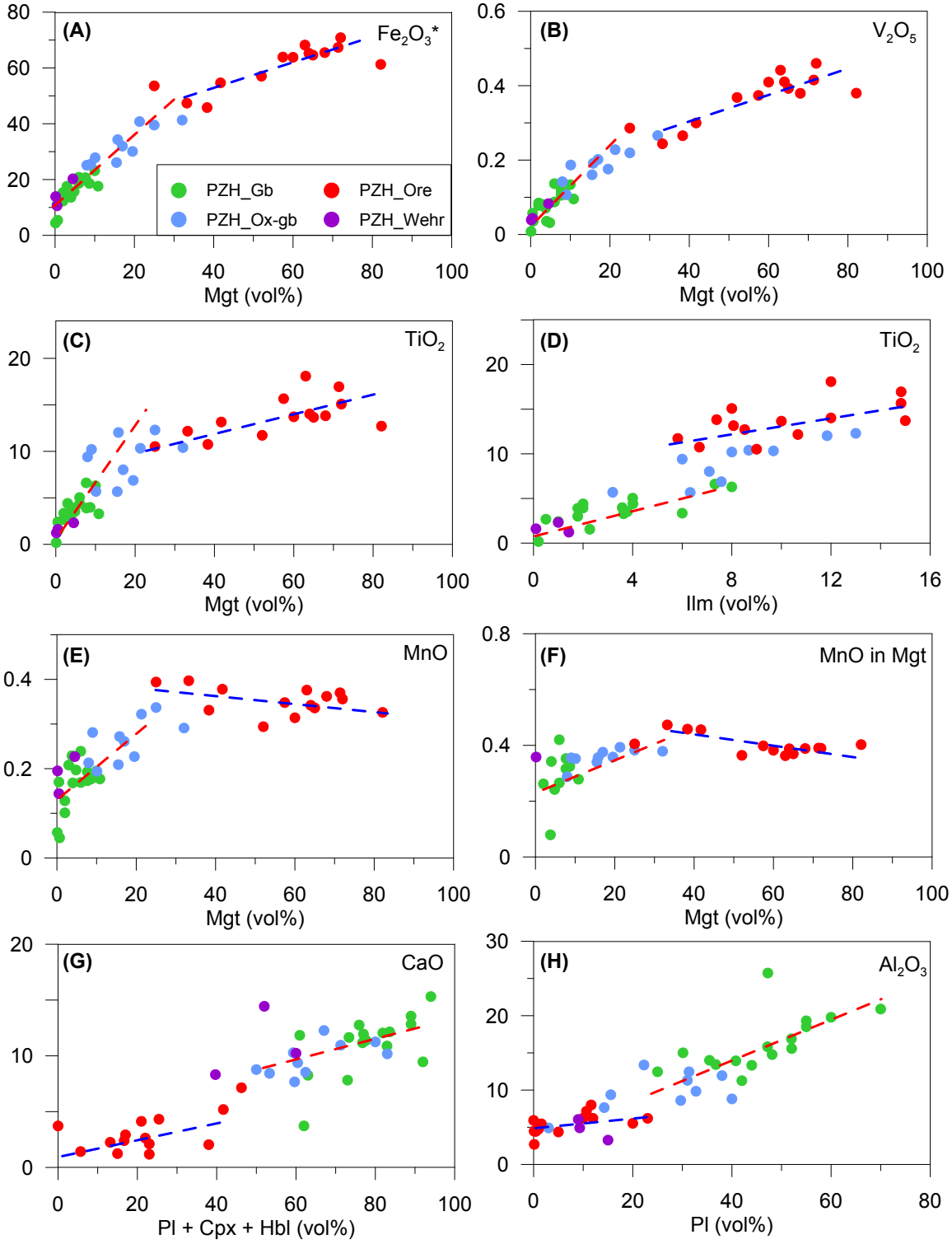

Fig. 4.5 Binary diagrams illustrating the correlation between mineral modal proportions and whole rock major element composition. Note the different slopes of mineral modal proportions and whole rock major oxide compositions for Fe-Ti oxide ores and for gabbros. Also note the negative correlation between magnetite mode and whole rock MnO contents in ore rocks.

plots is the different slopes found in trends for Fe-Ti oxide ores and Fe-Ti oxide-poor gabbroic rocks (Fig. 4.5). It may be inferred that the oxide mineral assemblage and silicate mineral assemblage may have crystallized separately in distinct crystallization methods.

The modal proportions of magnetite shows positive correlation with whole rock $Fe_2O_3^*$, V_2O_5, and TiO_2 contents, supporting magnetite controls on these elements (Fig. 4.5 A-C). The TiO_2 contents are also controlled by ilmenite as shown by positive correlation (Fig. 4.5 D). However, the much lower amount of ilmenite relative to magnetite in most rocks has reduced this effect to some extent. With increasing magnetite amounts, the whole rock MnO content increases in gabbroic rocks, but decreases in Fe-Ti oxides (Fig. 4.5 E). This is in accordance with the observations that MnO content in magnetite increases as decreasing Mgt modal proportion.

The contents of CaO are positively correlated with total amount of plagioclase, clinopyroxene and hornblende present in the rocks, whereas Al_2O_3 contents are closely related to the modal proportion of plagioclase only (Fig. 4.5 G and H). It is noticeable that one leucogabbro shows very low content of CaO (3.7 wt%), whereas one wherlite from the contact shows enriched CaO content (14.44 wt%), both of which are offset the general trend for Fe-Ti oxide poor rocks (Fig. 4.5 G). These are interpreted as albite-dominated plagioclase in the leucogabbro and rapid cooling in the contact wehrlite, respectively. Another leucogabbro is distinct from others in terms of high content of Al_2O_3 (Fig. 4.5 H). Overestimation or underestimation of plagioclase modal proportion is in low possibility as it is measured by MLA method. Since this leucogabbro is coarse-grained, the problem may have aroused from atypical and different selections of rock sample used for MLA and whole rock chemistry analysis.

4.1.3 Whole-rock Trace Element Composition

Whole rock trace elements were determined using both XRF and ICP-MS methods. For elements measured by both techniques, concentrations are compared to assess the consistency between the analytical methods (Fig. 4.6). As shown on the diagrams, the XRF and ICP-MS data follow 1:1 relationship ($R^2 > 0.99$) for the most trace elements (0.98 for Zn and Ba). In general, for trace elements with high concentration, e.g. V, Ni, Cu, Zn, Sr and Ba, the values obtained by XRF are slightly higher than those obtained by ICP-MS, whereas the low concentration trace elements (e.g. Y, Zr) are the opposite (Fig. 4.6). This is also true for Cr, excluding samples with very high concentrations of Cr. The differences observed are not significant for the purposes of this study. The following discussion will focus on ICPMS data as this method

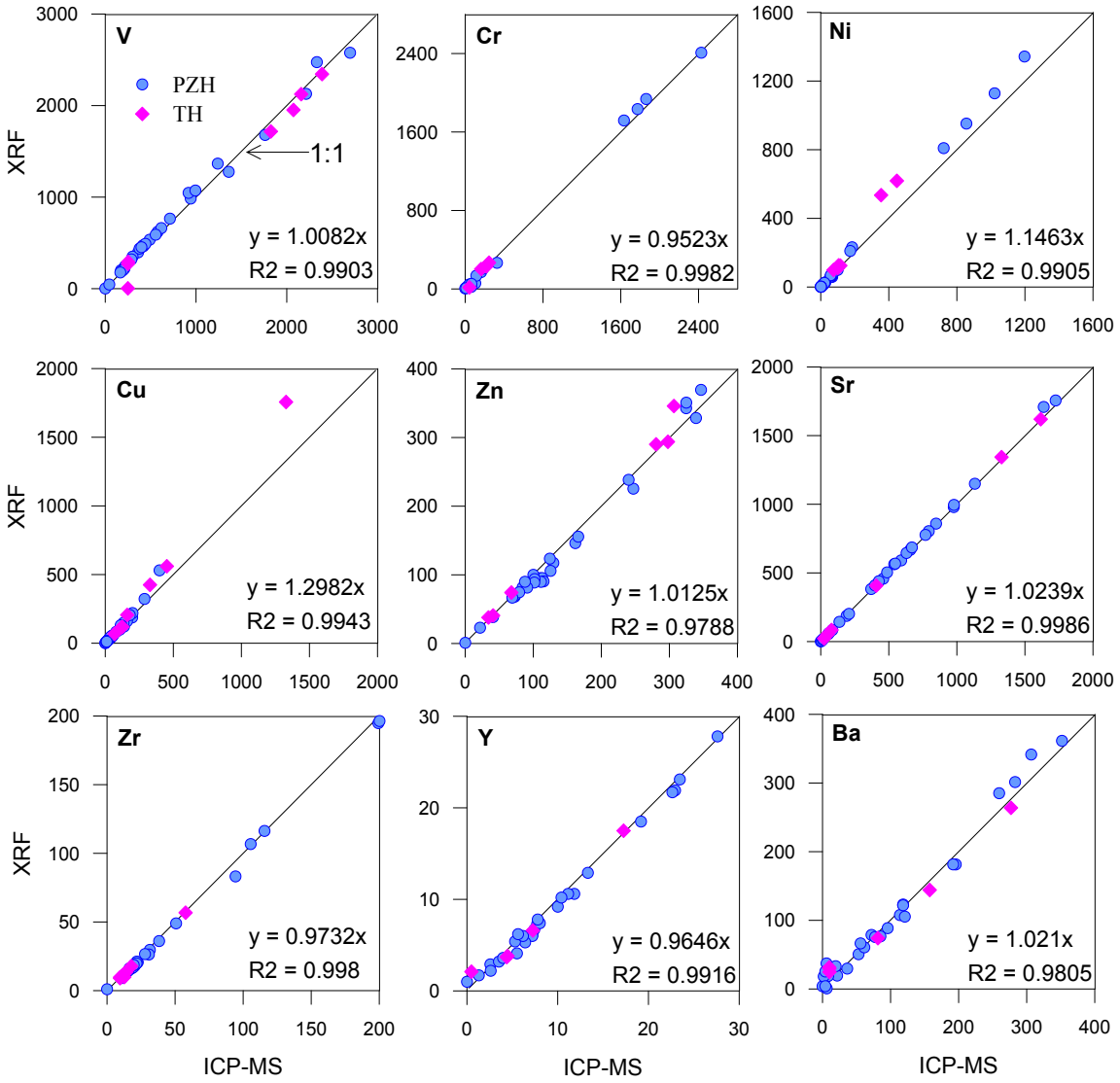

Fig. 4.6 Comparison between XRF and ICP-MS data of whole rock trace element concentrations.

covers a wider compositional range than XRF, having significantly lower detection limits.

4.1.3.1 First Row Transition metals (FRTM) and Ga

The first row transition metals (FRTM), including Sc, Ti, V, Cr, Mn, Fe, Co, Ni, Cu and Zn, have multiple valance states and hence variable behaviour in mantle partial melting and magma differentiation processes. With the exception of Mn, the FRTM are either siderophile and/or chalcophile. Their geochemical behaviour ranges from moderately incompatible (Ti, Cu, Zn) to strongly compatible (Cr, Ni, Co), but may vary significantly in different circumstances. A compiled partition coefficient of trace elements between common minerals and basaltic liquid are presented in Table 4.3.

Figure 4.7 and 4.8 show the concentrations of FRTM elements in various types of rocks

Table 4.3 Trace element partition coefficients in common mineral-basalt system.

Element	Ol	Cpx	Plag	Mgt	Ilm	Sul	Hbl	Ap	Grt	Opx	Rutile
Sc	0.25	1.4	0.008	0.73	1.8		2.2	0.22	4	1.2	
Ti	0.02	0.48	0.08	7.5		0.05			0.3	0.1	
V	0.08	0.74	0.1	3.4			0.69		1.5	0.6	118
Cr	1.25	3.8	0.05	153		0.9			2	10	
Mn	1.47	0.86	0.1	1.4	1.9	0.3	0.94	0.13			0.34
Fe	1.03	0.81	0.22								
Co	2.33	1.35	0.56	3.4	2.2	70		0.03			
Ni	15.5	7.8	0.64	48		265	2.6		5.1	5	
Cu	0.55	0.36	0.17		1.46			0.28			
Zn	0.86	0.5	0.11	2.6	0.38			0.25			
Ga	0.04	0.74	1.7	2	0.14			0.25			
K	0.007	0.038	0.17						0.015	0.014	
Rb	0.011	0.011	0.107						0.0007	0.0006	
Sr	0.014	0.06	1.83						0.012	0.04	
Ba	0.01	0.026	0.23						0.023	0.013	
Th											
U	0.002	0.04	0.01								
Y	0.004	0.41	0.009						3.1	0.18	
Zr	0.012	0.12	0.048	0.1	0.28		0.36		0.27	0.02	
Hf	0.01	0.02	0.01				0.67		0.24	0.01	
Nb	0.01	0.005	0.08	0.9	0.8		0.8		0.02	0.15	
Ta		0.14	0.11		1.27		0.38		0.09		
La	1E-04	0.056	0.068	0.015	0.098		0.17	8.6	0.016	0.002	
Ce	1E-04	0.09	0.047	0.016	0.11		0.26	11.2	0.065	0.003	
Nd	3E-04	0.18	0.072	0.026	0.14		0.44	14	0.363	0.007	
Sm	0.001	0.29	0.055	0.024	0.15		0.76	14.6	1.1	0.01	
Eu	0.001	0.46	0.508	0.025	0.1		0.88	9.6	2.02	0.05	
Gd	0.003	0.64	0.092	0.018	0.14		0.86	15.8	0.498	0.013	
Yb	0.01	0.4	0.071	0.018	0.17		0.59	8.1	3.88	0.049	

*Data are compiled from GERM and Rollinson (1993). References include: Aignertorres *et al*. (2007); Beattie (1994); Bindeman *et al*. (1998); Bougault & Hekinian (1974); Duke (1976); Dunn (1987); Foley *et al*. (2000); Hart & Dunn (1993); Hauri *et al*. (1994); Higuchi & Nagasawa (1969); Jenner *et al*. (1993); Keleman & Dunn (1992); Kloeck & Palme (1988); Leeman & Lindstrom (1978); Lemarchand *et al*. (1987); McCallum & Charette (1978); McKenzie & O'Nions (1991); Mysen (1978); Nielsen (1992); Paster *et al*. (1974); Pedersen (1979); Rajamani & Naldrett (1978); Skulski *et al*. (1994); and reference in Rollinson (1993).

in this study. Compared with the lowermost contact wehrlite (PZ-1), the most prominent characteristic of FRTM of all gabbro, oxide-gabbro and ore rocks is the strong depletion in Cr and Ni (Fig.4.7). The depletion in Cr and Ni in Panzhihua rocks is generally 1-3 orders of magnitude, but sometimes may reach up to 5 orders of magnitude in some gabbroic rocks (Fig.4.7 A-D). Taihe ore rocks show larger degree of depletion in Cr and Ni than that in gabbroic rocks (Fig.4.7 E-F). Ti, V and Fe are enriched by approximately 1 order of magnitude in ore rocks compared to wehrlite and gabbroic rocks, confirming accumulation of Fe-Ti oxides in these rocks. Cu is variable in all rock types, however, all Taihe rocks show enrichment of Cu in comparison to Panzhihua wehrlite (Fig.4.7 E-F). Overall, the Panzhihua and Taihe rocks show comparable distribution patterns of FRTM elements, indicating genetic relationship between various types of rocks. The same stands for wehrlites occurring at various stratigraphic heights in Panzhihua. These wehrlites may have originated from a relatively more primitive magma than the parental magma to Panzhihua gabbro.

Four types of gabbro are compared for concentrations of FRTM due to great variations (Fig. 4.8). The Panzhihua melanogabbro show large variation in Cr, Ni and Cu, but the other FRTM elements are relatively concentrated (Fig. 4.8 A). In compared with melanogabbro, hornblende-rich gabbro show less depletion in Cr and Ni, but the other elements are within

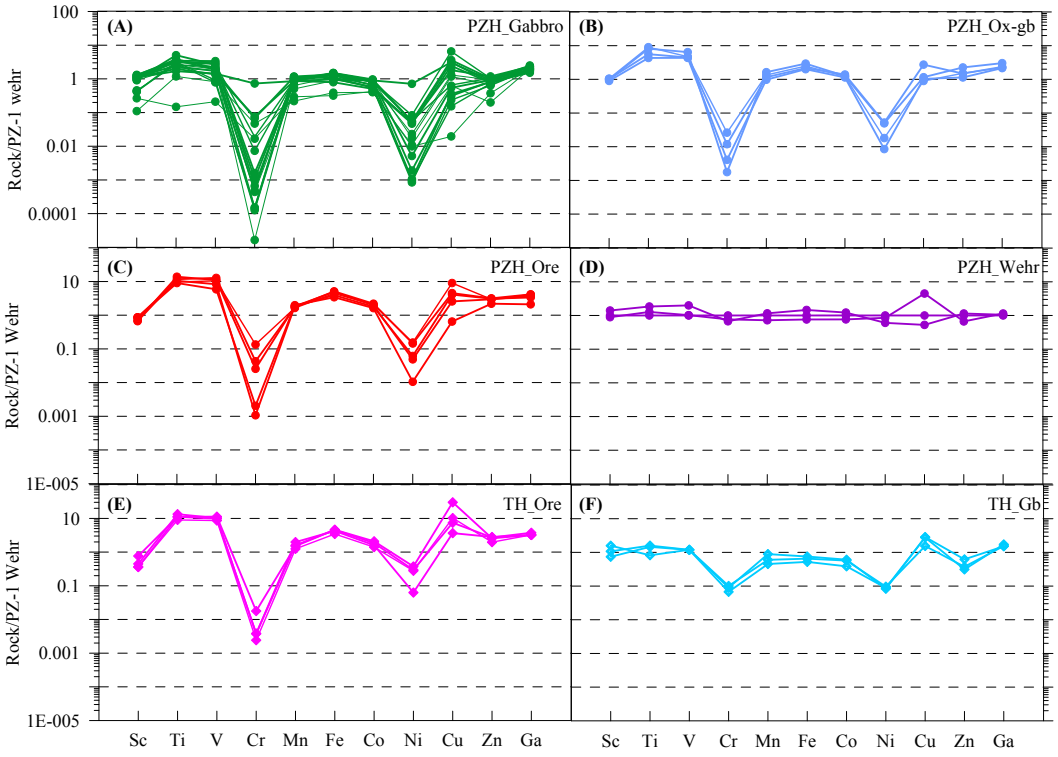

Fig. 4.7 Concentrations of FRTM elements in various rocks in Panzhihua and Taihe Intrusions normalized to wehrlite PZ-1

the ranges of melanogabbro (Fig.4.8 B). Leucogabbro display the greatest depletion in Cr, variable Sc, Ti, V and Cu concentrations but concentrated Ni (Fig.4.8 C). Apatite-gabbro show comparable distribution patters of FRTM concentrations to that of the Cr-Ni-depleted melanogabbro (Fig.4.8 D).

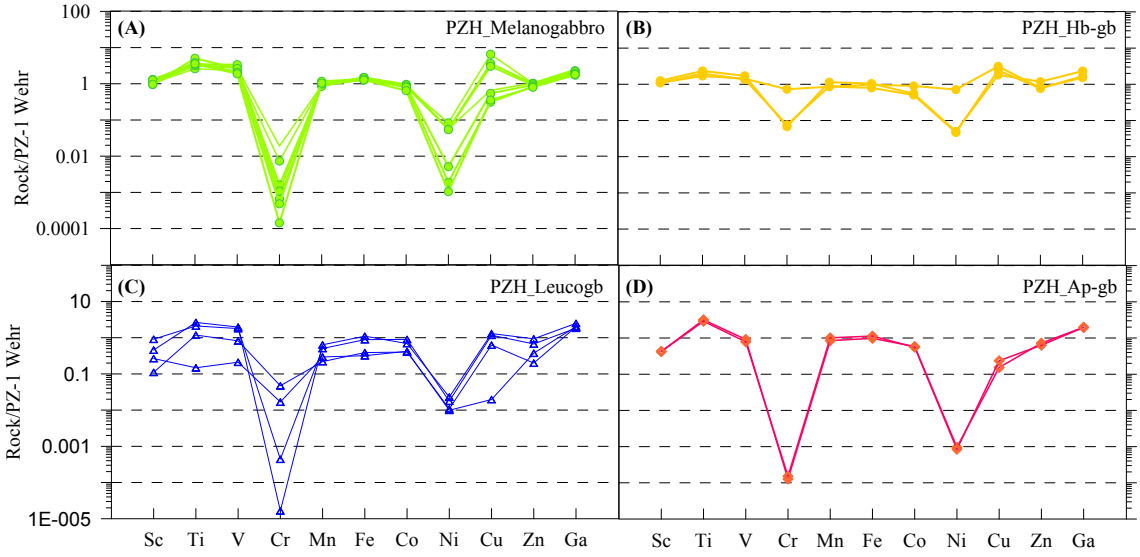

Fig. 4.8 Concentrations of FRTM elements in various gabbroic rocks in Panzhihua and Taihe Intrusions normalized to wehrlite PZ-1.

Nevertheless, all FRTM and Ga, are compatible in one or more cumulus minerals occurring in the Panzhihua and Taihe layered intrusions. Hence, the concentrations of these compatible elements in a cumulate are strongly dependant on their relative partition coefficicients in various minerals and mineral modal proportions. The relationship of compatible element concentrations and mineral modal proportions are shown in Figure 4.9.

Scandium (Sc), with concentrations ranging from 3 to 38 ppm in the Panzhihua rocks, and 10 to 42 ppm in the Taihe samples, displays a positive correlation with the amount of clinopyroxene (Fig. 4.9 A), indicating incorporation of Sc into clinopyroxene, which is consist with the experimental result (Jenner *et al.*, 1993). A relatively low correlation coefficient (R^2=0.56) and the scatter observed for the gabbroic rocks, are probably caused by the presence of hornblende. One ore rock (PZ-4) has no clinopyroxene but relatively high amount of ilmenite (8.5 vol%), which may explain the high Sc concentration in this rock, as Sc is also compatible in ilmenite and hornblende (Higuchi & Nagasawa, 1969; Paster *et al.*, 1974).

The other compatible elements show two distinct trends against mineral modal proportions (Fig. 4.9), reflecting controls by two different mineral assemblages: oxides and silicates,

as observed in whole rock major element compositions. Cr and Ni show opposite trends in oxide-rich ores and oxide-poor gabbros (Fig. 4.9 B and C), whereas V, Mn, Ga, Co, Cu and Zn always show positive correlation with mineral modal proportions (Fig. 4.9 D-I).

The concentration of Cr ranges between 0.04 (detection limit) to 2428 ppm in Panzhihua and a narrower range in Taihe (Table 4.1, 4.2). Cr is a strongly compatible element in magnetite, and moderately compatible in clinopyroxene (e.g. $D_{Cr}^{mgt/liq}$=153, $D_{Cr}^{cpx/liq}$=3.8) (Esperança *et al.*, 1997; Hart & Dunn, 1993). Cr is incompatible to slightly compatible in olivine (e.g. $D_{Cr}^{ol/liq}$=0.6-1.8) (Beattie, 1994), but strongly incompatible in plagioclase (e.g. $D_{Cr}^{plag/liq}$=0.02) (Bougault & Hekinian, 1974). The mineral liberation analysis of selected Panzhihua rocks shows the increase of magnetite is accompanied by a dramatic decrease of clinopyroxene and olivine (R^2=0.8325), while the reverse correlation is more obvious when taking ilmenite into consideration (R^2=0.8494). In comparison, Mgt show less correlation with olivine and clinopyroxene (R^2=0.3874). Hence, in oxide rich rocks, Cr concentration is mainly controlled by magnetite, whereas in oxide-poor gabboic rocks, Cr concentration reflects accumulation of clinopyroxene and plagioclase, and in some cases, olivine (Fig. 4.9 B). This is similar to the two-pole control on major element compositions.

The concentrations of Ni show a broad range, 1 to 1197 ppm and 75 to 447 ppm in

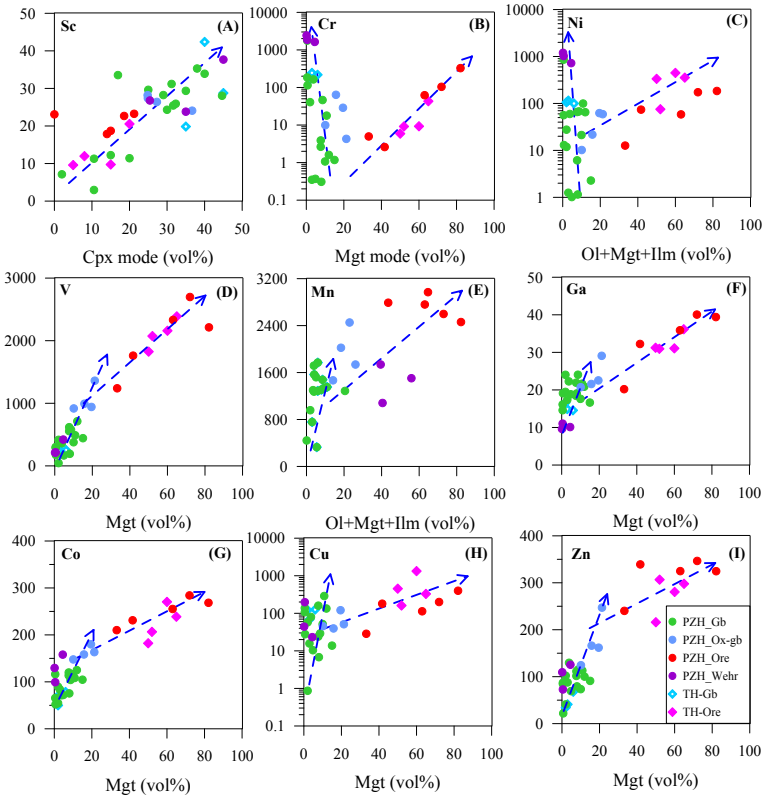

Fig. 4.9 Concentrations of compatible elements as a function of mineral modal proportions.

the Panzhihua and Taihe rocks, respectively. The compatibility of Ni in minerals decreases in the sequence of sulphide (e.g. $D_{Ni}^{sul/liq}$=265) (Rajamani & Naldrett, 1978), magnetite (e.g. $D_{Ni}^{mgt/liq}$=48) (Nielsen, 1992), and olivine (e.g. $D_{Ni}^{ol/liq}$=15.5) (Mysen, 1978), although Ni may become incompatible in the last stages of magma fractionation (Longhi & Walker, 2006; Filiberto *et al.*, 2009). However, sulphide in ore rocks is usually ranging between 1 to 3 vol%, therefore, the whole rock Ni content in oxide-rich rocks is mainly controlled by magnetite (Fig. 4.9 C). The effects of sulphide and olivine on whole rock Ni abundance may be magnified in gabbroic rocks relatively depleted in magnetite.

The concentration ranges for V, Mn, Ga, Co, Cu and Zn are also broad in the Panzhihua rocks (in ppm): 45 to 2698 V, 329 to 2970 Mn, 10 to 40 Ga, 52 to 284 Co, 1 to 399 Cu, 22 to 349 Zn. The concentrations of the above elements in Taihe rocks are comparable to that in Panzhihua, but show more variability, likely due to a limited number of samples.

In oxide-rich rocks, V, Mn, Ga, Co, Cu and Zn show the same positive correlation with magnetite abundance, while the slope becomes steeper in the gabboric rocks (Fig. 4.9 D-I). These relationships indicate that in oxide ore rocks, magnetite is the dominated mineral accounting for abundance of these elements, whereas in oxide-poor rocks, the large variation in element concentration may indicate that silicate minerals have played a more important role than magnetite. This is because of the fact that these elements are compatible not only in magnetite and/or ilmenite, but also in silicate minerals such as olivine, clinopyroxene, plagioclase, and in sulphide. For example, V is compatible in clinopyroxene besides magnetite (Hart & Dunn, 1993; Jenner *et al.*, 1993; Hauri *et al.*, 1994), Mn is incorporated into olivine and ilmenite (Dunn, 1987; Paster *et al.*, 1974), Ga may be incorporated into plagioclase (Paster *et al.*, 1974), Co may be incorporated into olivine, clinopyroxene, sulphide and ilmenite (Beattie, 1994; Duke, 1976; Paster *et al.*, 1974), Cu may be incorporated into sulphide and ilmenite (Paster *et al.*, 1974; Rajamani & Naldrett, 1978), and Zn may be incorporated into olivine (Paster et al., 1974). The steeper slope of element against mineral modal proportion in oxide-poor rocks may be resulted from the larger difference in bulk partition coefficients. The enrichment (Mn, Ga, Cu) and depletion (V, Co, Zn) relative to that extrapolated from the magnetite trend, are explained by the difference between element partition coefficients for magnetite and other minerals (Fig. 4.9 D-I).

4.1.3.2 Large iron iithophile elements (LILE), Li and Be

The concentrations of large-ion-lithophile elements (LILE) in the studied samples are approximately 1-3 orders of magnitudes above the detection limits. Gabbroic rocks generally have more abundant LILE than ore rocks, as shown by positive correlations with whole rock SiO_2 contents, indicating control of silicate pole of plagioclase and clinopyroxene (Fig. 4.10 A-F). The larger scatter in some Taihe rocks may result from limited sampling. Concentrations of Li, Ba and Sr are 1 to 3 orders of magnitudes higher than Be, Cs and Rb, respectively (Table 4.1, Table 4.2, Fig.4.10). Sr enrichment in studied samples reflects plagioclase accumulation, as it is compatible in plagioclase (Bindeman et al., 1998, Aigner-Torres et al., 2007, Bindeman and Davis, 2000). Note the average LILE concentrations of Emeishan high-Ti basalts are higher than most studied rocks, indicating little amounts of intercumulus liquid present in the cumulate rocks from the studied intrusions.

4.1.3.3 Incompatible elements: Rare-Earth-Elements (REE)

The Panzhihua rocks are characterized by the total REE contents (excluding Y) of 1 to 73 times that of CI chondrite (Table 4.1). For Panzhihua gabbroic rocks, the enrichment is 8 to 19 times for melonogabbro, 8-34 times for leucogabbro, 54 to 57 times for apatite-gabbro, and 39 to 73 times for hornblende-rich gabbro. The total REE content is 1 to 4 times that of chondrites for Panzhihua ore, 6 to 10 times for Panzhihua oxide-rich gabbro, and 7 to 18 times for Panzhihua wehrlite (Table 4.1). The enrichments in the total REE for the Taihe rocks are comparable to those in the Panzhihua rocks: 9 to 22 times and 1 to 7 times chondrite for Taihe gabbro and Taihe ore, respectively (Table 4.2). This enrichment in the total REE in the gabbroic rocks is in accordance with the relatively higher partition coefficient of REE in hornblende and apatite than other rock-forming minerals (McKenzie and O'Nions, 1991, Paster et al., 1974).

Figure 4.11 shows the Chondrite-normalized REE patterns for various rock types from the Panzhihua and Taihe layered intrusion, which are comparable in both concentrations and distribution patterns. The Panzhihua rocks display slightly to highly fractionated LREE/HREE patterns (La/Yb_N=1.4 to 15.6). The Panzhihua melanogabbro have less fractionated LREE/HREE patterns (La/Yb_N=1.8 to 7.0) than the other gabbroic rocks (La/Yb_N=7.0 to 15.6), but comparable to oxide-rich rocks and wehrlites from Panzhihua (La/Yb_N=1.2 to 4.3). Taihe rocks show moderately to highly fractionated REE patterns (La/Yb_N=3.2 to 11.2).

Except for some ore rocks, the LREE abundances for both Panzhihua and Taihe rocks

are largely overlapping the compositional range of low-Ti basalts, but lower than high-Ti basalts (Fig. 4.11). They show negative to positive slopes for the Panzhihua gabbroic rocks and wehrlite (La/Sm_N=0.4 to 5.5), but negative slopes for oxide-rich rocks (La/Sm_N=0.6 to 1.0), in contrast with the high enrichment and fractionation of LREE for the high-Ti basalts (La/Sm_N=2.5) (Fig. 4.11). The HREE patterns for all studied rocks show slight to moderate fractionation (Gd/Yb_N =1.7 – 7.2), and are consistently parallel, although at a much lower abundance, to the high-Ti basalts (Fig. 4.11). These similarities in HREE patterns among the intrusive rocks and Emeishan high-Ti basalts indicate a genetic relationship.

Slight positive Eu anomaly is observed in both Panzhihua melanogabbro and leucogabbro (δEu=1.4 to 2.8), except for gabbro with abundant apatite and/or hornblende, and wehrlite, which have almost no Eu anomaly (δEu=0.9 to 1.1). Positive Eu anomaly is observed in most of Taihe rocks (δEu=1.6 to 2.2), although this anomaly is minor in some samples

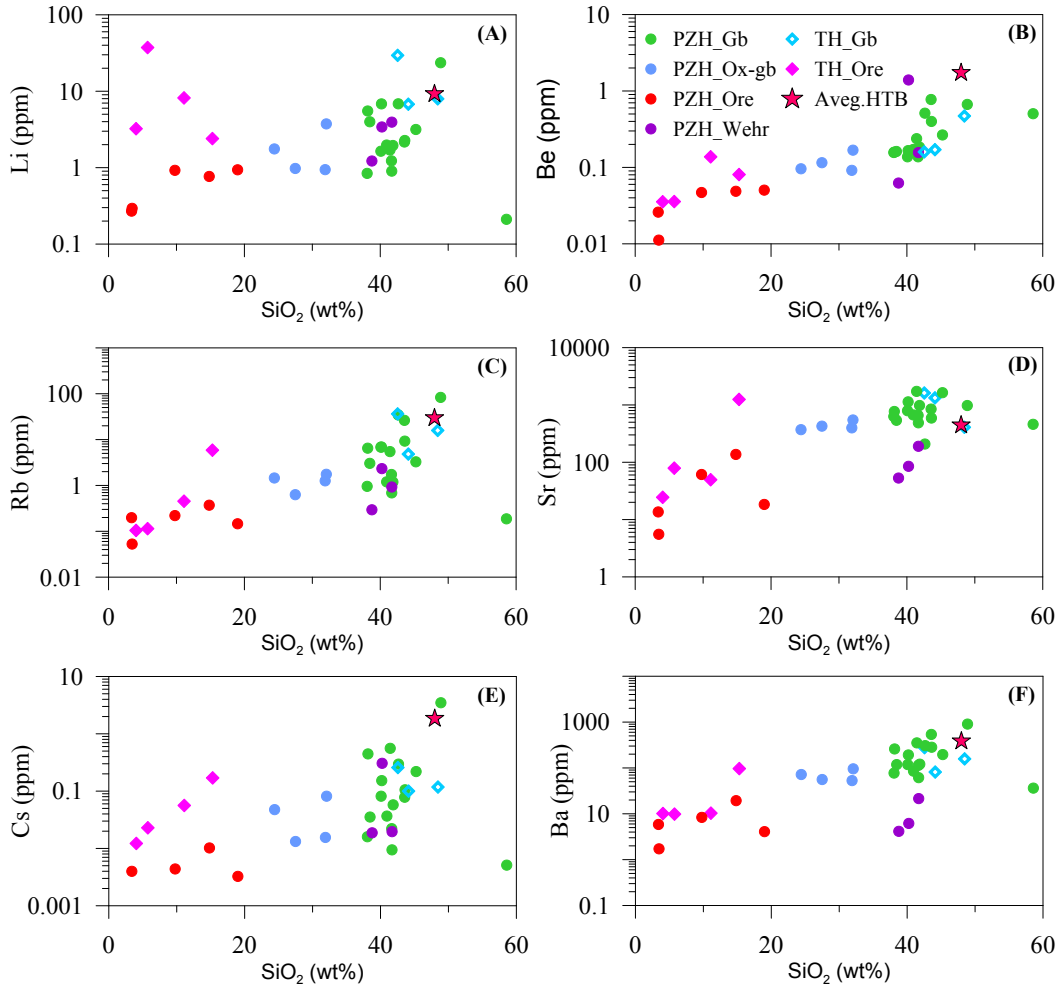

Fig. 4.10 Binary diagrams showing correlation between LILE and SiO_2 contents. Also shown is the average value of LILE in high-Ti basalts in Emeishan Large Igneous Province. Data source for basalts are the same as on Fig. 4.1.

(δEu=1.0 to 1.2). The positive Eu anomaly reflects accumulation of plagioclase in that rock, since Eu is more compatible in plagioclase than other REE (Aigner-Torres *et al.*, 2007; McKenzie & O'Nions, 1991).

Experimental studies on the partition coefficient of REEs in various minerals have shown that they are usually strongly incompatible in silicate minerals, except for Eu, which is more compatible in plagioclase. However, the relative compatibility of REEs in a specific mineral differs. For example, relative to Sm, La is more compatible in apatite, less incompatible in plagioclase, and more incompatible in all other minerals in the Panzhihua and Taihe rocks. Relative to Yb, La is slightly more compatible in apatite, less incompatible in plagioclase, but more incompatible in the other minerals. Gd is twice more compatible in apatite than Yb, slightly less compatible in hornblende, more incompatible in olivine, clinopyroxene and ilmenite, but similarly incompatible in plagioclase and magnetite. (Aigner-Torres *et al.*, 2007; Sobolev *et al.*, 1996; Bindeman *et al.*, 1998; Vannucci *et al.*, 1998; Mckenzie & Onions, 1991; Lemarchand *et al.*, 1987; Paster *et al.*, 1974). Hence, accumulation of plagioclase in a rock should elevate the ratio of La/Sm and Gd/Yb, but does little to La/Yb. Apatite accumulation will decrease La/Sm, but increase greatly Gd/Yb, and to a lesser extent, La/Yb. Accumulation

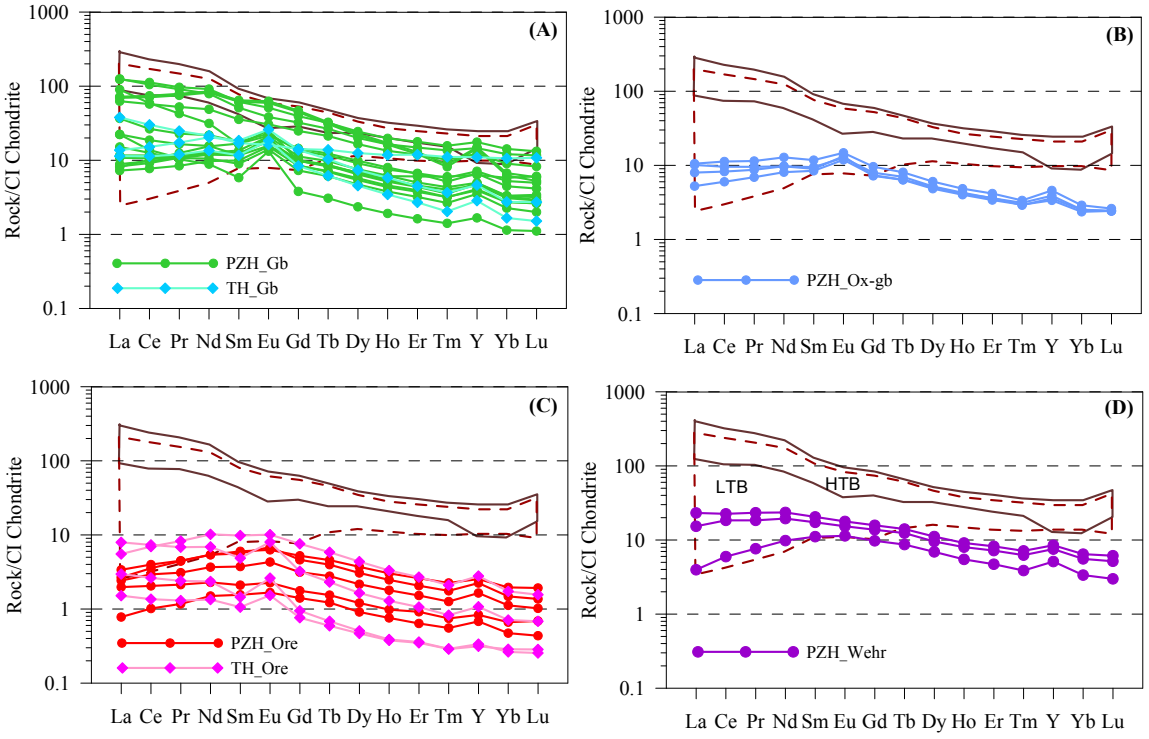

Fig. 4.11 Chondrite-normalized rare earth element patterns for various rock types from the Panzhihu and Taihe Intrusions. Chondrite values are from McDonough and Sun (1995). Fields constrained by brown solid line and dash line represent the REE concentrations of Emeishan high-Ti basalt (HTB) and low-Ti basalts (LTB), respectively.

of olivine, clinopyroxene and Fe-Ti oxides will decrease all of the three ratios. Accumulation of hornblende will decreases La/Sm and La/Yb, but elevates Gd/Yb (Fig. 4.12). Therefore, the fractionation of REE in the whole rock chemical composition may be explained by accumulation of various mineral(s).

4.1.3.4 Incompatible elements: HFSE (Y, Zr, Nb, Hf, Ta, Th, U)

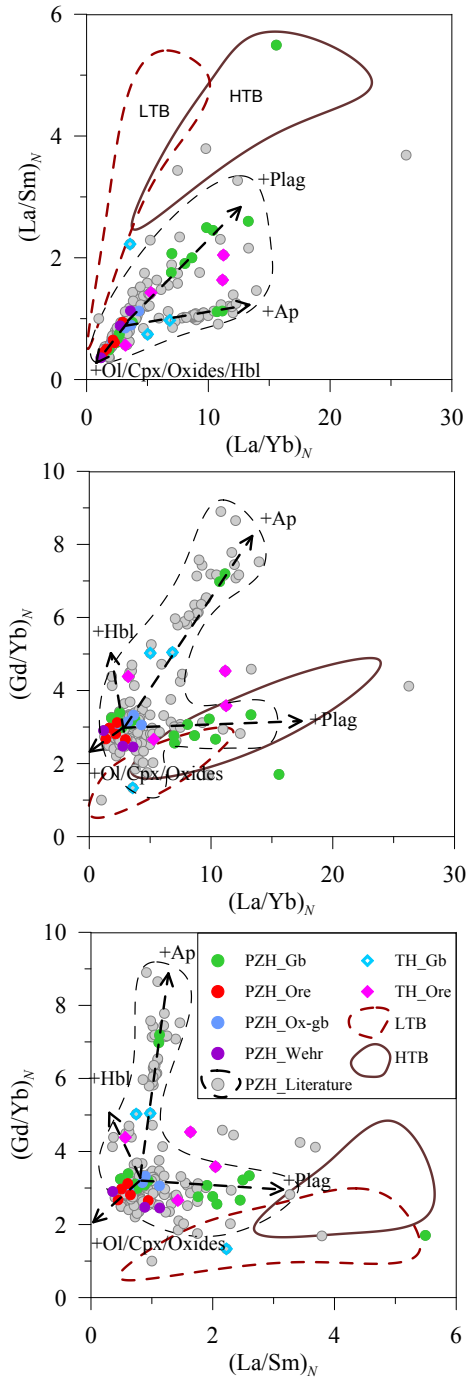

Fig. 4.12 Binary diagrams showing the control of minerals or mineral assemblages on REE fractionation. LTB-Emeishan low-Ti basalts; HTB-Emeishan high-Ti basalts.

These elements behave as strongly to slightly incompatible in the following silicate minerals (arranged as increasing $D^{mineral/melt}$): olivine, plagioclase, clinopyroxene and amphibole (Rollinson, 1993). Zr and Nb are slightly incompatible in ilmenite (D_{Zr}=0.8, D_{Nb}=0.28) (Aigner-Torres *et al.*, 2007; Sobolev *et al.*, 1996; Bindeman *et al.*, 1998; Vannucci *et al.*, 1998; Mckenzie & Onions, 1991; Lemarchand *et al.*, 1987; Paster *et al.*, 1974). Nb, Ta, Zr and Hf are incompatible to compatible in magnetite (Nielsen, 1992; Nielsen & Beard, 2000). However, differences exist in relative compatibility of these elements, for example, Zr is more incompatible than Y, but less incompatible than Nb, in olivine, plagioclase and clinopyroxene, which means a cumulate with these minerals would have decreased Zr/Y ratio and elevated Zr/Nb.

Except for a few samples, the majority of the Panzhihua and Taihe rocks have low contents of HFSE, also suggesting minor amounts of the inter-cumulus liquid. The Panzhihua and Taihe intrusive rocks have Zr content mostly below 50 ppm (Table 4.1, 4.2; Fig. 4.13). Several exceptions have Zr up to 200 ppm, indicating areas of enrichment in

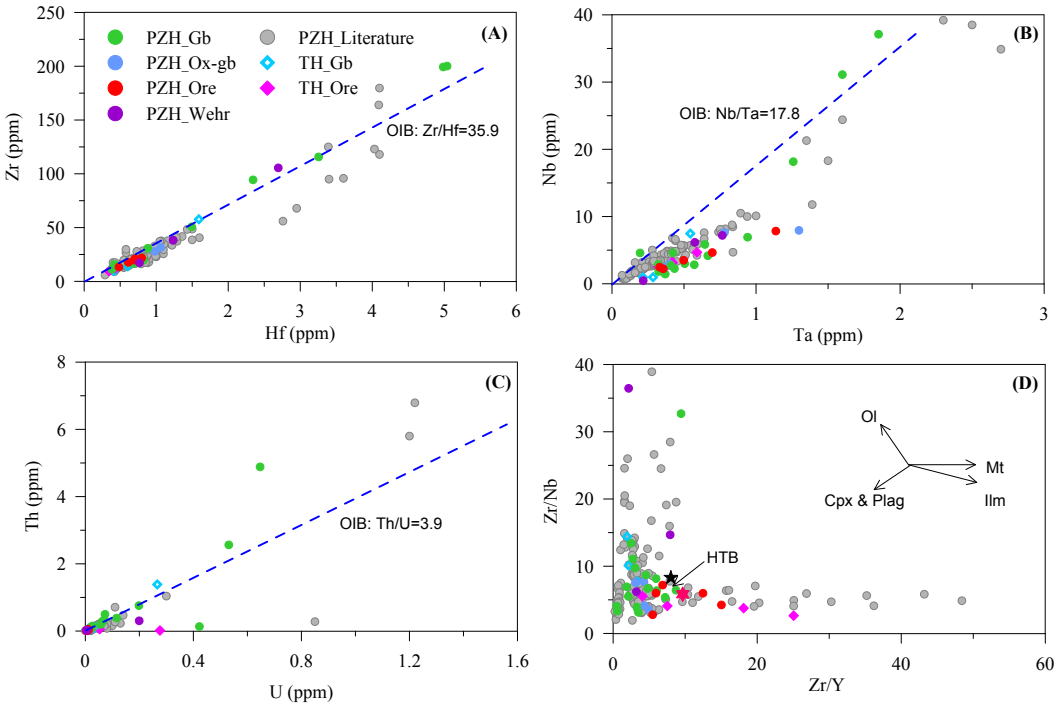

Fig. 4.13 Binary diagrams showing correlation between HFSE.

the late-stage fractionated trapped liquids. Zr/Hf ratio is similar to that of OIB (Zr/Hf=35.9, Sun & McDonough, 1989), indicating the rocks lack minerals that would fractionate Zr and Hf. The contents for Nb and Th are ranging from 0 to 40 ppm and 0 to 5 ppm, relatively enriched compared to Ta and U. Nb and Ta show a departure from the trend defined by OIB (Nb/Ta=17.8, Sun & McDonough, 1989), indicating the appearance of certain minerals that would incorporate Ta more than Nb. Th and U show little fractionation in the Panzhihua and Taihe rocks. The ratio of Zr/Y is mainly controlled by accumulation of magnetite and ilmenite, whereas Zr/Nb ratio reflects accumulation of silicate minerals, mostly clinopyroxene and plagioclase.

Figure 4.14 and Figure 4.15 show the wehrlite (PZ-1) normalized incompatible trace element concentrations. All Panzhihua and Taihe rocks show a strong Pb enrichment, and a strong Ti enrichment is found in Panzhihua and Taihe oxide-rich ores (Fig. 4.14).Moderate Sr enrichment is found in the Panzhihua melonogabbro and leucogabbro;, and P enrichment is found in Panzhihua apatite gabbro, indicating accumulation of plagioclase and apatite, respectively (Fig. 4.15). Th and U show large variations and up to 2 orders of magnitudes enrichment in Panzhihua and Taihe gabbroic rocks (Fig. 4.14, Fig. 4.15). The oxide-rich rocks have La enriched relative to Ce, whereas it is opposite in the gabbroic rocks. Zr is enriched in hornblende gabbro, and depleted in all the other gabbros and oxide-rich rocks. Since Zr is a strongly incompatible element, the extremely low abundance of Zr in the studied samples

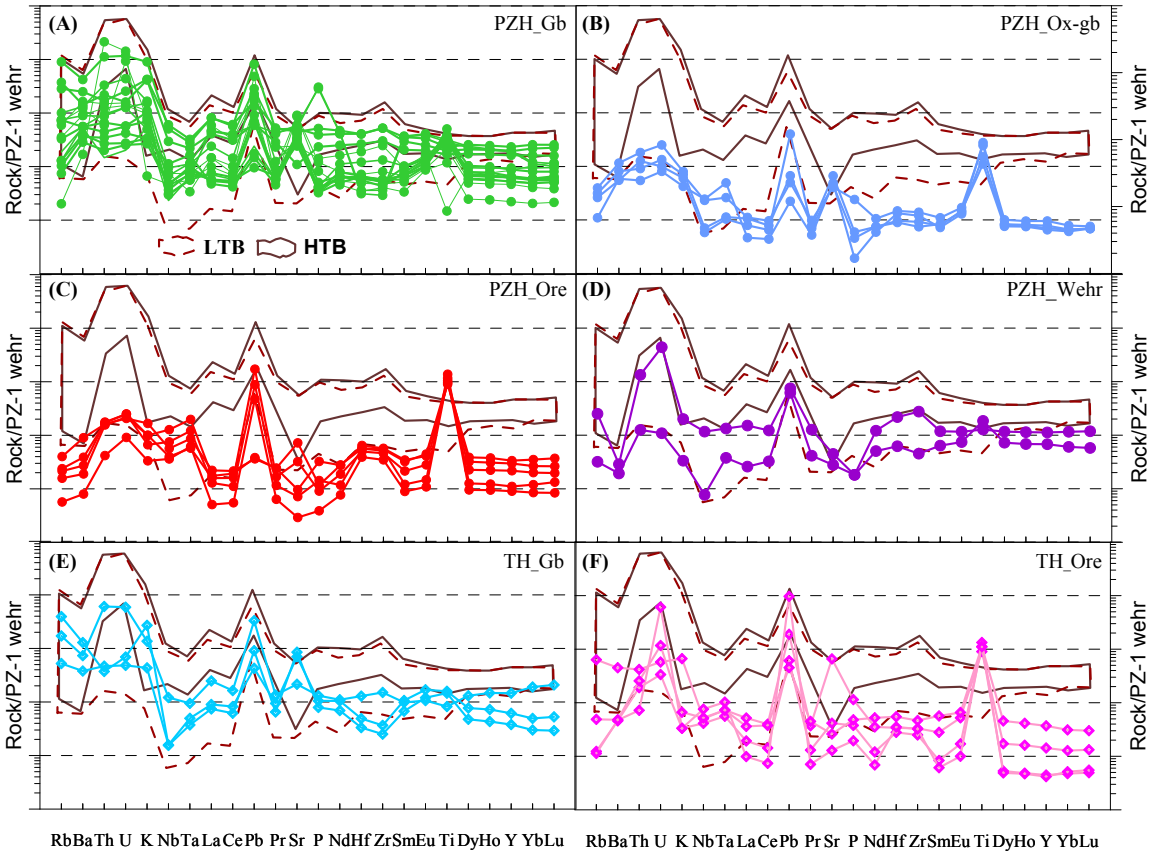

Fig. 4.14 Trace element concentrations of Panzhihua and Taihe rocks normalized to the composition of a wehrlite (PZ-1), Panzhihua Intrusion. From left to right, element compatibility increases.

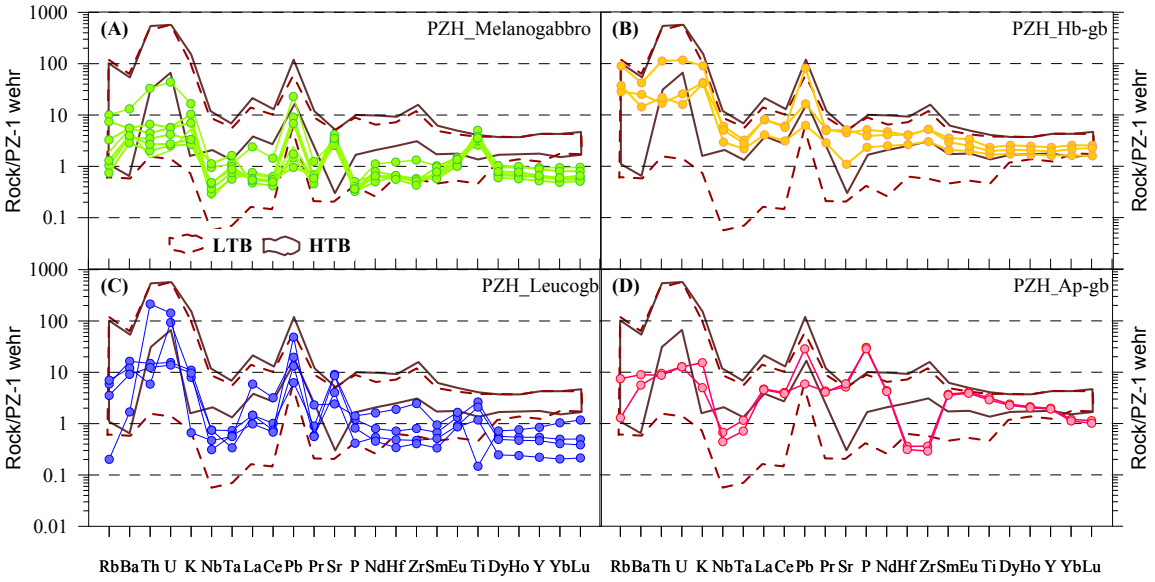

Fig. 4.15 Trace element concentrations of Panzhihua gabbroic rocks normalized to the composition of a wehrlite (PZ-1), Panzhihua Intrusion. From left to right, element compatibility increases.

indicates a low amount of the inter-cumulus liquid trapped between cumulus minerals.

Compared with the incompatible trace elements in the Emeishan continental flood basalts, it is found that, besides the enrichment in Ti and Sr in intrusive oxide-rich rocks and gabbroic rocks, respectively, the basalts contain much higher concentrations of incompatible elements. However, the overall distribution patterns in the gabbroic rocks are similar to that of the Emeishan high-Ti basalts, especially for the fine-grained hornblende gabbro occurring in the MGZ in Panzhihua, indicating genetic relationship between the Panzhihua and Taihe layered intrusions and Emeishan high-Ti basalts.

In summary, the Panzhihua and Taihe intrusions both show overall enrichments in Fe and Ti. The gabbroic rocks show similar tholeiitic differentiation trend to that of the Emeishan basalts. The whole rock compositions in both the Panzhihua and Taihe gabbroic layered intrusion are closely related to mineral modal proportions, indicating cumulus nature of the intrusive rocks. The whole rock major element compositions may be explained as a mixture of two poles of mineral assemblages: one silicate pole consisting mainly of plagioclase and clinopyroxene, and the other oxide pole consisting mainly of magnetite and to a lesser extent ilmenite. Mixing of the two mineral poles in various proportions can explain the major element composition of the intrusive rocks.

The concentrations of trace elements reflect mineral accumulation, and can also be explained by the two-pole accumulation hypothesis. For example, the concentrations of compatible elements (Cr, Ni, V, etc) are controlled mainly by the magnetite modal proportions, whereas the concentrations of incompatible trace elements (LILE, REE, HFSE) are controlled by the silicate mineral assemblages and the amount of trapped liquids. REE fractionations reflect the relative abundance of cumulus minerals and locally enrichment of trapped liquids. The low amount of trapped liquid is inferred by overall low contents of strongly incompatible elements, such as Zr, K and others. Migration of trapped liquids during crystallization may have complicated element distribution. Neverthless, in some cases, the effects of trapped liquid on incompatible elements distribution, as well as mineral compsoitions, may not be ignored.

4.2 Mineral Chemistry

This part describes (1) the major element composition of Panzhihua olivine, plagioclase and clinopyroxene; (2) major and trace elements in magnetite and ilmenite from both the Panzhihua and Taihe intrusions; and (3) major and trace elements in pyrrhotite from both

intrusions. Mineral major element compositions were analyzed by EMPA at the Central Science Laboratory, and trace element compositions were analyzed by LA-ICP-MS at CODES, both at the University of Tasmania. Sample preparation and analysis procedures are presented in the Appendix XI.

4.2.1 Silicate Minerals

Silicate minerals, including olivine, clinopyroxene, and plagioclase, are analyzed for major elements using electron microprobe analysis (EMPA). The results and calculated stoichiometry are presented in Table 4.4 to Table 4.8.

4.2.1.1 Olivine

The Panzhihua olivine show a large compositional range (Fo85 to 63) between various types of host rocks (Table 4.4 and Fig. 4.16). This range corresponds well with previous published data on the lower ~ 700m of stratigraphy in Panzhihua (Fo82 to 63) (Pang *et al.*, 2009), and overlaps with the olivine compositions in the lower zone of the Baima gabbroic layered intrusion (Fo75 to 65) and the Xinjie ultramafic rocks of the ELIP (Fo74 to 70) (Wang *et al.*, 2008; Zhang *et al.*, 2012).

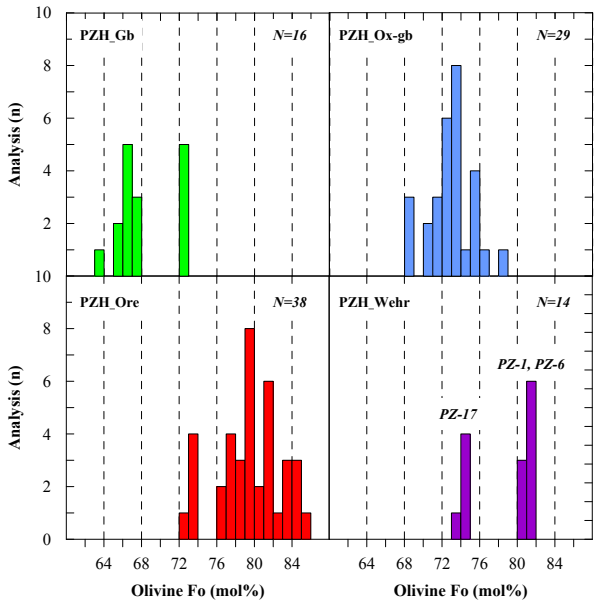

Fig. 4.16 Histograms of Ol compositions in different rock types.

Within an individual sample, olivine Fo may vary by 1-3 Fo units in oxide-poor rocks, and up to 5 Fo units in oxide-rich rocks. Olivine in gabbroic rocks has Fo number varying from 63 to 73, with most below 68 (Fig. 4.16). In contrast, Panzhihua ore rocks contain the most Mg-rich olivine (Fo85), and 33 in 38 analyses contain Fo greater than 76. Olivine in oxide-rich gabbro show moderately evolved olivine with Fo number between 68 to 78. Olivine in wehrlite display bimodal Fo number that associated with stratigraphic levels. An evolved population of olivine (averaged at Fo74.3) occurs in the Middle Zone A (MZa) wehrlite, whereas a relatively undifferentiated population (averaging Fo=81.3) occurs in the Marginal Zone (MGZ) wehrlite. This is consistent with the upper level wherlite being formed by a more

Table 4.4 Representative EMPA analyses of the olivine from the Lanshan and Zhujiabaobao open-pit mines of the Panzhihua Intrusion.

Sample	PZ-1	PZ-3	PZ-6	PZ-7	PZ-11	PZ-12	PZ-13	PZ-15	PZ-17	PZ-18	PZ-20
Rock	Wehr	Gb	Wehr	Hb-gb	Ore	Ore	Ore	Ore	Wehr	Ore	Ox-gb
n.	4	3	5	5	4	6	3	5	5	2	4
SiO_2	38.92	37.08	39.23	37.61	39.23	39.05	40.24	38.89	37.36	39.21	38.10
FeO	18.03	29.24	17.29	25.12	18.23	17.43	14.83	19.12	23.50	15.56	22.87
MnO	0.30	0.58	0.38	0.47	0.34	0.29	0.24	0.34	0.39	0.26	0.41
MgO	42.70	33.39	43.28	37.28	42.38	43.70	45.53	42.00	37.83	44.60	38.58
CaO	0.05	0.07	0.23	0.05	0.08	0.12	0.09	0.13	0.07	0.11	0.10
NiO	0.31	<0.04	0.16	0.26	<0.04	<0.04	<0.04	<0.04	0.19	<0.04	<0.04
Total	100.2	100.3	100.5	100.7	100.2	100.5	100.9	100.4	99.31	99.75	100.0
Number of ions on the basis of 4 O											
Si	0.991	0.996	0.992	0.987	0.998	0.987	0.999	0.992	0.988	0.991	0.994
Fe^{2+}	0.346	0.638	0.334	0.495	0.379	0.317	0.305	0.375	0.467	0.292	0.474
Fe^{3+}	0.025	0.012	0.021	0.035	0.006	0.034	0.002	0.022	0.033	0.024	0.016
Mn	0.006	0.013	0.008	0.011	0.007	0.006	0.005	0.007	0.009	0.006	0.009
Mg	1.621	1.337	1.632	1.458	1.607	1.647	1.686	1.597	1.491	1.681	1.501
Ca	0.001	0.002	0.006	0.001	0.002	0.003	0.002	0.004	0.002	0.003	0.003
Ni	0.006	0.000	0.003	0.006	0.000	0.000	0.000	0.000	0.004	0.000	0.000
Sum	2.996	2.997	2.997	2.993	2.999	2.995	3.000	2.997	2.993	2.997	2.997
Atomic percentages of End-members											
Fo	82.1	67.3	82.7	74.2	80.6	83.6	84.5	80.7	75.8	84.9	75.6
Fa	17.5	32.1	16.9	25.2	19.0	16.1	15.3	18.9	23.7	14.8	23.9
Te	0.3	0.7	0.4	0.5	0.4	0.3	0.3	0.4	0.4	0.3	0.5

n-number of analyses; $Fo=100Mg^{2+}/M^{2+}$; $Fa=100Fe^{2+}/M^{2+}$; $Te=100Mn^{2+}/M^{2+}$, $M^{2+}=Mg^{2+}+Fe^{2+}+Mn^{2+}$.

fractionated magma.

The increase of Fo in olivine with increasing magnetite modal proportion in that host rock is evident on Fig. 4.17, where olivine in ore rocks may originate from subsolidus re-equilibrium between olivine and magnetite ($Mg_{Mgt} + Fe_{Ol} = Mg_{Ol} + Fe_{Mgt}$), whereas olivine in the oxide-poor wehrlite and some gabbroic rocks may follow fractional crystallization trend and reflect original magmatic compositions, or probably somewhere between fractional and equilibrium if crystallization from trapped liquid. Assuming that 1) the most Mg-rich olivine (Fo85) in the massive ore rock is a result of re-equilibration of olivine (Fo74) in the MZa wehrlite, and 2) the re-equilibration rate remains constant, it may be inferred graphically that the massive ore and oxide-rich gabbro formed during magma fractionation interval that precipitated olivine Fo74 to 67 (Fig. 4.17). Magnetite fractionation continues, but decreases rapidly, until crystallization of olivine Fo64, when apatite occurs on the liquidus, and formation of the Fe-Ti oxide poor but apatite rich gabbro (MZb) in Panzhihua intrusion occurs.

Table 4.4 Representative EMPA analyses of the olivine from the Lanshan and Zhujiabaobao open-pit mines of the Panzhihua gabbroic layered intrusion (continued).

Sample	PZ-21	PZ-22	PZ-26	PZ-30	PZ-31	PZ-37	PZ-38	PZ-40	PZ-42	PZ-44
Rock	Ox-gb	Ox-gb	Ox-gb	Ore	Ore	Ore	Ox-gb	Gb	Ox-gb	Ap-gb
n.	4	5	8	5	7	5	5	6	3	3
SiO_2	38.12	38.20	37.85	38.58	37.93	38.27	37.94	37.09	37.26	36.55
FeO	24.05	23.93	24.33	18.95	21.06	24.21	24.91	29.3	28.41	31.61
MnO	0.43	0.43	0.53	0.32	0.35	0.48	0.48	0.65	0.59	0.7
MgO	38.07	37.98	37.07	42.11	40.16	37.24	36.67	32.65	34.27	31.79
CaO	0.06	0.05	0.07	0.12	0.11	0.1	0.08	0.08	0.05	0.05
NiO	<0.04	<0.04	0.09	<0.04	<0.04	<0.04	<0.04	<0.04	<0.04	<0.04
Total	100.7	100.5	99.85	100.1	99.62	100.3	100	99.76	100.5	100.6
Number of ions on the basis of 4 O										
Si	0.993	0.996	0.997	0.988	0.987	1.002	0.999	1.002	0.994	0.991
Fe^{2+}	0.495	0.504	0.521	0.357	0.402	0.53	0.545	0.662	0.609	0.676
Fe^{3+}	0.019	0.012	0.009	0.032	0.036	0	0.002	0	0.016	0.025
Mn	0.009	0.009	0.012	0.007	0.008	0.011	0.011	0.015	0.013	0.016
Mg	1.479	1.476	1.455	1.608	1.558	1.453	1.44	1.316	1.363	1.285
Ca	0.002	0.001	0.002	0.003	0.003	0.003	0.002	0.002	0.001	0.001
Ni	0.000	0.000	0.002	0	0	0	0	0	0	0
Sum	2.996	2.998	2.998	2.995	2.993	2.998	3.000	2.998	2.996	2.994
Atomic percentages of End-members										
Fo	74.6	74.2	73.2	81.6	79.2	72.9	72.1	66	68.7	65
Fa	25.0	25.3	26.2	18.1	20.4	26.6	27.3	33.2	30.7	34.2
Te	0.5	0.5	0.6	0.3	0.4	0.5	0.5	0.8	0.7	0.8

According to models of olivine-liquid equilibrium (e.g. Roeder & Emslie, 1970), the calculated Mg# of liquid that in equilibrium with Fo74, Fo67 and Fo64 are 0.46, 0.38 and 0.35, respectively (Kd=0.3). The liquid with Mg# of 0.46 is similar to average Panzhihua gabbro composition reported previously (Zhou *et al.*, 2005). The parental magma crystallized the MGZ to MZa of Panzhihua gabbroic intrusion has Mg# between 0.46 to 0.35. However, the liquid in equilibrium with the most MgO-rich olivine in the MGZ wehrlite (PZ-6, Fo82) has a Mg# of 0.58. This high value indicates olivine in this wehrlite crystallized from a much more primitive magma.

Except for a few samples that contain olivine with NiO between 0.14 to 0.32 wt%, most of Panzhihua olivine crystals are Ni-depleted (Fig. 4.18), indicating crystallization from a Ni-poor magma or Ni-Mn exchange between olivine and magnetite ($Ni_{Ol}+Mn_{Mgt}=Ni_{Mgt}+Mn_{Ol}$). However, the overall depletion of Ni in both olivine and magnetite suggests a Ni-depleted parental magma origin. The MnO content of olivine varies from 0.25 to 0.75 wt%, and display an excellent negative correlation with Fo (R^2=0.93) (Fig. 4.18). It is surprising that our MnO

data are systematically higher than those published previously (Pang *et al.*, 2009; Zhang *et al.*, 2011).The discrepancy in MnO content may be related to differences in analytical conditions and background calculation methods in different laboratories.

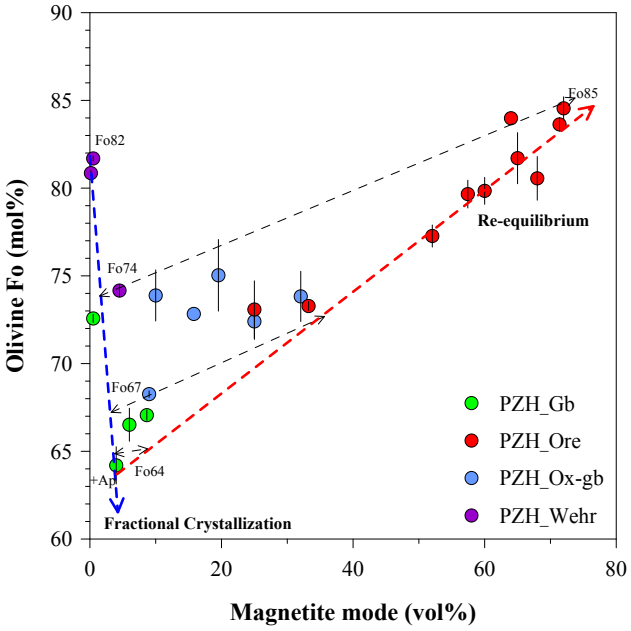

Fig. 4.17 Ol compositions as a function of Mgt modal proportions, showing normal fractional crystallization and re-equilibration trends.

Panzhihua olivine contain small amount of CaO (0.03 to 0.16 wt%), with most of them below 0.1 wt%, comparable to olivines in ultramafic rocks from the Xinjie layered intrusion (Wang *et al.*, 2008), but much lower than olivines in Emeishan picrite (CaO: 0.25 to 0.45 wt%) (Hanski *et al.*, 2010; Zhang *et al.*, 2006). However, limited data on olivine in Emeishan basalts range from 0.09 to 0.17 wt% CaO content (Wang *et al.*, 2011), within the compositional range of the Panzhihua ore. The most CaO-rich olivine occurs at the contact wehrlite (PZ-6), which may be related to fast crystallization rates due to a likely large temperature gradient over the MGZ.

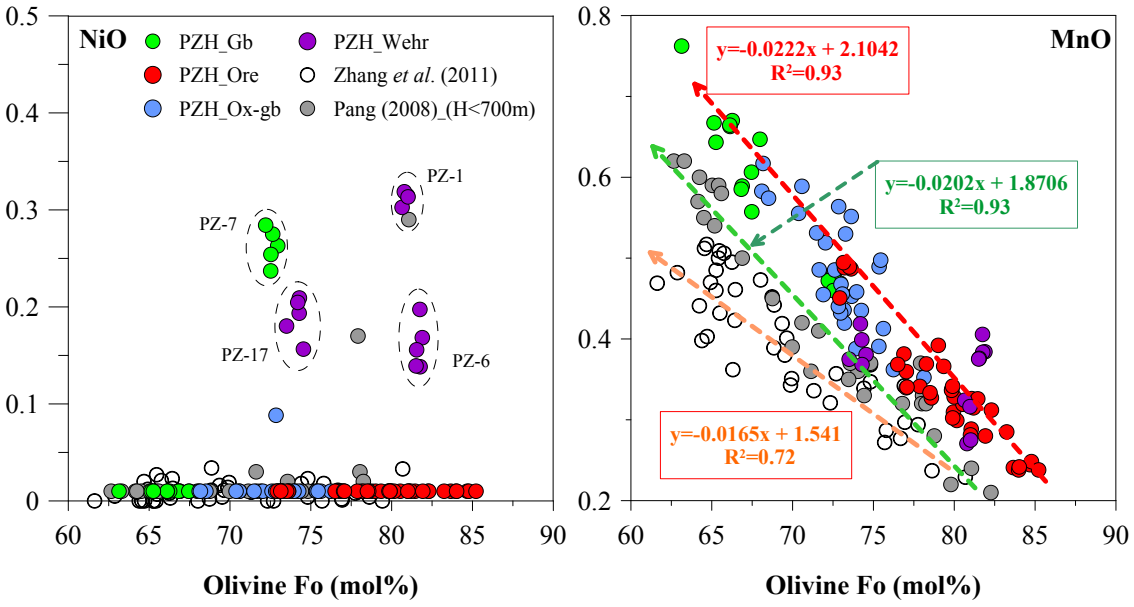

Fig. 4.18 Ol NiO and MnO contents as a function of Fo.

4.2.1.2 Clinopyroxene

Ca-rich clinopyroxene is the most important rock-forming ferromagnesian silicate mineral in the Panzhihua gabbroic layered intrusion, whereas only a few Ca-poor orthopyroxene grains occur as small subhedral grains in the wehrlite (PZ-1) at the contact with footwall rocks. The closure temperature for clinopyroxene in various rocks ranges approximately from 500 to 1120˚C based on the projection of clinopyroxene composition onto the pyroxene quadrilateral (Fig. 4.19) (Lindsley, 1983). Using a two-pyroxene thermometer (Putirka, 2008), the calculated temperature for coexisting clinopyroxene and orthopyroxene in a wehrlite (PZ-1) varies between 959 to 977˚C, under pressure ranging between 1 to 5 kbar. However, the equilibrium constant (Kd) for Fe-Mg exchange between two pyroxenes is too low for equilibrium (Kd=0.86), which means dis-equilibrium between clinopyroxene and orthopyroxene.

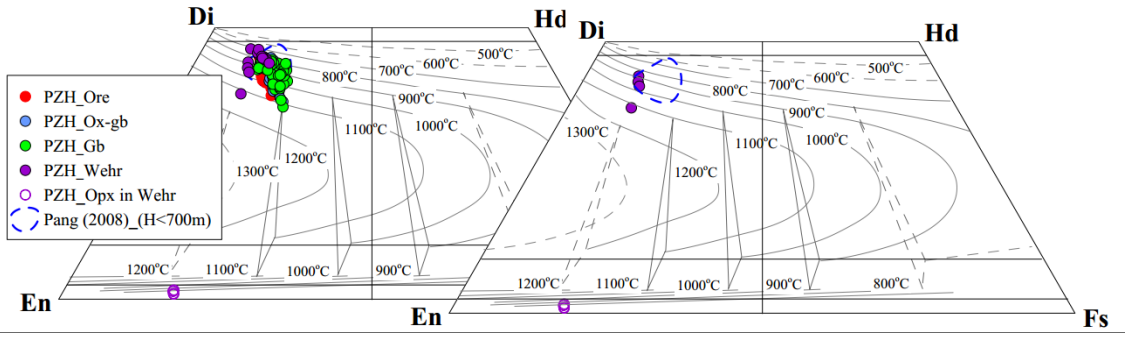

Fig. 4.19 Composition ranges of Panzhihua Cpx and Opx projecting in the diopside (Di)-hedenbergite (Hd)-enstatite (En)-ferrosilite (Fs) quandrilateral. The isotherms for 1 atm are from Lindsley (1983).

The Mg# of clinopyroxene in various Panzhihua rocks vary from 72 to 85 (Table 4.5, Fig. 4.20). Except for wehrlite that contains olivine with Fo mostly greater than 80 (clinopyroxe average is Mg#83.7 and Mg#80.6 for MGZ and MZa wehrlite, respectively), gabbro and ore rocks in the Panzhihua intrusion have olivine with Fo generally well below Fo80. The average Mg# of clinopyroxene increases slightly from 76 in gabbroic rocks to 77 in oxide ore rocks. The large overlaps and relatively small variation of clinopyroxene Mg# in all samples indicate that the rock-type control on clinopyroxene composition is limited.

Figure 4.21 shows the relationship between Mg# of clinopyroxene and the magnetite modal proportion in host rocks. Two contrasting trends are observed: a slight increase of Mg# with increasing magnetite mode for the oxide-rich rocks, and a sharp decrease for oxide-poor gabbro and wehrlite. The first trend may be a result of Fe-Mg exchange between clinopyroxene

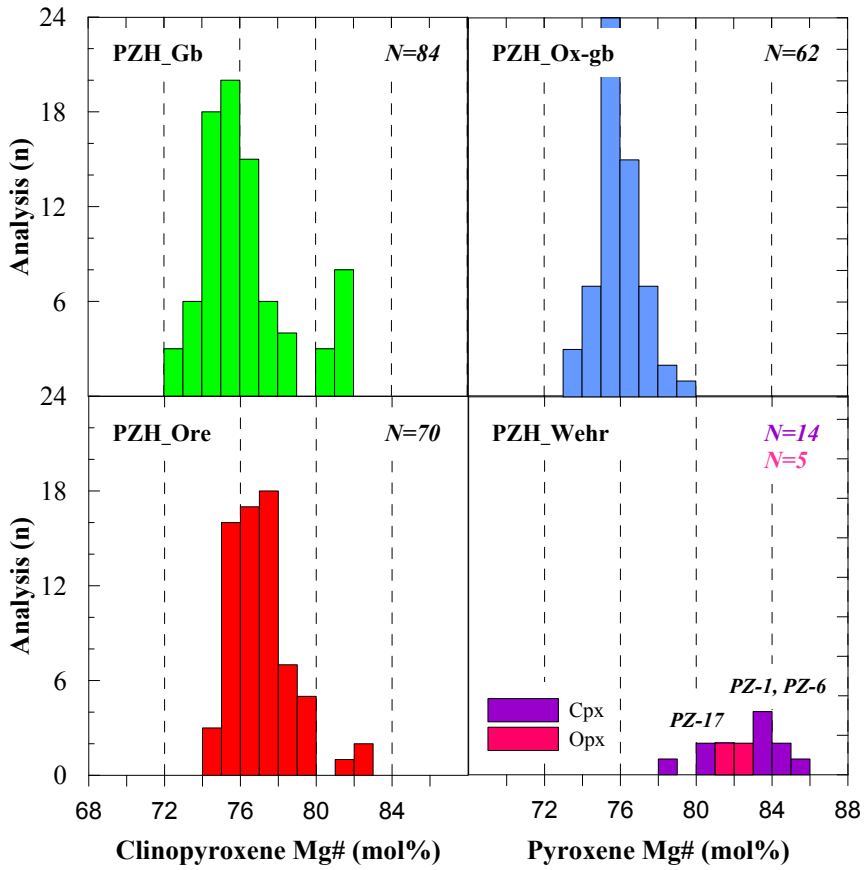

Fig. 4.20 Histograms of Cpx Mg# in various rock types from the Panzhihua Intrusion.

and surrounding oxide minerals. However, the modification of Mg# of clinopyroxene during this re-equilibrium process is not as prominent as that of olivine Fo content (Fig. 4.16). The oxide-rich gabbro and ore have clinopyroxene with Mg# between 77 and 75, which means massive magnetite accumulated during magma fractionating clinopyroxene with this composition. It may be inferred that the composition of magma from which clinopyroxene crystallized was constant during the formation of magnetite ore formation. The oxide-poor wehrlite and gabbro follow a fractional crystallization trend, with Mg# of clinopyroxene decreasing with increasing amount of magnetite. Clinopyroxene in these rocks may have been little affected by the re-equilibration with Fe-Ti oxides due to their low abundance in these rocks. In addition, this high Mg# nature of clinopyroxene couldn't be completely explained by trapped liquid effects (Barnes, 1986), as whole rock geochemistry indicates that the trapped liquid fraction is too small to account for the large variation in clinopyroxene (ΔMg#>10). However, it may not be ruled out that compaction and expulsion of the intercumulus melt occurred after compositional modification on clinopyroxene.

Clinopyroxene in wehrlite rocks have Cr_2O_3 contents ranging from 0.1 to 0.35 wt%, whereas it is near or below detection limit (0.03 wt%) in clinopyroxene in other rocks (Table

4.5). Most Panzhihua clinopyroxene contain 20 to 23 wt% CaO, 2 to 5 wt% Al_2O_3, 0.5 to 2 wt% TiO_2, and 0.15 to 0.35 wt% MnO. Compared with that in other rocks, clinopyroxene in the wehrlite from the MGZ (PZ-1) and LZ (PZ-6) have distinct higher Mg# (Fig. 4.22). Clinopyroxene in the LZ wehrlite (PZ-6) are characterized by much higher CaO, TiO_2, Al_2O_3, but lower MnO content than that in other rocks (Fig. 4.22). CaO enrichment is also observed in olivine in this wehrlite (Table 4.4). Hence, it supports the suggestion that rapid crystallization operated at the contact of the Panzhihua intrusion. Clinopyroxene in some hornblende-rich gabbros have lower TiO_2, Al_2O_3 but higher MnO than the other rocks. These rocks may have been modified by a late-stage fluid, as indicated by abundant hornblende and strong folication.

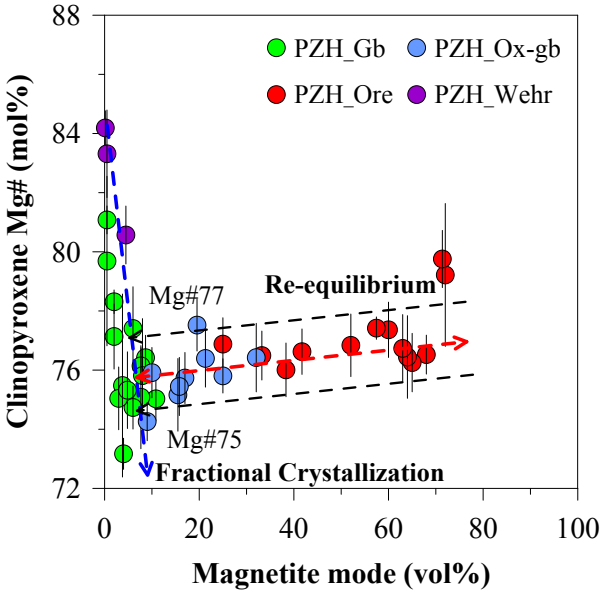

Fig. 4.21 Mg# number of Cpx as a function of Mgt mineral proportion, showing fractional crystallization and re-equilibration trends. Massive Mgt crystallization occurs during crystallization of Cpx of Mg#77 to Mg#75.

The equilibrium temperature may be calculated using olivine-clinopyroxene thermometers (e.g. Loucks, 1996). Since olivines have undergone extensive re-equilibration with magnetite in Fe-Ti oxide rich rocks, only oxide-poor rocks with coexisting olivine and clinopyroxene are used in the calculation. To expand the sample population, it includes olivine and clinopyroxene data from Jianshan section (Pang, 2008), to investigate the temperature change across the more complete stratigraphic profile. Clinopyroxene-olivine pairs with Kd outside the calibrated range (Kd=1.19 to 1.80; (Loucks, 1996) are excluded from calculations. The results show 1165˚C for the MGZ wehrlite (PZ-1) and 1134˚C (PZ-17) for the MZa wehrlite. The calculated temperature intervals for LZ and MZa are 1126 to 1176˚C, compared with 1121 to 1171˚C which are calculated based on data from Pang *et al.* (2008a). The calculated temperature for gabbros below and above massive ores are 1142 and 1121˚C, respectively. This small temperature interval (~21˚C) is occurrings in a stratigraphy distance of approximately 250 m, implies that massive oxide ores were formed at a very short temperature interval.

Table 4.5 Representative EMPA analyses of the Cpx from the Lanshan and Zhujiabaobao open-pit mines of the Panzhihua Intrusion.

Sample	PZ-1	PZ-2	PZ-3	PZ-5	PZ-6	PZ-7	PZ-8	PZ-9	PZ-10	PZ-11
Rock	Wehr	Gb	Gb	Hb-gb	Wehr	Hb-gb	Hb-Gb	Gb	Ox-gb	Ore
n	4	12	11	5	5	4	6	6	5	5
SiO_2	51.17	50.93	51.31	51.89	46.2	52.19	53.02	49.99	50.19	50.01
TiO_2	0.97	0.84	0.84	0.51	2.69	0.39	0.24	1.2	1.18	1.59
Al_2O_3	3.08	2.8	2.71	2.03	8.07	1.68	1.08	3.58	3.28	4.1
FeO	5.49	8.55	8.22	8.59	4.69	7.15	6.58	8.08	8.03	7.91
MnO	0.19	0.34	0.3	0.37	0.07	0.27	0.4	0.27	0.28	0.25
MgO	16.37	14.41	14.95	14.83	13.17	15.7	15.82	14.47	14.58	14.46
CaO	21.77	21.54	21.45	21.45	24.71	21.84	22.02	21.47	21.55	20.95
Na_2O	0.33	0.37	0.4	0.38	0.3	0.4	0.57	0.45	0.48	0.56
Total	99.35	99.78	100.17	100.04	99.9	99.63	99.73	99.5	99.57	99.82
Mg#	84.18	75.03	76.41	75.48	83.34	79.65	81.08	76.15	76.39	76.52
Number of ions on the basis of 6 O										
Si	1.895	1.905	1.907	1.933	1.721	1.941	1.965	1.873	1.88	1.863
Ti	0.027	0.024	0.023	0.014	0.075	0.011	0.007	0.034	0.033	0.045
Al(IV)	0.105	0.095	0.093	0.067	0.279	0.059	0.035	0.127	0.12	0.137
Al(VI)	0.029	0.028	0.025	0.022	0.075	0.014	0.012	0.031	0.025	0.044
Fe^{2+}	0.102	0.198	0.181	0.202	0.033	0.144	0.128	0.162	0.156	0.18
Fe^{3+}	0.068	0.069	0.074	0.066	0.113	0.078	0.076	0.091	0.096	0.066
Mn	0.006	0.011	0.009	0.012	0.002	0.009	0.013	0.008	0.009	0.008
Mg	0.904	0.803	0.828	0.823	0.731	0.871	0.874	0.808	0.814	0.803
Ca	0.864	0.863	0.854	0.856	0.986	0.87	0.874	0.862	0.865	0.836
Na	0.023	0.027	0.029	0.027	0.022	0.029	0.041	0.033	0.035	0.04
Sum	4.023	4.023	4.025	4.022	4.038	4.026	4.025	4.03	4.032	4.022
Atomic percentages of End-members										
En	46.51	41.32	42.53	42.04	39.19	44.15	44.48	41.84	41.97	42.42
Fs	9.04	14.29	13.61	14.25	7.96	11.72	11.03	13.54	13.44	13.42
Wo	44.45	44.39	43.86	43.71	52.85	44.13	44.49	44.62	44.59	44.16

En=100*Mg^{2+}/M^{2+}, Fs=100*Mn^{2+}/M^{2+}, Wo=100*Ca^{2+}/M2+. $M^{2+}=Mg^{2+}+Mn^{2+}+Fe^{2+}+Fe^{3+}+Ca^{2+}$

Table 4.5 Representative EMPA analyses of the clinopyroxene from the Lanshan and Zhujiabaobao open-pit mines of the Panzhihua gabbroic layered intrusion (continued).

Sample	PZ-12	PZ-13	PZ-14	PZ-15	PZ-16	PZ-17	PZ-18	PZ-19	PZ-20	PZ-21
Rock	Ore	Ore	Ore	Ore	Leuco	Wehr	Ore	Gb	Ox-gb	Ox-gb
n	6	8	4	4	4	5	4	5	5	5
SiO_2	49.59	50.05	49.34	49.23	50.39	49.57	49.18	50.23	49.78	50.2
TiO_2	1.52	1.6	1.58	1.75	1.22	1.33	1.75	1.37	1.62	1.47
Al_2O_3	3.91	4.29	4.27	4.35	3.24	3.86	4.54	3.53	3.91	3.69
FeO	8.09	6.8	7.94	7.52	7.07	6.38	6.56	7.66	7.61	7.99
MnO	0.23	0.19	0.24	0.24	0.29	0.16	0.21	0.26	0.25	0.26
MgO	14.54	14.48	14.45	14.47	14.33	14.83	14.48	14.72	14.72	14.53
CaO	21.43	22.14	21.45	21.59	22.25	22.73	22.11	21.77	21.47	21.16
Na_2O	0.52	0.54	0.49	0.74	0.81	0.51	0.71	0.47	0.55	0.52
Total	99.83	100.1	99.76	99.88	99.6	99.38	99.53	100.01	99.91	99.83
Mg#	76.23	79.14	76.45	77.42	78.31	80.56	79.74	77.4	77.51	76.42
Number of ions on the basis of 6 O										
Si	1.854	1.856	1.845	1.838	1.884	1.854	1.837	1.87	1.855	1.872
Ti	0.043	0.045	0.044	0.049	0.034	0.037	0.049	0.038	0.045	0.041
Al(IV)	0.146	0.144	0.155	0.162	0.116	0.146	0.163	0.13	0.145	0.128
Al(VI)	0.026	0.043	0.033	0.03	0.027	0.024	0.037	0.025	0.027	0.034
Fe^{2+}	0.144	0.136	0.146	0.104	0.102	0.074	0.086	0.147	0.138	0.177
Fe^{3+}	0.108	0.075	0.102	0.131	0.119	0.126	0.119	0.092	0.099	0.072
Mn	0.007	0.006	0.008	0.008	0.009	0.005	0.007	0.008	0.008	0.008
Mg	0.811	0.801	0.806	0.805	0.799	0.827	0.806	0.817	0.818	0.808
Ca	0.859	0.88	0.859	0.864	0.891	0.911	0.885	0.869	0.857	0.845
Na	0.038	0.039	0.035	0.053	0.059	0.037	0.051	0.034	0.04	0.037
Sum	4.036	4.025	4.034	4.044	4.04	4.042	4.04	4.031	4.033	4.024
Atomic percentages of End-members										
En	42.01	42.2	41.94	42.13	41.6	42.58	42.38	42.28	42.59	42.28
Fs	13.48	11.44	13.32	12.69	11.99	10.54	11.11	12.77	12.77	13.47
Wo	44.51	46.36	44.73	45.18	46.41	46.89	46.5	44.94	44.64	44.24

Table 4.5 Representative EMPA analyses of the clinopyroxene from the Lanshan and Zhujiabaobao open-pit mines of the Panzhihua gabbroic layered intrusion (continued).

Sample	PZ-22	PZ-24	PZ-25	PZ-26	PZ-27	PZ-29	PZ-30	PZ-31	PZ-33	PZ-35
Rock	Ox-gb	Ore	Ox-gb	Ore	Ore	Ox-gb	Ore	Ore	Ore	Ox-gb
n	6	6	9	3	7	4	5	4	6	8
SiO_2	50.31	50.39	51.02	50.8	50.39	49.94	49.14	48.93	49.21	49.81
TiO_2	1.41	1.35	1.03	1.12	1.36	1.12	1.62	1.57	1.62	1.43
Al_2O_3	3.53	3.58	3	3.12	3.23	3.47	4.18	4.15	3.97	3.47
FeO	8.23	7.73	8.51	7.94	8.11	7.67	7.44	7.71	7.75	8.35
MnO	0.27	0.29	0.31	0.26	0.28	0.25	0.2	0.23	0.25	0.3
MgO	14.55	14.21	14.42	14.78	14.4	14.5	14.27	14.35	14.33	14.61
CaO	20.73	21.89	21.4	21.04	21.29	22.01	21.78	21.53	21.48	21.01
Na_2O	0.51	0.54	0.41	0.46	0.49	0.41	0.49	0.53	0.62	0.48
Total	99.54	99.97	100.11	99.52	99.55	99.38	99.13	99.01	99.24	99.47
Mg#	75.91	76.62	75.13	76.85	76	77.12	77.39	76.84	76.72	75.72
Number of ions on the basis of 6 O										
Si	1.881	1.878	1.9	1.897	1.886	1.873	1.847	1.844	1.85	1.869
Ti	0.04	0.038	0.029	0.032	0.038	0.032	0.046	0.045	0.046	0.04
Al(IV)	0.119	0.122	0.1	0.103	0.114	0.127	0.153	0.156	0.15	0.131
Al(VI)	0.036	0.035	0.032	0.034	0.028	0.027	0.033	0.029	0.026	0.023
Fe^{2+}	0.197	0.165	0.205	0.188	0.186	0.141	0.138	0.128	0.129	0.169
Fe^{3+}	0.061	0.076	0.06	0.06	0.068	0.099	0.096	0.115	0.115	0.093
Mn	0.009	0.009	0.01	0.008	0.009	0.008	0.006	0.007	0.008	0.01
Mg	0.811	0.79	0.801	0.823	0.804	0.811	0.8	0.807	0.803	0.817
Ca	0.831	0.874	0.854	0.842	0.854	0.885	0.877	0.87	0.865	0.845
Na	0.037	0.039	0.03	0.034	0.036	0.03	0.036	0.039	0.045	0.035
Sum	4.02	4.025	4.020	4.020	4.023	4.033	4.032	4.038	4.038	4.031
Atomic percentages of End-members										
En	42.52	41.26	41.5	42.85	41.85	41.71	41.72	41.86	41.83	42.27
Fs	13.94	13.06	14.24	13.34	13.68	12.79	12.52	13	13.12	14.05
Wo	43.54	45.68	44.26	43.82	44.46	45.5	45.76	45.14	45.05	43.68

Table 4.5 Representative EMPA analyses of the clinopyroxene from the Lanshan and Zhujiabaobao open-pit mines of the Panzhihua gabbroic layered intrusion (continued).

Sample	PZ-36	PZ-37	PZ-38	PZ-39	PZ-40	PZ-41	PZ-42	PZ-43	PZ-44	PZ-45
Rock	Gb	Ore	Ox-gb	Gb	Gb	Ox-gb	Ox-gb	Gb	Ap-gb	Ap-gb
n	2	6	8	6	8	5	6	8	3	3
SiO_2	50	50.72	50.59	50.63	51.07	50.63	50.57	50.68	51.07	51.41
TiO_2	1.37	1.35	1.44	1.39	1.18	1.39	1.29	1.11	1.09	0.89
Al_2O_3	3.41	3.26	3.31	3.05	2.99	3.37	3.04	3.06	2.61	2.53
FeO	9.05	7.98	8.28	8.91	8.58	8.4	9.08	8.5	9.38	8.38
MnO	0.29	0.28	0.3	0.29	0.32	0.28	0.34	0.31	0.39	0.4
MgO	14.81	14.56	14.55	14.97	14.23	14.48	14.69	14.33	14.35	14.35
CaO	20.58	21.04	21.16	20.47	21.28	21.17	20.29	21.29	20.76	21.6
Na_2O	0.43	0.55	0.5	0.4	0.44	0.51	0.45	0.46	0.42	0.55
Total	99.94	99.75	100.13	100.11	100.1	100.23	99.76	99.56	100.07	100.11
Mg#	74.47	76.48	75.8	74.96	74.73	75.44	74.25	75.04	73.17	75.32
Number of ions on the basis of 6 O										
Si	1.87	1.891	1.883	1.886	1.902	1.883	1.891	1.895	1.908	1.915
Ti	0.039	0.038	0.04	0.039	0.033	0.039	0.036	0.031	0.031	0.025
Al(IV)	0.13	0.109	0.117	0.114	0.098	0.117	0.109	0.105	0.092	0.085
Al(VI)	0.02	0.034	0.028	0.02	0.033	0.031	0.025	0.03	0.023	0.026
Fe^{2+}	0.187	0.191	0.189	0.209	0.222	0.193	0.22	0.198	0.235	0.189
Fe^{3+}	0.096	0.058	0.068	0.069	0.045	0.068	0.065	0.067	0.058	0.072
Mn	0.009	0.009	0.01	0.009	0.01	0.009	0.011	0.01	0.012	0.013
Mg	0.825	0.809	0.807	0.831	0.79	0.803	0.819	0.799	0.799	0.797
Ca	0.825	0.84	0.844	0.817	0.849	0.843	0.813	0.853	0.831	0.862
Na	0.031	0.04	0.036	0.029	0.032	0.037	0.032	0.033	0.03	0.04
Sum	4.032	4.019	4.023	4.023	4.015	4.023	4.022	4.022	4.019	4.024
Atomic percentages of End-members										
En	42.5	42.43	42.08	42.96	41.23	41.89	42.51	41.45	41.29	41.23
Fs	15.05	13.51	13.93	14.82	14.47	14.09	15.3	14.3	15.78	14.17
Wo	42.45	44.06	43.98	42.21	44.3	44.02	42.2	44.25	42.93	44.61

4.2.1.3 Plagioclase

Plagioclase in gabbroic rocks displays a wide range of compositions (An42 to 73), with most (~91%) below An64 (Table 4.6 and Fig. 4.23). In contrast, the plagioclase in oxide-rich rocks shows narrower composition ranges, with An 54-64 for oxide gabbro, and An53 to 77 for ore rocks. The average An content of plagioclase increases slightly from 57.8 in gabbroic rocks, through 58.1 in oxide-rich gabbro, to 64.8 in Panzhihua ore rocks. Similar to olivine and clinopyroxene compositions in wehrlite, the plagioclase in wehrlite have two populations: high-An plagioclase (averaged at An83.3) occurs in the MGZ wehrlite (PZ-1), whereas the low-An plagioclase (averaged at An67.5) occurs in the MZa wehrlite (PZ-17), which is similar to plagioclase in adjacent gabbros.

The Panzhihua plagioclase have comparable An range to that of the Upper Zone of the Bushveld Complex (e.g, An47.0 to 75.5, Cawthorn & Ashwal, 2009; Harney *et al*., 1996), but much higher than that of the Upper Zone of the Skaergaard Layered intrusion (e.g. An32 to 49, Tegner, 1997; Tegner & Cawthorn, 2010). The plagioclase from Skaergaard and Bushveld show opposite trend of plagioclase An against FeO^* content (Tegner & Cawthorn, 2010).

After comparison of the observed cumulate composition with the calculated FeO^* abundance in the residual liquid in equilibrium with plagioclase, it was suggested that the Bushveld liquid follows a Fe-poor and Si-rich fractionation trend following magnetite saturation, whereas the reverse situation occurs in the Skaerggard. The Panzhihua plagioclase exhibits positive An and FeO* correlation, similar to that of Bushveld plagioclase (Fig. 4.24). The first magnetite ore layer occurs in the MGZ of the Panzhihua gabbroic layered intrusion. The average FeO^* content of microgabbro crystallized subsequent to the first ore layer in Lanshan and Jianshan sections, ranges between 13.1 to 15.5 wt% FeO^* (recalculated from Fe_2O_3, this study and Pang (2008). This is almost the same as the average FeO* content of Panzhihua gabbro (15.6 wt%) (Zhou *et al*., 2005). However, it is much lower than the average composition of melonogabbro that forming the LZ and MZa (FeO^*=21.4 wt%) (this study and Pang, 2008). Hence, the Panzhihua liquid may have followed an Fe-depletion trend similar to that of Bushveld liquid, but opposite to the iron-enrichment Fenner trend in the Skaergaard liquid (Tegner & Cawthorn, 2010).

The temperature of residual liquid in equilibrium with the Panzhihua plagioclase are estimated graphically using the experimental results of Toplis and Carroll (1995) (Fig. 4.25). Plagioclase in gabbros below the first and above the last massive ore layers have composition

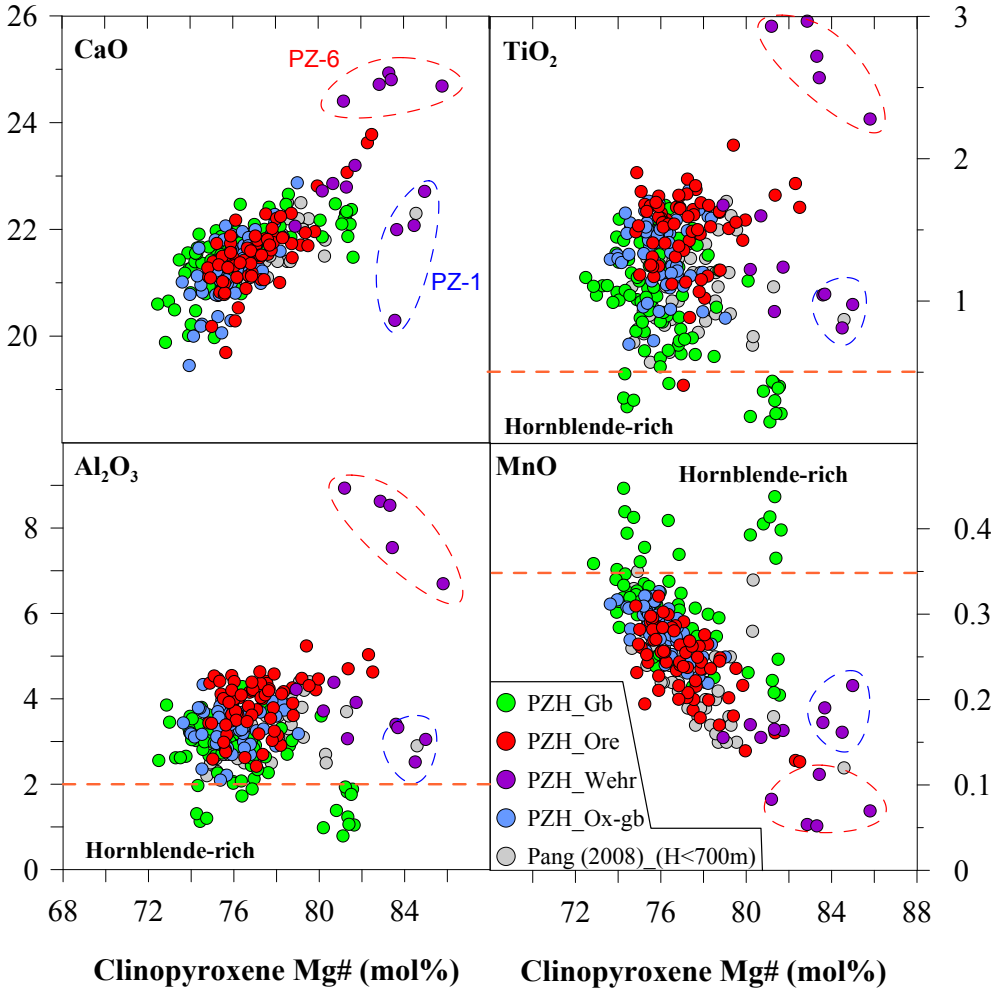

Fig. 4.22 The major and minor element composition of Cpx as a function of Mg#. PZ-1 and PZ-6 are wehrlites from the MGZ and the LZ of the Panzhihua layred intrusion, respectively..

of An62 and An55, corresponding to a temperature of 1106 and 1085°C (FMQ), respectively. This temperature range is approximately 40°C lower than that estimated from the Cpx-Ol thermometer (Loucks, 1996), and slightly narrower than reported by Zhang *et al* (2011) (1079 to 1121°C). However, the small temperature interval (ΔT=21°C) (1104-1085°C) is the same as calculated with Cpx-Ol thermometer (Loucks, 1996).

The temperature at the onset of apatite crystallisation is ~1076°C. At this point Fe-Ti oxides account for less than 10 vol% and continue to decrease rapidly in the subsequent cumulates. High An plagioclase (An72), corresponding to a temperature of 1138°C, are observed in one ore rock (PZ-31) in MZa and olivine-clinopyroxenite in UZ (Pang, 2008).This high-An plagioclase could result from early crystallization and flotation due to lower density than the surrounding residual liquid. Plagioclase buoyancy has been widely accepted for genesis of anorthosite on both the Earth and Moon (Namur *et al.*, 2011; Wood *et al.*, 1970;

Table 4.6 Representative EMPA analyses of Plag from the Lanshan section of Panzhihua Intrusion.

Sample	PZ-1	PZ-2	PZ-3	PZ-5	PZ-9	PZ-10	PZ-11	PZ-14	PZ-16	PZ-17
Rock	Wehr	Gb	Gb	Hb-gb	Gb	Ox-gb	Ore	Ore	Leuco	Wehr
n	4	4	6	3	6	4	3	8	3	5
SiO_2	46.7	53.59	53.28	52.47	52.44	53.34	52.88	50.44	51.22	50.27
TiO_2	0.03	0.06	0.04	0.03	0.05	0.08	0.09	0.08	0.15	0.05
Al_2O_3	33.9	29.18	29.46	30.16	30.41	29.6	30.26	31.51	31.19	31.4
FeO	0.4	0.26	0.25	0.36	0.25	0.23	0.21	0.26	0.46	0.22
MgO	0.03	0.03	0.03	0.03	0.03	0.03	0.03	0.03	0.02	0.02
CaO	17.05	11.72	12.03	12.37	12.47	11.58	12.45	13.87	13.09	13.86
Na_2O	1.88	4.72	4.63	4.38	4.43	4.86	4.43	3.61	3.95	3.69
K_2O	0.04	0.17	0.17	0.26	0.19	0.22	0.06	0.06	0.24	0.15
Total	100.01	99.73	99.89	100.02	100.27	99.91	100.41	99.85	100.3	99.64
Number of ions on the basis of 32 O										
Si	8.594	9.724	9.663	9.524	9.493	9.664	9.545	9.204	9.301	9.2
Ti	0.005	0.008	0.005	0.004	0.007	0.011	0.012	0.01	0.02	0.006
Al	7.353	6.24	6.296	6.451	6.489	6.32	6.437	6.777	6.676	6.772
Fe^{2+}	0	0.044	0	0	0	0	0.005	0	0	0
Fe^{3+}	0.211	0	0.055	0.152	0.177	0.141	0.026	0.133	0.202	0.255
Mg	0.007	0.007	0.008	0.007	0.009	0.007	0.008	0.009	0.005	0.006
Ca	3.363	2.279	2.338	2.405	2.42	2.248	2.408	2.711	2.548	2.717
Na	0.672	1.661	1.628	1.541	1.557	1.708	1.552	1.276	1.389	1.31
K	0.01	0.04	0.04	0.061	0.043	0.05	0.015	0.014	0.055	0.034
Sum	20.215	20.003	20.034	20.146	20.195	20.15	20.008	20.135	20.195	20.301
Atomic percentages of End-members										
An	83	57	58	60	60	56	61	68	64	67
Ab	16.6	41.7	40.6	38.5	38.7	42.6	39	31.9	34.8	32.2
Or	0.3	1	1	1.5	1.1	1.2	0.4	0.3	1.4	0.8

An=100*Ca/(Ca+Na+K); Ab=100*Na/(Ca+Na+K); Or=100*K/(Ca+Na+K).

Table 4.6 Representative EMPA analyses of plagioclase from the Lanshan section of Panzhihua gabbroic layered intrusion (continued)

Sample	PZ-19	PZ-21	PZ-22	PZ-24	PZ-25	PZ-26	PZ-28	PZ-31	PZ-32	PZ-36
Rock	Gb	Ox-gb	Ox-gb	Ore	Ox-gb	Ore	Leuco	Ore	Gb	Gb
n	5	6	5	4	7	6	6	8	4	11
SiO_2	50.78	51.72	53.34	52.73	53.51	52.11	53.02	49.47	53.33	52.86
TiO_2	0.07	0.04	0.05	0.09	0.04	0.09	0.08	0.07	0.07	0.08
Al_2O_3	31.71	30.73	29.59	30.01	29.61	30.51	29.64	32.17	30.17	29.62
FeO	0.38	0.35	0.25	0.24	0.22	0.33	0.25	0.3	0.25	0.25
MgO	0.04	0.04	0.03	0.04	0.03	0.04	0.03	0.04	0.05	0.03
CaO	14.02	13.05	11.64	12.4	11.96	12.85	11.6	14.92	12.4	11.78
Na_2O	3.5	3.99	4.69	4.6	4.75	4.19	4.73	3.21	4.46	4.72
K_2O	0.19	0.1	0.18	0.05	0.14	0.17	0.22	0.07	0.17	0.23
Total	100.67	100.04	99.77	100.15	100.25	100.28	99.58	100.24	100.88	99.57
Number of ions on the basis of 32 O										
Si	9.2	9.398	9.673	9.549	9.665	9.445	9.642	9.027	9.582	9.621
Ti	0.009	0.006	0.007	0.012	0.006	0.012	0.011	0.01	0.009	0.01
Al	6.771	6.581	6.324	6.406	6.303	6.517	6.353	6.919	6.389	6.355
Fe^{2+}	0	0	0.027	0	0	0	0	0	0	0
Fe^{3+}	0.137	0.065	0.011	0.155	0.078	0.132	0.099	0.253	0.037	0.165
Mg	0.011	0.011	0.009	0.012	0.007	0.01	0.007	0.01	0.012	0.007
Ca	2.721	2.542	2.262	2.406	2.315	2.496	2.26	2.918	2.386	2.297
Na	1.23	1.406	1.649	1.615	1.662	1.474	1.668	1.134	1.555	1.667
K	0.044	0.023	0.041	0.011	0.032	0.038	0.052	0.016	0.04	0.054
Sum	20.122	20.032	20.004	20.166	20.069	20.124	20.091	20.285	20.011	20.177
Atomic percentages of End-members										
An	68	64	57	60	58	62	57	72	60	57
Ab	30.8	35.4	41.7	40.1	41.5	36.8	41.9	27.9	39.1	41.5
Or	1.1	0.6	1	0.3	0.8	1	1.3	0.4	1	1.4

Table 4.6 Representative EMPA analyses of plagioclase from the Lanshan section of Panzhihua gabbroic layered intrusion (continued)

Sample	PZ-38	PZ-39	PZ-40	PZ-41	PZ-42	PZ-43	PZ-44	PZ-45
Rock	Ox-gb	Gb	Gb	Ox-gb	Ox-gb	Gb	Ap-gb	Ap-gb
n	9	6	5	5	6	5	7	7
SiO_2	53.42	53.17	54.55	53.97	54	54.2	55.25	55.71
TiO_2	0.09	0.09	0.06	0.07	0.08	0.06	0.06	0.08
Al_2O_3	30.11	30.16	29.4	29.58	29.58	29.45	28.64	28.42
FeO	0.25	0.25	0.23	0.2	0.36	0.27	0.27	0.21
MgO	0.03	0.04	0.03	0.03	0.04	0.03	0.02	0.02
CaO	12.07	12.12	11.26	11.58	11.3	11.11	10.52	9.92
Na_2O	4.57	4.5	4.94	4.79	4.96	5.02	5.44	5.78
K_2O	0.21	0.18	0.22	0.15	0.19	0.22	0.25	0.15
Total	100.75	100.48	100.68	100.37	100.51	100.35	100.45	100.28
Number of ions on the basis of 32 O								
Si	9.605	9.585	9.785	9.719	9.719	9.758	9.921	9.997
Ti	0.012	0.012	0.008	0.01	0.01	0.009	0.008	0.011
Al	6.382	6.407	6.216	6.277	6.275	6.25	6.063	6.011
Fe^{2+}	0	0.015	0.086	0.07	0	0.009	0	0
Fe^{3+}	0.042	0.023	0	0	0.066	0.031	0.048	0.031
Mg	0.008	0.01	0.007	0.008	0.01	0.009	0.007	0.005
Ca	2.326	2.341	2.164	2.234	2.179	2.142	2.025	1.908
Na	1.595	1.573	1.718	1.674	1.73	1.751	1.894	2.012
K	0.049	0.041	0.05	0.035	0.044	0.051	0.057	0.035
Sum	20.019	20.007	20.035	20.027	20.033	20.01	20.023	20.01
Atomic percentages of End-members								
An	59	59	55	57	55	54	51	48
Ab	40.2	39.8	43.7	42.4	43.8	44.4	47.6	50.9
Or	1.2	1	1.3	0.9	1.1	1.3	1.4	0.9

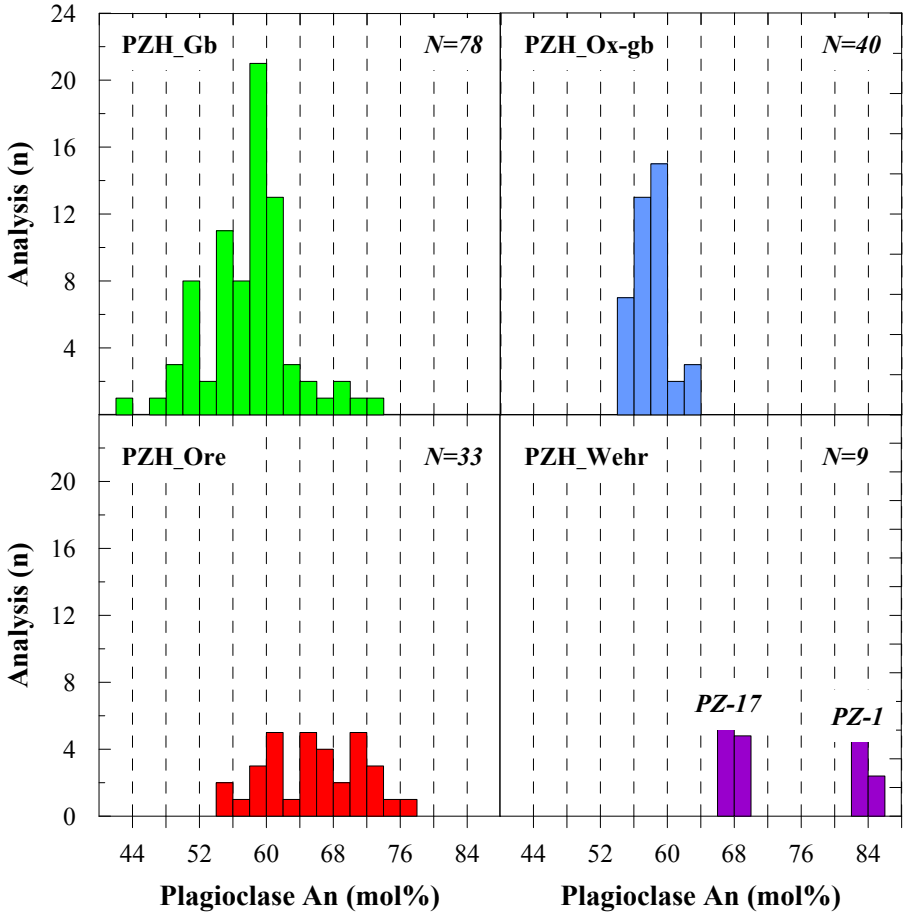

Fig. 4.23 Histograms showing distribution of An content of Plag in various types of Panzhihua Intrusion. Note two populations of Plag in wehrlite, similar to that of Ol.

Warren, 1990; Ohtake *et al.*, 2009; Duchesne *et al.*, 1999; Charlier *et al.*, 2010). It can also reflect higher activety of H_2O at the time of plagioclase crystallization (Botcharnikov *et al.*, 2008, Feig *et al.*, 2010). Magnetite fractionation may have started at a temperature below 1138˚C, and probably the main Fe-Ti oxide precipitation occurred above 1085˚C.

The relative effects of re-equilibration with magnetite on silicate mineral compositions are shown on Fig. 4.26. The degree of compositional modification decreases in the order of olivine, clinopyroxene and plagioclase. Olivines are significantly changed their

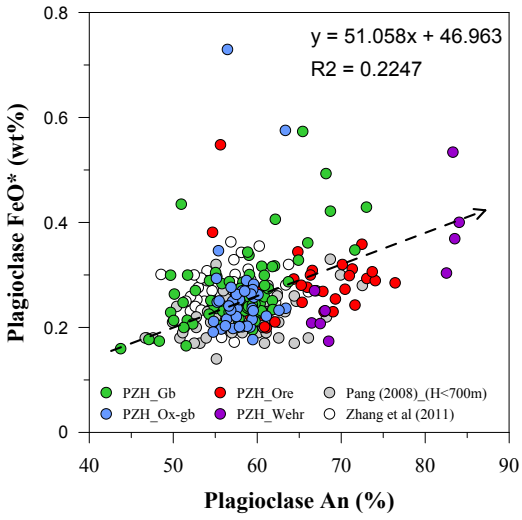

Fig. 4.24 Total FeO* contents in Plag against An (mol%) for Panzhihua Intrusion. Recently published data of Plag composition are shown for comparison.

composition in oxide-rich rocks during re-equilibration. The shift of clinopyroxene composition is much less obvious. Variations in plagioclase composition are not observed.

4.2.2 Magnetite Chemistry

A set of 37 samples from the Panzhihua intrusion has been selected for the EMPA and LA-ICP-MS analysis for major and trace element composition of magnetite. The EMPA analyses were performed on polished thin sections, whereas trace element analyses were performed on polished rock blocks in 1-inch diameter mounts. The methods of EMPA and LA-ICP-MS are attached in Appendix I. Representative analysis results are given in Table 4.7 to Table 4.8.

4.2.2.1 Major element compositions of magnetite

The Panzhihua magnetites are enriched in titanium (TiO_2: 0.05 to 19.77 wt%, mostly >4 wt% and averaged at 11.3 wt%), and hence may be defined as titanomagnetite. Using the method of Lindsley and Spencer (1982) and Sauerzapf *et al.* (2008), the calculated proportion of ulvospinel in the solid solution of magnetite-ulvospinel (X_{Usp}) is 0.1 to 0.6 for Panzhihua and 0.04 to 0.5 for Taihe. The X_{Usp} calculated using two methods is differing up to 0.02. The

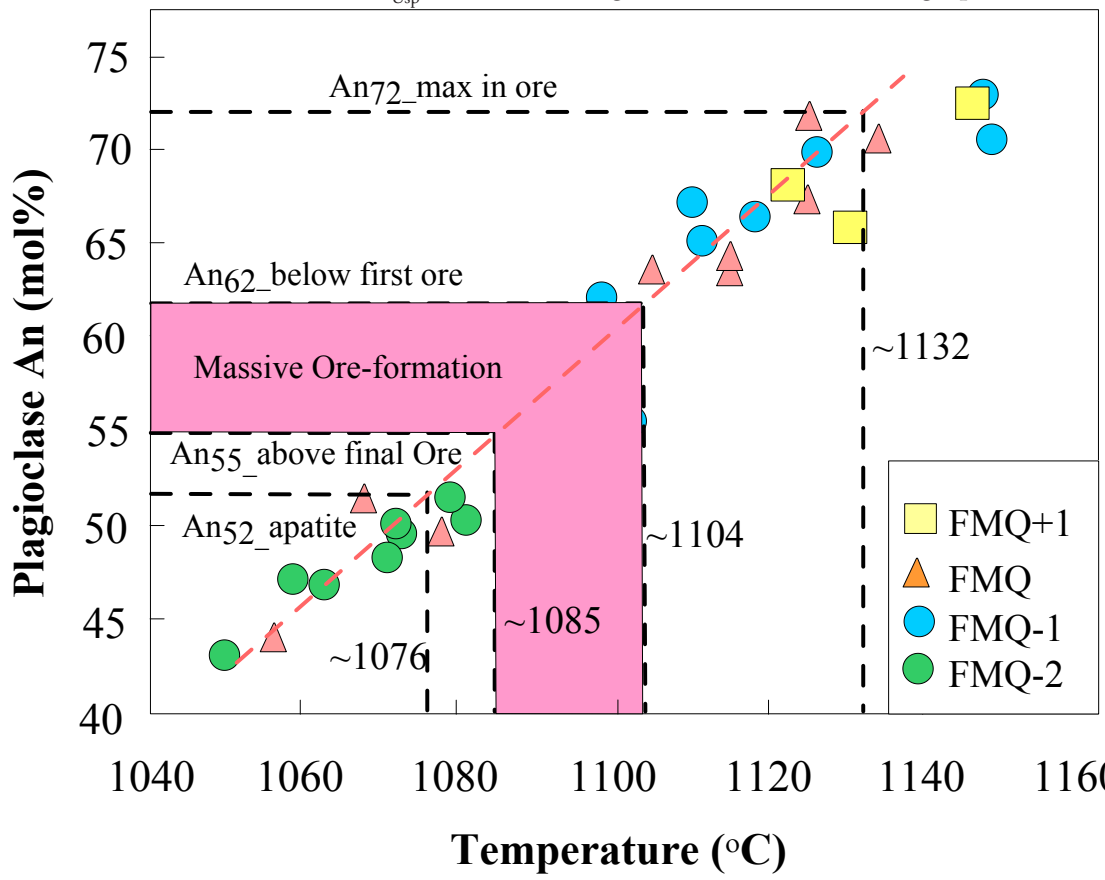

Fig. 4.25 Binary plot of Plag An content as a function of temperature. (After Toplis & Carroll, 1995).

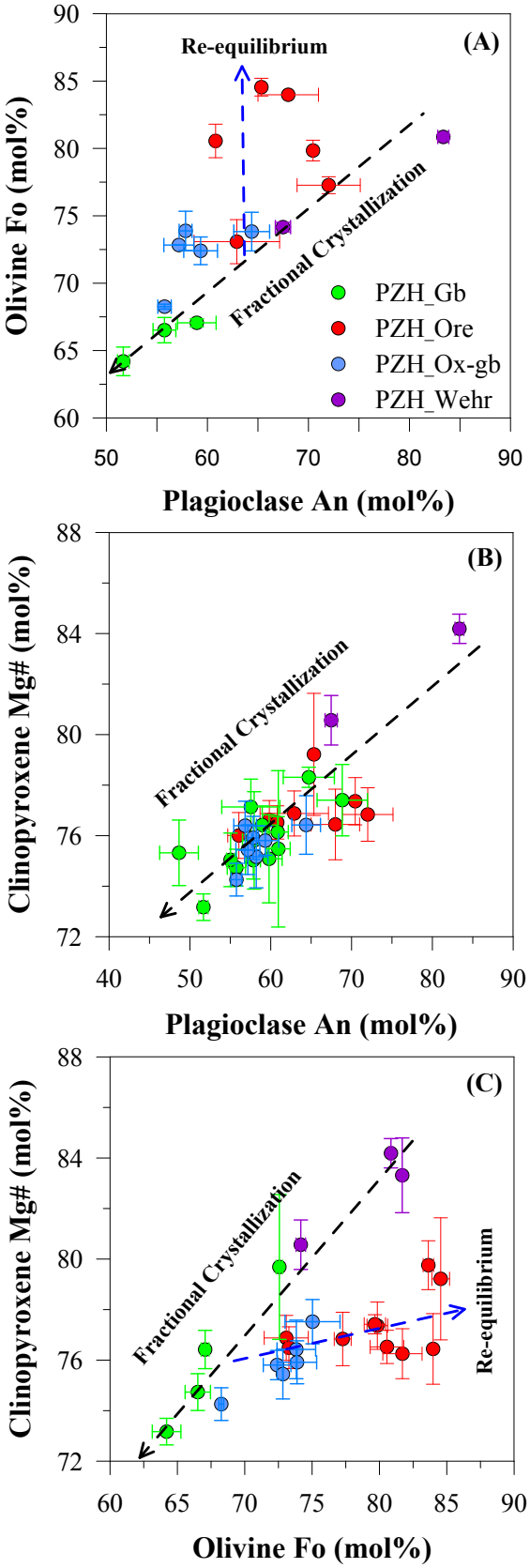

Fig. 4.26 Binary plots showing covariation of mineral compositions. Trends of fractional crystallization re-equilibration with magnetite are shown.

Panzhihua magnetite contain 61.42 - 92.40 wt% FeO^* and wide ranges of the other major elements (in wt%): 0.01 to 19.04 Cr_2O_3, 0.05 to 8.31 Al_2O_3, 0 to 5.22 MgO, 0.16 to 1.46 V_2O_5, 0.04 to 1.62 MnO, 0 to 0.37 NiO, 0 to 0.26 ZnO (Table 4.7). However, most of the magnetites are depleted in NiO (<0.05 wt%) and Cr_2O_3 (<0.1 wt%). Similarly, the Taihe magnetite is also a Ti-rich variety. The Taihe magnetite have a narrower compositional range, except for higher content of ZnO (up to 0.52 wt%) and absence of high-Cr type (Table 4.8; Fig. 4.27). They are more oxidized than the Panzhihua magnetite, as evidenced by the ratio of Fe^{3+} to Fe^{2+}, which is averaged at 1.08 for the former (64 analyses) and 0.9 for the latter (290 analyses).

Based on Cr contents, the Panzhihua magnetite may be divided into a high-Cr type (2.9 to 16.7 wt%) that is hosted in wehrlite, and a low-Cr type (Cr_2O_3 < 0.3 wt%) in gabbro and ore. The high-Cr type magnetite shows a large compositional spectrum in the Cr-Al-Fe^{3+} plot (Fig. 4.27). Part of the high-Cr Ti-Mgt compositional field is comparable to spinels from the Noril'sk-Talnakh intrusion (Barnes & Kunilov, 2000). The Panzhihua high-Cr magnetite narrows the compositional gap between Cr-rich spinel and Cr-poor spinel from many other tholeiitic layered intrusions (Fig.

4.27). The low-Cr magnetite displays low Cr, but a broader range of Al and Fe^{3+} compared with low-Cr spinel from other layered intrusions. Magnetites from the Taihe gabbroic layered intrusion are Cr-depleted, with composition within the range of Panzhihua low-Cr magnetite.

The major element compositions of Panzhihua and Taihe magnetite show no clearly positive or negative correlations with Mg# ($Mg/Mg+Fe^{2+}$). But the compositions of magnetite become more variable as the Mg# of magnetite decreases. The major and minor elements of magnetites from most rocks correlate well with one another, e.g. positive relationships between MgO and Al_2O_3, and negative for MgO, Al_2O_3, TiO_2 as a function of total iron (FeO^*) (Fig. 4.28). As increasing X_{usp}, the variation in MgO becomes greater, but smaller in Al_2O_3 (Fig. 4.29). It is clearly shown that magnetites in wehrlite and fine-grained gabbro in MGZ are following a distinct trend of enriched Cr, Al, Ni (to a less extent of V), and depleted Fe and Ti. The magnetite found in wehrlite has greatly reduced the spinel gap between Cr-rich spinel and Fe^{3+}-rich spinel (Barnes & Kunilov, 2000). It may indicate that magnetite in wehrlite crystallized from a less evolved magma, whereas magnetite in other rocks may have crystallized from a relatively evolved parental magma. The consistent trend of low-Cr magnetite from Panzhihua and Taihe gabbroic layered intrusion may indicate the common parental magma origin.

Except for Xinjie magnetites, which have similar ranges in TiO_2 and Al_2O_3 but larger range in FeO^*, Panzhihua magnetites have more variable FeO, MgO, TiO_2 and Al_2O_3 than that from other intrusions (Fig. 4.30). Some of Panzhihua magnetites have very high concentration of MgO (up to 5.2 wt%), whereas magnetite from the other intrusions generally have lower than 2 wt% MgO. Xinjie magnetites have MgO slightly higher, but still well below 3 wt%. The FeO-MgO and TiO_2-Al_2O_3 trends are different from those of magnetite from Panzhihua, Taihe and Baima gabbroic layered intrusions. A few magnetites from Panzhihua intrusion have comparable TiO_2 and Al_2O_3 concentration with that of magnetite from Xinjie intrusion.

Magnetite from the Suwalki anorthosite-hosted deposit are characterized by higher MgO content at a given FeO content, and higher Al_2O_3 content at a given TiO_2 content of magnetite (Fig. 4.30). The Grader layered intrusion contains magnetite with extremely high abundance of FeO^*, but depleted MgO, Al_2O_3 and TiO_2. The Sept Iles layered intrusion has magnetite with a limited compositional range, likely due to a small number of analyses. Magnetites from the Fedorivka layered intrusion show low content of MgO but high content of TiO_2. The Bushveld magnetites are distinct from others with prominent higher content of TiO_2 at a given FeO^*, and MgO content is lower than 1.5 wt%.

Table 4.7 Representative analyses of major (EMPA) and trace (LA-ICPMS) element composition in Mgt from the Panzhihua Intrusion.

Sample	PZ-1	PZ-2	PZ-3	PZ-4	PZ-6	PZ-9	PZ-10	PZ-11	PZ-13	PZ-14
Rock	Wehr	Gb	Gb	Ore	Wehr	Gb	Ox-gb	Ore	Ore	Ore
n	6	5	10	5	3	7	9	8	10	8
TiO_2	3.05	6.94	9.63	13.92	9.87	11.97	12.12	13.84	16.03	15.89
Al_2O_3	7.19	2.81	3.43	2.24	2.66	2.79	3.57	3.68	2.33	2.79
FeO*	65.44	82.45	79.21	74.87	68.1	78.06	77.26	73.74	73.63	72.21
FeO	37.88	51.65	45.26	40.29	40.43	41.62	40.95	38.36	36.01	35.96
Fe_2O_3	31.35	35.97	38.48	38.62	31.72	40.61	40.42	39.22	41.23	39.85
MnO	0.49	0.39	0.38	0.46	3.39	0.44	0.5	0.42	0.51	0.53
MgO	2.08	0.91	0.86	3.36	2.98	0.81	1.19	3.03	2.92	3.73
Cr_2O_3	16.7	0.07	0.08	0.09	5.57	0.06	0.04	0.05	0.07	0.1
NiO	0.35	0.04	0.03	0.02	0.19	0.02	0.01	0.01	0.02	0.02
V_2O_3	1.15	0.68	0.7	0.66	0.56	0.69	0.68	0.66	0.63	0.65
ZnO	0.17	0.04	0.06	0.02	0.09	0.08	0.04	0.04	0.05	0.04
Total	100.42	99.50	98.91	99.68	97.46	99.09	99.51	99.31	99.80	99.56
Number of ions on the basis of 4 O										
Ti	0.082	0.196	0.272	0.384	0.279	0.338	0.339	0.381	0.442	0.436
Al	0.304	0.124	0.152	0.097	0.118	0.124	0.156	0.159	0.101	0.120
Fe^{2+}	0.942	1.130	1.209	1.185	0.996	1.276	1.256	1.202	1.265	1.215
Fe^{3+}	1.024	1.461	1.280	1.113	1.142	1.177	1.145	1.057	0.994	0.987
Mn	0.015	0.012	0.012	0.014	0.108	0.014	0.016	0.013	0.016	0.016
Mg	0.111	0.051	0.048	0.184	0.167	0.045	0.066	0.165	0.160	0.203
Cr	0.474	0.002	0.002	0.003	0.165	0.002	0.001	0.001	0.002	0.003
Ni	0.010	0.001	0.001	0.001	0.006	0.001	0.000	0.000	0.001	0.001
V	0.033	0.020	0.021	0.019	0.017	0.021	0.020	0.019	0.019	0.019
Zn	0.005	0.001	0.002	0.001	0.002	0.002	0.001	0.001	0.001	0.001
Sum	3.000	3.000	3.000	3.000	3.000	3.000	3.000	3.000	3.000	3.000
X_{Usp}	0.11	0.21	0.29	0.40	0.31	0.36	0.36	0.41	0.46	0.46
n	11	11	9	10	11	12	8	11	12	11
Sc	4.6	6.11	7.92	13.24	2.59	8.18	7.68	10.54	13.43	13.28
V	6098	4291	3940	3802	5040	4280	4273	4031	3476	3693
Cr	105298	182	327	342	136419	32	13	13	188	199
Mn	2773	2157	2513	3118	15215	2732	3045	3009	3015	3003
Co	324	198	245	172	220	158	192	173	236	245
Ni	2965	166	279	113	1314	80	69	49	128	121
Cu	0.54	9.27	1.96	3.79	2.46	12.03	9.21	1.55	1.04	1.85
Zn	1945	757	770	379	1648	669	646	495	398	448
Ga	122	79	70	56	76	71	65	52	40	47
Zr	0.88	6.58	4.9	8.74	4.01	8.73	7.51	6.7	7.62	7.89
Y	0.02	0.01	0.01	0.02	0.31	0.01	0.01	0.01	0.02	0.06
Nb	0.57	6.58	0.15	0.85	9.13	0.67	0.4	0.64	1.06	0.97
Sn	2.83	2.55	1.7	1.55	0.9	1.86	1.94	1.57	1.17	1.33
Hf	0.06	0.32	0.3	0.35	0.12	0.4	0.34	0.31	0.3	0.31

1. Fe^{3+} and Fe^{2+} were recasted from FeO* on the basis of ideal stoichiometry (Fe_3O_4).

2. X_{Usp} was calculated followed the metahod of Lindsley & Spencer (1982). It differs up to 0.02 from the results calculated followed the method of Sauerzapf et al (2008).

Table 4.7 Representative analyses of major (EMPA) and trace (LA-ICPMS) element composition in magnetite from the Panzhihua gabbroic layered intrusion (continued).

Sample	PZ-15	PZ-17	PZ-18	PZ-21	PZ-24	PZ-25	PZ-26	PZ-27	PZ-30	PZ-31
Rock	Ore	Wehr	Ore	Ox-gb	Ore	Ox-gb	Ore	Ore	Ore	Ore
n	7	6	7	11	11	9	9	8	10	12
TiO_2	14.41	12.54	14.99	13	13.26	9.64	12.78	14.7	14.45	12.66
Al_2O_3	2.97	3.37	2.87	2.77	3.31	2.94	3.62	3.21	1.72	3.45
FeO*	72.8	73.84	73.37	76.9	76.06	80.15	75.66	74.87	75.8	75.26
FeO	38.8	41.17	40.56	41.49	41.46	39.5	40.75	42.77	42.74	39.8
Fe_2O_3	37.78	36.31	36.46	39.36	38.45	45.17	38.79	35.68	36.74	39.41
MnO	0.61	0.75	0.44	0.43	0.53	0.41	0.58	0.51	0.42	0.42
MgO	4.14	1.41	3.41	1.55	1.8	0.88	2.01	1.75	1.48	2.62
Cr_2O_3	0.08	2.94	0.1	0.05	0.05	0.05	0.28	0.04	0.11	0.1
NiO	0.02	0.22	0.01	0.01	0.01	0.03	0.04	0.01	0.01	0.02
V_2O_3	0.65	0.76	0.62	0.6	0.64	0.65	0.68	0.61	0.75	0.72
ZnO	0.05	0.1	0.05	0.04	0.06	0.04	0.05	0.06	0.06	0.06
Total	99.49	99.58	99.51	99.3	99.58	99.32	99.58	99.35	98.49	99.26
Number of ions on the basis of 4 O										
Ti	0.394	0.349	0.412	0.364	0.368	0.272	0.354	0.409	0.410	0.351
Al	0.127	0.147	0.124	0.122	0.144	0.130	0.157	0.140	0.076	0.150
Fe^{2+}	1.149	1.238	1.211	1.263	1.251	1.208	1.223	1.295	1.311	1.191
Fe^{3+}	1.064	1.046	1.031	1.131	1.099	1.305	1.107	1.022	1.078	1.125
Mn	0.019	0.024	0.014	0.014	0.017	0.013	0.018	0.016	0.013	0.013
Mg	0.224	0.078	0.186	0.086	0.099	0.049	0.110	0.097	0.083	0.144
Cr	0.002	0.086	0.003	0.001	0.001	0.001	0.008	0.001	0.003	0.003
Ni	0.001	0.007	0.000	0.000	0.000	0.001	0.001	0.000	0.000	0.001
V	0.019	0.023	0.018	0.018	0.019	0.020	0.020	0.018	0.023	0.021
Zn	0.001	0.003	0.001	0.001	0.002	0.001	0.001	0.002	0.002	0.002
Sum	3.000	3.000	3.000	3.000	3.000	3.000	3.000	3.000	3.000	3.000
X_{Usp}	0.41	0.38	0.43	0.38	0.39	0.29	0.38	0.43	0.42	0.37
n	12	21	13	9	12	12	12	11	11	12
Sc	12.85	9.55	12.57	7.98	6.98	4.94	7.13	10.38	12.31	11.13
V	3891	4634	3428	3856	3527	4033	3861	3534	3875	3894
Cr	388	20414	299	55	6	2	2137	2	592	319
Mn	3084	3966	3022	2934	3532	2635	3139	3548	2961	2820
Co	216	272	223	188	146	137	167	184	53	129
Ni	77	1779	77	25	25	10	220	16	92	138
Cu	1.22	1.24	1.11	0.63	1.05	7.31	0.41	0.61	7.39	37.4
Zn	417	627	476	547	605	615	488	695	709	477
Ga	46	66	45	52	49	73	69	59	59	48
Zr	5.79	4.51	7.02	5.69	6.84	3.46	5.55	9.74	7.35	8.39
Y	0.01	0.01	0.02	0.01	0.01	0.01	0.01	0.02	0.03	0.02
Nb	0.58	0.3	1.06	0.56	0.47	0.11	0.38	1.47	0.96	0.66
Sn	1.37	1.81	1.24	1.38	0.92	1.47	1.95	1.48	1.57	1.63
Hf	0.28	0.25	0.31	0.26	0.25	0.17	0.26	0.41	0.31	0.32

Table 4.7 Representative analyses of major (EMPA) and trace (LA-ICPMS) element composition in magnetite from the Panzhihua gabbroic layered intrusion (continued).

Sample	PZ-33	PZ-35	PZ-37	PZ-38	PZ-39	PZ-40	PZ-41	PZ-42	PZ-44	PZ-45
Rock	Ore	Ox-gb	Ore	Ox-gb	Gb	Gb	Ox-gb	Ox-gb	Ap-gb	Ap-gb
n	9	12	9	12	8	10	9	11	5	5
TiO_2	15.33	12.74	14.34	13.86	9.82	11.79	12.56	9.78	7.4	6.2
Al_2O_3	2.94	1.83	3.74	3.6	3.23	3.97	4.43	3.19	2.43	2.86
FeO*	74.05	77.57	74.81	74.64	79.11	76.94	75.11	80.28	83.08	83.46
FeO	42.63	41.78	42.17	41.75	39.59	40.97	40.75	39.42	37.83	36.48
Fe_2O_3	34.92	39.78	36.27	36.55	43.93	39.97	38.19	45.42	50.28	52.21
MnO	0.46	0.46	0.6	0.53	0.36	0.46	0.41	0.4	0.41	0.34
MgO	2.27	1.08	2.06	1.91	1.02	1.29	2.08	1.22	0.41	0.44
Cr_2O_3	0.05	0.06	0.04	0.05	0.05	0.04	0.08	0.04	0.02	0.03
NiO	0.02	0.01	0.02	0.02	0.01	0.02	0.01	0.01	0.02	0.02
V_2O_3	0.66	0.76	0.64	0.66	0.76	0.66	0.71	0.64	0.52	0.37
ZnO	0.06	0.06	0.06	0.06	0.05	0.09	0.04	0.06	0.09	0.07
Total	99.33	98.55	99.93	98.99	98.82	99.26	99.27	100.17	99.42	99.02
Number of ions on the basis of 4 O										
Ti	0.425	0.362	0.395	0.386	0.277	0.329	0.347	0.272	0.210	0.177
Al	0.128	0.082	0.161	0.157	0.143	0.174	0.192	0.139	0.108	0.128
Fe^{2+}	1.284	1.285	1.262	1.262	1.207	1.240	1.219	1.191	1.171	1.138
Fe^{3+}	1.000	1.169	1.029	1.050	1.278	1.147	1.090	1.296	1.455	1.507
Mn	0.014	0.015	0.019	0.017	0.011	0.014	0.013	0.013	0.013	0.011
Mg	0.125	0.061	0.112	0.105	0.057	0.071	0.114	0.067	0.023	0.025
Cr	0.001	0.002	0.001	0.001	0.001	0.001	0.002	0.001	0.001	0.001
Ni	0.001	0.000	0.001	0.001	0.000	0.001	0.000	0.000	0.001	0.001
V	0.020	0.023	0.019	0.020	0.023	0.020	0.021	0.019	0.016	0.011
Zn	0.002	0.002	0.002	0.002	0.001	0.002	0.001	0.002	0.003	0.002
Sum	3.000	3.000	3.000	3.000	3.000	3.000	3.000	3.000	3.000	3.000
X_{Usp}	0.45	0.38	0.42	0.41	0.29	0.35	0.37	0.29	0.22	0.19
n	11	11	10	9	13	8	11	10	6	8
Sc	12.31	7.03	10.41	8.34	5.45	7.82	8.13	5.45	4.83	1.05
V	3493	3899	3360	3528	4007	3498	3889	3836	2865	1789
Cr	94	21	12	9	17	5	289	1	1	2
Mn	2811	2909	3665	2966	2448	3253	2758	2751	2650	1873
Co	228	206	191	201	150	163	191	115	107	67
Ni	42	25	8	9	7	2	23	1	0	1
Cu	0.92	1.23	0.81	0.66	33.31	0.93	0.88	31.37	12.28	4.83
Zn	510	641	568	616	684	725	599	762	704	461
Ga	46	56	46	49	57	57	52	63	69	53
Zr	8.9	5.44	8.3	6.1	4.66	5.9	5.75	2.88	4.08	1.34
Y	0.03	0.02	0.02	0.02	0.01	0.01	0.02	0.01	0.02	0.5
Nb	0.96	0.34	1.75	1.41	0.27	0.6	0.76	0.2	0.07	0.04
Sn	1.32	1.34	1.15	1.22	1.24	1.06	1.26	1.22	1.42	0.71
Hf	0.39	0.29	0.42	0.37	0.22	0.33	0.34	0.2	0.16	0.05

Table 4.8 Representative analyses of major (EMPA) and trace (LA-ICPMS) element composition in Mgt from the Taihe Intrusion.

Sample	TH-1	TH-2	TH-3	TH-4	TH-5	TH-6	TH-7	TH-8	TH-9
Rock	Ore	Ore	Ore	Ore	Gb	Ore	Ore	Ore	Gb
n	4	8	7	5	7	7	10	7	10
TiO_2	4.14	15.19	12.97	11.31	4.86	14.39	10.64	13.04	0.87
Al_2O_3	1.01	1.01	0.48	1.21	0.93	1.75	1.8	0.57	0.39
FeO*	87.61	76.52	79.87	78.05	86.72	76.06	79.87	79.31	90.92
FeO	35.56	44.01	43.29	38.96	36.08	43.17	39.62	42.46	33.13
Fe_2O_3	57.85	36.13	40.65	43.44	56.27	36.55	44.73	40.94	64.23
MnO	0.13	0.44	0.41	0.32	0.15	0.33	0.37	0.35	0.05
MgO	0.55	0.98	0.21	1.8	0.72	1.02	1.46	0.82	0.06
Cr_2O_3	0.06	0.05	0.08	0.13	0.07	0.05	0.05	0.06	0.46
NiO	0.04	0.02	0.02	0.03	0.03	0.02	0.03	0.02	0.07
V_2O_3	0.9	0.73	0.8	0.63	1.02	0.68	0.76	0.74	0.88
ZnO	0.01	0.12	0.13	0.03	0.02	0.15	0.05	0.06	0.03
Total	100.27	98.68	99.03	97.86	100.14	98.11	99.51	99.07	100.17
				Number of ions on the basis of 4 O					
Ti	0.118	0.433	0.372	0.324	0.138	0.411	0.300	0.372	0.025
Al	0.045	0.045	0.022	0.054	0.041	0.078	0.079	0.026	0.018
Fe^{2+}	1.081	1.360	1.343	1.210	1.091	1.338	1.204	1.312	1.017
Fe^{3+}	1.690	1.065	1.207	1.275	1.649	1.077	1.297	1.205	1.891
Mn	0.004	0.014	0.013	0.010	0.005	0.011	0.012	0.011	0.002
Mg	0.031	0.055	0.012	0.102	0.041	0.058	0.082	0.046	0.003
Cr	0.002	0.001	0.002	0.004	0.002	0.002	0.001	0.002	0.014
Ni	0.001	0.001	0.001	0.001	0.001	0.001	0.001	0.001	0.002
V	0.027	0.022	0.024	0.019	0.031	0.021	0.023	0.023	0.027
Zn	0.000	0.003	0.004	0.001	0.001	0.004	0.001	0.002	0.001
Sum	3.000	3.000	3.000	3.000	3.000	3.000	3.000	3.000	3.000
X_{Usp}	0.12	0.44	0.38	0.33	0.14	0.43	0.31	0.38	0.03
n	10	9	11	11	8	8	8	9	8
Sc	5.6	10.15	9.35	12.06	4.31	9.19	7.43	9.14	1.43
V	4653	3979	4069	3875	5531	4238	4341	4103	5120
Cr	12	25	135	531	10	13	13	11	2560
Mn	1834	3088	3309	3092	1274	2241	2438	2886	420
Co	170	91	34	199	92	37	107	26	141
Ni	571	234	138	107	95	118	64	50	608
Cu	404.46	2802.44	1794.76	5.26	16.62	180.62	7.11	18.82	0.16
Zn	346	509	258	374	201	577	420	359	347
Ga	41.89	34	20.14	46.8	49.88	35.16	41.87	34.56	50.31
Zr	3.88	6.19	6.26	8.28	2.17	4.23	3.35	5.33	0.5
Y	0.04	0.84	0.21	0.02	0.01	0.24	0.06	0.85	0.04
Nb	0.17	0.76	0.77	0.65	0.02	0.42	0.12	0.74	0.02
Sn	1.42	0.89	0.69	1.48	1.74	1.3	1.35	0.99	1.17
Hf	0.17	0.27	0.3	0.33	0.11	0.21	0.17	0.26	0.02

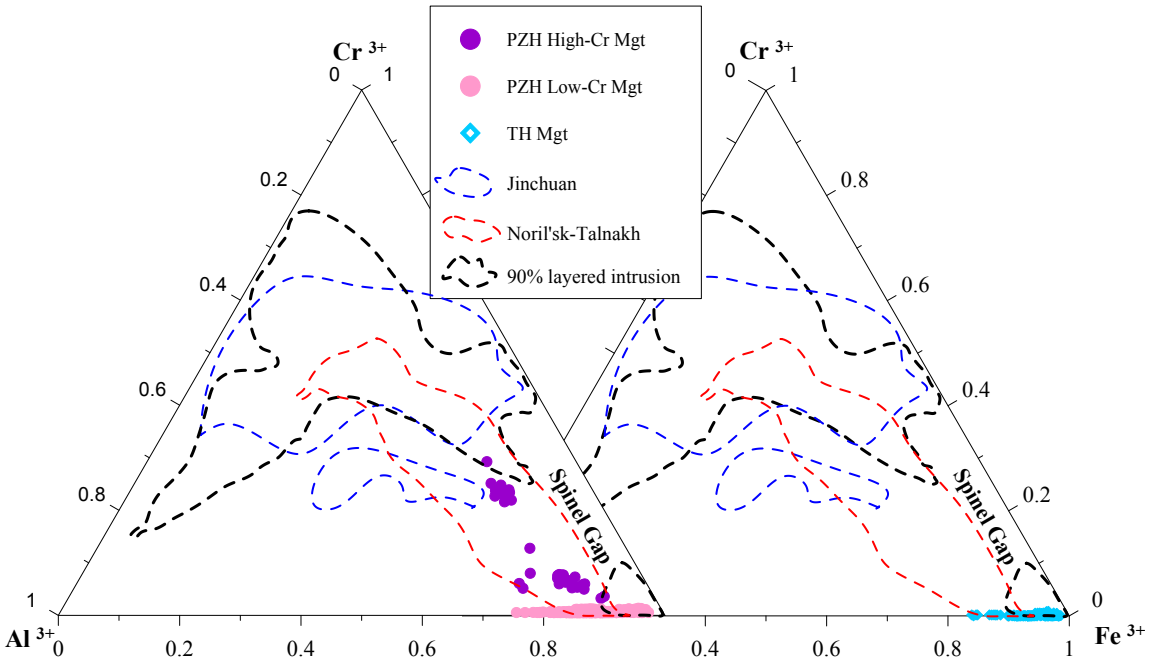

Fig. 4.27 A ternary diagram showing Cr-Al-Fe^{3+} proportions in Mgt from the Panzhihua and Taihe Intrusions. Compositions of Spl from other intrusions are from Barnes and Kunilov (2000). Note the compositional gap between Fe^{3+}-rich Mgt and Cr-rich Spl.

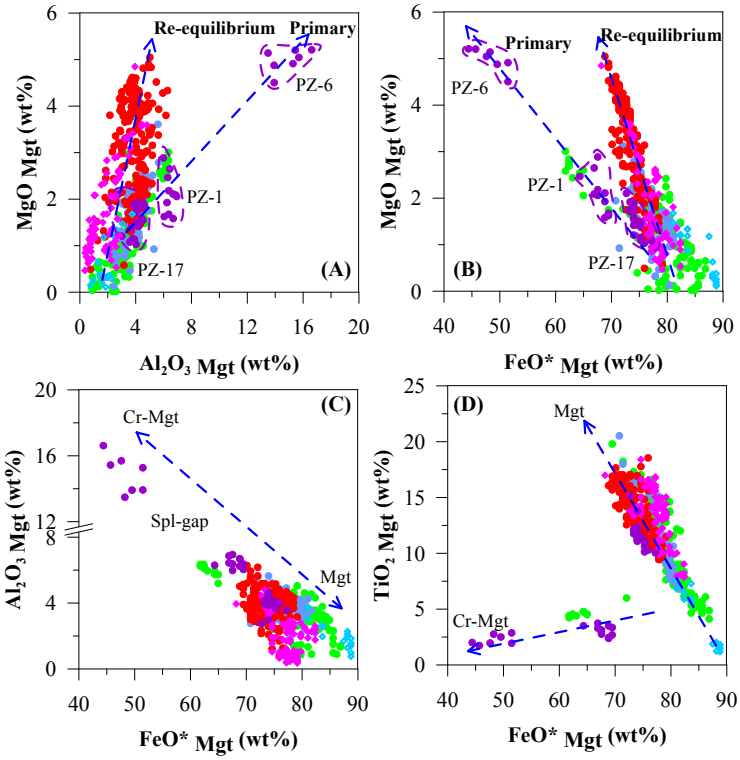

Fig. 4.28 Binary plots showing major element compositions in Mgt from Panzhihua and Taihe Intrusions. Note that Mgt in wehrlite is enriched in Cr, Al, Mg, and relatively depleted in Fe and Ti, and follows a distinct evolution trend from that of gabboric rocks and Fe-Ti oxide ores. The most Cr-rich Mgt in the Panzhihua wehrlite have reduced the Spl gap (Barnes and Kunilov, 2000). High-Mg nature of Mgt in wehrlite may be inherited from the parental magma.

4.2.2.2 Trace element composition of magnetite

4.2.2.2.1 Assessment of data quality

The Panzhihua and Taihe magnetites are characterized by abundant exsolution of ilmenite and Mg-Al spinel (pleonaste). As EMPA and LA-ICP-MS techniques use very different spot sizes (e.g. 2 μm vs 50 μm), this may significantly affect the results. The smaller the spot size used for LA-ICP-MS, the weaker the signal intensity becomes (Fig. 4.31). In our analyses, LA-ICP-MS results with spot size over 50 microns give consistent results, whereas analyses with smaller spot sizes yields significant scatter likely due to uneven distributions of lamellae within the ablated volume. (Fig. 4.32).

Exsolution of ilmenite from magnetite, should deplete the host in TiO_2 and enrich it in Fe_2O_3. However, the high abundance of Fe and Ti in magnetite and ilmenite, and the small amount of ilmenite exsolution relative to the host magnetite, as well as much smaller size of ilmenite lamellae than the laser spots, may have concealed this compositional modification.

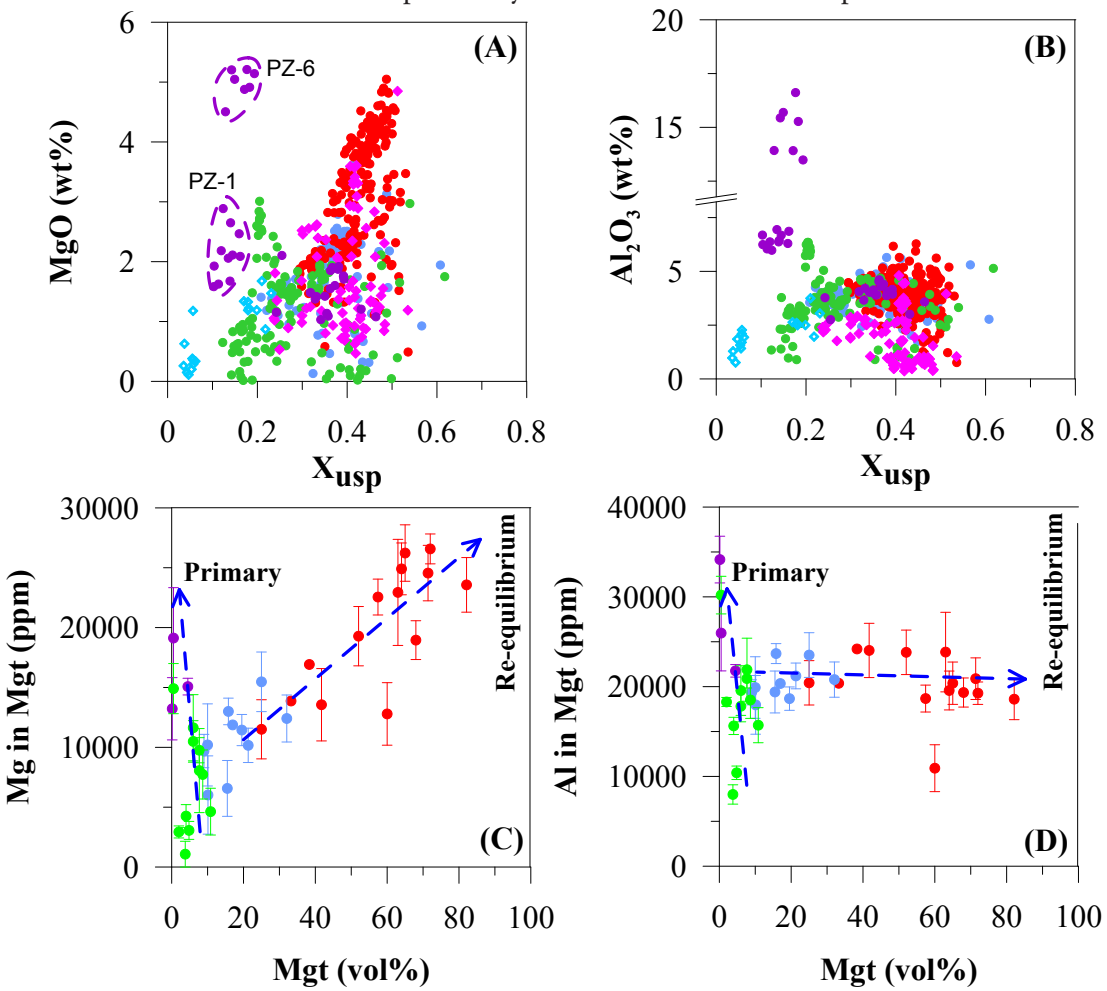

Fig. 4.29 MgO and Al_2O_3 concentrations in Mgt as a function of Usp proportion in Mgt-Usp solid solution. Note increasing MgO and Al_2O_3 contents and increasing scatter with increasing X_{Usp}.

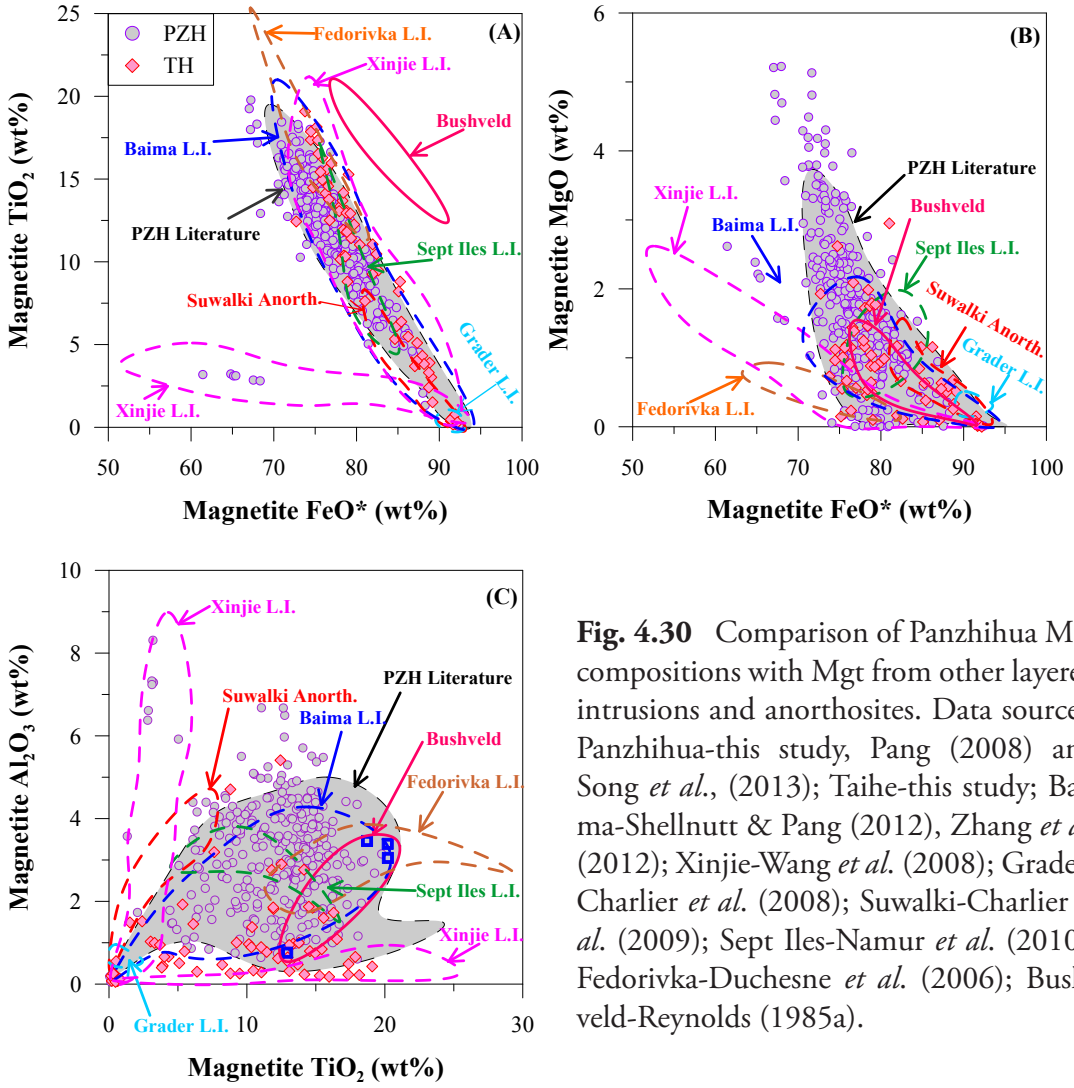

Fig. 4.30 Comparison of Panzhihua Mgt compositions with Mgt from other layered intrusions and anorthosites. Data sources: Panzhihua-this study, Pang (2008) and Song *et al.*, (2013); Taihe-this study; Baima-Shellnutt & Pang (2012), Zhang *et al.* (2012); Xinjie-Wang *et al.* (2008); Grader-Charlier *et al.* (2008); Suwalki-Charlier *et al.* (2009); Sept Iles-Namur *et al.* (2010); Fedorivka-Duchesne *et al.* (2006); Bushveld-Reynolds (1985a).

This may explain the consistency of $Fe_2O_3^*$, TiO_2 and V_2O_3 concentrations between EMPA and LA-ICP-MS results, with minor variations may be interpreted by within sample variation and analysis errors (Fig. 4.33).

However, these two factors obviously could not explain the departures of the other major elements. The high concentrations of Al_2O_3 and MgO of magnetite that measured by LA-ICP-MS are obviously due to the including of exsolution of pleonaste in the LA analysis, as these elements are more abundant in pleonaste than in magnetite. MnO concentration is higher in EMPA measurement than that in LA-ICP-MS, which is in accordance with the low concentration of MnO in pleonaste exsolution than in the host magnetite. Cr_2O_3 content of magnetite may be attributed to the contrasting detection limit of Cr in two methods (Cr: 300 ppm vs 0.2 ppm). ZnO content show large scatter in both analysis methods, due to its low concentration in magnetite.

To conclude, the LA-ICPMS data represent the mixture of host magnetite and exsolution of ilmenite and pleonaste lamellae, and are closer to the original magnetite composition than that of EMP analyses, which only represent the host magnetite composition.

4.2.2.2.2 Magnetite trace element abundances and variations

The Panzhihua magnetites have wide trace element compositional ranges (in ppm): 1747 to 5896 V, 1 to 116743 Cr, 576 to 4734 Mn, 0 to 2889 Ni, 373 to 1922 Zn, 0 to 127 Cu, 35 to 120 Ga, 1 to 13 Sc. The Panzhihua magnetite also contain a small amount of other elements (in ppm): 0 to 39 Pb, 0 to 27.6 Nb, 0 to 10.3 Bi, 0.9 to 12.5 Zr, 0.7 to 3.5 Sn, and up to 1 ppm of Y, Hf, Ta, In, Ag. The Taihe magnetite have comparable but narrower compositional ranges, except for higher Cu concentrations (up to 2516 ppm).

As shown above, the Panzhihua magnetite has high-Cr and low-Cr types (Fig. 4.27). Compared with the most Cr-rich magnetite in the wehrlite (PZ-6), magnetite in other rocks show consistent enrichment in Sc, Ti, Mn, Cu, Y, Zr, Hf, Ta and depletion in Cr, Ni, V and Pb between various types of rocks (Fig. 4.34). Taihe magnetite in ores shows a strong enrichment in Cu and Ag, which may be related to late-stage hydrothermal alteration.

Scandium (Sc) is incompatible to compatible in clinopyroxene (e.g. D_{Sc}^{Cpx}=0.8 to 1.4; Hart & Dunn, 1993, Hauri *et al.* 1994, Jenner *et al.* 1994), slightly more compatible than that

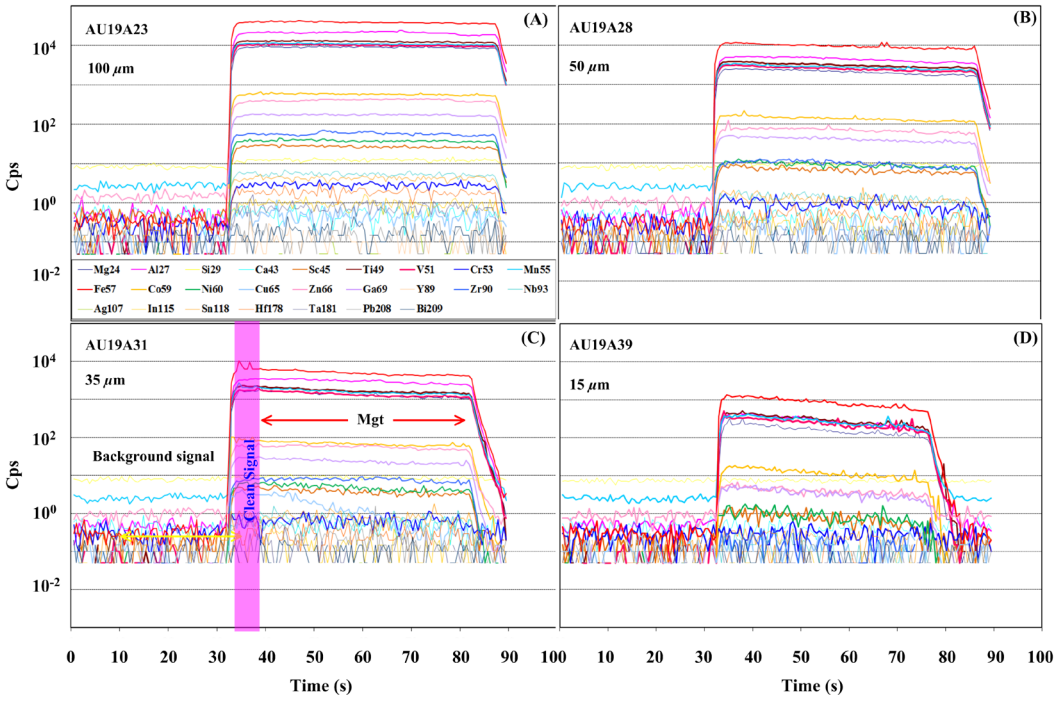

Fig. 4.31 Plots of count per second (CPS) as a function of analysis time for LA-ICP-MS analyses, showing magnetite elemental spectrum under various spot sizes. Note the drop-off in the signal intensity at smaller spot sizes.

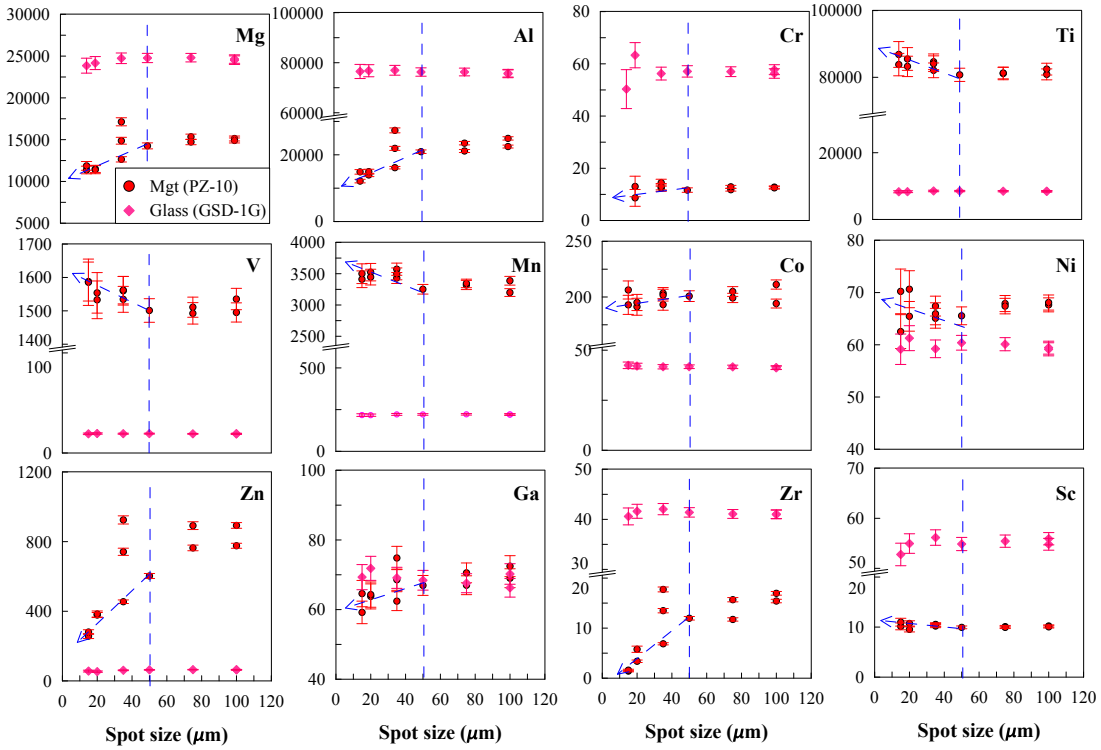

Fig. 4.32 Element concentrations as a function of spot size, showing the effect of LA spot size on the result. Note the concentration of elements vary greatly at spot sizes below 50 μm.

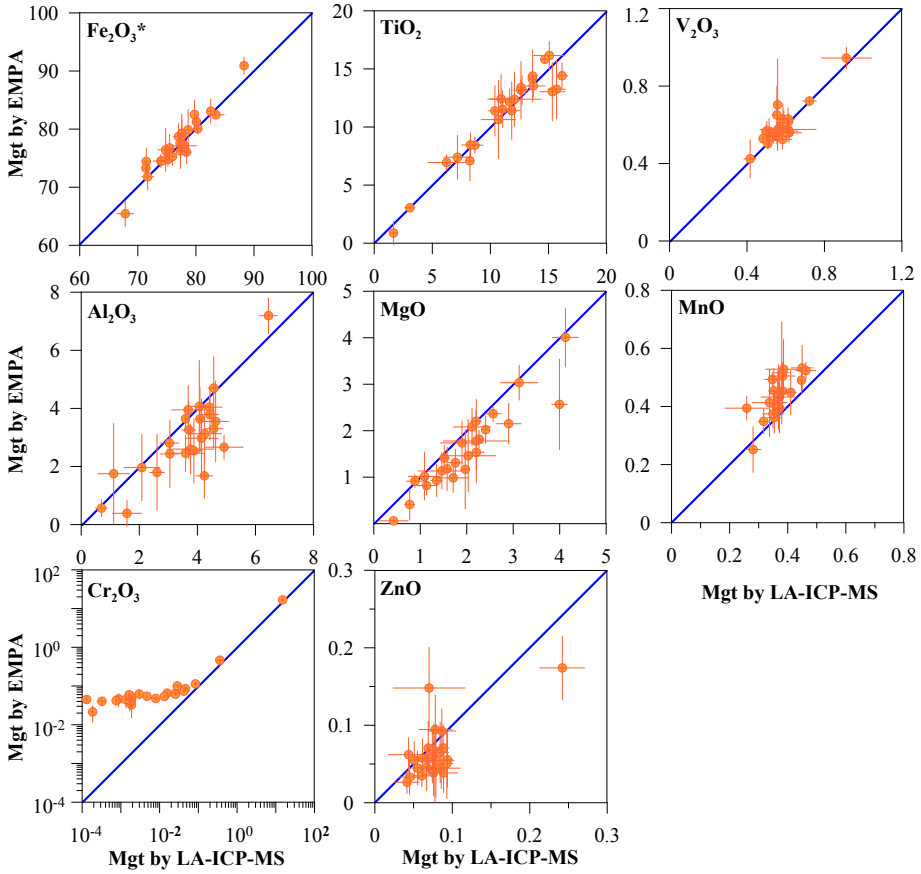

Fig. 4.33 Comparison of major element compositions of Mgt obtained by EMPA and LA-ICP-MS methods. The error bar represents 2σ. The laser spot is 50 μm.

in magnetite (e.g. D_{Sc}^{Mgt}=0.7; Lemarchand *et al*. 1987). Sc is also more compatible in ilmenite and amphibole (D_{Sc}^{Ilm}=1.8, D_{Sc}^{Amph}=2.18; Higuchi & Nagasawa, 1969; Paster *et al*. 1974), and more incompatible in olivine and plagioclase (D_{Sc}^{Ol}=0.23, D_{Sc}^{Plag}=0.008; Kloeck & Palme, 1988, Paster *et al*. 1974) (Table 4.3). The concentration of Sc varies from 1 to 18 ppm for the Panzhihua magnetite, and 1 to 13 ppm for the Taihe magnetite. Re-equilibration between magnetite with different minerals may partly account for the large variation of Sc concentration in magnetite (Fig. 4.35). It shows slightly positive correlation with the X_{Usp} of Mgt-Usp solid solution. But the magnetites in oxide ore rocks and in gabbroic rocks show differences in the ratios. Magnetites in ore rocks have higher content of X_{Usp}, and Sc in these magnetites increases rapidly with increasing X_{Usp} (Fig. 4.35 A). In comparison, magnetites in gabbro show a lower content of Sc and a slower increase with increasing X_{Usp}. The Panzhihua MGZ wehrlite and one Taihe fine-grained gabbro show a distinct low content of X_{Usp} and a relatively low amount of Sc (Fig. 4.35A). Magnetite Sc concentrations also correlate with magnetite modal proportion in the host rocks (Fig. 4.35B). Oxide-rich ores and oxide-poor gabbros display distinct trends of Sc and magnetite mode, which may be explained by re-equilibration with magnesium-rich silicate rocks and inherited from parental magma respectively. In low Mg# magnetite, Sc concents are more variable (Fig. 4.35 C). A strong positive correlation between Sc and Sc/V indicates that Sc is mainly controlled by magnetite (Fig. 4.35 D), whereas in gabbros, the variation of Sc concentration may reflect abundance of clinopyroxne.

Vanadium (V) is slightly compatible in both clinopyroxene and magnetite (e.g. D_V^{Cpx}=0.74, D_V^{Mgt}=3.4; Bougault & Hekinian, 1974), but incompatible in plagioclase and olivine (e.g. D_V^{Plag}=0.1, D_V^{Ol}=0.08; Bougault & Hekinian, 1974) (Table 4.3). The concentration of V varies from 1590 to 8499 ppm for Panzhihua magnetite, and 3311 to 5706 for Taihe magnetite. It shows no obvious relationships with Mg#, magnetite modal proportions (Fig. 4.36 A and B) or the R^{3+} (Al^{3+}+Fe^{3+}+Cr^{3+}, in formula units) of magnetite (Fig. 4.36 C). V shows a positive correlation with Sc/Ti (Fig. 4.36 D). The low concentration of V in the most Cr-rich magnetite in MGZ wehrlite (PZ-6) may reflect the transition of V from incompatible to compatible during magma differentiation, as the partition coefficient of V in basaltic magma is a function of temperature (T), oxygen fugacity (fO_2) and spinel composition (Righter *et al*., 2006; Mallmann & O'Neill, 2009).

Chromium (Cr) is strongly compatible in magnetite (e.g. D_{Cr}^{Mgt}=153; Esperanca *et al*. 1997), and much less compatible in clinopyroxene and olivine (e.g. D_{Cr}^{Cpx}=3.8,

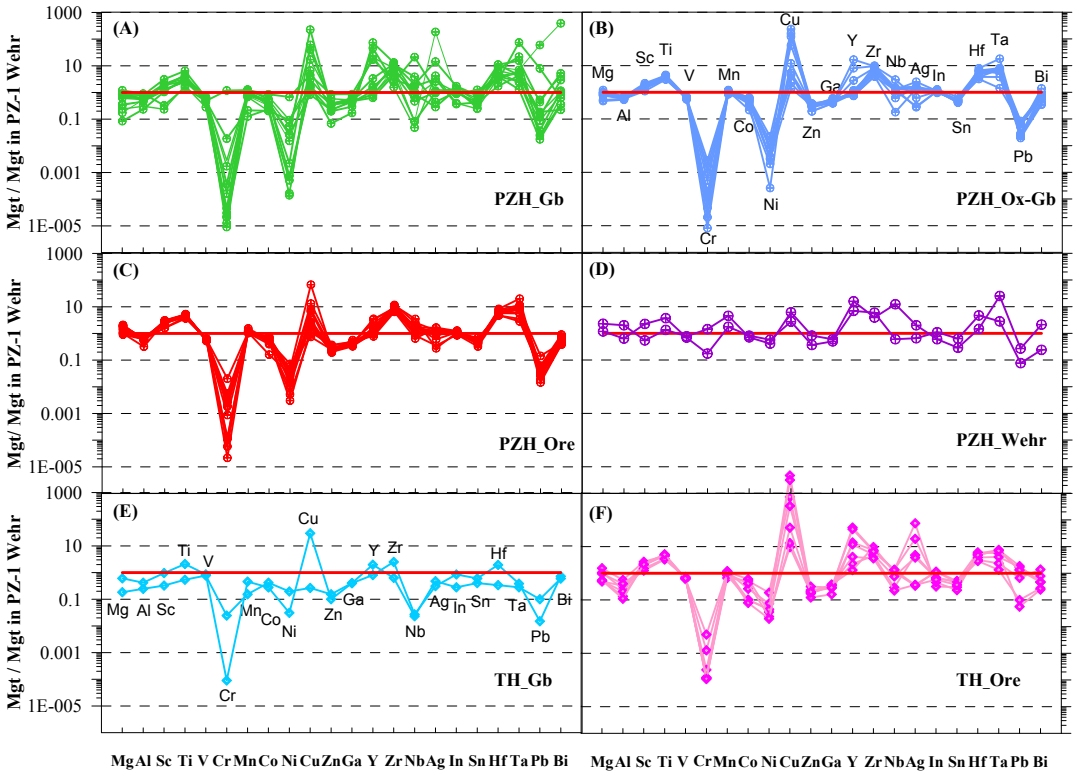

Fig. 4.34 Trace element contents in Mgt from Panzhihua and Taihe Intrusions normalised to the high-Cr Mgt.

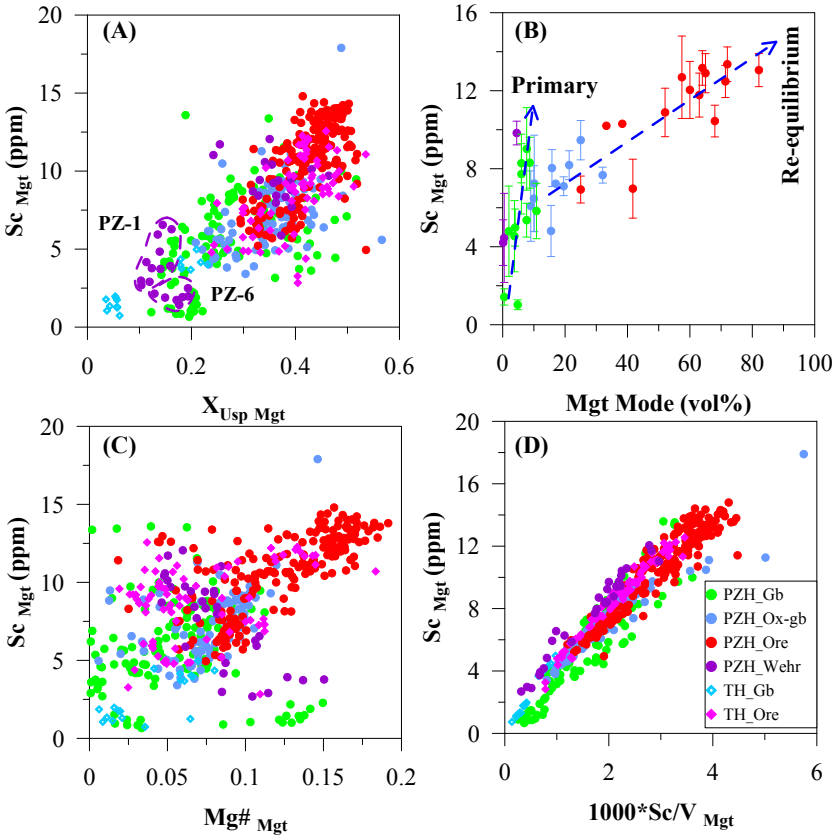

Fig. 4.35 Binary plots of Sc concentration in Mgt as a function of (A) X_{Usp}; (B) Mgt mode; (C) $Mg\#_{Mgt}$; (D) 1000*Sc/V.

D_{Cr}^{Ol}=0.63-1.85; Hart & Dunn, 1993, Beattie, 1994), and incompatible in plagioclase (e.g. D_{Cr}^{Plag}=0.038-0.064; Aignertorres *et al.* 2007). The Panzhihua magnetites have a wide range of Cr concentrations (Cr: 0.4 to 195392 ppm), with an average value of 9432 ppm. However, most of Panzhihua magnetites have Cr content below 1000 ppm (Fig. 4.37). The Taihe magnetites show a narrower Cr concentration range, between 8 to 3790 ppm, averaging at 343 ppm. Magnetite Cr concentrations show a positive correlation with magnetite Ni concentrations. The scatter patterns of magnetite Ni concentrations, especially for magnetite in Taihe ore and one olivine-bearing fine-grained Panzhihua gabbro, may be due to the post-cumulus re-equilibrium between magnetite and coexisting minerals with high affinity to Ni, such as sulphide (e.g. D_{Ni}^{Sul}=265) (Table 4.3).

Manganese (Mn) is slightly compatible in magnetite, ilmenite and olivine (e.g. D_{Mn}^{Mgt}=1.4, D_{Mn}^{Ilm}=1.9, D_{Mn}^{Ol}=1.46; Lemarchand et al. 1987, Paster et al. 1974, Kloeck & Palme, 1988), whereas it is incompatible in the other minerals (Table 4.3). The Panzhihua magnetites have Mn concentration varying between 119 to 8126 ppm. The Mn compositional range of Taihe magnetites is much smaller (272 to 3761 ppm). In general, most magnetite show a positive correlation between Mn concentration and X_{Usp} (Fig. 4.38 A), indicating Mn-Ti substitution for other bivariate elements (Fig. 4.38 B). However, there is no obvious correlation between Mn and Fe^{2+} of magnetite.

Cobalt (Co) and nickel (Ni) are siderophile elements that have affinity to Fe and tend to partition into sulphides and Fe-oxides. For instance, in basltic magma, D_{Co}^{Sul}=61-80, D_{Co}^{Mgt}=3.4, D_{Ni}^{Sul}=257-274, D_{Ni}^{Mgt}=48 (Lemarchand *et al.* 1987; Nielsen, 1992; Rajamani & Naldrett, 1978) (Table 4.3). The concentration of Co is 11 to 348 ppm for Panzhihua magnetite, with the most Co-rich magnetite occurring in wehrlite (PZ-1). The Taihe magnetites have a wider range of Co concentration (6 to 445 ppm) but narrower Ni concentration (30 to 1015 ppm), in comparison with Panzhihua magnetites. There is a weak positive correlation between Co and magnetite modal proportion (Fig. 4.39 A). The Panzhihua magnetite contains a wide range of Ni content, varying from 0.3 to 3448 ppm, with the most Ni-rich magnetite occurring in wehrlite PZ-1. Ni correlates with Ni/V ratio of magnetite (Fig. 4.39 B), indicating no significant amount of sulphides separated during magnetite fractionation. The average Co and Ni concentrations are much lower in low-Cr magnetite (Co: 166 ppm; Ni: 128 ppm) than in high-Cr magnetite (Co: 270 ppm; Ni: 1878 ppm), supporting the early crystallization of high-Cr magnetite.

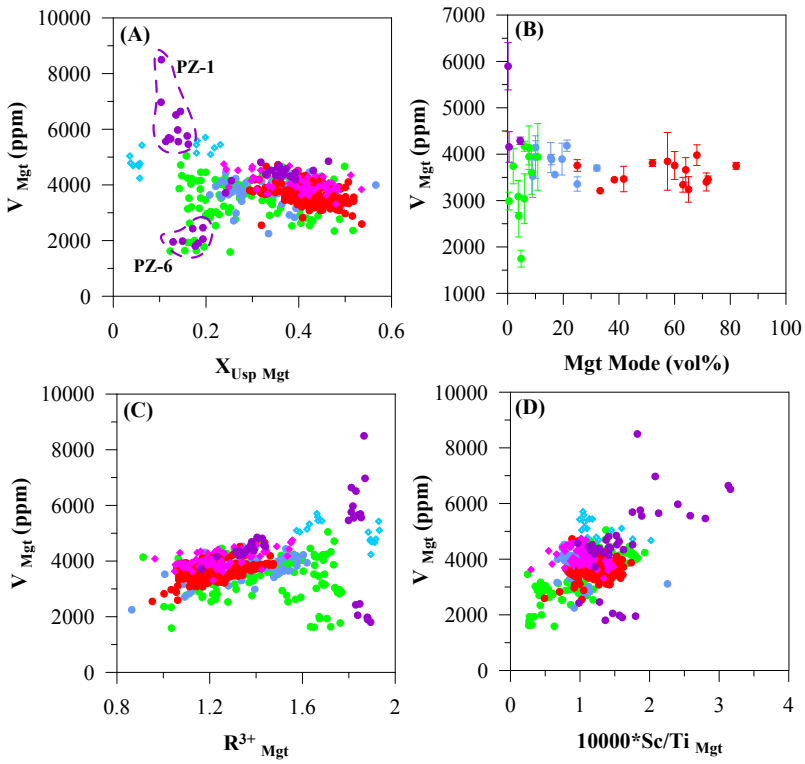

Fig. 4.36 Binary plots of Mgt V concentration as a function of (A) X_{Usp}; (B) Mgt mode; (C) R^{3+}; (D) 10000*Sc/Ti. Note the most Cr-rich Mgt (PZ-6) have depleted V compared with Mgt in other wherlite.

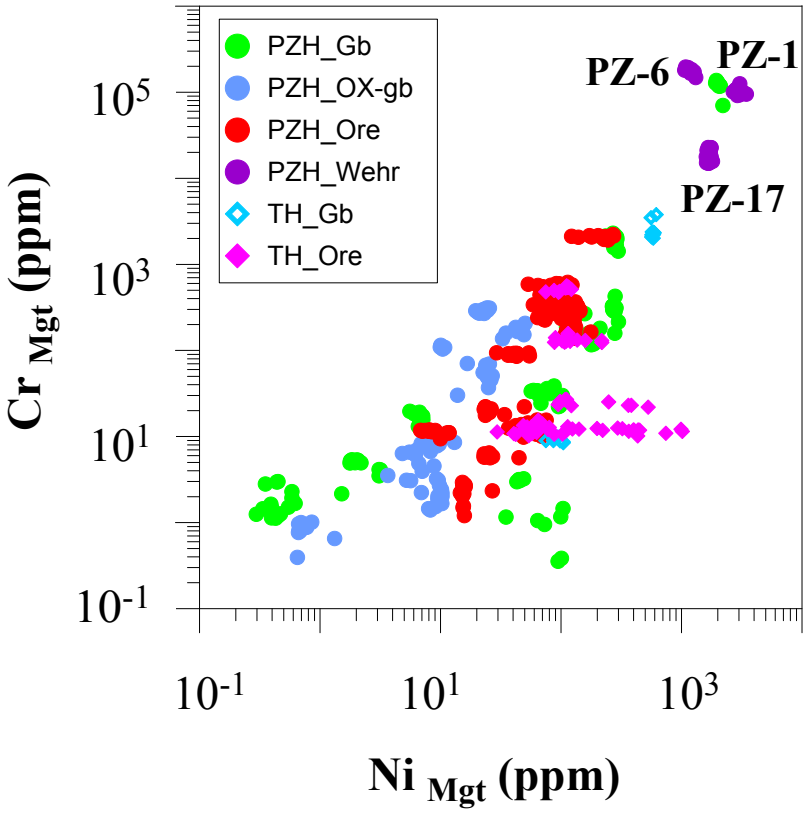

Fig. 4.37 Binary plots of Mgt Cr concentration as a function of Ni.

Copper (Cu) and zinc (Zn) are chalcophile elements that tend to partition into sulphide liquid during magma differentiation. The range of Cu concentration is 0.4 to 7 ppm for high-Cr Panzhihua magnetite, and 0.2 to 1519 ppm for low-Cr Panzhihua magnetite. The average Cu concentration is 1 ppm for high-Cr magnetite, and 18 for the low-Cr magnetite. The range of Zn concentration is 513 to 2343 ppm and 20 to 1991 for the high-Cr and low-Cr magnetite, averaged at 1140 and 588 ppm, respectively. Taihe ores generally have higher concentration of Cu (up to 11645 ppm) than Panzhihua magnetite (Fig. 4.39 C), but the range of Ni (67 to 1749 ppm) is within that of Panzhihua magnetite. Magnetite Cu and Zn display a positive correlation with Cu/Zn and Zn/Ga ratios, respectively (Fig. 4.39 C and D).

Gallium (Ga) shows both lithophile and siderophile geochemical behavior during magma evolution. It is compatible in both plagioclase and magnetite in the basaltic magma system, e.g. D_{Ga}^{Mgt}=2, D_{Ga}^{Plag}=1.7 (Lemarchand *et al.* 1987; Paster *et al.* 1974)(Table 4.3). The concentration of Ga ranges from 12 to 107 ppm and 46 to 125 ppm for Panzhihua low-Cr and high-Cr magnetite respectively. The high-Cr magnetite has an averaged Ga conten of 77, higher than that for low-Cr magnetite (Ga=55 ppm). The range of Ga for Taihe low-Cr magnetite is 17 to 58 ppm, averaged at 38 ppm. Magnetite Ga display positive correlation with Al concentration and Zn/Fe ratio (Fig. 4.39 E and F).

High field strength elements, such as Zr, Nb, Hf, Ta and Y, behave as strongly incompatible elements during magmatic differentiation processes. However, they are less incompatible in magnetite than in silicate minerals (Table 4.3). The compositional ranges of HFSE in Panzhihua magnetites are (in ppm): 0 to 5.0 for Y, 0.3 to 37.1 for Zr, 0 to 22.1 for Nb, 0-1.0 for

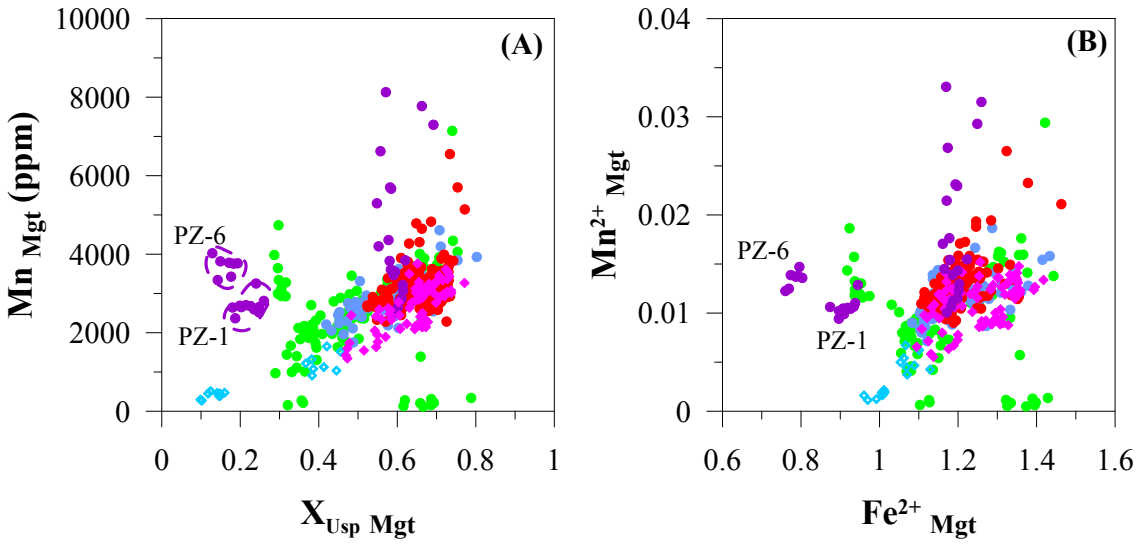

Fig. 4.38 Binary plots of Mgt Mn concentration as a function of (A) X_{Usp}; (B) Fe^{2+}_{Mgt}.

Hf, and 0 to 1.4 for Ta. In general, high-Cr magnetites in MGZ in Panzhihua intrusion have slightly lower contents of HFSE than low-Cr magnetite. The Taihe magnetites have HFSE contents much lower than that of Panzhihua magnetite (Fig. 4.40). Most of the magnetites show positive correlation between X_{Usp} and HFSE (Fig. 4.40). However, magnetites in the MGZ wehrlite and one fine-grained gabbro show abnormal enrichments in Nb and Ta but lower Zr and Hf, compared with that in other rocks at a given X_{Usp} content (Fig. 4.40). It is noteworthy that the Taihe magnetites are generally lower in HFSE, compared to Panzhihua magentites.

Yttrium (Y) shows negative correlation with Al concentrations of low-Al magnetite, whereas in the high-Al magnetites, found in Panzhihua only, Y shows no correlation with Al (Fig. 4.41 A). The identical Zr-Hf relationship and differing Nb-Ta relationship between high-Cr and low-Cr magnetite indicate crystallization of magnetite from a Zr-Hf un-fractionated

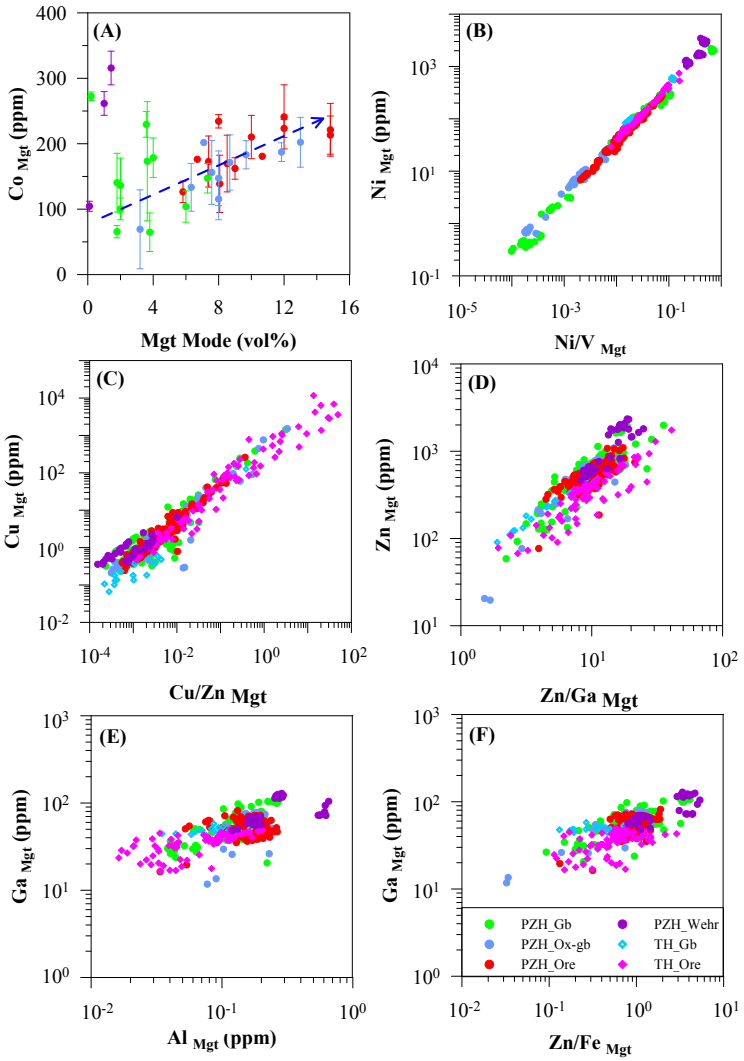

Fig. 4.39 Binary co-variation diagrams of Mgt composition (A) Co vs Mgt mode; (B) Ni vs Ni/V; (C) Cu vs Cu/Zn; (D) Zn vs Zn/Ga; (E) Ga vs Al; (F) Ga vs Zn/Fe.

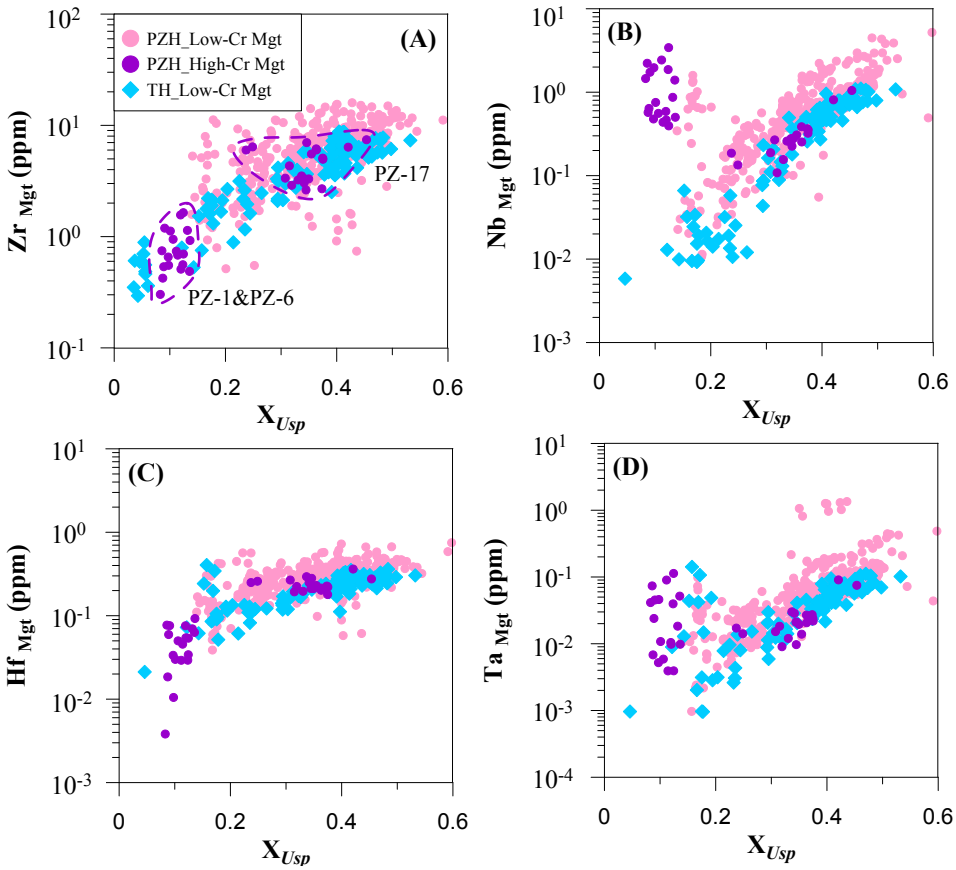

Fig. 4.40 Binary plots of Mgt X_{Usp} as a function of (A) Zr; (B) Nb; (C) Hf; (D) Ta.

but Nb-Ta fractionated parental magma. (Fig. 4.41 B-D). The ranges of Zr/Hf are 2 to 67 (averaged at 21) and 13 to 48 (averaged at 22) for Panzhihua and Taihe magnetite, respectively. The Nb/Ta ratio ranges from 0.2 to 111.2 (averaged at 13) and 1 to 27 (averaged at 10) for Panzhihua and Taihe magnetite, respectively. The average value of Zr/Hf and Nb/Ta ratios are much lower than primary magma (e.g. Zr/Hf=31.4, Nb/Ta=22.5) (McDonough *et al.*, 1992).

Figure 4.42 compare compositional variations of four textural types magetites. Except for Cr-rich magnetites, the compositions between various textural magnetites are not distinctive. However, it is obvious that low-Cr magnetite inclusions have higher contents of Mn but lower V (Fig. 4.42 A-B). No distinct differences are observed between massive and interstitial magnetite, probably due to complete reequilibration. Compared with the Panzhihua, Taihe magnetites show lower Mn but higher V and Co contents (Fig. 4.42 A-D).

Table 4.9 and Figure 4.43 show within sample differences of inclusion and non-inclusion magnetites. Since inclusions of magnetite in other minerals form during nucleation and growth of the host, if magnetite inclusions were formed earlier than magnetite crystals in the rock, they should be characterised by enrichment in strongly compatible elements (e.g. Cr, Ni, V, Mn), and depletion in strongly incompatible elements (e.g. Zr, Nb). However, except for

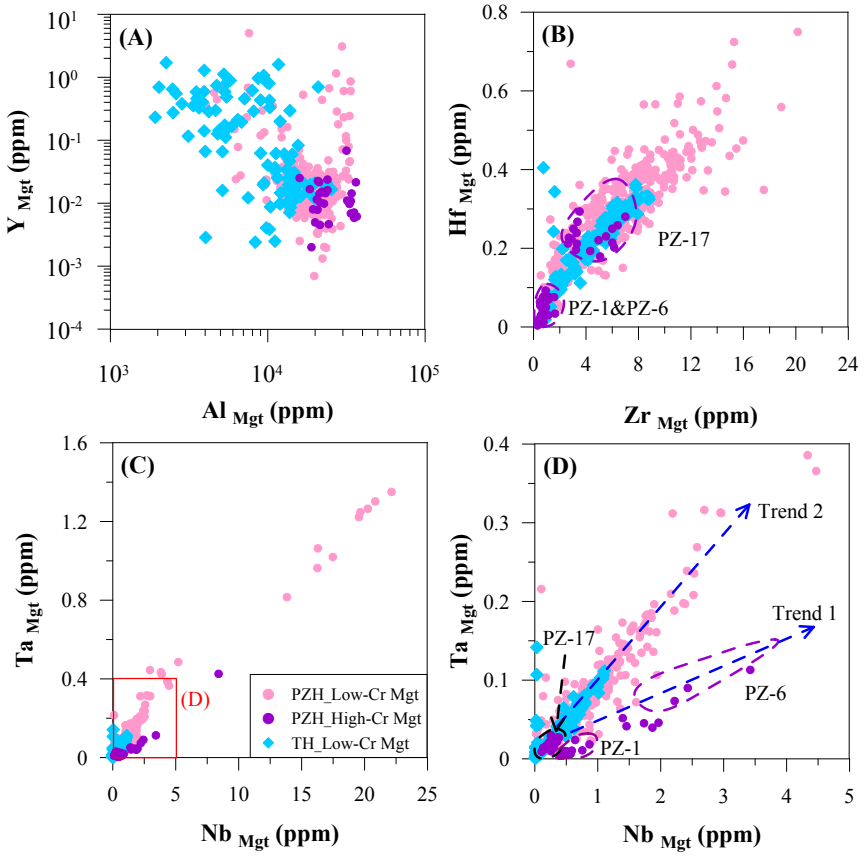

Fig. 4.41 Co-variation diagrams of (A) Y vs Al; (B) Hf vs Zr; (C) and (D) Ta vs Nb.

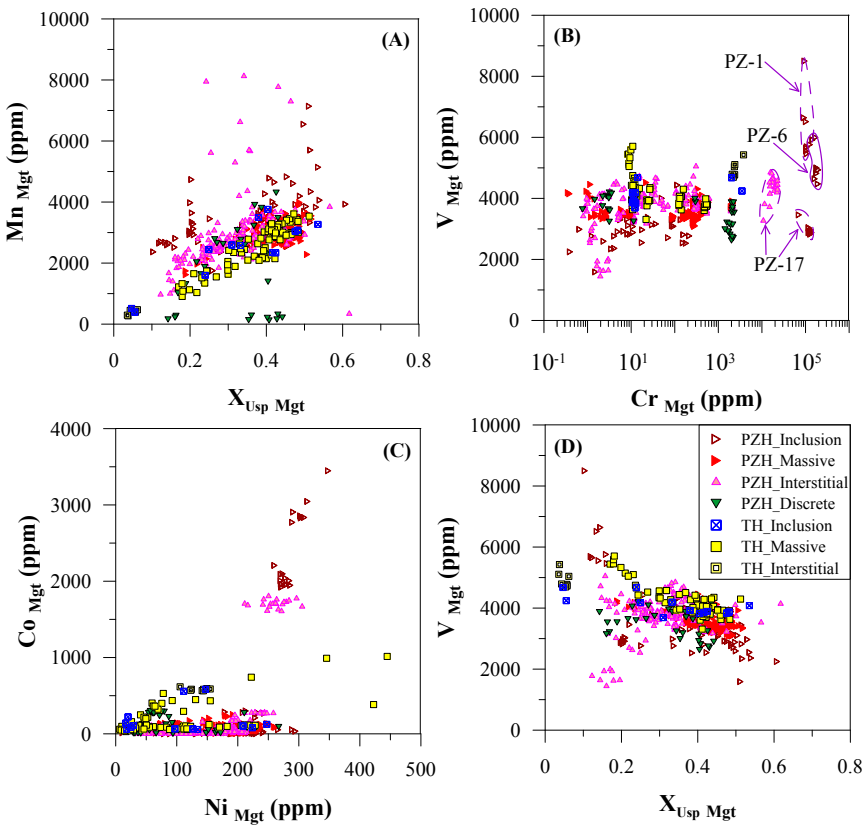

Fig. 4.42 Trace element composition of Mgt with different textures.

Ni, the observations from magnetite trace element concentrations do not support this. Magnetite inclusions show lower content of Cr, V, but higher content of Mn, Zr, Nb (Fig. 4.43). This may be explained by re-equilibration of magnetite inclusions with their host mineral during cooling.

Table 4.9 Representative LA-ICP-MS analyses of different textural magnetite within individual sample from the Panzhihua and Taihe Intrusions.

Sample	PZ-2		PZ-3		PZ-10		PZ-21		PZ-24	
n.	2	10	5	9	4	10	3	9	5	11
Texture	*inc.*	*n.inc*	*inc.*	*n.inc*	*inc.*	*n.inc*	*inc.*	*n.inc*	*inc.*	*n.inc*
Mg	752	5194	6197	8147	9885	10304	9722	13303	13174	13729
Sc	5.97	5.54	8.75	7.75	9.51	7.53	7.15	7.85	7.20	6.88
V	2536	4264	3355	3850	4159	4195	3432	3791	3431	3481
Cr	167	185	265	319	13	13	39	54	6	6
Mn	3803	1922	3095	2457	3101	2986	2894	2885	3669	3411
Co	139	157	215	240	173	188	131	185	120	147

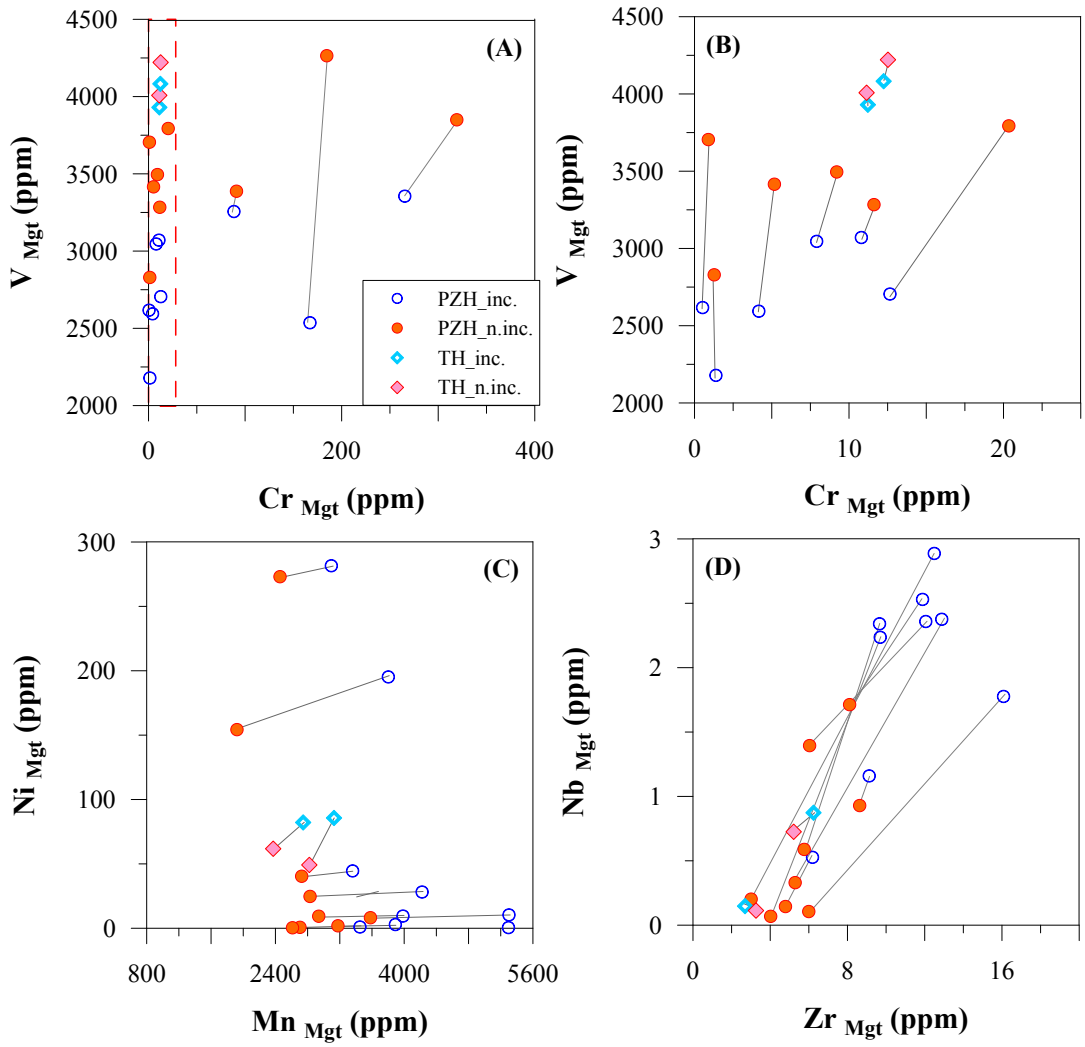

Fig. 4.43 Within sample differences of trace element composition of Mgt with different textures. Hollowed circles represent magnetite inclusions (PZH_inc., TH_inc.), whereas solid circle represents other textures (PZH_n.inc., TH_n.inc.).

Ni	195	154	282	273	61	68	22	25	29	25
Cu	1.86	27.27	0.60	1.92	17.32	38.20	506.74	0.62	9.94	0.84
Zn	770	697	786	753	764	634	501	537	620	591
Ga	64.36	78.25	63.79	68.57	68.57	63.51	46.51	51.29	47.36	48.46
Zr	16.08	6.00	6.19	4.79	10.20	7.36	6.77	5.59	6.20	6.72
Y	0.02	0.03	0.02	0.01	0.02	0.01	0.04	0.01	0.15	0.01
Nb	1.78	0.11	0.53	0.14	0.85	0.40	1.20	0.55	0.53	0.46
Sn	2.24	2.44	1.66	1.66	1.77	1.90	1.61	1.36	0.89	0.91
Hf	0.35	0.29	0.36	0.29	0.38	0.33	0.29	0.25	0.26	0.25

1. *inc.*-inclusion, *n.inc*-non-massive, interstitial and discrete magnetite.

Table 4.9 Representative LA-ICP-MS analyses of different textural magnetite within individual sample from the Panzhihua and Taihe Intrusions (continued).

Sample	**PZ-33**		**PZ-35**		**PZ-37**		**PZ-38**		**PZ-40**	
n.	**6**	**11**	**3**	**11**	**5**	**10**	**4**	**9**	**4**	**8**
Texture	***inc.***	***n.inc***	***inc.***	***n.inc***	***inc.***	***n.inc***	***inc.***	***n.inc***	***inc.***	***n.inc***
Mg	20830	24093	11888	11867	10653	15476	17635	14509	12229	10584
Sc	11.48	11.94	8.68	6.84	10.25	10.17	12.18	8.26	6.68	7.64
V	3256	3387	2705	3793	3071	3284	3046	3495	2594	3416
Cr	88	91	13	20	11	12	8	9	4	5
Mn	3359	2726	4223	2830	5303	3581	3985	2938	3891	3177
Co	228	221	209	200	169	187	209	199	219	159
Ni	45	40	28	25	10	8	9	9	3	2
Cu	1.48	0.90	1.30	1.20	0.81	0.79	0.99	0.66	0.81	0.91
Zn	462	494	505	623	545	555	654	611	724	708
Ga	41.69	44.74	34.77	54.46	36.12	45.25	46.12	48.64	45.09	55.38
Zr	9.13	8.63	12.88	5.29	11.89	8.11	12.06	6.04	9.66	5.76
Y	0.03	0.03	0.15	0.01	0.04	0.02	0.80	0.02	0.02	0.01
Nb	1.16	0.93	2.38	0.33	2.53	1.71	2.36	1.39	2.34	0.59
Sn	1.27	1.28	0.88	1.31	1.02	1.12	1.12	1.21	0.81	1.04
Hf	0.38	0.38	0.42	0.28	0.51	0.41	0.55	0.37	0.39	0.32

Table 4.9 Representative LA-ICP-MS analyses of different textural magnetite within individual sample from the Panzhihua and Taihe Intrusions (continued).

Sample	**PZ-42**		**PZ-44**		**TH-7**		**TH-8**		**TH-9**	
n.	**2**	**10**	**2**	**6**	**6**	**8**	**3**	**9**	**2**	**8**
Texture	***inc.***	***n.inc***	***inc.***	***n.inc***	***inc.***	***n.inc***	***inc.***	***n.inc***	***inc.***	***n.inc***
Mg	12409	9144	3032	4661	9306	14459	6967	6856	1480	2564
Sc	9.33	5.43	5.65	4.76	5.48	7.23	10.77	8.93	1.59	1.38
V	2617	3705	2179	2829	4082	4221	3930	4008	4459	4913
Cr	1	1	1	1	12	13	11	11	2747	2456
Mn	3451	2705	5296	2612	2745	2372	3128	2821	455	403
Co	161	106	84	106	173	104	24	25	129	136

Ni	1	1	1	0	82	62	86	49	571	583
Cu	1.67	103.59	0.67	12.18	7.88	6.92	56.39	18.34	0.12	0.15
Zn	729	747	786	694	410	408	506	350	163	333
Ga	46.17	60.74	48.91	67.78	42.69	40.73	36.54	33.75	49.24	48.31
Zr	12.49	3.01	9.70	4.02	2.70	3.26	6.24	5.21	0.74	0.48
Y	0.03	0.01	0.06	0.02	0.07	0.06	0.33	0.83	0.01	0.04
Nb	2.89	0.20	2.24	0.07	0.15	0.11	0.87	0.73	0.01	0.01
Sn	0.96	1.18	1.16	1.40	1.22	1.31	1.18	0.96	1.14	1.13
Hf	0.50	0.20	0.37	0.16	0.14	0.16	0.27	0.25	0.02	0.02

4.2.3 Ilmenite Chemistry

The major element and trace element compositions of ilmenite were measured using EMPA at the Central Science Laboratory and LA-ICP-MS method at CODES, University of Tasmania, respectively. EMPA analysis was performed on thin sections, whereas the LA analyses were performed on 1-inch in diameter polished mounts. The methods and procedures used in ilmenite analysis are the same as magnetite (See Appendix I). The major and trace element compositions for two intrusions are presented in Table 4.10 and Table 4.11.

4.2.3.1 Major element composition of ilmenite

A total of 238 and 77 ilmenite grains were analysed for the Panzhihua and Taihe respectively. The Panzhihua ilmenite (Ilm_{ss}) contain 70-97% ilmenite (X_{Ilm}) and up to 26% geikielite (X_{Geik}). The hematite end-member takes up to 14%, but most below 5%. The Panzhihua ilmenite are magnesium-rich with MgO content varying between 0-8.8 wt% and averaged at 4.4 wt%. The ranges for MnO and V_2O_3 are 0.5 to 3.1wt% and 0.01 to 0.42 wt%, with an average of 0.83 and 0.14, respectively. The Panzhihua ilmenite have small amounts of Al_2O_3 (0-0.05 wt%), Cr_2O_3 (0-0.54 wt%), NiO (0-0.11 wt%) and SiO_2 (0-0.11 wt%). The Taihe ilmenite show very similar major element composition to Panzhihua ilmenite, except for the absent of high-Cr ilmenite. The Taihe ilmenite contain 0-9.5 wt% MgO, 0.5-2.9 wt% MnO, 0.1-0.35 wt% V_2O_3 and trace amounts of Al_2O_3, Cr_2O_3 and NiO (<0.1 wt%).

The variations in major element composition of ilmenite show correlation, to some extent, with the types of host rocks. In general, X_{Ilm} decreases with increasing oxide modal proportions, e.g. the average X_{Ilm} in gabbroic rocks is 0.86, whereas it is 0.77 in massive ore rocks. MgO shows the same trend, with average MgO content decreasing from 6.3 wt% in massive ore, through 4.6 wt% in oxide-rich gabbro, to 2.1 wt% in oxide-poor gabbro (Table 4.10). Ilmenite in ore rocks are slightly enriched in TiO_2 (53.7 wt%) than those in gabbroic rocks (50.7 wt%). Ilmenite in oxide-rich rocks have a narrow range of MnO contents (0.5 to

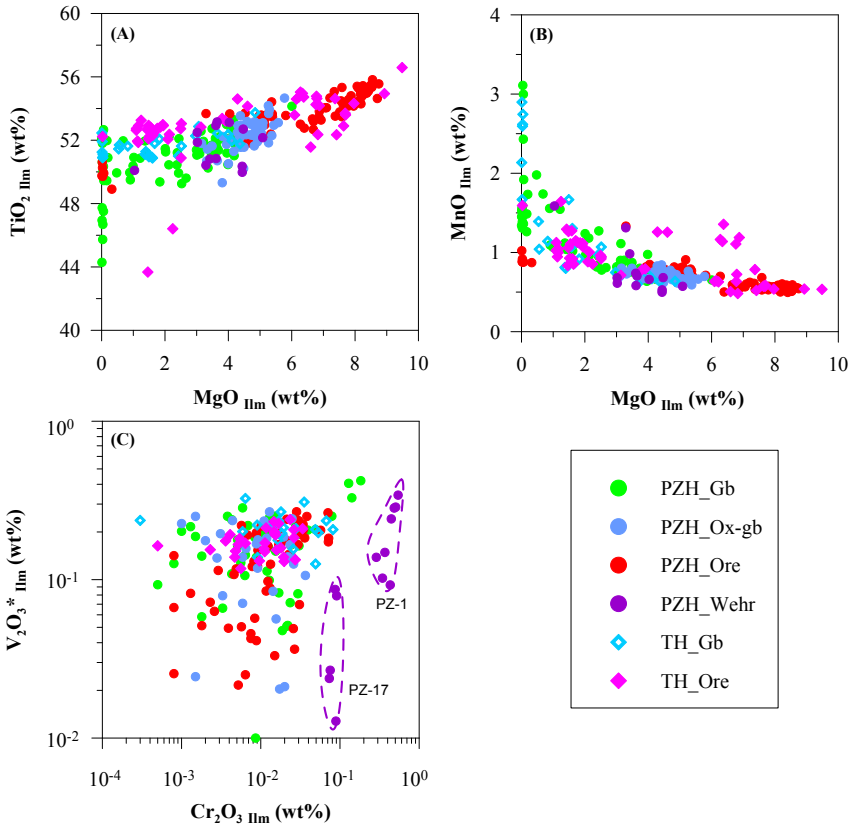

Fig. 4.44 Major element compositions of Panzhihu and Taihe Ilm: (A) MgO vs TiO_2; (B) MgO vs MnO; (3) Cr_2O_3 vs V_2O_3.

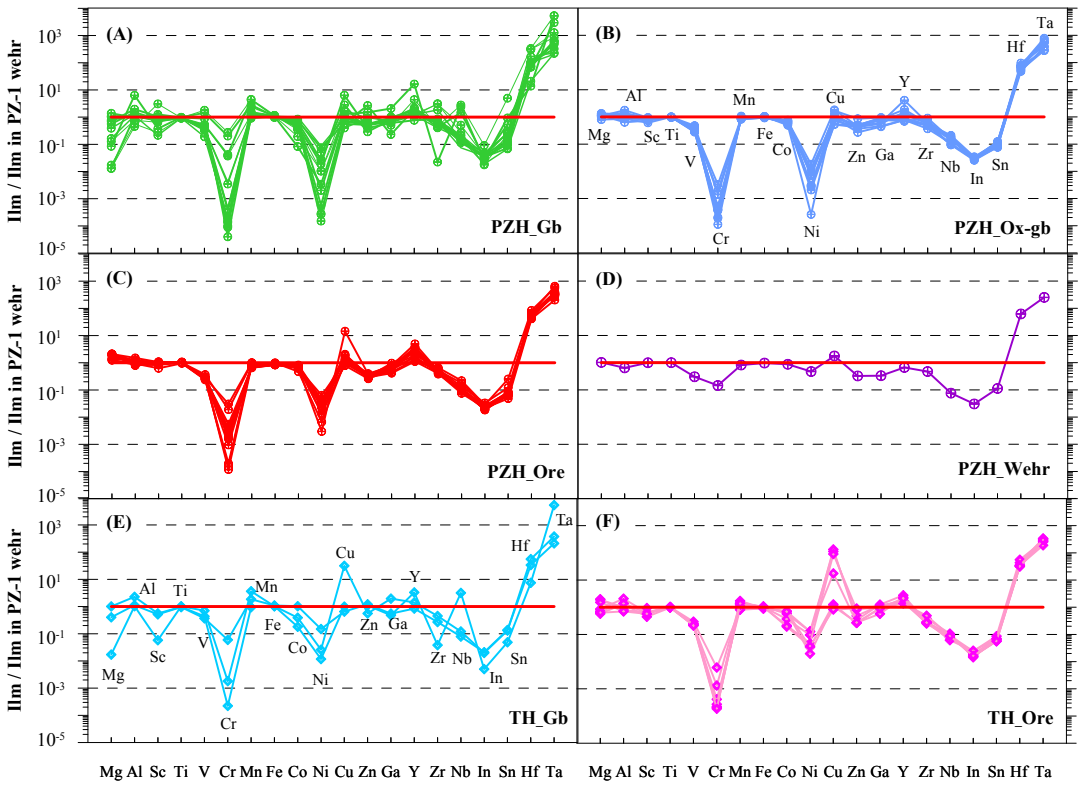

Fig. 4.45 Normalized multi-element variation diagrams for Ilm from Panzhihua and Taihe gabbroic Intrusions. Normalization values are the corresponding concentrations in Ilm from the lowermost wehrlite in Panzhihua Intrusion.

1 wt%), compared with ilmenite in gabbro (0.5 to 2.5 wt%). The V_2O_3 contents of ilmenite in most rocks are below 0.3 wt%. Only two analyses reach 0.45 wt% V_2O_3. The ilmenite in Panzhihua wehrlite have intermediate major element compositions, with MgO, TiO_2, V_2O_3 and X_{Ilm} between gabbros and ore rocks, except for MnO which shows comparable content with ore rocks. Taihe ore rocks contain ilmenite with lower X_{Ilm}, V_2O_3, but higher MgO and TiO_2 than Taihe gabbro (Table 4.11). However, the Taihe ilmenite have slightly lower content of MgO compared to the Panzhihua ilmenite in the same rock types. For example, the average MgO content is 2.1 wt% and 6.3 wt% for ilmenite in Panzhihua gabbro and ore respectively, whereas 1.8 wt% and 4.0 wt% for Taihe ilmenite in the same rock types.

The MgO content of ilmenite is correlated positively with TiO_2 (Fig. 4.44 A). MgO and MnO of ilmenite show a slightly negative correlation, which is more prominent in ilmenite in some gabbroic rocks and depleted in MgO (Fig. 4.44 B). Cr_2O_3 and V_2O_3 of ilmenite show no correlation (Fig. 4.44 B). However, ilmenite in the MGZ whelrite (PZ-1) have more abundant Cr_2O_3 and V_2O_3 (Fig.4.44 C), indicating crystallisation from a less evolved magma. Ilmenite in the MZa wehrlite (PZ-17) have comparably high Cr_2O_3 but much lower V_2O_3 contents (Fig.4.44 C), implying crystallization from a more evolved magma.

4.2.3.2 Trace element composition of ilmenite

Similar to the classification of magnetite (high-Cr and low-Cr), the Panzhihua ilmenite may be also divided into high-Cr ilmenite occurring in wherlite and low-Cr ilmenite in the other rock types. The high-Cr ilmenite contain (in ppm): Cr: 351-613 (averaged at 477), V: 109-621 (310), Co: 124-162 (136), Ni: 267-400 (308), Cu: 1.4-8.7 (3.7), Zn: 18-81 (35), Sc: 44-61 (52), Zr: 77-130 (101), and Nb: 21-24 (23). Ilmenite from other rocks contain Cr: 0.1-1206 (36), V: 95-2885 (392), Co: 5-164 (98), Ni: 0.1-60 (12), Cu: 0.6-211 (3), Zn: 15-318 (55), Sc: 2-189 (47), Zr: 3-837 (145) and Nb: 7-1154 (69) (Table 4.10).

Compared to ilmenite in the lowermost wherlite (PZ-1), low-Cr ilmenite in gabboric rocks and ores have significantly depleted Cr and Ni, and to a lesser extent V, Zn, Zr, Nb, In, Sn, but enriched Hf and Ta (Fig. 4.45 A-C). The variation may be as big as 4 orders of magnitude. Ilmenite in the other wherlite (PZ-17) higher in the stratigraphic column, show a similar pattern but with less fractionation (Fig. 4.45 D).

The concentrations of trace elements in Taihe ilmenite are within the range of Panzhihua ilmenite, except for the larger variation of Cu in Taihe gabbro, and significant Cu enrichment in Taihe ore rocks (Table 4.11). However,Taihe rocks display very consistent distribution

Table 4.10 Representative analyses of major (EMPA) and trace (LA-ICPMS) element composition in Ilm from the Panzhihua Intrusion.

Sample	PZ-1	PZ-2	PZ-3	PZ-4	PZ-5	PZ-8	PZ-9	PZ-10	PZ-11	PZ-12
Rock	Wehr	Gb	Gb	Ore	Hb-gb	Hb-Gb	Gb	Ox-gb	Ore	Ore
n1	8	6	6	4	3	6	4	6	5	4
TiO_2	50.92	51.3	51.63	54.63	49.16	47.12	52.56	52.49	54.63	55.32
Al_2O_3	0.04	0.04	0.05	0.03	0.03	0.09	0.04	0.08	0.04	0.04
FeO*	43.78	44.2	44.09	36.67	47.81	49.84	44.33	42.42	37.98	36.38
FeO	38	39.52	40.46	34.18	41.3	41.12	41.91	38.87	35.66	34.24
Fe_2O_3	6.43	5.2	4.03	2.77	7.24	9.69	2.7	3.94	2.58	2.37
MnO	0.84	0.85	0.83	0.56	2.7	1.6	1.03	0.81	0.62	0.55
MgO	3.72	3.31	2.94	8.15	0.19	0.08	2.49	4.3	7.26	8.46
Cr_2O_3	0.43	0.01	0.01	0.01	0.03	0.12	0.01	0.01	0.01	0
NiO	0.08	0.02	0.03	0.01	0.03	0.02	0.03	0.02	0.01	0.03
V_2O_3	0.20	0.09	0.07	0.08	0.11	0.33	0.08	0.06	0.04	0.07
Total	100.66	100.34	100.05	100.42	100.79	100.17	100.85	100.58	100.85	101.08
Number of ions on the basis of 3 O										
Ti	0.935	0.949	0.959	0.972	0.928	0.895	0.972	0.960	0.975	0.976
Al	0.001	0.001	0.002	0.001	0.001	0.003	0.001	0.002	0.001	0.001
Fe2+	0.775	0.812	0.836	0.676	0.866	0.868	0.862	0.790	0.707	0.672
Fe3+	0.118	0.096	0.075	0.049	0.137	0.184	0.050	0.072	0.046	0.042
Mn	0.017	0.018	0.017	0.011	0.057	0.034	0.022	0.017	0.012	0.011
Mg	0.136	0.121	0.108	0.288	0.007	0.003	0.091	0.156	0.257	0.296
Cr	0.008	0.000	0.000	0.000	0.001	0.002	0.000	0.000	0.000	0.000
Ni	0.002	0.000	0.001	0.000	0.001	0.000	0.001	0.000	0.000	0.001
V	0.003	0.001	0.001	0.001	0.002	0.006	0.001	0.001	0.001	0.001
Sum	1.996	2.000	2.000	2.000	2.000	1.999	2.000	2.000	2.000	2.000
Atomic percentages of End-members										
X_{Ilm}	0.806	0.832	0.855	0.719	0.866	0.867	0.878	0.816	0.747	0.716
X_{Geik}	0.111	0.098	0.088	0.242	0.006	0.002	0.073	0.127	0.214	0.249
X_{Pyr}	0.018	0.018	0.018	0.012	0.057	0.034	0.022	0.017	0.013	0.012
X_{Hem}	0.064	0.052	0.04	0.028	0.072	0.097	0.027	0.039	0.026	0.023
n2	9	10	9	8	10	7	7	12	11	10
Sc	53	54	57	53	38	21	55	48	51	56
V	503	414	446	392	572	1844	384	420	333	314
Cr	3297	11.26	13.55	10.93	139	607	1.32	1.00	0.40	7.73
Mn	5275	6126	5288	4096	22170	14242	6270	5675	4298	3703
Co	156	119	157	119	114	12	70	107	99	101
Ni	654	30	57	25	50	3	13	13	9	20
Cu	2.09	2.25	1.88	6.92	1.64	2.49	188.69	3.85	3.8	4.08
Zn	109	61	56	35	281	152	42	98	47	36
Ga	0.86	0.87	0.67	0.89	1.23	2.97	0.85	1.8	0.61	0.5
Zr	214	381	156	107	215	8	180	186	110	109
Y	0.08	0.09	0.12	0.19	0.8	1.24	0.06	0.05	0.1	0.25
Nb	301	50	22	27	505	711	48	44	33	30
Hf	0.05	7.38	4.72	2.82	5.71	0.88	4.77	4.31	2.97	2.83

1. *n1* and *n2*-number of EMP and LA-ICP-MS analysis. 2. Fe^{3+} and Fe^{2+} were recasted based on stoichiometry. 3. Endmembers were calculated using QUILF (Anderson *et al.*, 1993).

Table 4.10 Representative analyses of major (EMPA) and trace (LA-ICPMS) element composition in Ilm from the Panzhihua Intrusion (continued).

Sample	PZ-13	PZ-14	PZ-15	PZ-17	PZ-18	PZ-19	PZ-20	PZ-21	PZ-22	PZ-24
Rock	Ore	Ore	Ore	Wehr	Ore	Gb	Ox-gb	Ox-gb	Ox-gb	ore
n1	5	5	4	5	5	6	5	5	6	7
TiO_2	55.27	55.16	54.85	52.71	54.74	51.51	52.97	53.05	51.85	52.82
Al_2O_3	0.02	0.03	0.28	0.02	0.04	0.03	0.04	0.06	0.05	0.05
FeO*	36.5	36.65	36.18	42.7	36.76	45.46	41.05	41.73	42.69	40.99
FeO	34.28	34.26	33.70	40.52	34.07	41.81	37.19	38.28	38.40	37.87
Fe_2O_3	2.47	2.66	2.76	2.42	2.99	4.06	4.29	3.84	4.77	3.47
MnO	0.52	0.54	0.56	0.68	0.55	1.35	0.65	0.7	0.7	0.77
MgO	8.36	8.3	8.44	3.46	8.19	1.77	5.49	4.89	4.22	4.97
Cr_2O_3	0	0.01	0.02	0.08	0.01	0.02	0.01	0.01	0.02	0.01
NiO	0.01	0.02	0.03	0.04	0.02	0.01	0.02	0.02	0.01	0.01
V_2O_3	0.06	0.08	0.03	0.05	0.06	0.07	0.07	0.05	0.08	0.07
Total	100.99	101.06	100.67	99.98	100.67	100.63	100.73	100.89	100.10	100.04
Number of ions on the basis of 3 O										
Ti	0.977	0.975	0.971	0.976	0.972	0.961	0.960	0.964	0.954	0.967
Al	0.001	0.001	0.008	0.001	0.001	0.001	0.001	0.002	0.001	0.001
Fe2+	0.674	0.673	0.663	0.834	0.673	0.867	0.749	0.773	0.786	0.770
Fe3+	0.044	0.047	0.049	0.045	0.053	0.076	0.078	0.070	0.088	0.064
Mn	0.010	0.011	0.011	0.014	0.011	0.028	0.013	0.014	0.015	0.016
Mg	0.293	0.291	0.296	0.127	0.288	0.065	0.197	0.176	0.154	0.180
Cr	0.000	0.000	0.000	0.002	0.000	0.000	0.000	0.000	0.000	0.000
Ni	0.000	0.000	0.001	0.001	0.000	0.000	0.000	0.000	0.000	0.000
V	0.001	0.002	0.001	0.001	0.001	0.001	0.001	0.001	0.002	0.001
Sum	2.000	2.000	2.000	2.000	2.000	2.000	2.000	2.000	2.000	2.000
Atomic percentages of End-members										
X_{Ilm}	0.720	0.720	0.711	0.858	0.717	0.880	0.783	0.804	0.813	0.803
X_{Geik}	0.246	0.245	0.251	0.103	0.242	0.052	0.162	0.144	0.126	0.148
X_{Pyr}	0.011	0.011	0.012	0.014	0.012	0.028	0.014	0.015	0.015	0.016
X_{Hem}	0.023	0.025	0.027	0.024	0.029	0.039	0.041	0.037	0.046	0.033
n2	11	11	10	7	12	9	11	11	14	9
Sc	49	54	57	52	55	62	39	44	44	33
V	274	297	272	310	323	440	191	240	303	314
Cr	5.28	7.18	12.41	477	6.23	0.41	6.23	1.73	5.29	0.51
Mn	3649	3547	3619	4341	3799	5193	4453	4517	4358	5197
Co	129	109	109	136	108	99	93	102	98	73.26
Ni	29	24	14	308	15	17	8	5	2	4.33
Cu	2.45	4.27	3.14	3.68	3.76	4.37	1.92	2.56	2.34	2.23
Zn	31	45	37	35	44	43	29	40	64	32
Ga	0.54	0.77	0.51	0.28	0.68	1.06	0.38	0.4	1.18	0.36
Zr	82	94	94	101	102	226	79	102	100	86
Y	0.2	0.13	0.22	0.05	0.29	0.1	0.06	0.06	0.06	0.09
Nb	28	29	31	23	31	63	32	28	47	23
Hf	2.24	2.57	2.52	2.89	2.96	6.63	2.2	2.76	3.02	1.93

Table 4.10 Representative analyses of major (EMPA) and trace (LA-ICPMS) element composition in Ilm from the Panzhihua Intrusion (continued).

Sample	PZ-25	PZ-26	PZ-27	PZ-28	PZ-29	PZ-30	PZ-31	PZ-32	PZ-33	PZ-35
Rock	Ox-gb	ore	ore	Leuco	Ox-gb	Ore	Ore	Leuco	Ore	Ox-gb
n1	3	5	5	7	7	7	6	6	9	8
TiO_2	51.25	52.86	53.6	51.87	52.4	53.89	53.29	49.86	54.45	52.25
Al_2O_3	0.04	0.06	0.05	0.03	0.07	0.05	0.07	0.02	0.04	0.07
FeO*	44.11	41.29	40.7	46.25	42.42	37.76	39	48.62	37.49	41.92
FeO	39.30	37.63	38.46	44.71	38.96	34.52	35.26	43.78	35.27	37.74
Fe_2O_3	5.35	4.07	2.49	1.71	3.85	3.61	4.15	5.38	2.46	4.65
MnO	0.76	0.82	0.75	1.28	0.69	0.53	0.57	0.91	0.64	0.7
MgO	3.38	5.09	5.04	0.36	4.19	7.52	6.78	0.08	7.32	4.79
Cr_2O_3	0.02	0.01	0	0.01	0.01	0.02	0.02	0.06	0.01	0.02
NiO	0.01	0.02	0.01	0.01	0.01	0.02	0.01	0.01	0.01	0.02
V_2O_3	0.13	0.09	0.06	0.17	0.19	0.19	0.21	0.21	0.18	0.2
Total	100.24	100.65	100.46	100.15	100.37	100.34	100.37	100.31	100.39	100.44
Number of ions on the basis of 3 O										
Ti	0.948	0.961	0.976	0.982	0.962	0.965	0.959	0.946	0.976	0.954
Al	0.001	0.002	0.001	0.001	0.002	0.001	0.002	0.001	0.001	0.002
Fe2+	0.808	0.761	0.779	0.941	0.795	0.687	0.706	0.923	0.703	0.766
Fe3+	0.099	0.074	0.045	0.032	0.071	0.065	0.075	0.102	0.044	0.085
Mn	0.016	0.017	0.015	0.027	0.014	0.011	0.012	0.019	0.013	0.014
Mg	0.124	0.183	0.182	0.014	0.152	0.267	0.242	0.003	0.260	0.173
Cr	0.000	0.000	0.000	0.000	0.000	0.000	0.000	0.001	0.000	0.000
Ni	0.000	0.000	0.000	0.000	0.000	0.000	0.000	0.000	0.000	0.000
V	0.003	0.002	0.001	0.003	0.004	0.004	0.004	0.004	0.003	0.004
Sum	2.000	2.000	2.000	2.000	2.000	2.000	2.000	2.000	2.000	2.000
Atomic percentages of End-members										
X_{Ilm}	0.833	0.794	0.812	0.948	0.826	0.733	0.749	0.928	0.748	0.8
X_{Geik}	0.1	0.151	0.149	0.011	0.124	0.223	0.201	0.002	0.217	0.142
X_{Pyr}	0.016	0.017	0.016	0.027	0.015	0.011	0.012	0.019	0.014	0.015
X_{Hem}	0.051	0.039	0.023	0.014	0.035	0.033	0.038	0.05	0.021	0.043
n2	10	10	5	10	10	10	10	7	10	11
Sc	31	44	43	35	40	49	50	17	51	45
V	191	140	178	444	197	129	339	607	319	437
Cr	1.2	101.04		0.52	1.27	18.22	63.09	160.71	3.15	1.28
Mn	5195	5306	4716	8862	4472	3448	5138	6661	3884	5079
Co	91.63	96.67	92.19	56.51	90.63	103.69	97.92	53.3	112.95	118.47
Ni	2.19	41.63	2.88	5.63	1.35	19.71	24.63	19.3	8.55	5.32
Cu	1.13	2.19	1.99	2.1	1.1	1.64	2.69	3.74	1.96	2.15
Zn	67	33	67	53	45	28	43	110	34	46
Ga	1	0.62	0.85	0.72	0.71	0.48	0.63	0.84	0.45	0.48
Zr	110	127	112	599	147	87	141	582	101	126
Y	0.07	0.09	0.11	0.08	0.09	0.13	0.14	0.09	0.29	0.12
Nb	31	39	44	128	53	34	66	70	28	28
Hf	2.46	2.93	2.8	13.41	3.31	2.08	3.83	14.01	2.6	3.31

Table 4.10 Representative analyses of major (EMPA) and trace (LA-ICPMS) element composition in Ilm from the Panzhihua Intrusion (continued).

Sample	PZ-36	PZ-37	PZ-38	PZ-39	PZ-40	PZ-41	PZ-42	PZ-43	PZ-44	PZ-45
Rock	Gb	Wehr	Ox-gb	Gb	Gb	Ox-gb	Ox-gb	Gb	Ap-gb	Ap-gb
n1	7	8	8	6	5	8	6	8	3	8
TiO_2	52.69	53.42	53.2	51.44	51.76	52.4	50.72	50.76	50.11	50.16
Al_2O_3	0.04	0.45	0.06	0.08	0.07	0.06	0.07	0.06	0.05	0.04
FeO*	42.37	40.41	41.08	43.03	43.52	41.95	43.98	46.23	45.54	46.04
FeO	39.39	38.17	38.28	38.13	39.12	37.59	37.61	41.22	39.84	41.51
Fe_2O_3	3.31	2.49	3.11	5.44	4.89	4.85	7.08	5.57	6.34	5.03
MnO	0.74	0.74	0.67	0.67	0.77	0.66	0.7	0.98	0.94	1.63
MgO	4.05	5.12	4.98	4.18	3.73	4.97	4.09	1.93	2.4	1.09
Cr_2O_3	0	0.02	0.01	0.02	0.01	0.01	0.01	0.02	0.01	0.02
NiO	0.04	0.01	0.02	0.01	0.01	0.02	0.02	0.01	0.01	0.02
V_2O_3	0.2	0.17	0.17	0.2	0.17	0.2	0.22	0.2	0.2	0.15
Total	100.46	100.59	100.50	100.18	100.53	100.76	100.52	100.75	99.89	99.65
Number of ions on the basis of 3 O										
Ti	0.967	0.969	0.969	0.947	0.952	0.953	0.932	0.945	0.938	0.950
Al	0.001	0.013	0.002	0.002	0.002	0.002	0.002	0.002	0.001	0.001
Fe2+	0.804	0.770	0.775	0.780	0.800	0.760	0.768	0.853	0.829	0.874
Fe3+	0.061	0.045	0.057	0.100	0.090	0.088	0.130	0.104	0.119	0.095
Mn	0.015	0.015	0.014	0.014	0.016	0.014	0.014	0.021	0.020	0.035
Mg	0.147	0.184	0.180	0.152	0.136	0.179	0.149	0.071	0.089	0.041
Cr	0.000	0.000	0.000	0.000	0.000	0.000	0.000	0.000	0.000	0.000
Ni	0.001	0.000	0.000	0.000	0.000	0.000	0.000	0.000	0.000	0.000
V	0.004	0.003	0.003	0.004	0.003	0.004	0.004	0.004	0.004	0.003
Sum	2.000	2.000	2.000	2.000	2.000	2.000	2.000	2.000	2.000	2.000
Atomic percentages of End-members										
X_{Ilm}	0.835	0.81	0.811	0.811	0.828	0.795	0.797	0.871	0.849	0.885
X_{Geik}	0.12	0.152	0.147	0.124	0.111	0.147	0.121	0.057	0.072	0.032
X_{Pyr}	0.016	0.016	0.014	0.014	0.016	0.014	0.015	0.021	0.02	0.035
X_{Hem}	0.029	0.022	0.028	0.051	0.046	0.044	0.067	0.052	0.06	0.048
n2	11	8	10	12	9	8	13	10	6	11
Sc	41	47	50	41	47	48	43	43	38	11
V	364	295	368	563	416	450	543	487	458	246
Cr	1.11	0.65	0.67	1.37	0.5	10.64	0.37	0.33	0.29	1.08
Mn	5217	4990	4740	4793	5512	4744	5169	7090	7815	12817
Co	108.33	98.82	109.45	98.51	89.32	110.64	77.01	77.25	72.81	61.94
Ni	2.41	1.96	1.97	1.32	0.38	4.77	0.17	0.18	0.1	0.18
Cu	1.7	30.23	1.51	2.18	1.54	1.93	3.55	1.19	0.83	1.43
Zn	39	40	49	59	55	54	93	56	98	127
Ga	0.63	0.68	0.53	0.66	0.59	0.81	0.82	0.77	0.87	0.85
Zr	223	110	127	129	117	124	122	130	167	83
Y	0.39	0.38	0.31	0.09	0.17	0.2	0.09	0.16	0.13	0.56
Nb	76	54	54	62	42	42	63	50	67	49
Hf	5.35	3.08	3.61	3.46	3.39	3.44	3.59	3.53	4.14	0.95

Table 4.11 Representative analyses of major (EMPA) and trace (LA-ICPMS) element composition in Ilm from the Taihe Intrusion.

Sample	TH-1	TH-2	TH-3	TH-4	TH-5	TH-6	TH-7	TH-8	TH-9	TH-10
Rock	Ore	Ore	Ore	Ore	Gb	Ore	Ore	Ore	Gb	Gb
n1	7	6	7	6	10	8	9	9	10	5
TiO_2	50.48	54.84	53.27	52.75	52.16	52.43	54.42	52.51	51.42	51.32
Al_2O_3	0.04	0.01	0.02	0.04	0.04	0.03	0.02	0.04	0.03	0.02
FeO*	46.47	37.26	42.2	33.95	43.56	44.48	39.11	44.21	45.6	45.18
FeO	41.22	35.72	40.39	33.86	40.58	43.25	37.79	42.81	42.61	43.47
Fe_2O_3	5.83	1.72	2.01	0.10	3.32	1.37	1.47	1.56	3.32	1.90
MnO	1.02	0.62	0.95	0.54	0.72	0.91	1.21	1.09	1.22	2.6
MgO	1.76	7.28	3.68	7.31	3.14	1.67	5.57	1.86	1.34	0.03
Cr_2O_3	0.02	0.01	0.01	0.01	0.01	0.01	0.02	0.01	0.04	0.02
NiO	0.02	0.01	0.01	0.01	0.02	0.02	0.01	0.01	0.02	0.01
V_2O_3	0.18	0.15	0.17	0.17	0.19	0.16	0.17	0.18	0.2	0.29
Total	100.57	100.35	100.51	94.79	100.17	99.85	100.68	100.07	100.20	99.66
Number of ions on the basis of 3 O										
Ti	0.943	0.983	0.979	0.997	0.967	0.985	0.985	0.983	0.966	0.978
Al	0.001	0.000	0.001	0.001	0.001	0.001	0.001	0.001	0.001	0.001
Fe2+	0.856	0.712	0.825	0.711	0.836	0.903	0.760	0.891	0.890	0.921
Fe3+	0.109	0.031	0.037	0.002	0.061	0.026	0.027	0.029	0.062	0.036
Mn	0.021	0.013	0.020	0.011	0.015	0.019	0.025	0.023	0.026	0.056
Mg	0.065	0.259	0.134	0.274	0.115	0.062	0.200	0.069	0.050	0.001
Cr	0.000	0.000	0.000	0.000	0.000	0.000	0.000	0.000	0.001	0.000
Ni	0.000	0.000	0.000	0.000	0.000	0.000	0.000	0.000	0.000	0.000
V	0.004	0.003	0.003	0.003	0.004	0.003	0.003	0.004	0.004	0.006
Sum	2.000	2.000	2.000	2.000	2.000	2.000	2.000	2.000	2.000	2.000
Atomic percentages of End-members										
X_{Ilm}	0.872	0.757	0.855	0.762	0.862	0.92	0.798	0.909	0.904	0.931
X_{Geik}	0.052	0.216	0.109	0.229	0.093	0.05	0.165	0.055	0.04	0.001
X_{Pyr}	0.022	0.013	0.02	0.012	0.015	0.019	0.026	0.023	0.026	0.055
X_{Hem}	0.055	0.014	0.017	-0.003	0.03	0.011	0.011	0.012	0.03	0.013
n2	11	8	10	5	10	8	11	8	13	4
Sc	23	34	33	49	30	32	33	30	28	3
V	395	306	275	367	535	276	287	265	455	887
Cr	0.68	1.35	4.37	20.28	0.71	0.78	0.89	0.63	218.08	5.97
Mn	7361	4507	7491	4283	5097	6582	9085	7512	10968	19247
Co	92	108	57	112	63	32	105	29	164	28
Ni	84	84	63	23	17	31	13	24	104	8
Cu	213	36	278	4	85	662	18	16	2	2
Zn	52	29	37	34	61	91	30	97	122	118
Ga	0.93	0.77	1.07	1.05	1.48	1.03	0.49	0.81	0.45	0.41
Zr	98	59	61	103	97	54	62	58	57	8
Y	0.13	0.12	0.21	0.1	0.12	0.14	0.17	0.16	0.07	0.25
Nb	56	28	30	27	37	23	18	26	22	953
Hf	4.6	2.35	2.88	2.31	3.29	2.16	1.6	2.58	1.64	45.88

patterns of multiple elements (Fig. 4.45 E-F)

The ilmenite trace element concentrations show little correlation with the rock types. Instead, their variations mainly reflect substitution in ilmenite structure. For example, the positive correlations between V and V/Sc, and between Sc and Sc/V on the log-log plots indicate V and Sc substitute one another (Fig. 4.46). Cr and Ni in ilmenite follow a fractional crystallization trend; however, some ilmenite, especially in Taihe ore rocks, show an enrichment in Ni and Cu (Fig.4.7).

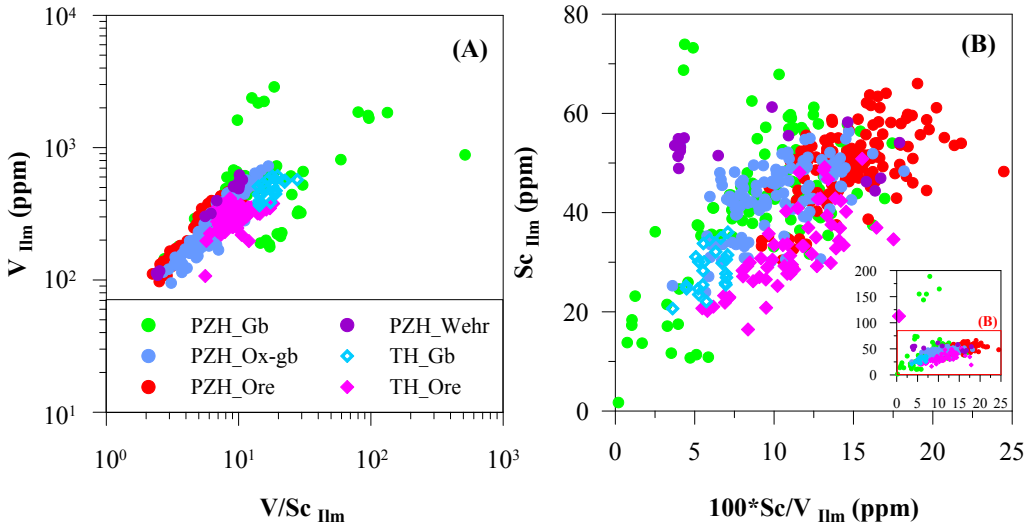

Fig. 4.46 Trace element contents in Ilm from the Panzhihua and Taihe Intrusion. (A) V vs V/Sc; (B) Sc vs 100*Sc/V.

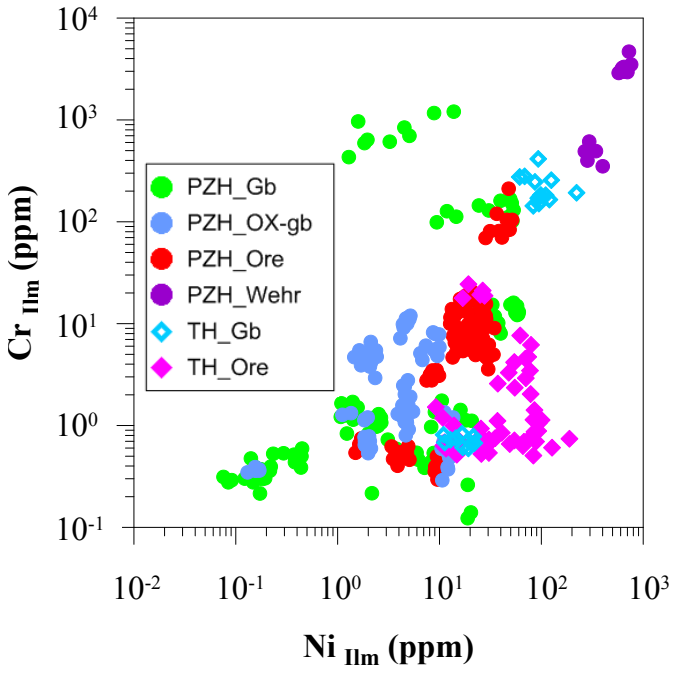

Fig. 4.47 Correlation of Cr contents and Ni in Ilmemite.

Co and Ni show a slightly positive correlation on the logarithm scale (Fig. 4.48 A). The positive correlation between Ni and Ni/Cu, Cu and Cu/Zn, Zn and Zn/Cu, indicate substitution between Ni, Cu and Zn in ilmenite, and little sulphide segregation (Fig. 4.48 B-D). Substitutions of Ga for Al and Ga for Zn in ilmenite are documented by their strong positive correlations (Fig. 4.48 E-F). It is noteworthy that some ilmenites in Panzhihua gabbros and Taihe ore rocks have significant enrichment in Cu and Ni, but depletion in Co.

Figure 4.49 show the co-variation between HFSE in ilmenite. The positive Zr and Hf, and Nb and Ta, indicate most of ilmenites have crystallized from a common magma. A few ilmenite in Panzhihua gabbro have high Hf at low Zr concentration, and fall off the trend defined by the most ilmenite (Fig. 4.49 A-B). Ilmenite in wehrlite (PZ-1) have a distinct lower Hf but high Zr, A few ilmenite in Panzhihua gabbro show high concentrations and large fractionation of Nb and Ta (Fig. 4.49 C-D).

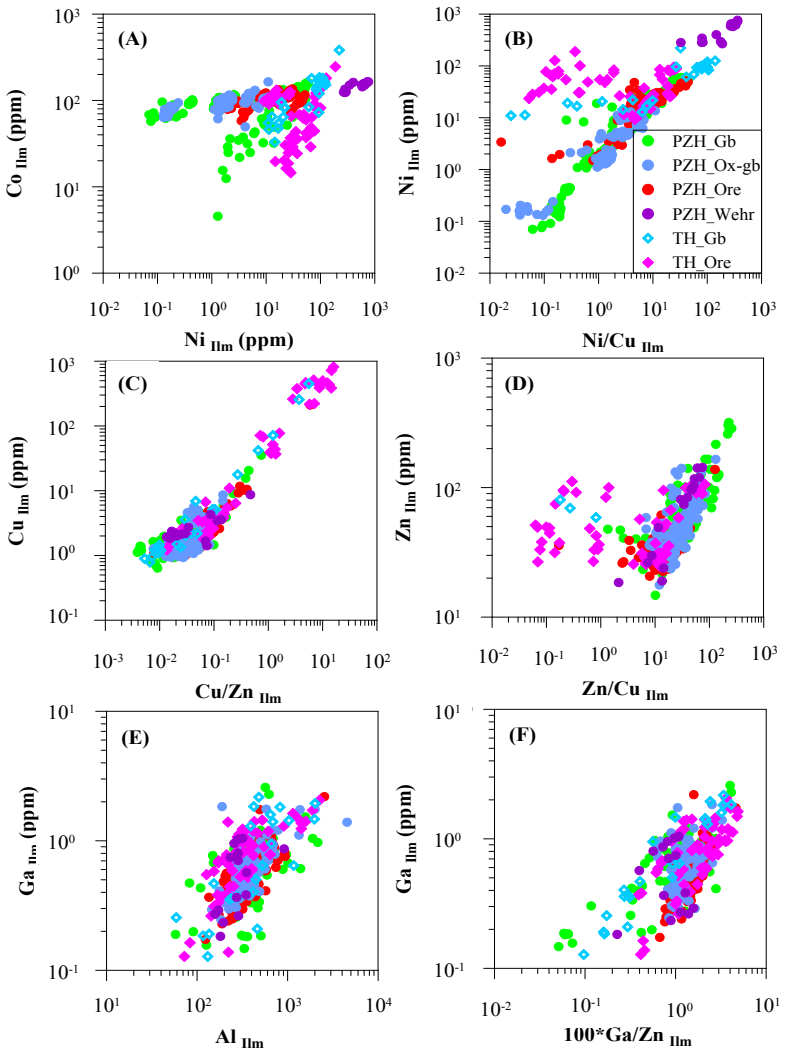

Fig. 4.48 Binary variation between trace elements and ratios in Ilm.

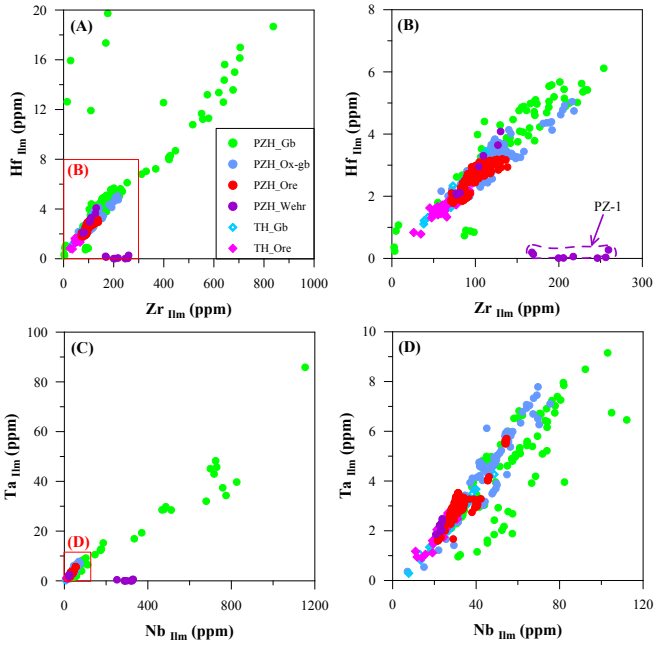

Fig. 4.49 Covariation between HFSE in Ilm.

4.2.3.3 Comparison with ilmenite from other Fe-Ti oxide deposits

Based on the relative proportion of ore minerals, the Fe-Ti oxide ores may be divided into four types: (1) Magnetite ore with significant amount of ilmenite, e.g. ilmenite accounts for up to 15 vol% in the Panzhihua and Taihe gabbroic layered intrusions, southwest China, the Sept-Iles layered intrusion, Quebec, Canada (Namur *et al.*, 2010); (2) Magnetite ore with minor ilmenite, e.g. Skaergaard in East Greenland and Bushveld in South Africa (Jang & Naslund, 2003); (3) Ilmenite ore with minor magnetite, e.g. Tellnes in southwest Norway and Allard Lake anorthosite in Quebec, Canada (Charlier *et al.*, 2007; Charlier *et al.*, 2010); (4) Nelsonite-type with about two-thirds ilmenite, e.g. the Grader layered intrusion in Quebec, Canada (Charlier *et al.*, 2008).

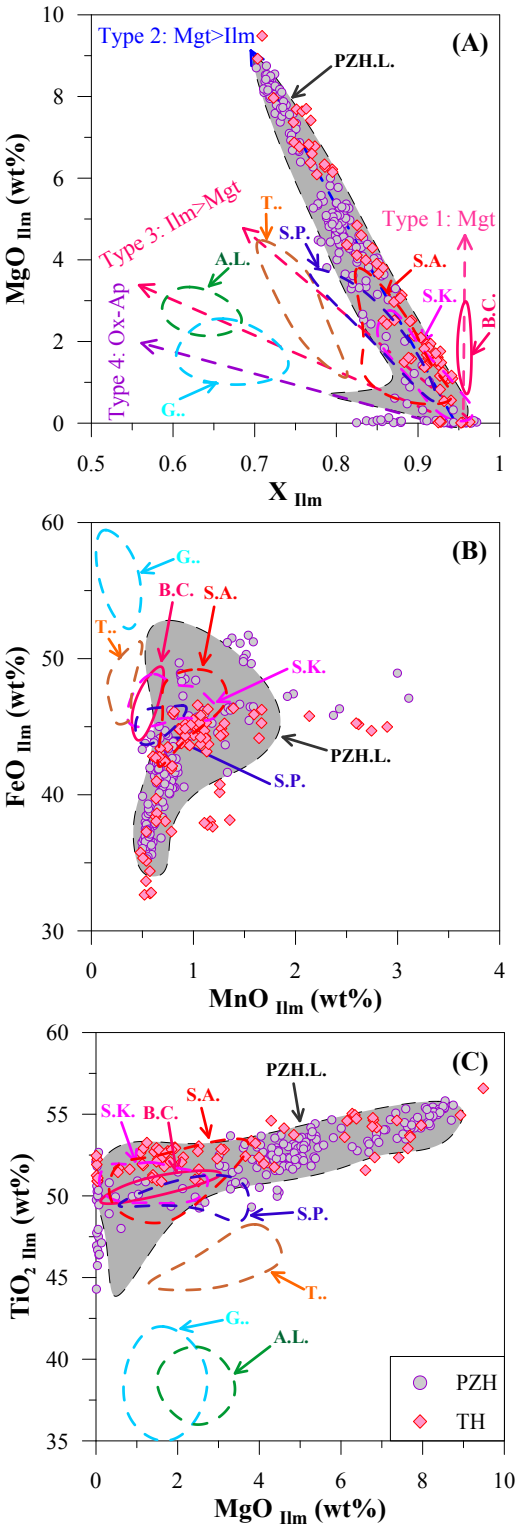

Fig. 4.50 Comparison of major element composition of Ilm from various intrusions.

The Panzhihua-type ilmenites show a wide range of major element compositions, and are characterized by high X_{Ilm}, MgO and MnO contents (Fig. 4.50). The magnetite-dominated deposits in the other layered intrusions contain ilmenite with composition comparable to that of Panzhihua. However, ilmenites from ilmenite-dominated ore that associate with anorthosite have much lower content of MgO, MnO and X_{Ilm}, but high FeO content. Ilmenite hosted in anorthosite show composition between the above two types of ilmenite.

The differences in ilmenite chemistry may have resulted from different parental magma composition, time onset of Fe-Ti oxide crystallization, crystallization conditions and post-cumulus re-equilibrim. In general, the Panzhihua and Taihe ilmenite may crystallize from less evolved magma than the others. Crystallization conditions, e.g. *f*O2, H_2O, etc, may have played an important role in ore diversity. The Fe-Ti-V oxide deposits in the Pan-Xi district may be a new ore type in related to large igneous province (LIP) .

4.2.3.4 Magnetite-ilmenite thermobarometer

In general, magnetite and ilmenite in an individual sample from a layered intrusion should be in equilibrium due to slow cooling. However, since the relatively large variation within a sample, it is inappropriate to use the average composition of magnetite and ilmenite to calculate their equilibrium temperature. Thus, only magnetite and ilmenite (~ 30 pairs) grains with a joint contact were chosen for calculations.

The equilibrium temperature and oxygen fugacity (fO_2) are calculated following the formulation of Ghiorso and Evans (2008). The data show temperature ranging from 485-710˚C and fO_2 from ΔNNO-0.4 to ΔNNO-5.2. However, 90% of the data are falling above 550 ˚C and fO_2 between ΔNNO-1.2 to ΔNNO-3.1. These results are overall higher than previous calculations utilizing QUILF program of Andersen *et al* (1993), which givaen a temperature range of 500 to 650˚C and fO_2 of ΔFMQ-1 to ΔFMQ-3 (Pang *et al*., 2008b). These inconsistences arise from the difference in calculation methods, as the QUILF program consistently underestimates both temperature and fO_2 by average absolute deviation of 60˚C and 1.09 log units, respectively (Blundy & Cashman, 2008). Hence, the exsolution textures may start developing at 710˚C and fO_2 of ΔNNO-0.4. This is in accordance with the estimates based on on the combination of the two-oxides and oxide-clinopyroxene equilibria (Pang *et al*., 2008b).

4.2.4 Pyrrhotite Chemistry ($Fe_{1-x}S$)

Base-metal sulphides in Panzhihua gabbroic layered intrusion include pyrrhotite, cobaltian pentlandite, pentlandite, chalcopyrite, and secondary pyrite and vaesite (Pang, 2008). Pyrrhotite ($Fe_{1-x}S$) is the main phase that accounts for over 80% of the total sulphides amount. Representative major and trace element composition of pyrrhotite from the Panzhihua intrusion are present in Table 4.12. The Fe and S of pyrrhotite show a well correlation (R^2=0.98, Fig. 4.51). Fe/S ratio vary between 0.84 to 1.00, slightly wider range than previoous results (Fe/S=0.85 to 0.99, Pang, 2008). Two populations, seperated by a gap of Fe/S ratio (0.925

to 0.945) have been observed (Fig. 4.52, Fig. 4.53). Over 80% of pyrrhotite have Fe/S ratios between 0.850 to 0.925 (Fig. 4.52).

Figure 4.53 shows that all pyrrhotite in massive ores from the Lanshan mine have high Fe/S ratio, in conpared with only one sample from the Zhujiabaobao mine (Fig. 4.53). Moreover, pyrrhotite in gabbroic rocks of the Lanshan mine show higher Fe/S ratio than the Zhujiabaobao gabbro. In general, pyrrhotite in gabbroic rocks are less Fe-rich, as shown by lower Fe/S ratio (<0.90).

Pyrrhotites contain up to 1.12 wt% Co, 0.55 wt% Ni and 0.34 wt% Cu. The LA-ICP-MS *in-situ* analysis on pyrrhotite have shown the ranges are: 35 to 4168 ppm Co, 35 to 5006 ppm Ni, and 1.2 to 100.1 ppm Cu. The Se concentration of pyrrhotite varies from 23.6 to 98.5 ppm. Other trace elements include (in ppm): 0.05 to 0.9 Ag, 0.06 to 4.45 Pb, 0.02 to 0.33 Bi, 0.22 to 0.67 Te, 0.08 to 0.7 Cd, 0 to 0.8 As, 0 to 0.02 Au. The Panzhihua pyrrhotites are PGE-depleted with PPGE higher than IPGE. The Pt and Pd abundances are ranging between 0-0.31 and 0-0.16 ppm, respectively, in comparison to up to 0.04 ppm of Ir. The averaged total Pt+Pd is 0.05 ppm.

Figure 4.54 show correlations between S and Co, Ni and Cu. The scatter pattern may be a result from re-equilibria with Fe-Ti oxides, as observed from the mineral textures (e.g. Fig. 3.12 b and h; Fig. 3.13 g). This re-

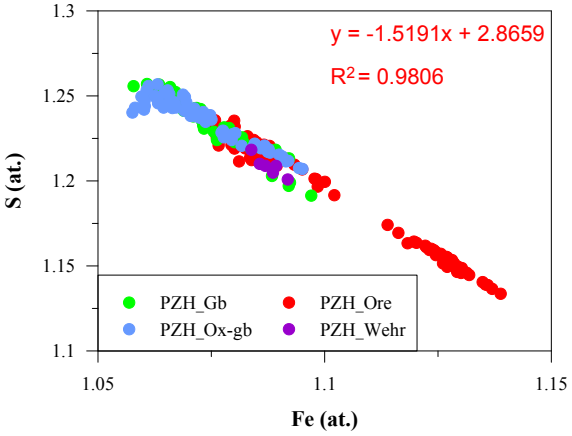

Fig. 4.51 Correlation between Panzhihua Po atomic Fe and S.

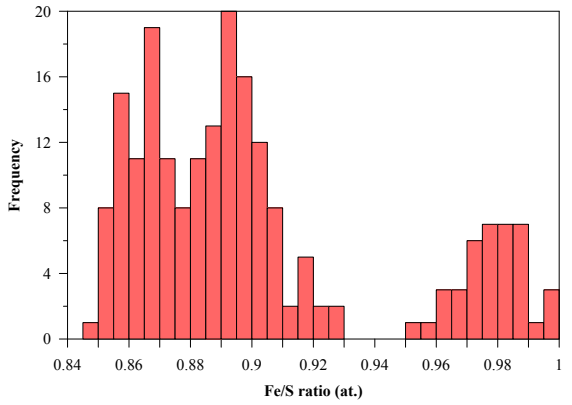

Fig. 4.52 Frequency distribution of atomic metal/sulfur ratios observed in 205 Po analyses from the Panzhihua Intrusion.

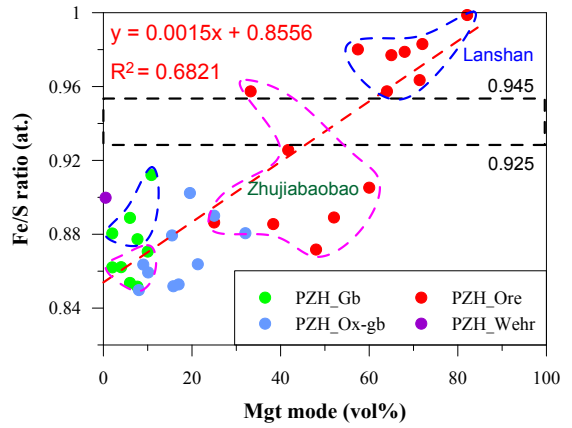

Fig. 4.53 Correlation between Po Fe/S ratios and Mgt modal proportion in the host rocks.

Table 4.12 Representative analyses of major (EMPA) and trace (LA-ICPMS) element composition in Po from the Panzhihua Intrusion.

Sample	PZ-6	PZ-9	PZ-27	PZ-28	PZ-15	PZ-33	PZ-37	PZ-41	PZ-42
Rock	Wehr	Gb	ore	Leucogb	Ore	Ore	Ox-gb	Ox-gb	Ox-gb
n1.	6	6	12	4	5	6	8	7	7
Fe	60.747	60.184	60.562	59.763	63.023	60.068	62.453	59.390	59.868
S	38.755	39.379	39.260	39.796	36.912	39.556	37.446	40.023	39.797
Ni	0.494	0.262	0.038	0.138	0.011	0.119	0.009	0.106	0.010
Cu	0.001	0.015	0.017	0.053	0.010	0.008	0.053	0.035	0.060
Co	0.004	0.160	0.124	0.304	0.045	0.249	0.092	0.445	0.266
Total	100.00	100.00	100.00	100.05	100.00	100.00	100.05	100.00	100.00
Number of ions									
Fe	1.069	1.071	1.067	1.050	1.119	1.062	1.098	1.049	1.061
S	1.188	1.221	1.205	1.218	1.142	1.218	1.146	1.232	1.229
Ni	0.008	0.004	0.001	0.002	0.000	0.002	0.000	0.002	0.000
Cu	0.000	0.000	0.000	0.001	0.000	0.000	0.001	0.001	0.001
Co	0.000	0.003	0.002	0.005	0.001	0.004	0.002	0.007	0.004
Fe/S	0.90	0.88	0.89	0.86	0.98	0.87	0.96	0.85	0.86
Co/Ni	0.01	0.61	3.28	2.20	4.24	2.09	10.42	4.18	26.70
Ni/Cu	525.65	18.53	2.44	2.79	1.18	16.27	0.18	3.24	0.18
Trace element (ppm)									
n2.	10	12	11	13	7	11	0	10	11
Co	35.38	1828	1329	2764	459.6	2516	731.4	4168	2939
Ni	5006	3165	395	1992	35.42	1281	35.19	1231	49.32
Cu	100.10	2.34	1.46	3.86	0.90	1.19	12.15	6.54	2.38
Ag	0.47	0.28	0.06	0.17	0.90	0.10	0.05	0.13	0.06
Pb	4.45	1.14	0.43	2.91	2.64	1.86	0.10	0.25	0.06
Bi	0.33	0.08	0.08	0.08	0.27	0.32	0.02	0.18	0.05
Te	0.22	0.65	0.29	0.26	0.37	0.67	0.23	0.59	0.37
Re	b.d.l	b.d.l	b.d.l	b.d.l	b.d.l	b.d.l	b.d.l	b.d.l	b.d.l
Ir	b.d.l	b.d.l	b.d.l	b.d.l	b.d.l	b.d.l	b.d.l	b.d.l	b.d.l
Pt	b.d.l	b.d.l	0.01	b.d.l	0.02	b.d.l	0.02	b.d.l	b.d.l
Au	0.02	0.01	0.02	b.d.l	0.01	b.d.l	0.02	b.d.l	b.d.l
As	b.d.l	b.d.l	0.80	b.d.l	0.41	0.81	b.d.l	b.d.l	b.d.l
Cd	0.17	0.11	0.30	b.d.l	0.47	0.12	0.31	0.20	0.08
Se	23.57	62.84	46.72	56.39	61.27	58.64	26.85	98.49	67.23
Pd	0.002	b.d.l	0.004	0.004	0.004	b.d.l	0.003	0.014	0.002

1. ***n1*** and ***n2***: number of analyis of EMP and LA-ICPMS
2. b.d.l- below the detection limit

equilibrium process enriched Fe but depleted in Co and Ni in pyrrhotite. This observation may explain the roughly positive correlation between magnetite Co and Ni contents and modal proportions (Fig. 4.55), as Co and Ni were exchanged with the coexisting pyrrhotite. The negative correlations between pyrrhotite Co, Ni contents and magnetite modal proportions may be obscured by partition behaviors of Co and Ni in multiple cumulus minerals, e.g. olivine, magnetite (Table 4.3).

Sulfur fugacity may be calculated using pyrrhotite composition by the method of Toulmin Iii and Barton Jr (1964). The Cu content in our pyrrhotite is small (Cu<0.34 wt%), hence the effect of Cu on overestimation of fS_2 is limited (Mengason *et al.*, 2010). With the temperature derived from plagioclase composition, the calculated fS_2 in gabbro below the first and above the last ore rocks are -0.078 and 0.77, respectively.

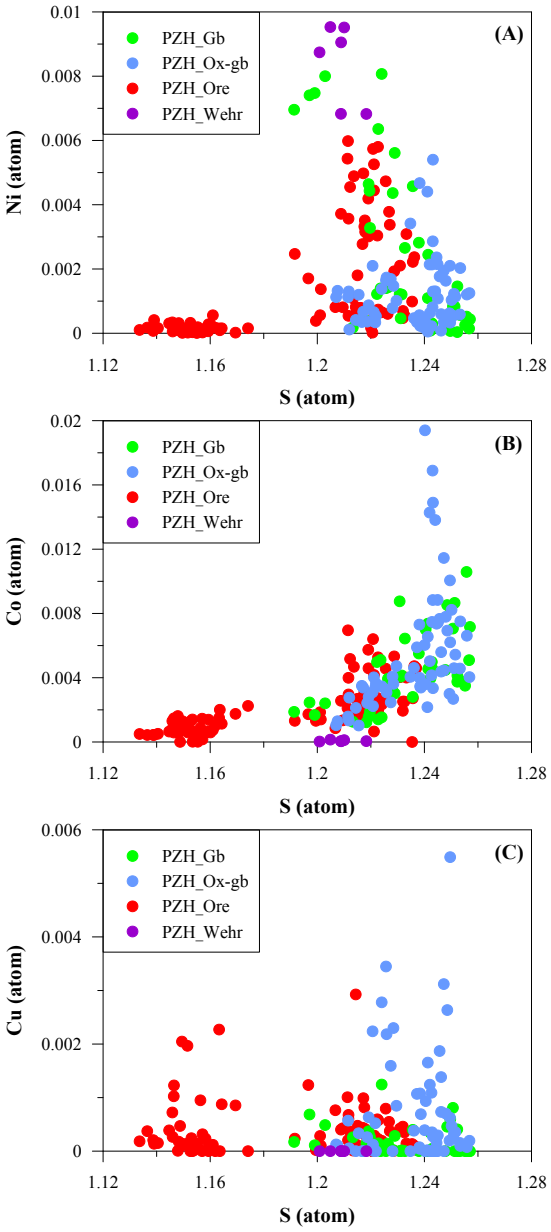

Fig. 4.54 Correlation between S and Ni, Co atomic content.

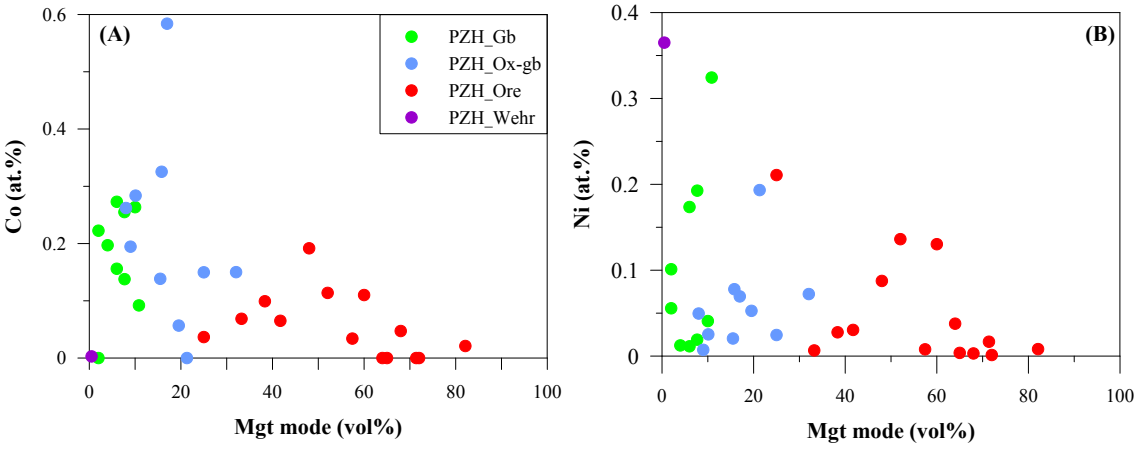

Fig.4. 55 Correlation between Mgt mode and Co, Ni contents in Po.

4.3 Summary

The main points envisaged from detail examination of whole rock and mineral chemistry, as well as genetic implications, are summarized as follow.

1. The Panzhihua rocks have a wide range of bulk compositions, which bracket that of the Taihe Intrusion. These rocks have consistent strong Cr, Ni depletion, Pb, Sr, Eu and Ti enrichment, flat LREE and moderately fractionated HREE, and comparable incompatible elements distribution patterns, indicating a common origin.
2. The Panzhihua and Taihe whole rock geochemistry are apparently controlled by mineral modal proportions and compositions, and likely to be mixtures of Fe-Ti oxides and silicate minerals in various proportions. The Fe-Ti oxide pole has a limited compositional range, reflecting a relatively constant ratio of Mgt to Ilm (e.g. Mgt/Ilm close to 4), in contrast with the wide variations of the silicate pole, due to great variation of ratios of Cpx to Plag. Besides, addition of cumulus Ol and/or Ap, and prevasive Hbl may have promoted the diversity of silicate pole composition. Trapped liquids may have little effect on shift of whole rock (and minerals) composition, due to very small amount.
3. The Fo content of Ol varies between 62 to 86 for the Panzhihua rocks. Ol in massive ore rocks have much higher Fo contents (Fo=72-86) than gabbroic rocks (Fo<73, mostly<68), whereas Ol in oxide-gabbro contain moderately compositions (Fo=68-79), indicating re-equilibration between Mgt and Ol, resulting in elevation of Fo. Ol in the MGZ wehrlite (Fo=80-82) are relatively more primitive than that from the MZa wehrlite (Fo=73-75) and other rocks except for one ore rock. The Panzhihua Ol are Ni-depleted except for that in wehrlite and one fine-grained gabbro in the MGZ.
4. The Mg# of Cpx varies from 72 to 82 in the gabbro. Cpx in the oxide-gabbro and massive ore rocks have composition within that of gabbro, however, it is more primitive in wehrlite ($Mg\#_{Cpx}$=78-85). Re-equilibration with Fe-Ti oxides has little effect on Cpx compositional changes.
5. The An content of Plag in gabbro varies between 42 to 74 in gabbro, 54 to 64 in oxide-gabbro, 54 to 78 in massive ore. The Plag in MGZ wehrlite show extremely calcic-rich composition (An=82-85) than that of the MZa wehrlite (An=66-70). Rapid cooling and/or wall-rock contamination may have contributed the formation of high-An Plag in the MGZ wehrlite.
6. Temperature calculation based on Ol-Cpx Fe-Mg exchange equilibrium show that the LZ

and MZa were formed in the temperature interval of 1126 to 1176 °C, but the main ore formation period was between 1121 to 1142 °C .The temperature calculated based on Plag composition is 1085 to 1106 °C for the massive ores formation period. The much lower temperature may indicate later crystallization of Plag in the parental magma. However, the small temperature interval is the same as that calculated using Ol-Cpx thermometer. It hence indicates that the Panzhihua Fe-Ti oxide ores were formed from a parental magma with relatively constant compositions at an early stage of magma differentiation.

7. Panzhihua Mgt have high-Cr and low-Cr populations. The former only occur in three wehrlite from the MGZ and MZa, whereas the latter form Fe-Ti oxide deposit. No high-Cr Mgt are found in the Taihe intrusion in this study. High-Cr Mgt contain higher content of Ni, MgO, but lower FeO and TiO_2 than low-Cr Mgt. The high-Cr Mgt may represent a intermediate composition between that of the Noril'sk-Talnakh intrusion and layered intrusions. Mgt in various rock types show comparable distribution patterns of elements, indicating they may have the same origin. The MgO content in low-Cr Mgt show positive correlation with Mgt modal proportion, whereas HFSE and Sc show correlation with X_{Usp}. The Taihe Mgt have composition within range of Panzhihua Mgt.
8. No distinctive composition have been found between different textural Mgt, indicating a result of relatively complete re-equilibria during slow cooling. However, Mgt inclusions contain lower content of Cr, V but higher content of Mn, Zr and Nb than that in other appaerances. This may be a result of subsolidus re-equilibratia of Mgt inclusions with their host minerals.
9. Ilm in wehrlite have higher Cr, Ni and Mg contents, compared with other rocks that are significantly depleted in these elements. Ilm in various rocks have similar elemental distribution patterns. Except for some grains, trace elements in Ilm show substitution for one another in crystal structures. Post-cumulus process have more significance in modification of Taihe Ilm. The Panzhihua Ilm are more MgO rich than Ilm from other Fe-Ti oxide deposits, probably reflecting crystallization from less evolved parental magma.
10. Po is the dominated sulphide mineral in both Panzhihu and Taihe intrusion. Po are depleted in PGE and Ni. Re-equilibria with oxides and silicates may account for the scatter Ni, Co and Cu data. A small gap of Fe/S ratio has been recognized, as well as differences between Po from Lanshan and Zhujiabaobao mines.

CHAPTER 5

VERTICAL PROFILES THROUGH THE INTRUSIONS

5.1 Introduction

This chapter presents chemical and mineralogical variations along vertical profiles throught the Panzhihua and Taihe gabbroic layered intrusions. The purpose of these investigations is to derive information on magma differentiation processes, parental magma compositions and their changes as differentiation continuous, and processes involved in the formation of Panzhihua-type deposits, such as magma replenishment, mixing, crustal contamination, and fractional crystallization.

5.2 Vertical Profiles through the Panzhihua Intrusion

5.2.1 Whole-rock Chemistry

In some studies, the appearance of apatite in the Panzhihua intrusion was used as an identifier of the upper middle zone (MZb) (Pang *et al*., 2008), whereas other studies used it to mark the beginning of the upper zone (Li & Mao, 1982; Wang, 1982; Song *et al*., 2013). Here we use the former classification. However, based on our new geochemical data for the ~ 700 m thick Fe-Ti oxides concentration zone (the LZ and lower part of the middle subzone MZa), we have combined this part of the intrusion into the Main Mineralization zone (MMZ). The upper part of the middle subzone MZa, which contains oxide-rich gabbros, is called in this study the Subordinate Mineralization Zone (SMZ) (See Table 2.2). MZb is used following Pang *et al* (2008).

5.2.1.1 Whole-rock major element compositions

The marginal zone (MGZ) consists mainly of fine-grained gabbro, some of which contain abundant hornblende and olivine. Wehrlite and massive Fe-Ti oxide ore layers are also observed in the MGZ. These variations in mineralogy result in large variations in whole rock compositions (Fig.5.1). A systematic increase in Mg# within the MGZ above the massive ore layer (Mg# 18.5) to wherlite (Mg# 82.0) reflects increasing amount of olivine, as can be seen by higher rock MgO contents (Fig.5.1 A, B). The $SiO_2/Fe_2O_3^*$ ratio, an indication of the pro-

portions between the silicate pole (gabbro) and the oxide pole (Fe-Ti oxides), ranges from 0.2 to 4.4. The lowest values occur in the massive ore. The ratios of elements concentrated in the oxide pole (e.g. $Fe_2O_3^*/TiO_2$, TiO_2/V_2O_5) show little variations, in contrast to the ratios of silicate components (e.g. CaO/SiO_2, CaO/Al_2O_3) (Fig. 5.1 F-G). CaO/Al_2O_3 values are higher in wehrlite, and are relatively similar in gabbros and ores. P_2O_5 is anti-correlated with Fe within the MGZ (Fig. 5.1 H). Ratios of P_2O_5/K_2O and Na_2O/K_2O display a general decrease trend upwards to the lower contact of the MMZ (Fig. 5.1 I-J).

The main mineralization zone (MMZ) comprises a lower coarse-grained but less layered gabbro, and an upper layered medium-grained gabbro. Fe-Ti oxide ores (massive or disseminated) occur as layers or lenses interlayered with gabbro. One layer of fine-grained wehrlite and several leucogabbros are found within the MMZ. Compared to the MGZ, the major element compositions of rocks from this interval are nearly constant, especially for the massive ore rocks (Fig. 5.1). Variations within different gabbros are fairly small. Significant differences are observed between the compositions of different rock types, which suggests the control of mineral modal porportions on whole rock major element compositions, e.g. ore rocks have lower Mg#, $SiO_2/Fe_2O_3^*$, P_2O_5, and Na_2O/K_2O, but higher $Fe_2O_3^*/P_2O_5$ than gabbros.

The subordinate mineralization zone (SMZ) is largely made up of oxide-rich gabbros. No massive ores have been found in this zone, but the Fe-Ti oxides are much more abundant than in the MZb above. One anorthositic leucogabbro occurs in the middle, and another leucogabbro occurs at the top of the SMZ. The SMZ is characterised by a progressive increase of TiO_2/V_2O_5 values (from 39.1 to 54.5), and a general upward change in $Fe_2O_3^*/P_2O_5$ from 2949 to 628, and Na_2O/K_2O from 7.5 to 19.5. Note significantly different compositions of the anorthositic leucogabbro in the middle of the SMZ immediately above an oxide-rich gabbro. The other major element content and ratio trend are similar to the MMZ.

The main rock within the MZb is layered apatite-gabbro. Whole rock P_2O_5 increases sharply from 0.03 to 2.35 wt%, accompanied by an increase in TiO_2/V_2O_5, and a decrease in $Fe_2O_3^*/P_2O_5$ (54.5 to 110.5, and 628 to 6, respectively). These changes reflect an increase in ilmenite relative to magnetite, and increases of the apatite mode.

5.2.1.2 Whole-rock trace element composition

A representative set of samples, covering all major rock types, have been analysed for trace element contents.

The MGZ, compared with the other subzones, has more complex variation patterns in

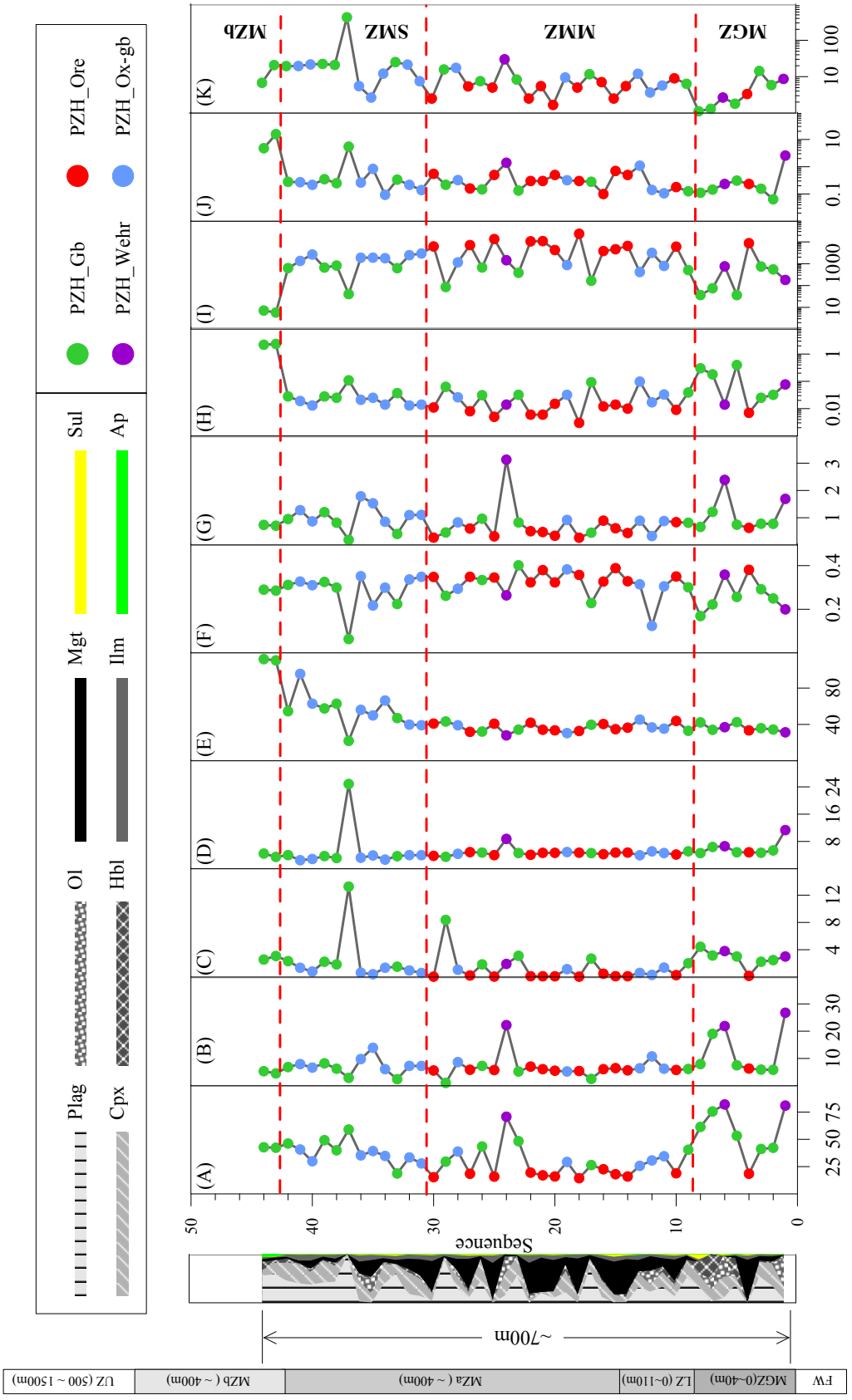

Fig. 5.1 Variations of whole-rock major element compositions and ratios agaist stratigrapgic height of the Panzhihua Intrusion.

whole rock trace elements (Fig. 5.2). The concentration of strongly compatible elements Cr and Ni varies over two orders of magnitude from 18 to 2428 ppm for Cr and 56 to 1197 ppm for Ni, reflecting olivine and magnetite control on Cr and Ni. Major changes in Mg# are also seen in Cr concentrations, which display a 'Z'-type pattern within the MGZ. Ni, on the other hand, is nearly constant in all rock but the olivine-rich wherlites and one gabbro. The V, Co, Zn and Sc concentrations in MGZ rocks are less variable, with 288 ~ 577 ppm V, 71 ~ 116 ppm Co, and 84 ~ 130 ppm Zn (with a maximum in the ore for all 3 elements), and 23 ~ 30 ppm Sc. The MGZ rocks have variable Sr contents reflecting variations plagioclase modal proportions. The Cu/Ni values show a general anti-correlation wiith Ni. The Zr content, Zr/Y ratio and total amount of REE display overall upwards increases, indicating the increasing amount of intercumulus liquids.

The MMZ shows much less variation in the most elements and ratios when compared with the MGZ (Fig. 5.2). However, three cyclic units have been identified in terms of Cr and Sr, as these elements strongly concentrate in two minerals, magnetite and plagioclase. Cr decreases from massive ore through oxide-rich gabbro to gabbro, whereas Sr displays the opposite trend. The large difference in magnetite modal proportions is the likely cause of large variations in Cr and Sr in the MMZ gabbro. These cyclic features are not as obvious for other elements. It is noteworthy that the massive ore rocks in the MGZ and at different levels of MMZ show very similar elemental concentrations and ratios, except for slightly higher Cr content in the MGZ ore. The three cyclic units shown on Fig. 5.2 correspond to the lower three cyclic units identified by Zhang *et al*. (2011) and Song *et al*. (2013) who identified a total of five cyclic units within the lower mineralized stratigraphy.

Another two cyclic units starting with oxide-rich gabbro are found in the SMZ (Fig. 5.2). These units are less prominent due to smaller differences in mineral modal porportions. Up the sequence through the SMZ, decreases in Cr, Ni, V, Zr contents and Zr/Y ratio, and increases in Sr, total REE contents and Cu/Ni ratio are observed.

The MZb is marked by an abrupt increase in the total amount of REE (from 23.8 to 142.2 ppm), and decreases in Sc content (from 25.9 to 11.4 ppm) and Zr/Y ratio (from 2.1 to 0.6) (Fig. 5.2). However, the concentrations and ratios of the other elements in apatite gabbro are either similar to, or forming continuous trends with those in the topmost SMZ gabbro beneath the apatite-gabbro.

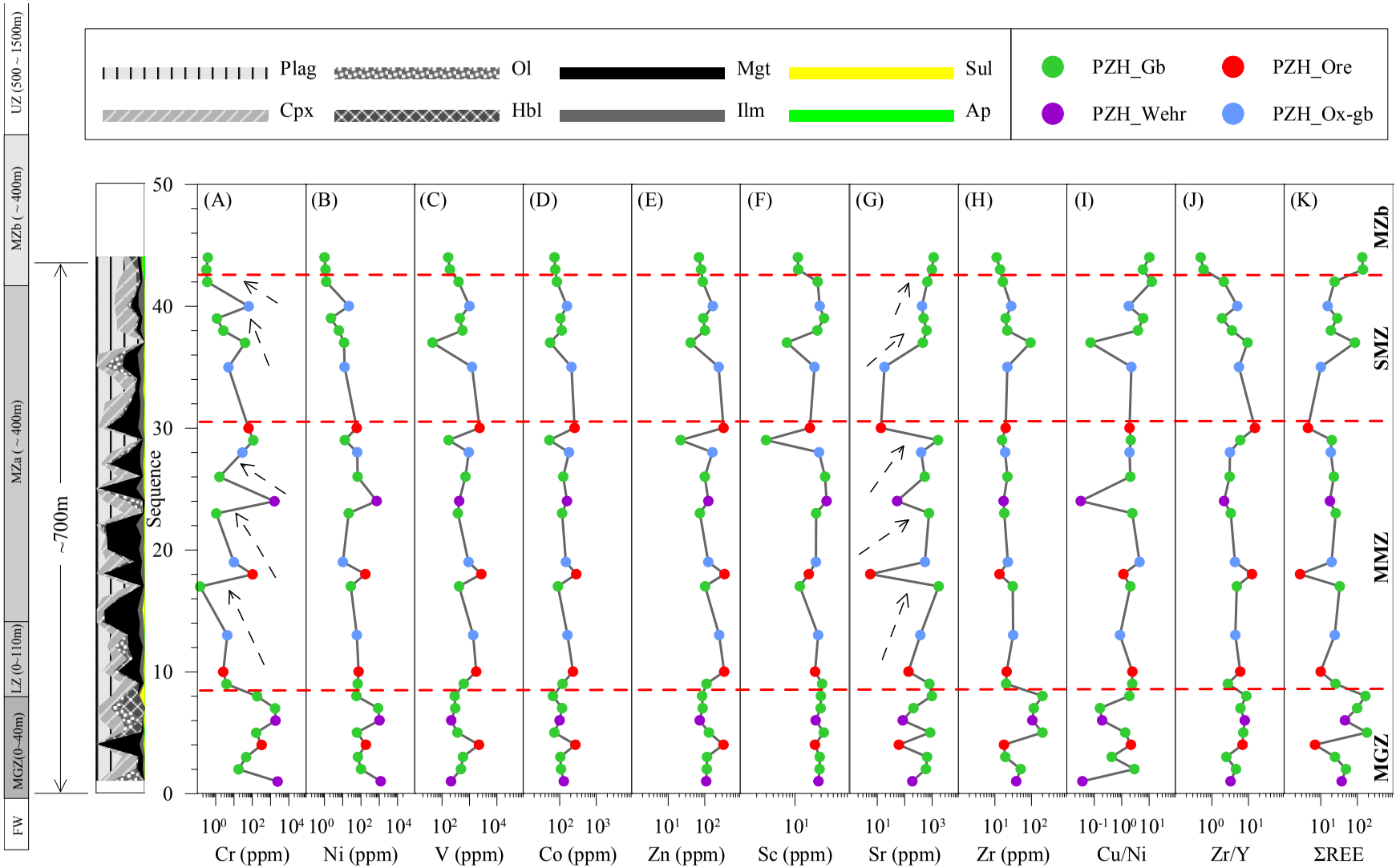

Fig. 5.2 Variations of whole-rock trace element compositions and ratios agaist stratigrapgic height of the Panzhihua Intrusion.

5.2.2 Mineral Chemistry

5.2.2.1 Silicate minerals

Figure 5.3 shows the variations of the main compositional parameters and minor oxide components in silicate minerals (clinopyroxene plagioclase and olivine) from the Panzhihua Intrusion. clinopyroxene is the most common cumulus mineral in Panzhihua, followed by plagioclase. In comparison, olivine is not present in all of the studied rocks. The data represent averaged values of appoximately 6 grains of clinopyroxene, 5 grains of plagioclase, and 4 grains of olivine in an individual sample. The error bars denote 2σ standard deviation, which covers 95 % of the compositional scatter within the sample.

The MGZ shows no systematic variations of silicate mineral compositions (Fig. 5.3). Two reversals are recognized in terms of Mg# of clinopyroxene. The lower one (R1 in the diagram) is represented by a slight increase of $Mg\#_{Cpx}$ from 74.8 to 76.4, and the upper reversal (R2) is marked by a sudden increase from 74.3 to 83.3 (Fig. 5.3 A). TiO_2 and Al_2O_3 contents of clinopyroxene are much higher in the second wherlite, but otherwise show a steady deacrease up the section (Fig. 5.3 B-C). R1 is possibly reflected in plagioclase composition (Fig. 5.3 D-F). Olivine is absent in some rocks in the MGZ. Wherlites are characterised by higher Fo and lower Mn contents compared to gabbros (Fig. 5.3 G-H).

The MMZ is characterised by nearly constant clinopyroxene compositions (Fig. 5.3 A-C), after an abrupt change at the boundary with the MGZ ($Mg\#_{Cpx}$ decreases from 81.1 to 75.9). Nevertheless, three reversals (R3-R5) are recognizable in silicate mineral composition, particularly that of clinopyroxene and plagioclase (Fig. 5.3 A-F).

The first reversal in the MMZ (R3) occurs within the lower zone of MZa (Pang *et al.*, 2009). It is identified by subtle increases in $Mg\#_{Cpx}$ from 75.2 to 76.9, TiO_2 from 1.0 to 1.2 wt%, and Al_2O_3 from 3.0 to 3.3 wt% (Fig. 5.3 A-C). This reversal is also seen in plagioclase composition, with An_{Plag} increases from 58.0 to 62.9, FeO from 0.23 to 0.33 wt% (Fig. 5.3 D-E). The second and third reversals (R4 and R5) are characterized by similar increases ($\Delta Mg\#_{Cpx}$=3-4, $\Delta TiO_{2\ Cpx}$=0.3-0.5 wt%, $\Delta Al_2O_{3\ Cpx}$=0.8-1 wt%, ΔAn_{Plag}=5.2-9.2, $\Delta P_2O_{5\ Plag}$=0.02-0.03 wt%). Note the most Ca-rich plagioclase in these reversals are always occuring at a higher level than the most Mg-rich clinopyroxene (Fig. 5.3 A, D), which implies redistribution of crystals due to plagioclase buoyancy and crystal settling. In addition, the FeO contents decrease in plagioclase in R4 and R5 (ΔFeO_{Plag}=0.07-0.32 wt%), in contrast to that in

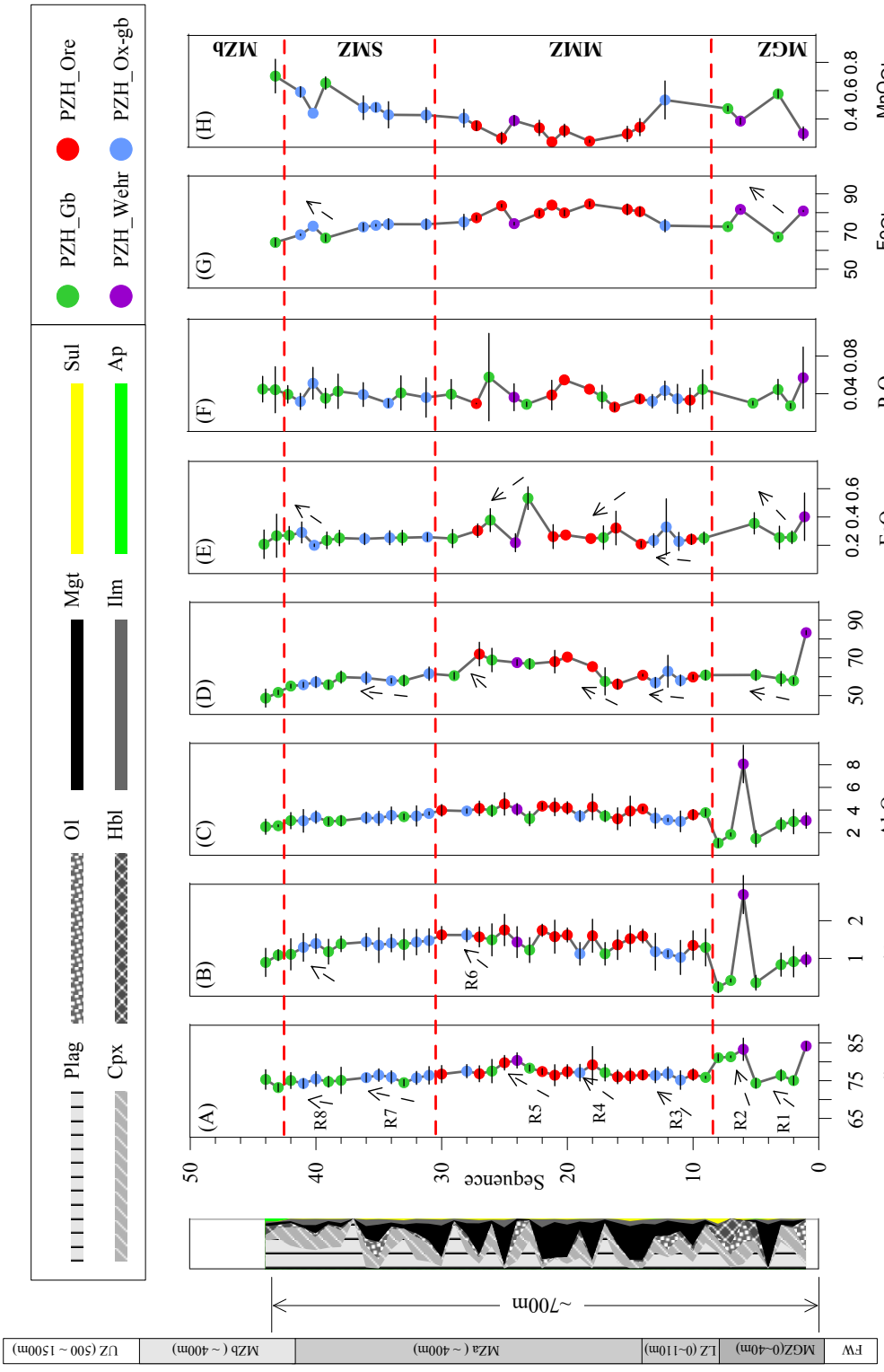

Fig. 5.3 Variations of silicate mineral compositions agaist stratigraphic height of the Panzhihua Intrusion. The data are plotted with 2σ error ellipses. R1 represents reversal 1, and so on.

R1, indicating depletion of iron in parental magma due to massive fractional crystallization of magnetite. As documented in the previous chapter, the olivine compositions have been modified by re-equilibration with Fe-Ti oxides, resulting in elevated Fo contents within the ore. However, olivine in the oxide-rich gabbro below and above massive ore rocks has compositions similar to the oxide-poor wehrlite in the MMZ (Fo ~74).

The SMZ is characterized by decreasing Fo from 73.8 to 66.5, and increasing MnO contents (Fig. 5.3 G-H). A similar general decrease is seen in $Mg\#_{Cpx}$ and An_{Plag} (Fig. 5.3 E-F). Two small reversals are identified in the SMZ. The lower one (R7) is recognized by a slight increase of $Mg\#_{Cpx}$ and An_{Plag} (Fig. 5.3 A and D). The upper reversal (R8) is identified by increases in $Mg\#_{Cpx}$, $TiO_{2\ Cpx}$, An_{Plag}, FeO_{Plag} and Fo_{Ol} (Fig. 5.3 A, B, E, G).

The $Mg\#_{Cpx}$ in the MZb apatite-gabbro increase slightly from 73.2 to 75.3 (Fig. 5.3 A), whereas the continuous decreases in TiO_2 and Al_2O_3 contents of clinopyroxene extend from the SMZ to MZb (Fig. 5.3 B-C). The An_{Plag} also exhibits a continuous upwards decrease from 51.7 to 48.7 (Fig. 5.3 D). The FeO_{Plag} decreases but $P_2O_{5\ Plag}$ increases, although their ranges are relatively wide (Fig. 5.3 E-F). Descending Fo and increasing MnO of olivine from SMZ to MZb are also observed (Fig. 5.3 G-H).

5.2.2.2 Fe-Ti oxide minerals: Magnetite and Ilmenite

Figure 5.4 and 5.5 show vertical variations of magnetite and ilmenite compositions, respectively. Due to extensive exsolution of spinel and ilmenite in magnetite, all minor and trace elements are plotted using data from LA-ICP-MS analyses which represent a large mineral volume than EMPA. However, the X_{Usp} and X_{Hem} values are calculated based on the major element composition measured by EMPA.

Panzhihua magnetite are enriched in titanium in massive ores (higher Ulvospinel component) compared to oxide-poor gabbros and wehrlite (Fig. 5.4 A). Exsolution of Mg-Al spinel alone cannot explain the nearly constant content of Al but variable Mg (Fig. 5.4 B-D). Post-magmatic re-equilibraion between magnetite and olivine, which leads to increased Fo content in olivine, is unlikely to account for higher Mg content of magnetite, as Mg diffuses into olivine. The higher Mg content of magnetite in massive ores likely reflects the original magmatic composition of magnetite.

A total of eight reversals (R1-R8) can be identified based on Cr content of magnetite (Fig. 5.4 E). LA-ICP-MS mapping of element distributions in silicates and magnetite have shown little zoning for all elements but Cr in clinopyroxene. This suggests that diffusion of

Cr under subsolidus conditions is too slow to re-equilibrate Cr contents. Thus Cr appears to be the best element to assess variations in parental magma compositions as it is inert, strongly compatible in magnetite, and resistant to changing redox conditions.

Two reversals (R1 and R2) are found in the MGZ, where Cr increases from 182 to 342 ppm and 2087 to 177063 ppm. Similar trends are observed for Ni, X_{Usp}, Mg and Mn contents in magnetite for both reversals. However, the R1 is not seen in the abundance of moderately compatible to incompatible elements such as V, Zn and Ga (Fig. 5.4 G-I). Incompatible elements (e.g. Zr and Sn) do not follow the trends observed in compatible elements (Fig. 5.4 J-K)

The MMZ has four (R3-R8) reversals recognized at different levels of stratigraphy, similar to what is observered in clinopyroxene compositions. R3 occurs within the LZ of Zhou *et al.*(2005) and Pang *et al.* (2009). The concentrations of Cr in magnetite increase by 3 orders of magnitude from 2 to 2137 ppm (Fig. 5.4 E). The overlying Cr-rich magnetite hosted in oxide-gabbro contain more abundant olivine than the underlying Cr-poor magnetite hosted in oxide-gabbro. This reversal is also evident in X_{Usp}, Mg and Ni contents of magnetite (Fig. 5.4 A, C, F). R4 is marked by an abrupt increase of Cr, from 3 ppm in the underlying leucogabbro to 188 ppm in the overlying massive ore. Also, X_{Usp}, Mg and Ni display similar increasing trends, but Ga and Sn show opposite trends (Fig. 5.4 I, K). R5 is characterized by a dramatic increase in Cr content from 388 ppm in a massive ore to 21971 ppm in an overlying wehrlite (Fig. 5.4 E). Cr correlate positively with Ni but negatively with Mg in R5 (Fig. 5.4 C, F). V, Zn and Ga show similar trends with Cr and Ni (Fig. 5.4 G-I). R6 is recognized by an abruptly increase in Cr, from 1 ppm in a leucogabbro to 319 ppm in the overlying ore (Fig. 5.4 E). Less pronounced reversals are seen in X_{Usp}, Mg, Mn, Ni, Zr contents, however, V, Ga and Sn show normal trend of decrease.

Increases of Cr contents from 21 to 110 ppm and 5 to 289 ppm, which occur against a progressive decrease in Cr contents, mark R7 and R8 in the subordinate mineralization zone (SMM) (Fig. 5.4 E). For both reversals, contents of Mg, Mn, V and Ga increase along with increasing Cr contents, however, X_{Usp} and Ni decrease in R7, but increase in R8.

Magnetite in the MZb is characterized by progressive decrease in X_{Usp}, Al, Mg, V, Zr and Sn, but slight increases in Cr and Ni (Fig. 5.4). This may be explained by the cessation of crystallization of significant amounts of magnetite.

Ilmenite compositions are shown in Fig. 5.5. The Panzhihua ilmenite contain 1 to 11% hematite endmember ($0.01<X_{Hem}<0.11$), less than in the ores (Fig. 5.5 A). However, Mg con-

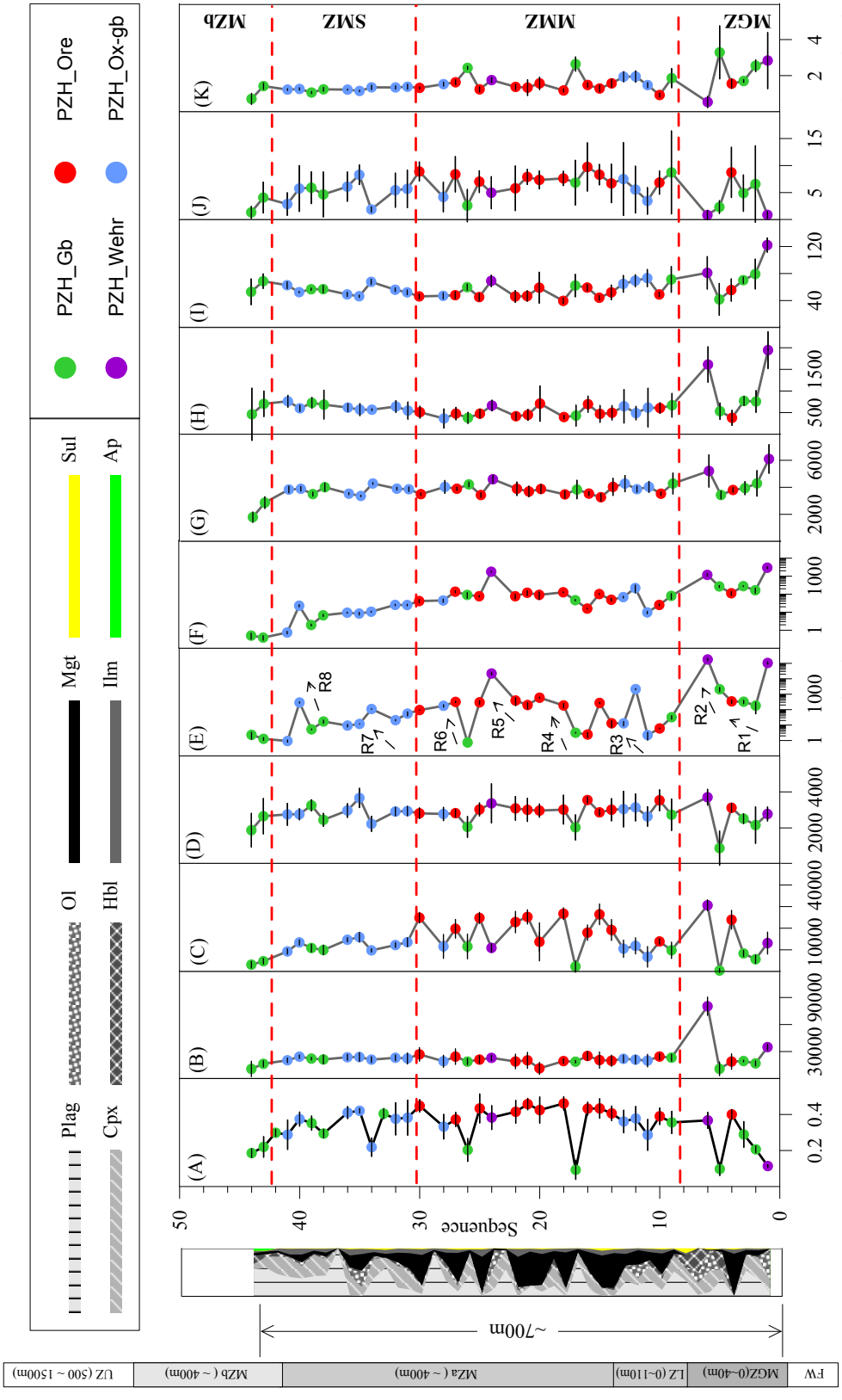

Fig. 5.4 Variations of Mgt compositions agaist stratigrapgic height of the Panzhihua Intrusion. Note except for the X_{Usp} which is calculated from the EMPA data, all of the other elements, including Al, Mg and Mn, are from LA-ICP-MS analyses. The data are plotted with 2σ error ellipses. R1 represents reversal 1, and so on.

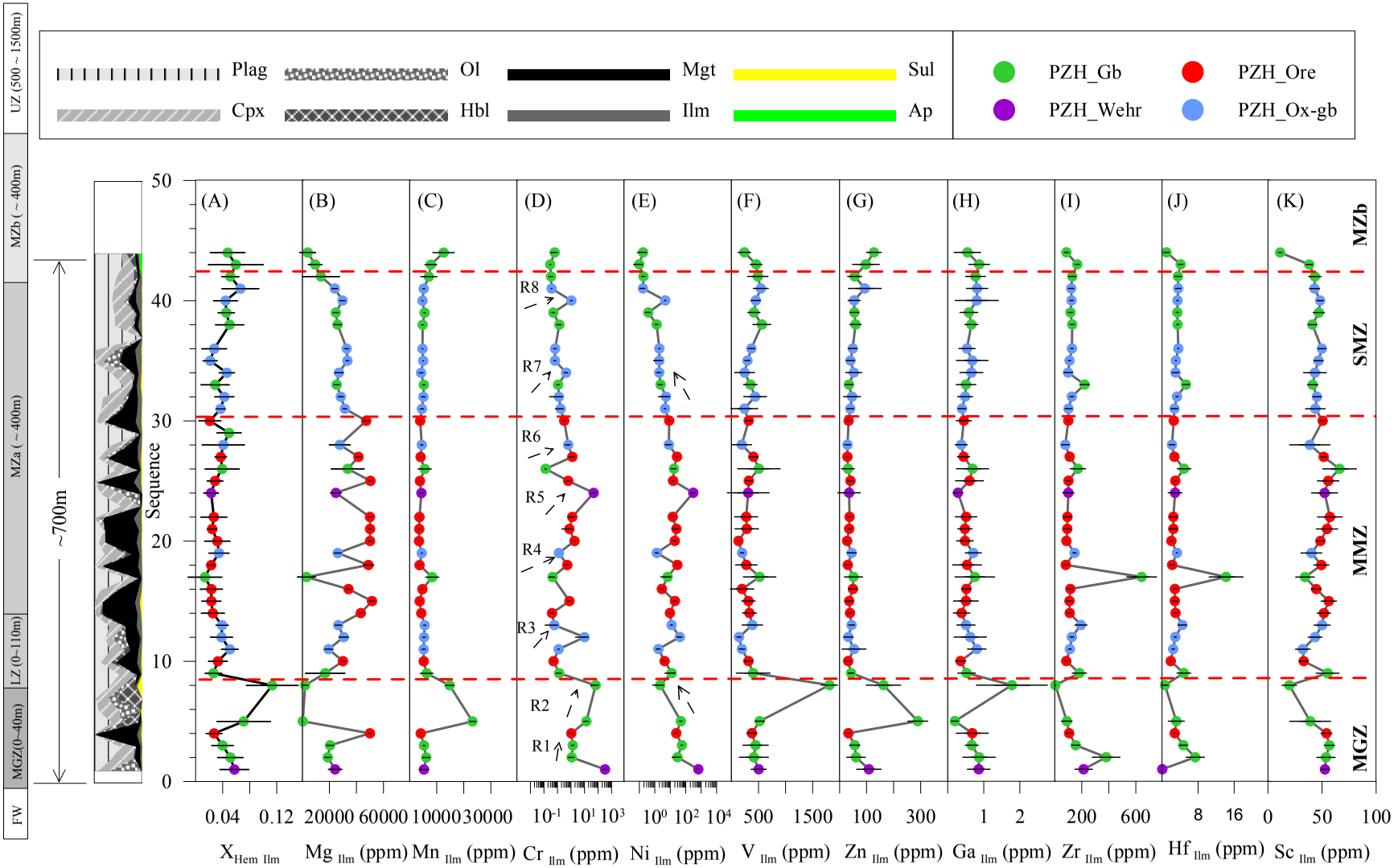

Fig. 5.5 Variations of Ilm compositions agaist stratigraphic height of the Panzhihua Intrusion.

tent and Fe-Ti oxide mode correlate (Fig. 5.5 B). Mn content does not show variation above the MGZ, increasing gradually from the top of SMZ to MZb. Ilmenite in two gabbros in the MGZ have elevated Mn content (Fig. 5.5 C).

Eight reversals have also been identified in the profile of Cr contents in ilmenite (Fig. 5.5 D). The stratigraphic location of each reversal is in agreement with that observed in the magnetite vertical profiles. Ni and Mg in ilmenite usually increase with increasing Cr content (e.g. R1, R3, R4, R6 and R8). Exceptions are found in the other reversals, for example, Cr correlates positively with Ni but negative with Mg in R5, whereas these relationships reverse in R2 and R7 (Fig. 5.5 B and E). For the former, the higher Mg content of ilmenite in most massive ores is unlikely to reflect crystallization from a more primitive magma, because there is little difference in terms of compatible element concentrations between ilmenite in massive ores and gabbros. We suggest that subsolidus re-equilibration of ilmenite with olivine leads to increased Mg in ilmenite.

Overall, except for Cr, most trace elements in ilmenite in the MMZ show no systematic compositional changes and do not correlate with changing mineral modal proportions (Fig. 5.5 E-J). Ni and Mg show a gradual decrease from the SMZ up to the MZb (Fig. 5.5 B, E), whereas V, Zn and Ga show an obvious increase from the top of SMZ to MZb (Fig. 5.5 F-H). It is interesting that incompatible elements Zr and Hf do not show an upward increasing trend as would expected from magma differentiation. Instead, they decrease slightly into the MZb (Fig. 5.5 I-J). This may reflect a lower amount of interstitial liquid due to postcumulus compaction. Sc remains constant in the SMZ and decreases rapidly in the MZb (Fig. 5.5 K), in accordance with the decreasing ratio of clinopyroxene to plagioclase.

5.2.2.3 Pyrrhotite

The Panzhihua pyrrhotites (Po) are PGE depleted, with concentrations of Pt and Pd mostly below the detection limit (Pt<0.05 ppm, Pd<0.005 ppm). In one sample (PZ-8) in the MGZ, the concentration of Pt and Pd are 0.31 ppm and 0.16 ppm, respectively. These are the highest values measured in all samples in this study. However, obvious veins of quartz and euhedral pyrite are observed, hence, the Pt and Pd is likely to be related to post-magmatic fluid activities.

The compositional profile of pyrrhotite is shown in Figure 5.6. The variations in Fe/S ratio of pyrrhotite is closely related to the Fe-Ti oxide modal proportions. Pyrrhotite with elevated Fe/S ratio occur in massive ore rocks, whereas gabbroic rocks contain pyrrhotite with

much lower Fe/S ratios (Fig. 5.6 A). This indicates that pyrrhotite in massive ores may have crystallized from an iron-rich immiscible sulphide melt.

Seven reversals are also observed in the pyrrhotite composition, most in terms of Fe/S ratios (Fig. 5.6 A). These reversals are corresponding to the eight reversals recorded in Cr content of Fe-Ti oxides and Mg# of clinopyroxene, except for R2.

In the MGZ, R1 is recognized by a sudden increase in Fe/S ratio from 0.912 to 0.999. The contents of Ni, Co, Cu, Zn, Sn decrease as Fe/S ratio increases, but Pb and Bi increase (Fig. 5.6 B-H). Ni/Co and Pb/Bi values display negative correlation with Fe/S (Fig. 5.6 I-J). R2 reversal is not observed due to the absence of pyrrhotite at this level within the intrusion.

In the MMZ, all four reversals (R3-R6) are identified (Fig. 5.6 A-B). R3 is recognized by increases of Ni, and Bi, and to a lesser extent Cu, Zn, and Pb. R4, R5 and R6 are characterized by a sudden increase in Fe/S from 0.87~0.89 to 0.91~0.97. However, other elements are relatively constant throughout the MMZ.

R7 in the SMZ is identified on the basis of increases in Fe/S and Co/Ni, Zn and Bi, but decreases in Co, Sn and Pb/Bi (Fig. 5.6 A, C, E, F, H, I, J). R8 is marked by an increase in Ni and Bi (Fig. 5.6 B, H). In general, trace elements of pyrrhotite show systematical upward decrease in Ni, Pb and Bi. Co, Cu and Zn are relatively constant in the SMZ. Pyrrhotite in the MZb is characterized by low Ni and Co, but higher Cu, Zn, Sn, Pb and Bi. Pb/Bi ratio increases significantly in pyrrhotite in the MZb.

Overall, compositions of pyrrhotite change little throughout the intrusion. Combined with similarly constant compositions of the Fe-Ti oxides, this argues against *in-situ* fractional crystallization of these minerals. Instead, crystallization of minerals from magmas with similar compositions is suggested as the most likely origin of these rocks. Whether the reversals observed in different subzones of the stratigraphy were in response to periodical replenishment of less fractionated magma, or a result of other processes, will be discussed in the next chapter.

5.3 Vertical Profiles through the Taihe Intrusion

5.3.1 Whole-rock Chemistry

Taihe Fe-Ti-V oxide deposit is hosted in the lower part of the intrusion, similar to the Panzhihua deposits. The massive ores are divided into a lower mineralization zone (LMZ) and a middle mineralization zone (MMZ), separated by a low-level gabbro. The gabbros above massive ores are referred to as high-level gabbros.

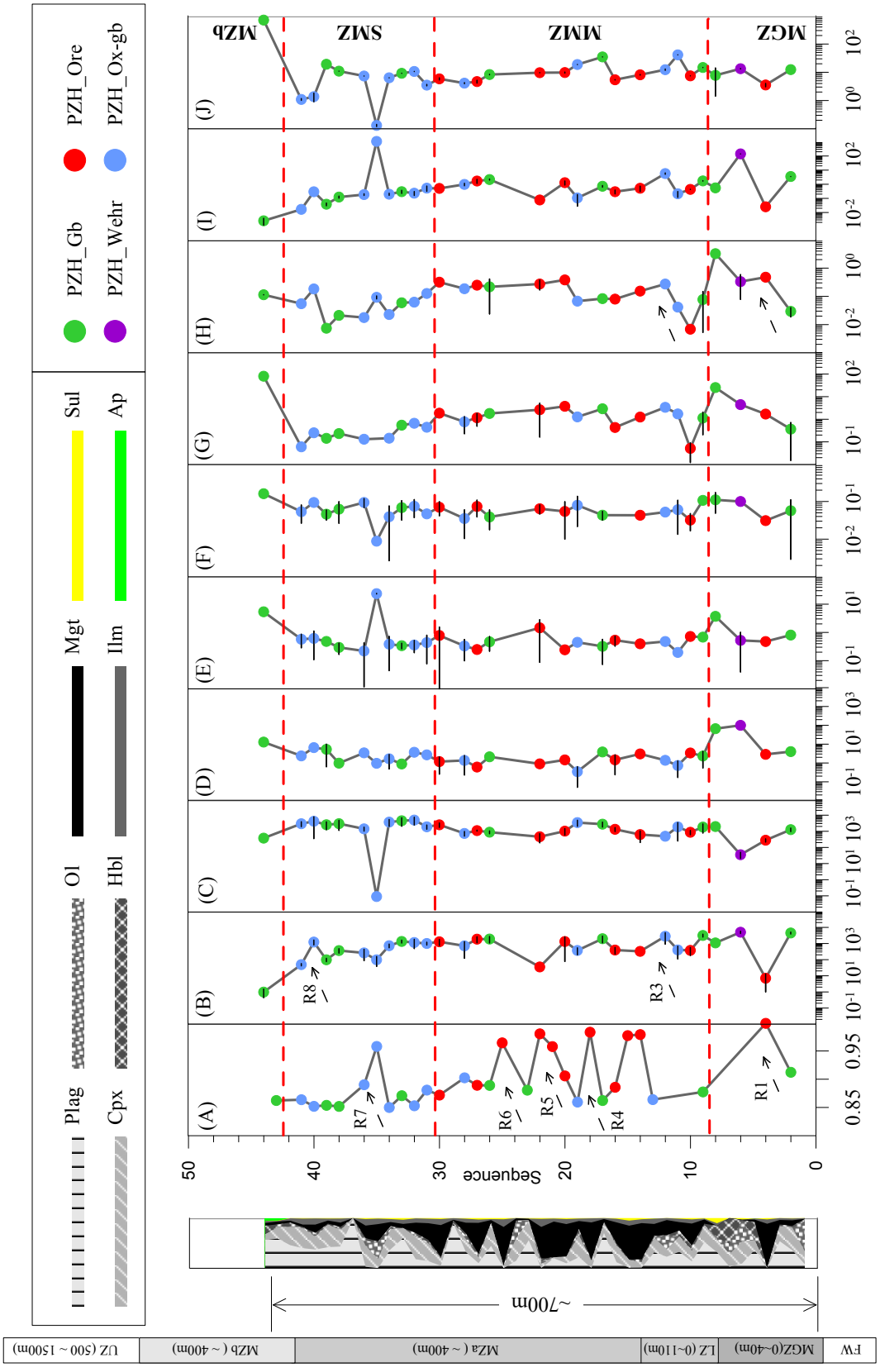

Fig. 5.6 Variations of Po compositions agaist stratigrapgic height of the Panzhihua Intrusion.

The massive ores have nearly constant Mg# and $Fe_2O_3^*/TiO_2$ ratios (Fig. 5.7 A-B). One gabbro interlayered with massive ores, has slightly higher Mg# but lower $Fe_2O_3^*/TiO_2$ ratio. However, this gabbro is distinct from gabbros overlying the massive ore zone (Fig. 5.7 A). One of the high-level gabbros has an elevated $Fe_2O_3^*/TiO_2$ ratio (Fig. 5.7 B), which is a result of low ilmenite content relative to magnetite. TiO_2/V_2O_5 ratios are different in the ores below and above the middle gabbro, with the higher ores having higher values (Fig. 5.7 C). The content of vanadium shows little variation in the massive ores, but is lower in high-level gabbros (Fig. 5.7 D). Cr is higher in high-level gabbros than in massive ores (Fig. 5.7 E). Ni, Co and Zn are relatively constant ores, except for Ni in the uppermost ore sample (Fig. 5.7 F-H). Co and Zn decrease gradually from the uppermost ore to the high-level gabbros (Fig. 5.7 G-H). Sc shows constant content in massive ores, but increases upwards to the gabbros (Fig. 5.7 I). Sr shows large variations in massive ores (24.5 to 1249.4 ppm), reflecting changes in plagioclase mode. Sr is more abundant in high-level gabbros (407.9 to 1616.1 ppm) (Fig. 5.7 J). The content of Zr is similar in all rocks (9.6 to 17.8 ppm), except for one gabbro, which has 57.7 ppm Zr. The high Zr content indicates more abundant interstitial liquid in that gabbro.

5.3.2 Fe-Ti Oxides

Magnetite in the massive ore rocks contain slightly lower vanadium content (V:3850~4610 ppm) than gabbroic rocks (V:5120~5552 ppm), but the difference is relatively small between LMZ and MMZ magnetite, and between gabbros occuring at different levels (Fig. 5.8 A). A pronounced increase of Cr content in magnetite in the LMZ is observed, with Cr increasing from 12 to 519 ppm, followed by a sharp drop to 10 ppm in the low-level gabbro (Fig. 5.8 B). However, the Cr content in magnetite in the lowermost ore (~12 ppm) is within the range of Cr in magnetite in the MMZ (10~13 ppm). Ni in magnetite shows a progressive decrease from the LMZ to MMZ, from 406 ppm to 53 ppm, but then increases to 608 ppm in the high-level gabbro (Fig. 5.8 C). Co concentrations in magnetite show non-systematic variations (Fig. 5.8 D). Higher Co contents are associated with lower Fe-Ti oxide modal proportions. There is a gradual increase in Zn content up the section (Fig. 5.8 E)

The variations in ilmenite are comparable to those in the magnetite (Fig. 5.8 F-J). For example, ilmenite in gabbroic rocks have higher V compared to massive ores (Fig. 5.8 F). A strong increase in Cr contents in ilmenite mimics that in magnetite (Fig. 5.8 G). The gradual decrease of Ni up-section is also similar to that in magnetite (Fig. 5.8 H). The general behaviour of Co and Zn in magnetite and ilmenite are also similar (Fig. 5.8 I-J).

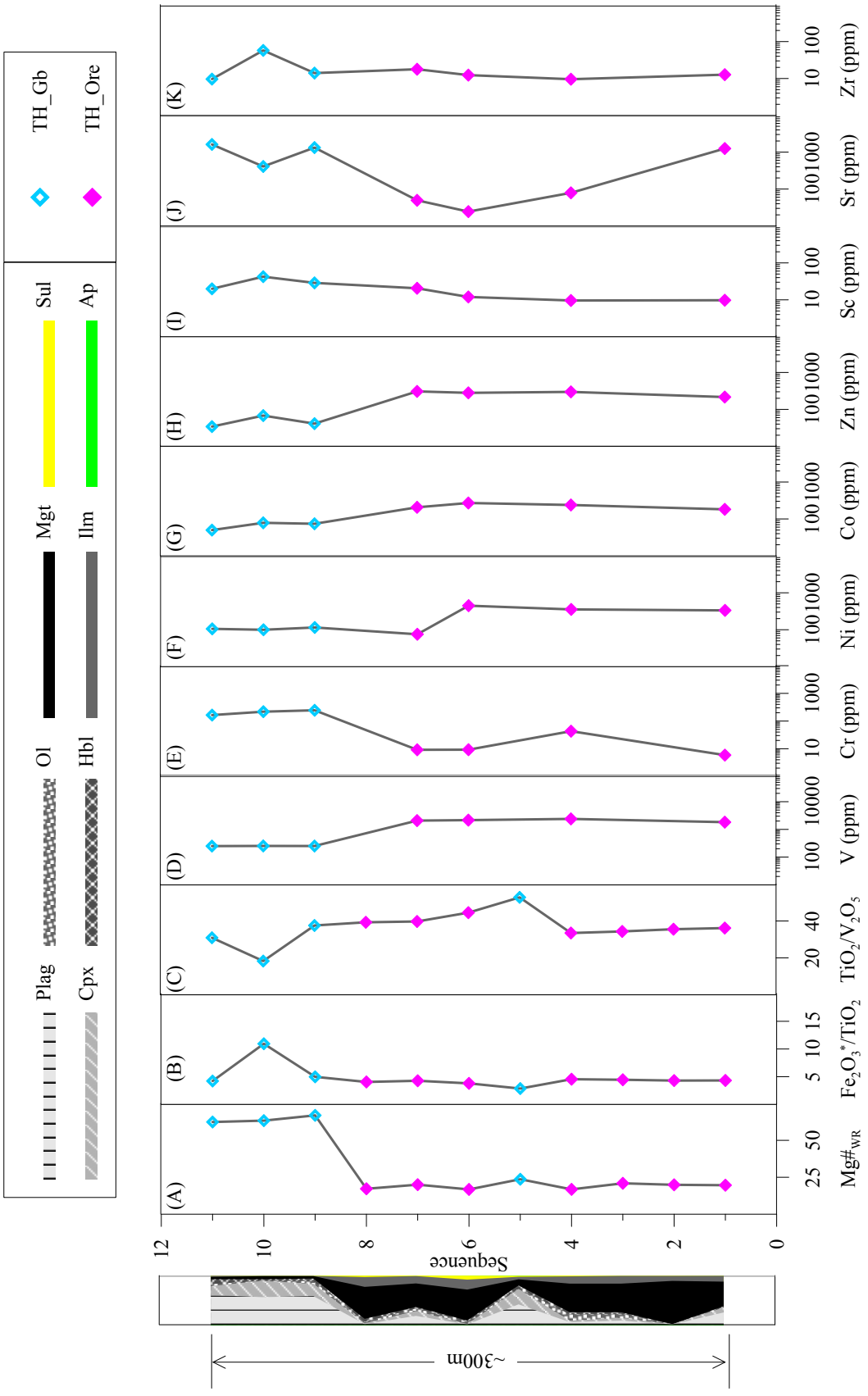

Fig. 5.7 Whole rock geochemical profile of rocks from the Taihe Intrusion.

5.4 Summary

The key features of the compositional changes through the vertical profiless of the Panzhihua and Taihe intrusions are summarized as follows:

1. The vertical variations in whole-rock geochemistry are closely related to mineral modal proportions, e.g. massive ore rocks have more abundant $Fe_2O_3^*$ and TiO_2, but lower Mg#, CaO, Al_2O_3, Na_2O, K_2O, Zr and REE. These features confirm cumulus nature of samples in this study.
2. The P_2O_5 is also lower in massive ore than in gabbro, which is against the hypothesis that magnetite crystallized from Fe-rich immiscible liquid, since P is also concentrated in the Fe-rich liquid.
3. A new stratigraphic classification, which is based on our geochemical observations, has been proposed. The major difference from the previous stratigraphy is the combining of the LZ and the lower MZa into the Main Mineralization Zone (MMZ), and identification of the Subordinate Mineralization Zone (SMZ) as the upper MZa. The Marginal Zone (MGZ) and the Middle Zone b (MZb) are the same as in the previous stratigraphy.
4. A total of eight reversals have been identified in terms of mineral compositions. Reversals 1 and 2 (R1 and R2) occur in the MGZ, R3 to R6 are in the MMZ, and R7 and R8 are in the SMZ.
5. R1 is recognized by increases of $Mg\#_{Cpx}$; An_{Plag}, FeO and P_2O_5 in plagioclase; Cr, Ni and Mg in magnetite; Cr and Ni in ilmenite, and a sudden increase in Fe/S values and Pb and Bi contents in pyrrhotite.
6. R2 is characterized by increases of $Mg\#_{Cpx}$; TiO_2 and Al_2O_3 contents of clinopyroxene; Fo of olivine; Cr, Ni and Mg in magnetite; Cr and Mg in ilmenite.
7. R3 is in two adjacent oxide-rich gabbros, with increases in $Mg\#_{Cpx}$, slight increases in TiO_2 and Al_2O_3 in clinopyroxene; increases in An and FeO in plagioclase; increases of Cr in magnetite by 3 orders of magnitude; increases of Cr, Ni and Mg in ilmenite; and increases in Ni and Bi in pyrrhotite.
8. R4 is from a leucogabbro to a massive ore, and is recognized by large increases in $Mg\#_{Cpx}$, TiO_2 and Al_2O_3 contents of clinopyroxene; An and P_2O_5 of plagioclase; a suddenly increase in Cr in magnetite and ilmenite; and an increase of Fe/S ratio in pyrrhotite.
9. R5 is from a massive ore to a wehrlite. It is characterized by a large increase in $Mg\#_{Cpx}$,

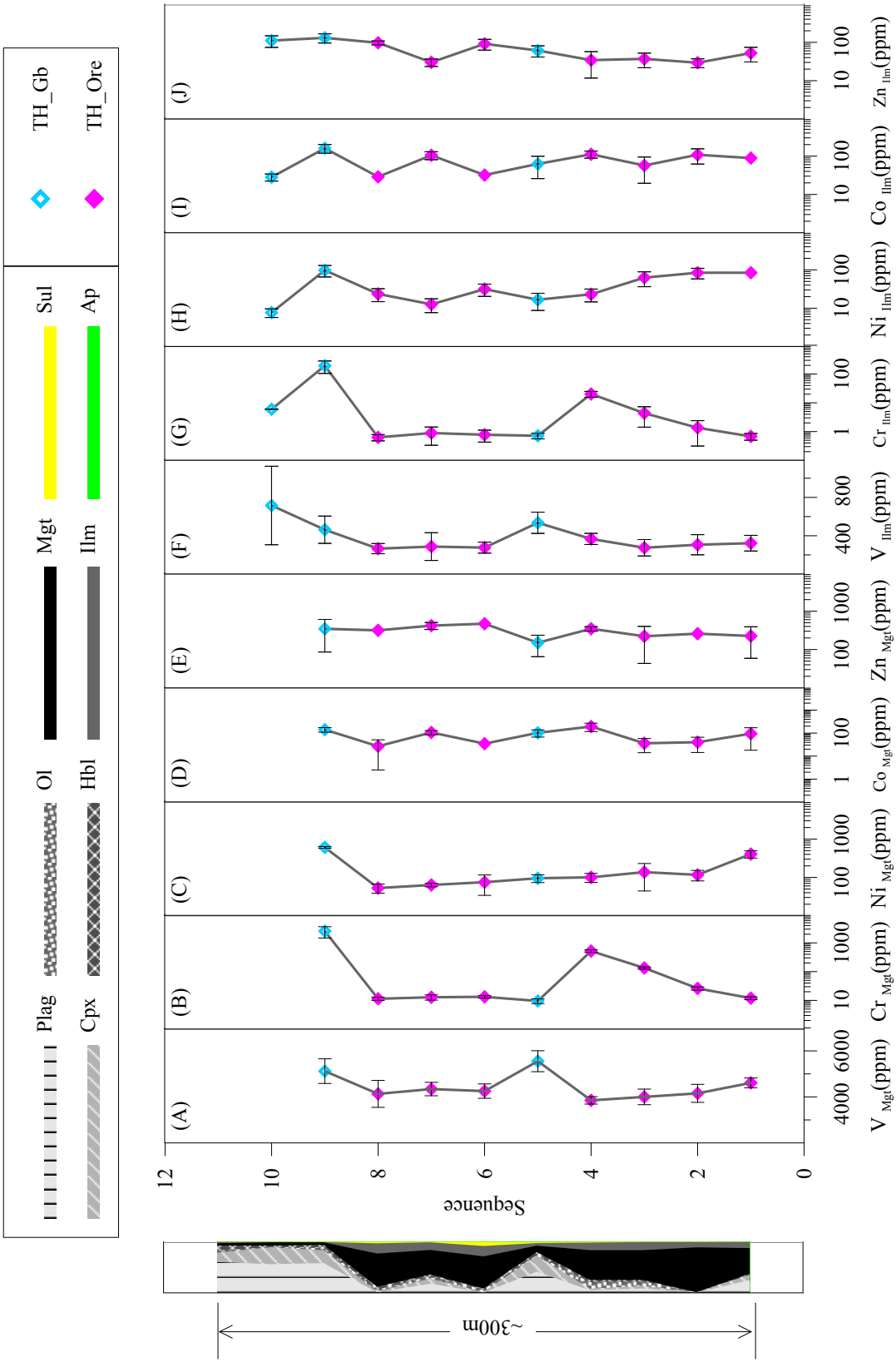

Fig. 5.8 Compositional profiles of Mgt (A-E) and Ilm (F-J) from the Taihe Intrusion.

TiO_2 and Al_2O_3 of clinopyroxene; increases in An and P_2O_5 of plagioclase; a sharp increase in Cr and Ni in magnetite; increases of Cr and Ni, but decrease of Mg in ilmenite; an increase in Fe/S ratio in pyrrhotite.

10. R6 is from a leucogabbro to a massive ore. It is recognized by an increase of TiO_2 content in clinopyroxene; increase of An in plagioclase; abruptly increase of Cr, Mg, Ni in magnetite, but decrease of V, Ga and Sn; increases in Cr, Ni and Mg in ilmenite; an abruptly increase of Fe/S ratio and constant trace elements in pyrrhotite.
11. R7 occurs between two oxide-rich gabbros. It is recognized by increases in $Mg\#_{Cpx}$; An of plagioclase; increases of Cr, Mg, Mn and Ga in magnetite, and a decrease of Ni; increases of Cr and Mg, and a decrease of Ni in ilmenite; increases of Fe/S Co/Ni, Zn and Bi in pyrrhotite.
12. R8 is from a gabbro to a oxide-rich gabbro. It is identified by increases in $Mg\#_{Cpx}$, TiO_2 of clinopyroxene, An and FeO of plagioclase; Fo of olivine; increases of Cr, Ni, Mg, Mn, V and Ga in magnetite; increases of Cr, Ni and Mg in ilmenite; increases of Ni and Bi in pyrrhotite.
13. Despite of these reversals, the massive ore rocks occuring at different stratigraphic heights have comparable whole rock and mineral compositions. The MGZ rocks varying considerably in compositions, however, the MMZ is almost constant, whereas the SMZ shows systematic changes. This suggests that different magmatic, and/or post-magmatic processes have operated in these subzones.
14. FeO in plagioclase decreases in R4 and R5, increases in R1. This likely reflects a decrease of Fe content in the parental magma due to massive crystallization of magnetite in the MMZ, whereas silicate mineral crystallisation leads to an enrichment of iron within the MGZ.
15. The most Ca-rich plagioclase in R3-R5 always occurs at a higher level than the most Mg# rich clinopyroxene, which may be explained by plagioclase buoyancy and crystal settling and sorting.
16. Magnetite in ores has higher MgO contents than in adjacent gabbros, which is likely to be inherited from the parental magma. Another possibility is that the parental magma is similar in composition, but much hotter than the cooling crystal mush. This liquid would dissolve early crystallized olivine and enrich the melt in Mg. Evidence for this may include resorbed olivine, olivine rims in massive ores, and elevated Fo in ore rocks.
17. The Taihe massive ore rocks have similar whole rock compositions, except for Sr, which is

affected by variations in plagioclase mode. The magnetite and ilmenite in the Taihe intrusion show similar compositional trends. Magnetite and ilmenite in the MMZ are fairly constant in compositions, whereas those in the LMZ are more variable. It may indicate different magmatic processes operated during formation of the Fe-Ti oxide ores.

CHAPTER 6 NUMERICAL MODELLING

6.1 Modelling Strategy

Several studies have performed modelling magma crystallization path of the gabbroic layered intrusions in the Pan-Xi district, e.g. Panzhihua (Ganino *et al.*, 2008; Howarth *et al.*, 2013; Howarth & Prevec, 2013a; Pang *et al.*, 2008a; Shellnutt & Jahn, 2010; Song *et al.*, 2013), Baima (Shellnutt & Pang, 2012; Zhang *et al.*, 2012), Taihe (Hou *et al.*, 2012a), Hongge and Xinjie (Bai *et al.*, 2012). In most of these studies, early crystallization of magnetite have been successfully modelled, and silicate mineral compositions have been reproduced. However, the crystallization sequences, especially the appearance of Fe-Ti oxides, vary significantly between different studies, e.g. the appearance of Mgt on the liquidus is between 1193 ~ 1055˚C. Since all studies have used the MELTs algorithm or its derivatives (e.g. PELE and pHMELTs) (Boudreau, 1999b; Ghiorso & Sack, 1995), this large variation is likely due to the differences in the assumed parental magma compositions and its crystallization conditions (e.g. fO_2, H_2O). This study aims at contributing further constraints on the crystallization history of Panzhihua based on adding mineral modal proportions as a further parameter to be reproduced during modelling.

In this study, an alternative modelling algorithm is used, Petrolog3 (Danyushevsky & Plechov, 2011), with calculations being performed using mineral-melt equilibrium models of Ariskin and coauthors (Ariskin *et al.*, 1993; Ariskin & Nikolaev, 1996; Ariskin & Barmina, 1999). Petrolog3 algorithm was preferred for three main reasons. Firstly, MELTs algorithm is not well calibrated at oxidizing conditions, due to the paucity of calibration experimental data derived at higher fO_2(e.g. ΔNNO>0) (Ghiorso & Sack, 1995). Recent experiments have also demonstrated that the Fe-Ti oxide geothermobarometer of Ghiorso & Sack (1991), which is based on a similar thermodynamic model to that within MELTS, tends to significantly overestimate both temperature and fO_2 at moderately to highly oxidized calc-alkaline magmatic conditions (Evans *et al.*, 2006; Lattard *et al.*, 2005). Secondly, during MELTs modelling of compositions similar to the parental melts for Panzhihua, ilmenite appears on the liquidus much later than magnetite at any conditions, which is inconsistent with field and petrographic observations of the Panzhihua intrusion. Thirdly, the MELTs modelled magnetite contains very

high MgO content, much higher than that measured in the Panzhihua magnetites, whereas Petrolog3 results are closer.

Although fractional crystallisation is a common process during evolution of basic magmas, a certain portion of crystallized minerals usually remains within the evolving magma. The crystallinity of mafic magmas may vary between a few per cents to up to 55%, with mostly vary between 25 to 55 vol% phenocrysts (Ariskin & Barmina, 2004; Marsh, 1989; Miller & Weiblen, 1990). Phenocrysts-rich magmas have been documented in many locations (e.g. the Hawaiian Lava Lake, Marsh, 1981).

In the low-Ti Emeishan basalts, phenocrysts of clinopyroxene may reach 25 to 30% in low-Ti basalts, whereas plagioclase is absent and olivine appears occasionally. In the high-Ti Emeishan basalts, plagioclase, and to a lesser extent clinopyroxene, are the two most abundant phenocrysts (e.g. 13 to 33% plagioclase and 3 to 10% clinopyroxene, Xu *et al.*, 2001). It is thus reasonable to assume that clinopyroxene and plagioclase were present in the erupting Eimeshan high-Ti magmas, whereas olivine and Fe-Ti oxides were likely fractionated before eruption.

Cumulus minerals in layered intrusion may be either crystallized *in-situ* from crystal-free or -poor magmas, or deposited from crystal-rich parental magmas after their emplacement into the intrusion. The nearly constant mineral compositions throughout the Panzhihua section (e.g. $Mg\#_{Cpx}$, this study and Pang *et al.*, 2009) are difficult to explain by either silicate-oxide liquid immiscibility (Zhou *et al.*, 2005), or by periodic magma replenishments and *in-situ* crystallization (Pang *et al.*, 2008b, 2009; Song *et al.*, 2013). Instead, an alternative model is favoured in this study, where crystal-laden Fe-Ti rich basaltic magmas continuously flow through the Panzhihua intrusion, precipitating suspended crystals (clinopyroxene, plagioclase and olivine) and also fractionated magnetite and ilmenite which were formed within the intrusion thus forming the layered gabbro and Fe-Ti oxide ores.

A successful model must reproduce both mineral compositions and the crystallisation sequence, and the mineral modal proportions. As described in previous chapters, the temperature interval over which accumulation of massive Fe-Ti oxide ores has occurred is relatively small (~ 20˚C), based on the Cpx-Ol geothermometer and plagioclase compositions. Thus, an important evaluation criterion of a successful model is that the Panzhihua parental magma should be capable of fractionating a sufficient amount of crystals within a small temperature interval. Otherwise, large compositional variations would be expected among silicate minerals,

as is observed, for example, within the Skaergaard Intrusion (McBirney, 1996).

6.2 Starting Compositions and Modelling Parameters

The composition of a parental magma can be estimated by mass balance, if the compositions and relative proportions of a) bulk intrusion and b) erupted residual magma are known. Three steps are undertaken to provide an estimate of the Panzhihua parental magma in this study. The first step is to identify a basaltic lava representative of the magmas erupted after passing through the Panzhihua intrusion. A successful candidate would be in equilibrium with clinopyroxene and plagioclase, which compositions are similar to those within the Panzhihua section (i.e. $Mg\#_{Cpx}$=76.9, An_{Plag}=58.1). Liquidus mineral associations were assessed for over 250 Emeishan high-Ti basalts collected from the vicinity of the intrusion and calculated for their liquidus associations using Petrolog3 (Danyushevsky & Plechov, 2011). The mineral-melt equilibrium models from Ariskin *et al.* (1993) were used for these calculations. The high-Ti basalt (HK-11) from the Jinping-Song Da district (Wang *et al.*, 2007) was the closest match. It is characterised by identical (within error) calculated liquidus temperatures for clinopyroxene ($Mg\#_{Cpx}$=74.1) and plagioclase (An_{Plag}=57.6).

Secondly, relative magnesian clinopyroxene compositions in the Panzhihua intrusion indicate the parental magma had not undergone extensive differentiation of primitive magma before eruption. Consistent with this observation, basalt HK-11 has Mg# of 0.45. It was assumed that the residual magma (similar to HK-11 basalt) erupted after 50% fractionation of the parental magma.

Thirdly, we have assumed that the bulk Panzhihua composition from Zhou *et al.* (2005) is essentially a sum of phenocrysts deposit by the passing magmas, with an insignificant amount of the residual melt.

Mass balance calculations with the above assumptions yields a composition close to a high-Ti basalt (EM-82) from the Ertan area (Xu *et al.*, 2001), which is only about 50 km away from the Panzhihua intrusion. This basalt is selected as representative of the Panzhihua parental magma. This composition is within range of published estimates modeling (Table 6.1).

Modelling of crystallisation of this composition results in Ilm appearing on the liquidus before magnetite (2.1 wt% crystallisation earlier), after 25.5% fractionation. Clinopyroxene appeared on the liquidus are 29 wt% fractionation, when 20 wt% of plagioclase has already crystallized. These results are not consistent with the observations from the Panzhihua intru-

sion, where magnetite crystallizes slightly earlier than ilmenite, and plagioclase is not abundant

Table 6.1 Comparison of starting compositions used in published crystallization models for the Panzhihua-type magmas.

Intrusion	Panzhihua						Baima		Hongge	Taihe
Ref.	This study	Ganino et al. (2008)	Pang et al.(2008)	Shelnutt & Jahn (2010)	Song et al.(2013)	Howarth et al. (2013b)	Zhang et al.(2012)	Shellnutt & Pang (2012)	Bai et al.(2012)	Hou et al. (2012)
Sample	EM-82[a]	YL-2 (3.6%)[b]	RY-7	GS03-003	M3-24 (46%)[c1]	Aveg. HTB[d]	M3-24 (61%)[c2]	EM-81	EM-55 (21.5%)[e]	Bulk
SiO_2	46.62	47.45	45.83	49.43	41.82	51.73	42.77	45.61	47.59	43.27
TiO_2	2.9	2.7	4.85	2.95	4.92	4.37	4.93	3.56	3.53	4.12
Al_2O_3	15.25	13.99	15.62	11.59	13.61	13.49	15.36	14.09	10	15.56
Fe_2O_3(*)	14.6	13.49	2.23	12.73	2.61	2.16	1.86	-	-	15.76
FeO(*)	-	-	11.36	-	13.91	11.09	15.88	15.09	14.6	-
MnO	0.2	0	0.23	0.2	0.16	0.21	0.15	0.23	0.18	-
MgO	6.44	7.09	7.18	8.79	8.21	4.94	5.61	7.1	9.45	5.42
CaO	9.93	10.59	7.52	10.59	10.41	7.26	8.6	10.4	11.29	12.25
Na_2O	2.59	2.7	3.26	2.29	2.74	3.39	3.35	2.46	1.77	2.61
K_2O	1.17	1.7	1.41	1.12	0.91	0.93	1.02	1.11	1.16	0.5
P_2O_5	0.3	0.3	0.51	0.31	0.68	0.42	0.46	0.36	0.29	0.5
Cr_2O_3	0.03	-	0.01	-	0.02	-	0.01	-	0.13	-
Total	100.03	100	100	100	100	100	100	100	100	100
Mg#[f]	0.49	0.54	0.53	0.6	0.57	0.44	0.76	0.48	0.56	0.43

Data sources: a: a high-Ti basalt from the Ertan area near the Panzhihua mine (Xu *et al.*, 2001); b: an evolved liquid produced by 3.6% fractional crystallization of the basalt YL-2 (Song *et al.* 2001); c1 & c2: evolved liquids produced by 46% and 61% fractional crystallization of the melt inclusion in primitive olivine (Kamenetsky *et al.* 2012); d: an average composition of Emeishan high-Ti basalts from Xiao *et al.* (2004); e: an evolved liquid produced by 21.5% fractional crystallization of the EM-55 picrite (Chung & Jahn, 1995); f: Mg#=Mg^{2+}/(Mg^{2+}+Fe^{2+}), assuming 0.9 total iron as Fe^{2+}.

in the lower part of the intrusion. Hence, the EM-82 composition is adjusted to a slightly lower TiO_2 (from 2.9 to 2.5 wt%) and higher CaO content (from 9.93 to 10.30 wt%). Moreover, the average value of 0.03 wt% Cr_2O_3 in high-Ti basalt is added to force crystallization of spinel (Xu *et al.*, 2001).

During Petrolog3 modelling, a temperature correction of 5 deg/kbar was applied to calculated pseudo-liquidus temperature of spinel, magnetite and ilmenite to account for the effect of pressure (Danyushevsky & Plechov, 2011). Clinopyroxene and plagioclase are assumed to be in equilibrium with the melt (0% of fractional crystallization), whereas olivine, spinel, magnetite and ilmenite are completely removed (100% of fractional crystallization). The model for melt oxidation state is from Borisov & Shapkin (1990). The models of Lange & Carmichael (1987) and Bottinga & Weill (1972) are chosen for calculating melt density and

viscosity, respectively. The calculation was stopped when the degree of crystallisation reached 65 wt%; a calculation step of 0.01 wt% was used during calculations.

The emplacement and crystallization of the parental magma was assumed to occur at a constant pressure of 1 Kbar. The melt oxidation state is set at NNO+0.3, reflecting likely more oxidised conditions for flood basalts compared to MORB. Note that Ganino *et al.* (2008) suggested that fO_2 of Panzhihua magma may have been increased from QFM to QFM+1.5 during interaction with dolomitic wall rocks. The fO_2 may also increase during fractionation of olivine and plagioclase. Although the exact oxidation state of Panzhihua parental magma is difficult to constrain, the value we have chosen results in magnetite appearing on the liquidus before ilmenite, and more importantly, yields magnetite/ilmenite proportions close to those observed.

H_2O has a significant effect on the evolution paths of basaltic magmas, mainly by suppressing plagioclase crystallization and therefore decreasing its cotectic proportion in the cumulus mineral assemblage (Almeev *et al.*, 2012; Botcharnikov *et al.*, 2008; Danyushevsky, 2001; Feig *et al.*, 2006; HousH and Luhr, 1991). Crystallization of Fe-Ti oxides, especially magnetite, is strongly controlled by fO_2, but independent of the water activity in ferrobasalt (Ariskin & Barmina, 1999; Berndt, 2005; Botcharnikov *et al.*, 2008; Feig *et al.*, 2010; Hammer, 2006; Toplis & Carroll, 1995). Hence, the crystallization modelling is performed under anhydrous condition.

6.3 Results

The modelled results are illustrated in Table 6.2 and Figures 6.1 to 6.4. According to our modelling, spinel is the first phase to crystallize at 1188.4˚C, closely followed by plagioclase at 1185.1˚C (Table 6.2, Fig. 6.1). The magma has only fractionated 4% when olivine joins the assemblage at 1168.3˚C. After approximately 16% of fractionation, magnetite arrives on the liquidus at 1148.7˚C, followed by clinopyroxene and ilmenite at almost the same temperature (1138.9 to 1138.5˚C). The earlier crystallization of plagioclase than clinopyroxene is evident by inclusions of plagioclase in clinopyroxene (Fig. 3.2 C and E). Magnetite and ilmenite saturation at a relatively early stage of differentiation is inconsistent with the presence of massive ores in the lower part of the intrusion. In this model, spinel disappears at the time of olivine crystallization, however, it re-appears after magnetite joins the solid assemblage (Table 6.1). In contrast, olivine disappears at the time of clinopyroxene saturation, and does not reappear.

Table 6.2 Melt and mineral compositions, and mineral modes along the crystallization path.

Calculated Melt Composition														
	F(%)	Phase	SiO_2	TiO_2	Al_2O_3	Fe_2O_3	FeO	MnO	MgO	CaO	Na_2O	K_2O	P_2O_5	Cr_2O_3
EM82*	100		46.62	2.5	15.25	14.6	-	0.2	6.44	10.3	2.59	1.17	0.3	0.03
melt1	99.99	Spl+	47.16	2.53	15.43	3.11	10.49	0.2	6.52	10.42	2.62	1.18	0.3	0.03
melt2	99.98	Plag+	47.17	2.53	15.43	3.11	10.49	0.2	6.52	10.42	2.62	1.18	0.3	0.03
melt3	96	Ol+/Spl-	47.02	2.63	14.76	3.31	10.86	0.21	6.78	10.27	2.58	1.23	0.32	0.03
melt4	87		46.85	2.91	14.01	3.91	11.14	0.23	6.35	10.37	2.53	1.36	0.35	0.03
melt5	84.4	Mgt+	46.76	3	13.76	4.13	11.22	0.24	6.24	10.42	2.49	1.4	0.36	0.03
melt6	79	Spl+	47.56	3.07	13.51	3.87	10.62	0.26	6.12	10.7	2.47	1.5	0.38	0.03
melt7	74.25	Cpx+/Ol-	48.34	3.13	13.26	3.6	10.03	0.27	6.02	11.01	2.44	1.59	0.41	0.03
melt8	73.4	Ilm+	48.42	3.15	13.27	3.58	9.96	0.28	5.99	10.99	2.44	1.61	0.41	0.03
melt9	50		51.86	2.28	14.34	2.7	8.41	0.4	4.94	9.59	2.74	2.37	0.61	0.02
melt10	45		52.97	2.07	14.72	2.41	7.87	0.45	4.67	9.01	2.81	2.63	0.67	0.01

Mineral Modes and Parameters														
T(°C)	F(%)	Phase	Spl_cum		Plag_mag		Ol_cum		Mgt_cum		Cpx_mag		Ilm_cum	
			Spl%	Cr#	Plag%	An	Ol%	Fo	Mgt.%	$Mg\#_{Mgt}$	Cpx%	$Mg\#_{Cpx}$	Ilm%	$Mg\#_{Ilm}$
1188.4	99.99	Spl+	0.001	47.79	-	-	-	-	-	-	-	-	-	-
1185.1	99.98	Plag+	0.005	47.79	0.01	-	-	-	-	-	-	-	-	-
1168.3	96	Ol+/Spl-	0.016	48.75	3.97	68.89	0.01	77.69	-	-	-	-	-	-
1153.4	87		0.016	-	10.5	64.79	2.48	75.84	-	-	-	-	-	-
1148.7	84.4	Mgt+	0.016	-	12.66	63.47	3.21	75.33	0.119	27.13	-	-	-	-
1143.7	79	Spl+	0.017	60.62	15.39	61.93	3.9	75.85	1.69	27.67		-	-	-
1138.9	74.25	Cpx+/Ol-	0.021	61.75	18.01	60.5	4.51	76.47	3.21	28.41	0.007	77.33	-	-
1138.5	73.4	Ilm+	0.023	61.75	18.3	60.33	4.51	-	3.4	28.36	0.41	77.33	0.001	29.31
1127	50		0.062	50.54	25.34	56.74	4.51	-	5.93	26.58	11.37	76.41	2.79	27.93
1122.9	45		0.072	44.45	26.9	55.88	4.51	-	6.6	26.44	13.69	76.41	3.23	27.88

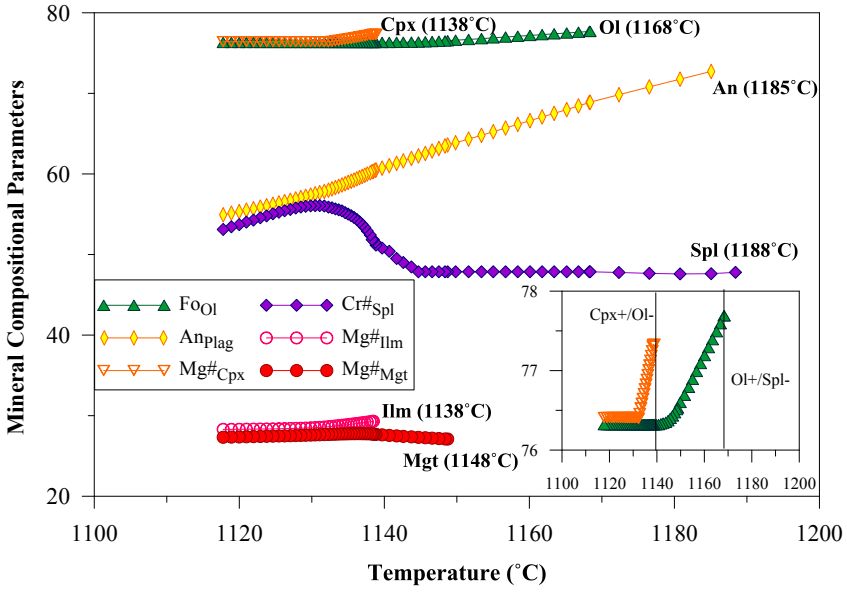

Fig. 6.1 Plot of temperature versus mineral compositional parameters illustrating the relative crystallization sequence and mineral compositions during Petrolog3 modeling. Numbers in brackets next to each phase correspond the temperature at which it appears on the liquidus. X axis is liquidus temperature of minerals. Spl-spinel, Plag-plagioclase, Ol-olivine, Mgt-magnetite, Cpx-clinopyroxene, Ilm-ilmenite. The insert magnifies the relationship betweene Fo and $Mg\#_{Cpx}$.

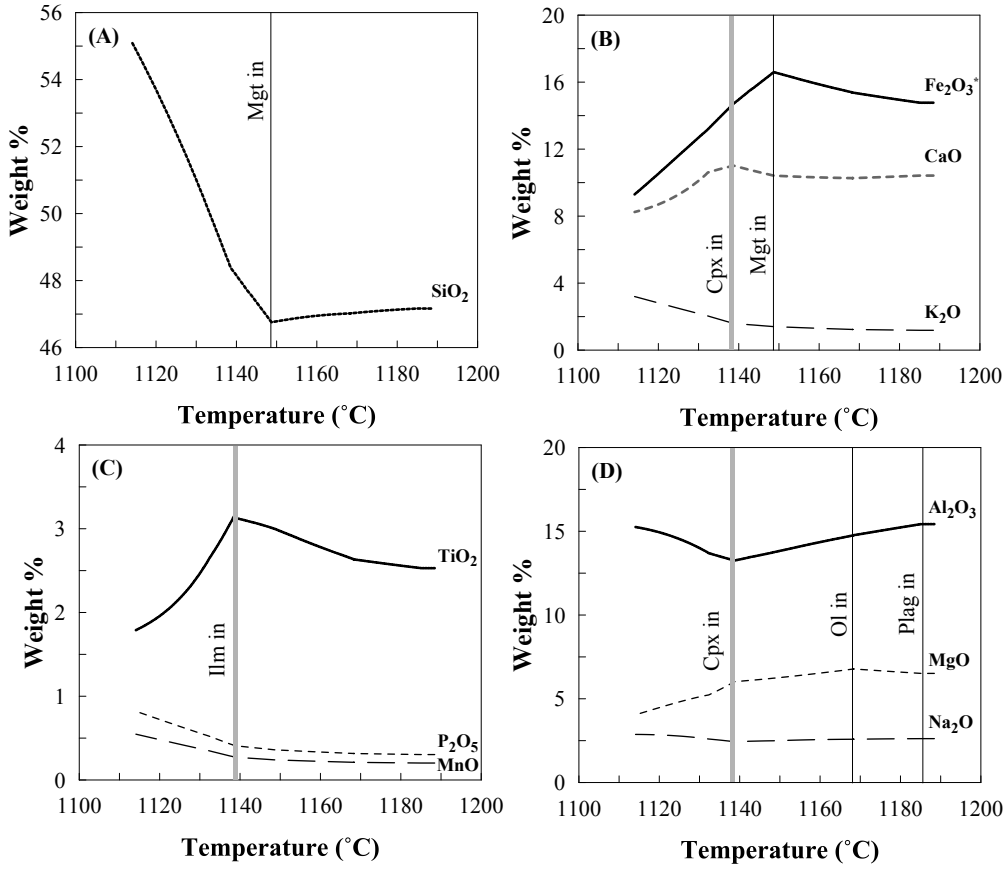

Fig. 6.2 Results of Petrolog3 modelling at fO_2=NNO+0.3, P=1 Kbar, anhydrous conditions. Modelling was stopped at 65%. Cpx and Plag remain in equilibrium with the magma during crystallisation, whereas Spl, Ol, Mgt and Ilm crystallise fractionally. Note Cpx and Ilm arrive on the liquidus almost simultaneously. Mgt crystallizes before Ilm.

Crystallization of plagioclase and olivine gradually decreases the residual melt in SiO_2 (Fig. 6.2 A). By the time of magnetite saturation, the magma has crystallized 0.016% spinel, 12.66% plagioclase and 3.21% olivine, increasing Fe_2O_3* and TiO_2 contents in the residual melt from 14.6 to 16.6 wt%, and 2.5 to 3.0 wt%, respectively (melt5 in Table 6.2). The melt shows rapid depletion of both FeO and Fe_2O_3, and a sharp increase in SiO_2 once magnetite appears (Fig. 6.2 A-B). The depletion in TiO_2 occurs when ilmenite arrives on the liquidus (Fig. 6.2 C), which leads to a more Si-rich differentiation trend, as shown by the increases in slope of the trend line on Fig. 6.2 A. The Al_2O_3 content in the melt decreases slightly (by ~ 10%). This is in accordance with the high content of Al_2O_3 (e.g. >12 wt%) in Emeishan high-Ti basalts with MgO < 8 wt% (Qi *et al.*, 2008; Song *et al.*, 2006b; Wang *et al.*, 2007; Xiao *et al.*, 2004; Xu *et al.*, 2001). Gradual decrease of CaO in the melt is observed (Fig. 6.2 B) as a result of clinopyroxene crystallisation. Clinopyroxene crystallization also results in a moderate increase in Al_2O_3 content (Fig. 6.2 D).

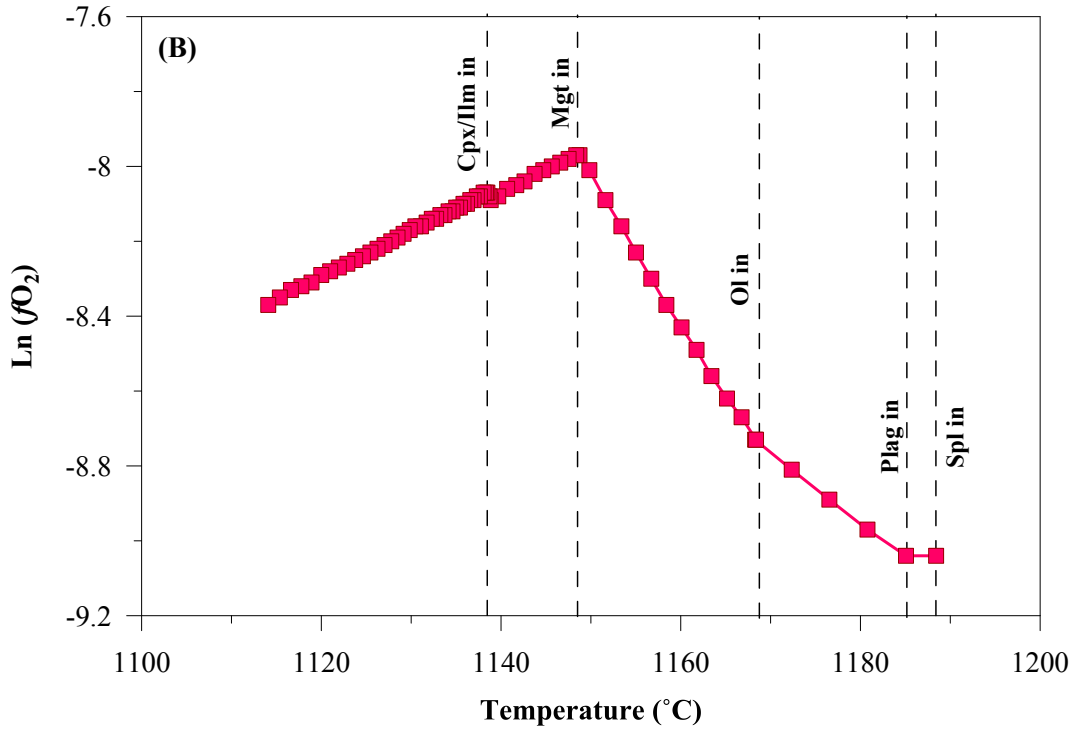

Fig. 6.3 Plot of temperature versus Ln (fO_2) illustrating the effect of mineral crystallization on melt oxidation state.

The melt becomes more oxidized as crystallization of plagioclase and olivine proceeds, due to removal of Fe^{2+} from the melt, however, this changes as soon as magnetite appears (Fig. 6.3). Fractionation of 12.66 wt% plagioclase and 3.21 wt% olivine increased Ln (fO_2) by ~ 1 unit. Therefore, crystallization of plagioclase and olivine assemblage may be a controlling factor on early magnetite crystallization.

The calculated liquidus minerals have compositions of An72.7, Fo77.7, $Mg\#_{Cpx}$77.3, $Mg\#_{Mgt}$27.1, and $Mg\#_{Ilm}$29.3 (Table 6.2), comparable to measured composition of An72.0, Fo78.1, $Mg\#_{Cpx}$79.8, $Mg\#_{Mgt}$16.0, and $Mg\#_{Ilm}$39.9. Note these latter data represent the most primitive minerals in rocks from the LZ to MZb in this study, and also within the UZ (Pang *et al.*, 2009). Note that Fo78.1 is the most Mg-rich composition of olivine found in oxide-rich gabbro, but it is higher in the massive ores due to subsolidus re-equilibration as described in previous chapters. The modelled magnetite contain up to 8.2 wt% MgO, much higher than the most MgO-rich magnetite measured in Panzhihua (5.2 wt%). It is interpreted as Fe-Mg exchange equilibrium between magnetite and olivine. The positive correlation between magnetite mode and MgO content in magnetite is a strong evidence for this prediction. In contrast, the modeled Ilm show lower MgO content than measured. It indicates that, like olivine, ilmenite may have increased its MgO content during subsolidus re-equilibration with

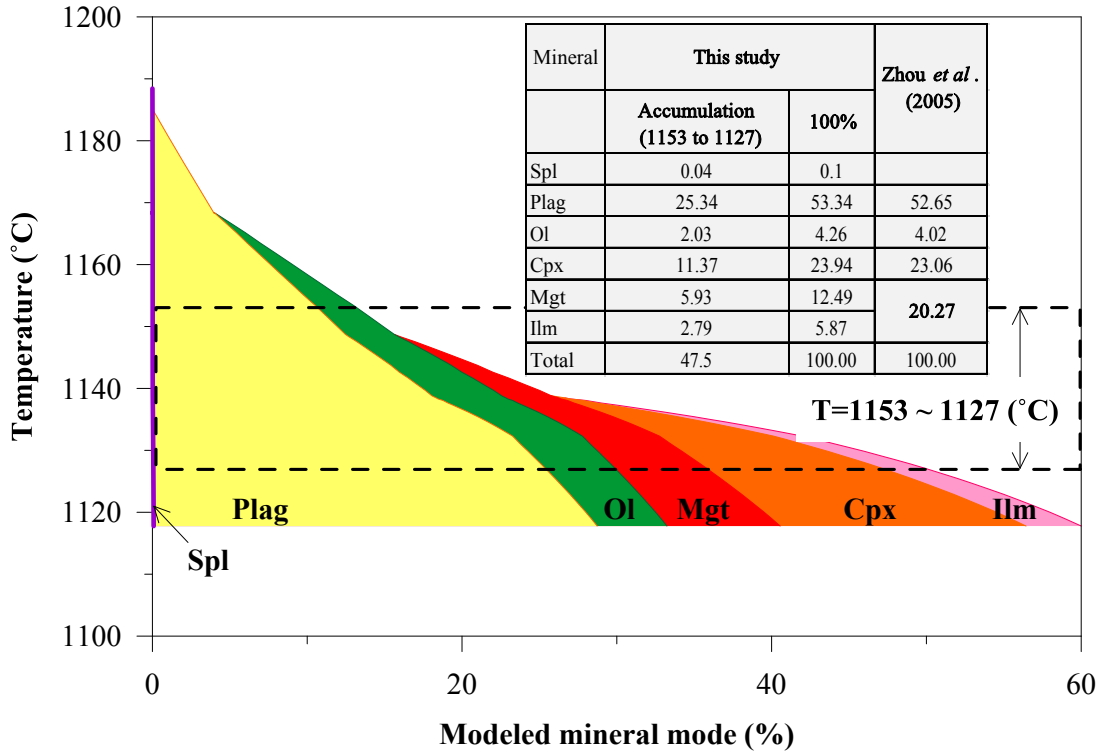

Mineral	This study		Zhou *et al*. (2005)
	Accumulation (1153 to 1127)	100%	
Spl	0.04	0.1	
Plag	25.34	53.34	52.65
Ol	2.03	4.26	4.02
Cpx	11.37	23.94	23.06
Mgt	5.93	12.49	20.27
Ilm	2.79	5.87	
Total	47.5	100.00	100.00

Fig. 6.4 Modelled mineral modes versus temperature, illustrating the relative abundance of crystallizaed minerals at different stages of magma differentiation. The shaded area denotes temperature interval of 1153 to 1127°C. The insert table compares the modal proportions of minerals crystallized within the above temperature interval, with those estimated by Zhou et al.(2005) from the Panzhihua Intrusion.

magnetite.

Mineral modes along the crystallization path are summarised in Table 6.2. At temperature interval 1153 to 1127°C, on a 100% normalized basis, the melt has fractionated 77.3 wt% clinopyroxene and plagioclase, 18.4 wt% Fe-Ti oxides and 4.3 wt% olivine, which is in excellent agreement with 75.7 wt%, 23.1 wt%, and 4.0 wt% estimates from Zhou *et al.*(2005) (Fig. 6.4). The ratio of modelled magnetite/ilmenite is ~ 2.1, within the range of that measured by MLA (0.1 to 9.6, averaged at 3.5). This indicates that the Panzhihua intrusion may represent accumulation of minerals fractionated during this temperature interval.

6.4 Summary

Numerical modelling with Petrolog3 not only successfully reproduce the crystallization sequence, mineral compositions that previous studies have achieved, but also similar mineral modal proportions, as well as the short crystallization interval. It reflects the assumed modelling strategy, starting magma composition and assumed modelling conditions are appropriate.

CHAPTER 7 DISCUSSION

7.1 Open Magmatic Plumbing System

Mass-balance calculations indicate that the Panzhihua intrusion contains too much Fe and Ti to be interpreted as crystallization from a single magma batch. Zhou *et al.*(2005) suggested the Panzhihua parental magma had concentrated Fe and Ti shortly before emplacement due to liquid immiscibility. According to this model, the Panzhihua gabbro and the Fe-Ti ore deposits represent cumulates from this Fe-Ti-rich but Si-poor magma, whereas the Si-rich liquid formed spatially associated syenite (Zhou *et al.*, 2008). Shellnutt and Jahn (2010) argued that the A-type granite in the vicinity of Panzhihua area may have a common parental magma with the gabbro and syenite, forming a complete plutonic-hypabyssal-volcanic igneous complex. Loss of evolved liquid from Panzhihua intrusion is confirmed by low abundance of strongly incompatible element Zr (Pang *et al.*, 2009). Hence, there is no doubt the Panzhihua intrusion is an open magmatic system. The other large gabbroic layered intrusions in the Pan-Xi district are also suggested as open systems, e.g. Hongge and Baima (Shellnutt & Pang, 2012; Zhong *et al.*, 2003, 2005).

Song *et al.* (2013) suggested, based on their mass balance calculations, the formation of ~ 100m thick massive ores in the lower Panzhihua intrusion requires ~ 3500m thick magma. These authors argued that this could not occur with a single magma batch, and requires repeat replenishment of more primitive magma. Although some cyclic units are observed in the LZ to MZa, in terms of concentrations of some trace elements in whole rock samples (Fig. 5.2), the model of Song *et al.* (2013) does not explain the nearly constant Mg# of clinopyroxene (Fig. 5.3). It is likely that different magma batches had similar compositions. The base of each cyclic unit (usually ore) have less evolved compositions, which may be explained by mixing of new less evolved magma with slightly evolved residual melt. Our modelling has shown that crystallization in the Panzhihua intrusion occurs within a small temperature interval. Re-equilibrium between magnetite and clinopyroxene may partly explain variations of Cr in magnetite, which is compatible in both minerals. Various rock-types contain different amounts clinopyroxene, and the ratio of magnetite/clinopyroxene may vary greatly. This may result in larger changes in Cr contents in magnetite in gabbros compared to ores.

Pang *et al*. (2009) recognized two distinct reversals in silicate mineral compositions. The lower one is recorded only in An content of plagioclase, but absent in $Mg\#_{Cpx}$ and Fo_{Ol}. In contrast, the upper one occurs at the sharp boundary between the MZb and the UZ, where all three minerals exhibit abrupt decrease in An_{Plag}, $Mg\#_{Cpx}$ and Fo_{Ol}. However, no gradual increase of these parameters up the section is observed. These authors interpreted both compositional reversals as evidences for replenishment of more primitive magma. However, this model does not explain the lack of compositional changes of clinopyroxene and olivine within the lower reversal. As described above, clinopyroxene display little variations across the entire stratigraphy, except at the boundary between the MZb and the UZ. This indicates that the composition of magmas from which clinopyroxene crystallized had similar compositions. The lower compositional reversal in An_{Plag} may be explained by introduction of H_2O-bearing fluids that originated from the interaction between intruding magmas and the wall-rocks, as many experiments have shown that H_2O may significantly increase An content of plagioclase (Almeev *et al*., 2012; Botcharnikov *et al*., 2008; Danyushevsky, 2001; Feig *et al*., 2006; HousH & Luhr, 1991). Crystallization under closed conditions is the likely explanation of the changes in mineral compositions at the boundary between MZb and UZ. It is proposed here that the Panzhihua magmatic system was open for most of the time, but closed after accumulation of approximately 1100m-thick cumulate from the bottom and at least 800m from the roof.

7.2 Generation of Fe-Ti-rich Parental Magma

According to the olivine-melt equilibrium model of Roeder and Emslie (1970), the melt in equilibrium with the most primitive olivine (Fo78) in oxide-rich gabbro from the Panzhihua intrusion has a Mg# of 0.52 (assuming Kd=0.3), slightly higher than in the starting composition used for Petrolog3 modelling (Mg#=0.49, Table 6.1). As magnetite-olivine subsolidus re-equilibration increases Fo content of olivine, it would be expected that the original olivine had lower Fo. Petrolog3 modelling has successfully reproduced mineral compositions and modes observed in the Panzhihua intrusion, and we believe that this starting material is close to the Panzhihua parental magma. However, the most Mg-rich olivine in wehrlite from the lower contact has composition of Fo82, which requires a Mg# of 0.58 in the equilibrium melt. This indicates that wehrlite crystallized from a less evolved parental magma. The least evolved olivine from the Hongge, Baima, Taihe and Xinjie layered intrusions have Fo content of 84, 76, 75 and 74, corresponding to Mg# of magma 0.61, 0.49, 0.47 and 0.46, respectively (Bai

et al., 2012; Hou *et al.*, 2012a; Ma *et al.*, 2003; Shellnutt & Pang, 2012; Wang *et al.*, 2008; Zhang *et al.*, 2012). Within this range of Mg# (0.46 to 0.61), the MgO content of Emeishan high-Ti basalts varies from 3.9 to 9.3 wt%. For less evolved high-Ti basalts (MgO>6.0wt%), the range of FeO* is 9.2 to 15.6 wt% (equal to 10.3 to 17.3 wt% $Fe_2O_3^*$). It is clear that not all starting compositions in published crystallization models fall within this large range.

It has been proposed that the Emeishan high-Ti basalts may have evolved from the Emeishan picrites (Wang *et al.*, 2007; Xiao *et al.*, 2004; Xu *et al.*, 2001). Experimental studies have shown that a ferropicrite may form either by partial melting of a garnet-bearing pyroxenite at high pressure (P≥5 GPa), or by partial melting of olivine-clinopyroxene at a lower pressure (P=2.2 GPa) (Tuff *et al.*, 2005). Gibson *et al.* (2000) interpreted the ferropicrite in the Pechenga complex to represent a low degree partial melt (<10%) of an Fe-rich peridotite at high pressure (35-45 kbar). Isotopic and geochemical studies have shown the ELIP ferropicrites reflect mantle source heterogeneity and show no evidence for crustal contamination. They may have formed by low-degree partial melting of a deep garnet-bearing mantle plume source (Chung & Jahn, 1995; Li *et al.*, 2012; Song *et al.*, 2001; Wang *et al.*, 2007; Zhang *et al.*, 2006). Xiao *et al.* (2004) and Song *et al.*(2008) suggested that the high-Ti basalts may have originated from a deep garnet-bearing mantle source, whereas low-Ti group may have originated from a shallower metasomatized subcontinental lithospheric mantle (SCLM).

The Emeishan picrites contain 9.6 to 17.6 wt% FeO*(mostly<12.5wt%), <9.3wt% Al_2O_3 and low HREE (e.g. Lu=~0.02) (Chung & Jahn, 1995; Li *et al.*, 2012; Song *et al.*, 2001; Zhang *et al.*, 2006). The FeO^* content is lower than typical ferropicrite reported elsewhere (e.g. Pechenga, Parana-Etendeka, Siberia, all with FeO^*=13 to19 wt%) (Gibson *et al.*, 2000; Hanski & Smolkin, 1989, 1995; Walker *et al.*, 1997). The ELIP high-Ti basalts with Mg# ranging from 0.46 to 0.61, contain an average of 11.8wt% FeO^* content. This suggests that the enrichment of Fe and Ti in the Emeishan basalts may reflect the composition of their parental melts, rather than being a result of fractional crystallization, as was suggested in some studies (e.g. Zhou *et al.*, 2005).

The effect of fractional crystallization on Fe-Ti enrichment in differentiated melts is determined by the liquidus mineral assemblage prior to magnetite saturation. Different studies have suggested several pre-magnetite liquidus mineral assemblages for the Panzhihua-type parental magmas: e.g. olivine only (Hou *et al.*, 2012b; Pang *et al.*, 2008a), olivine+clinopyroxene+Cr-spinel (Bai *et al.*, 2012), Cr-spinel+olivine+clinopyroxene+plagio

clase (Song *et al.*, 2013), olivine+clinopyroxene+plagioclase (Ganino *et al.*, 2008; Shellnutt & Pang, 2012), olivine+chromite+orthopyroxene+clinopyroxene+plagioclase (Zhang *et al.*, 2012), or Cr-spinel+plagioclase+olivine (this study).

Plagioclase contains very little Fe (likely dominated by Fe^{3+}), and thus crystallization of plagioclase leads to an increase in total Fe content and a slight decrease in Fe^{3+}/Fe^{2+} ratio (LAC, 2009; Phinney, 1992; Sugawara, 2001). Experiments on ferrobasaltic composition have shown that plagioclase appears on the liquidus before magnetite under most conditions (Toplis & Carroll, 1995), except for system with H_2O>~3.5 wt% at QFM+1 (Botcharnikov *et al.*, 2008), or H_2O-saturated and pressure>350MPa (Feig *et al.*, 2006). Extensive crystallization and fractionation of plagioclase have been suggested as an important mechanism for the genesis of anorthosites within layered intrusions. During this process the residual magma progressively becomes enriched in Fe (Charlier *et al.*, 2010; Duchesne, 1999; Namur *et al.*, 2011).

The effect of plagioclase crystallization on the Fe content in the residual magma is controlled by the proportion of plagioclase in the liquidus mineral assemblage and the total extent of fractionation. A substantial amount of plagioclase should form before magnetite appears on the liquidus in order to generate significant Fe enrichment. In some published crystallisation models for Panzhihua it was suggested that the temperature difference between the onset of plagioclase and magnetite crystallisation is very small, e.g. 6 to 10˚C (Shellnutt & Pang, 2012; Song *et al.*, 2013, Zhang *et al.*, 2012). This is significantly smaller than what was found in an experimental study (ΔT=~60˚C, Toplis & Carroll, 1995). Song *et al.*(2013) suggested that ~ 5.6 wt% plagioclase has formed before the appearance of magnetite on the liquidus, at a temperature 10˚C lower than that of plagioclase first appearance. Magma $Fe_2O_3^*$ and TiO_2 contents increased from 16.5wt% to 19.1wt%, and from 4.9wt% to 5.4wt%, respectively, corresponsing to increases by 15.8% and 10.2%.

In our modelling, the temperature difference between magnetite and plagioclase first appearance on the liquidus is ~ 36˚C. Crystallization of 12.66 wt% Plag and 3.21 wt% olivine over this temperature interval has resulted in a melt $Fe_2O_3^*$ increase from 14.6 wt% to 16.6 wt% (Table 7.1). The resultant $Fe_2O_3^*$ content is slightly lower than in the most Fe-rich high-Ti basalts with Mg#46-61 reported to date ($Fe_2O_3^*$=17.35 wt%). Our results are a better match for the range of known lava compositions than the results of Song *et al.*(2013). The difference in our results from those of Song *et al* (2013) may be related to the fact that we have modelled crystallisation as equilibrium (crystals remain within, and in equilibrium with, the

melt), whereas crystallisation was modelled as fractional in other studies.

The most primitive olivine crystal (Fo=82) in wehrlite PZ-6 from the Panzhihua intrusion contains ~17.2 wt% FeO^*, whereas the most primitive clinopyroxene (Mg#=85.8, PZ-6) contains 4.1 wt% FeO^*, compared with 14.6 wt% $Fe_2O_3^*$ in the starting composition used for our modelling. Thus crystallization of olivine slows Fe increase, whereas crystallization of clinopyroxene promotes Fe enrichment. As we suggest that clinopyroxene has appeared on the liquidus later than magnetite, its crystallisation does not contribute to producing high-Fe melt compositions.

In summary, our results suggest the Panzhihua-type parental magma was characterised by an Mg# between 0.46 to 0.61. This magma may be derived from Emeishan ferropicrites by crystallisation processes. The Fe-Ti enrichment in Panzhihua parental magma may have been caused by early crystallization of plagioclase. Clinopyroxene appears on the liquidus slightly later than magnetite.

7.3 Early Fractionation of Cr-Spinel before Emplacement

Cr is a strongly compatible element in magnetite, but less compatible in clinopyroxene and olivine (e.g. $D^{Mgt/Liq}$=153, $D^{Cpx/Liq}$=3.8, $D^{Ol/Liq}$=1.2) (Table 4.3). However, both the Panzhihua and Taihe magnetite show strong Cr depletion, except for those in wehrlite (Table 4.7 and 4.8; Fig. 4.27). This indicates that an early fractionation of Cr-spinel may have occurred before the magma emplacement into Panzhihua and Taihe intrusions. This is supported by the observation from the variation of Cr_2O_3 content in ELIP basalts, especially high-Ti basalts, as differentiation proceeds (Fig. 7.1). A remarkable drop of Cr_2O_3 content (from ~ 0.6 to 0.2 wt%) occurs within 7.2 to 7.5 wt% MgO. This composition is less evolved than the modelled Panzhihua parental magma (EM-82, MgO=6.44 wt%). Thus, if this sharp decrease of Cr_2O_3 is caused by Cr-spinel fractionation, it should have occurred before Panzhihua magma emplacement.

A more primitive high-Ti basalt (LZS-34, 9.03 wt% MgO) from Qi *et al.*(2008) has been chosen to model spinel crystallisation. The best results were achieved at fO_2 of NNO, with other conditions being similar to the modelling with sample EM-82, as described above. After ~10% fractional crystallization, the residual melt contained 7.61 wt% MgO. This composition was used as the starting composition for Stage 2 modelling at a more oxidized condition (NNO+1 for Stage 2-1, and NNO+1.5 for Stage 2-2) (Fig. 7.1). The modelled liquid line

of descent agrees well with the observations in high-Ti basalts, and suggests that the oxidation state of the magma may have increased by 1 to 1.5 log units of fO_2.

Our modelling suggests that Emeishan high-Ti basalt crystallisation history may have involved a period of early-stage Cr-spinel and/or clinopyroxene crystallization at 7.2 to 7.5 wt% MgO. The crystallization interval of Cr-spinel should be very short, as the magma would be Cr under-saturated soon after Cr-spinel crystallization. Meanwhile, clinopyroxene crystallization depletes the magma in Cr. As temperature decreases, the partition coeffetient of Cr in clinopyroxene increases, hence, it is likely that Cr depletion in magma is caused by clinopyroxene crystallization.

The oxidation state required to form spinel, as suggested by the crystallisation model we used (Borisov & Shapkin, 1990), is higher than what was suggested for Panzhihua type magmas previously (NNO vs QFM). We also found that crystallization at a constant oxidation state could reproduce the LLD comparable to high-Ti basalts only at very oxidised conditions

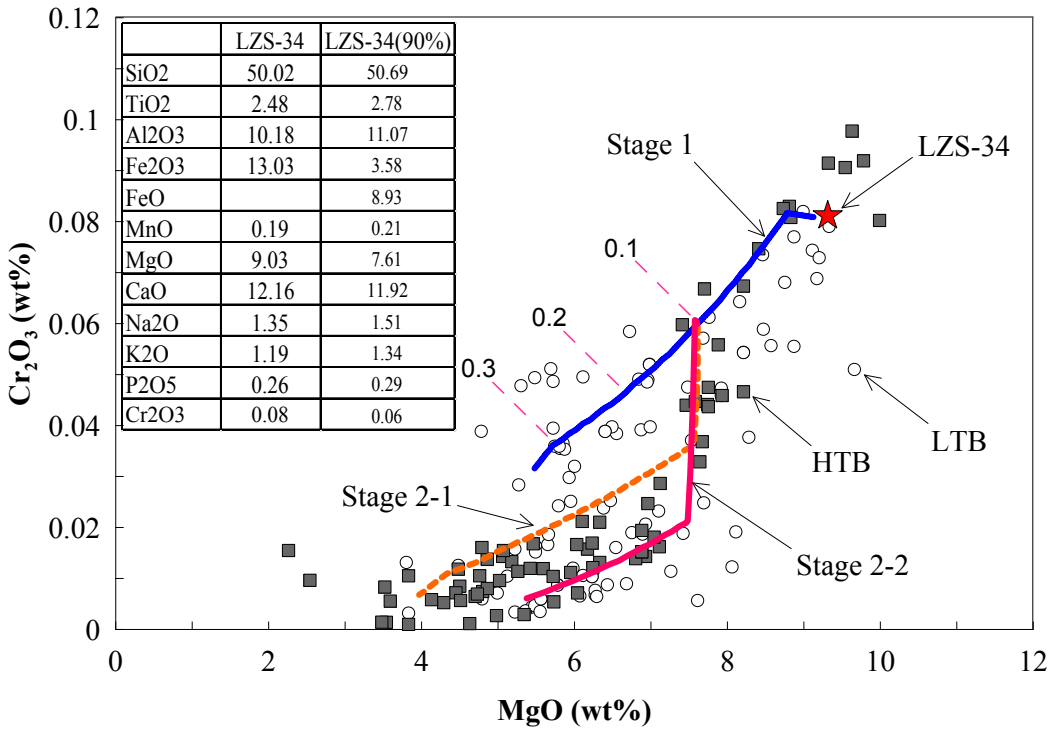

Fig. 7.1 MgO and Cr_2O_3 contents in Emeishan basalts (Xu *et al.*, 2001; Xiao *et al.*, 2003; 2004, Song *et al.*, 2001, 2008; Wang *et al.*, 2007; Qi *et al.*, 2008). HTB and LTB represent Emeishan high-Ti and low-Ti basalts, respectively. Also shown are the results of modelling of composition LZS-34 (high-Ti basalt from Qi *et al.*, 2008) with 0.08 wt% Cr_2O_3. The melt oxidation state at Stage 1 crystallization is set at NNO, and NNO+1 and NNO+1.5 for Stages 2-1 and 2-2. Stage 2 starts after ~ 10% fractional crystallization of LZS-34. For other modelling parameters see Section 6.1. Note the abrupt drop of Cr_2O_3 content in HTB, which is likely caused by crystallization of Cr-Spl under more oxidizing conditions.

(NNO + 1 ~ 1.5). We consider such a high oxidation state unlikely to persist for a long period of time on a large scale (e.g. in a deep-seated magma chamber). Instead, we consider it more likely that a relatively primitive magma became oxidized and saturated in Cr-spinel while ascending to the Panzhihua intrusion, possibly due to locallised assimilation of crustal rocks (Ganino *et al.*, 2008).

An increase in fO_2 for some Panzhihua parental magmas may also be inferred from the mineral compositions and proportions in the wehrlites from the MGZ. The lowermost wehrlite PZ-1 contains 0.17% magnetite, 1.54% ilmenite, 5.4% Hbl and no sulphide, whereas a higher level wehrlite PZ-6 contains 0.52% magnetite, 0.01% ilmenite, 1.1%Hbl, and 3.14% sulphide. Sample PZ-6 is also characterised by (1) Olivine with higher Fo but lower Ni contents (Fig. 4.18), (2) Clinopyroxene with high CaO, Al_2O_3 and TiO_2, and low MnO content (Fig. 4.22), (3) Magnetite with very low Fe^{2+}, (4) Ni-rich and Cu-, Co-poor pyrrhotite, with Ni/Cu and Co/Ni ratio of 525 and 0.01, respectively. This indicates sample PZ-1 was formed at more reduced conditions than PZ-6. During formation of the PZ-6, the magma may have undergone contamination by dolomitic wall rock, which has also induced sulphide saturation.

7.4 Origin of Wehrlite and high-An Plagioclase in the MGZ

7.4.1 Genesis of Wehrlite: Solidified Crystal-laden Primitive Magma

Three wehrlites were collected from the Lanshan mine section of Panzhihua. Wehrlites (PZ-1, PZ-6) occur as dykes or sills within the fine-grained gabbros in the MGZ or fine-grained gabbro and massive ore in the MZa (wehrlite PZ-17). Both MGZ wehrlites display porphyritic textures with phenocrysts of olivine and minor clinopyroxene in the MGZ wehrlite, and clinopyroxene-only in the MZa wehrlite (Fig. 3.6). In the latter, large clinopyroxene phenocrysts commonly display zoned-pattern of Fe-Ti oxide exsolution (Fig. 3.6 G-H, Fig. 3.7 F). Olivine also occurs as inclusions in clinopyroxene and to a lesser extent in plagioclase (Fig. 3.6 C, F). Plagioclase abundance (<15%) increases at higher stratigraphic levels. Fe-Ti oxides account for less than 5%. Ilmenite is more abundant than magnetite in wehrlite PZ-1, whereas it is the opposite in PZ-6 (Table. 3.1). Fe-Ti oxides occur as inclusions in olivine and to a lesser extent in clinopyroxene (Fig. 3.7). Note that the amount of magnetite inclusions in werhlite is much lower than in the gabbroic rocks. Spinel occurs at trace amount (<0.1%), mostly as granular exsolution along magnetite and ilmenite boundaries or within ilmenite.

The Mg# of MGZ wehrlite ranges from 81 to 82 (Table 4.1), indicating accumulation of primitive minerals. The Cr_2O_3 and NiO in magnetite and ilmenite, and NiO in olivine, in the MGZ wehrlites are higher than those in the MZa wehrlite. Mineral compositions in the MZa wherlite are less evolved than in the gabbroic rocks. This indicates that all wehrlites likely formed from more primitive magmas, however the parental magma of the MZa wehrlite is compositionally closer to those for the gabbros. Similar incompatible trace elements patterns in wehrlites and gabbros indicate that they are likely genetically related (Fig. 4.11, Fig. 4.14).

Petrographic observations suggest that olivine and clinopyroxene are both on the liquidus of the wehrlite parental magma during emplacement, rather than only olivine as was argued by Hou *et al* (2012b). Our modelling also showed that liquidus assemblage of LZS-34 is spinel+olivine+clinopyroxene. During the first 10% of crystallization, crystallizing Ol (Fo83.3-80.5) and clinopyroxene ($Mg\#_{Cpx}$ 85.0 -82.8) are similar in composition to the MGZ wehrlite (Fo81-82, $Mg\#_{Cpx}$81-86).

The textural features indicate both MGZ and MZa wehrlite may have formed by rapid solidification of crystal-loaded magmas, which intruded into already significantly solidified fine-grained gabbro. These injections of hot magma may have led to localised recrystallization of the gabbro, resulting in a coarser-grained texture observed in several locations.

7.4.2 High-An Plagioclase in wehrlite at contact (PZ-1)

Many experimental studies have shown that addition of H_2O to the melt results in crystallisation of more anorthitic plagioclase (Almeev *et al.*, 2012; Botcharnikov *et al.*, 2008; Danyushevsky, 2001; Feig *et al.*, 2010; HousH & Luhr, 1991; Mollo *et al.*, 2011; Panjasawatwong *et al.*, 1995).

Extremely calcic-rich plagioclase (An83) is found in the MGZ wehrlite at the contact with the wall rocks (sample PZ-1) (Table 4.6, Fig. 4.23, Fig. 5.3 A). These plagioclase occur as interstitial to clinopyroxene and Ol. The An content is much higher than the most Ca-rich plagioclase in other Panzhihua rocks (i.e. An72 in massive ores). The postcumulus nature of this plagioclase indicates that it has crystallised from the strongly evolved melts, which may have had substantial H_2O contents.

Howarth and Prevec (2013a) have suggested 0.5 to 1 wt% H_2O of the parental magma in Panzhihua-type deposit. Concentrations of up to 0.5 wt% H_2O where used in previous modelling of Panzhihua (Ganino *et al.*, 2008; Shellnutt & Jahn, 2010; Song *et al.*, 2013; Zhang *et al.*, 2012). Such concentration are consistent with what is suggested for other intra-

continental rift and LIP magmas (Dixon and Clague, 2001; Sobolev & Chaussidon, 1996). Thus the concentrations of H_2O in the post-cumulus liquid could have easily reached 1 wt%. Presence of minor amphibole and biotite throughout the Intrusion also support the presence of H_2O in the residual melts. Hydrous crystallization experiments by Botcharnikov *et al.*(2008) have shown that, on the liquidus though, addition of 1 wt% H_2O results in an increase of An content of plagioclase by about ~10%.

A relatively high cooling rate of PZ-1, supported by its fine-grained nature (Fig. 3.6a), could have also contributed to crystallisation of such high-An plagioclase. Mollo *et al.* (2011) have shown that faster cooling rates result in crystallisation of more anorthitic plagioclase, and this effect may have also contributed to the formation of high-An plagioclase in PZ-1. In additrion, calcium may have come from the assimilation of carbonate rocks.

7.5 Fe-Ti oxide ore formation processes

The ore formation processes involve two independent aspects: (1) the onset of Fe-Ti oxide crystallisation, and (2) concentration of these minerals to form an economic grade ore. If Fe-Ti oxide saturation occurs at a late stage of differentiation, when the crystallinity is very high, concentration of ore minerals would be inhibited. Two popular mechanisms have been proposed for the genesis of Fe-Ti±P±V oxide deposits in layered mafic intrusions: silicate liquid immiscibility (Charlier *et al.*, 2011; Jakobsen *et al.*, 2005; Reynolds, 1985a, 1985b; Ripley *et al.*, 1998; Scoon & Mitchell, 1994; Von Gruenewaldt, 1993; Zhou *et al.*, 2005, 2013) and periodic replenishment of more primitive basaltic magmas, where fractional crystallization is followed by crystal settling and sorting (Charlier et al., 2008; Namur et al., 2010; Pang et al., 2008a, 2008b, 2009; Shellnutt & Jahn, 2010; Song et al., 2013; Tegner et al., 2006; Wager and Brown, 1968). Neither of the hypotheses can explain mineral chemistry of the intrusion.

7.5.1 Fe-rich Liquid Immiscibility

The central issue with regards to the high-Fe liquid immiscibility hypothesis is not whether such an immiscibility can occur or not, but the time at which it can occur along a tholeiitic magma differentiation path. For the Skaergaard intrusion, it was suggested that silicate liquid immiscibility developed at the very advanced stage, during the formation of the Upper Zone of Layered Series (De, 1974; Jakobsen *et al.*, 2005; McBirney & Nakamura, 1974). Many other workers have argued for a much earlier onset of immiscibility at the top of LZ,

based on experimental results (Veksler *et al.*, 2007), compositionally distinct melt inclusions (Jakobsen *et al.*, 2011), the interstitial micro-textures (Holness *et al.*, 2011), and plagioclase compositions (Humphreys, 2011). Experiments which predicted high temperature liquid immiscibility (at ~1100˚C) has given rise to an intensive debate, where arguments based on field observations, representativeness of starting compositions, and achievement of stable phase segregation during the experiments were used to dispute the early immiscibility (McBirney, 2008; Morse, 2008; Philpotts, 2008; Veksler et al., 2008). Despite this ongoing controversy, liquid immiscibility has been invoked as a primary mechanism for Fe-Ti±P±V oxide deposits in some layered intrusions, e.g. the Sept Iles (Charlier et al., 2011; Namur et al., 2012), Bushveld Complex (VanTongeren & Mathez, 2012), Duluth Complex (Ripley *et al.*, 1998), Panzhihua and Hongge (Wang & Zhou, 2013; Zhou *et al.*, 2005, 2013).

The Panzhihua liquid immiscibility models either suggests that the layered gabbro and Fe-Ti oxide ores represent the Si-rich and the Fe-rich liquid, respectively (Zhou *et al.*, 2005), or that the bulk Panzhihua intrusion represents only the Fe-rich liquid, whereas the Panzhihua syenite represents the Si-rich liquid (Zhou *et al.*, 2013). The emphasis on the genetic relations between spatially close layered gabbroic intrusion, syenite and granites has emerged in recent studies (Shellnutt & Jahn, 2010; Zhou *et al.*, 2013). Shellnutt and Jahn (2010) suggested that the Panzhihua A-type granite may be intergrated into the gabbroic intrusion-syenite magmatic suite, forming a closed system. The Hongge layered intrusion and related Fe-Ti-V oxide deposit has also been attributed to silicate liquid immiscibility (Wang & Zhou, 2013). It should be pointed out that their evidence for liquid immiscibility is mainly from textural observations, e.g. net-textured ores, coronal olivine, eroded plagioclase and clinopyroxene commonly with hornblende rims, etc (Wang and Zhou, 2013; Zhou *et al.*, 2013). However, these textures may be caused by sub-solidus grain boundary readjustments, as oxides have a tendency to wet silicate minerals (Duchesne, 1999). Lindsley (2003) showed that experiments failed in generating Fe-Ti oxide melts and suggested that Fe-Ti-P oxides crystallized from silicate magma.

Several lines of geochemical evidence suggest that liquid immiscibility is unlikely to be the mechanism for Fe-Ti-V oxide ore formation in the Panxi district. Table 7.1 and Figure 7.1 show the relative enrichment of major oxides in two immiscible liquids based on published experimental results (Charlier & Grove, 2012; Dixon & Rutherford, 1979; Jakobsen et al., 2005; McBirney & Nakamura, 1974; Philpotts, 1982; Veksler et al., 2007). P_2O_5, TiO_2, MnO, MgO, and CaO preferentially partition into the Fe-rich liquid, whereas Al_2O_3 and al-

kalis concentrate in Si-rich liquid. The P_2O_5/K_2O ratio in the Fe-rich liquid is 14.5 to 235.7 times higher than in Si-rich liquid. Ratios of Na_2O/K_2O, FeO/MgO and MnO/FeO are simi -lar between the two immiscible liquids (Table 6.1).

The Fe-rich liquid contains > 40.67 wt% SiO_2 but < 30.85 wt% FeO^*, however, it is too enriched in SiO_2 but depleted in FeO^* when compared with Panzhihua and Taihe massive ores.

The Panzhihua and Taihe rocks display strong control of the mineral mode on the whole rock chemistry. For example, $Fe_2O_3^*$, TiO_2 and V_2O_5 are more abundant in massive ore rocks

Table 7.1 Compositions of conjugated immiscible silicate liquids from melt inclusions, natural lavas and experimental results.

Ref.	Jakobsen et al. (2005)		Philpotts (1982)		McBirney and Nakamura (1974)		Dixon and Rutherford (1979)		Charlier and Grove (2012)		Veksler et al. (2007)		Longhi (1990)	
	1		2		3		4		5		6		7	
	Lfe	LSi	Lfe	LSi	Lfe	LSi	Lfe	LSi	Lfe	LSi	Lfe	LSi	Lfe	LSi
SiO_2	40.67	65.58	41.5	73.3	51.4	65.5	43.9	68.5	42.5	68.5	44.4	63.4	45.3	67.3
TiO_2	1.86	0.22	5.8	0.8	2.4	1.2	4.61	1.7	4.1	1.2	3.4	3.1	3.3	1.2
Al_2O_3	7.87	12.95	3.7	12.1	6.7	9.6	7.01	1.1	6.8	12	9.6	11.5	9	11.2
FeO^*	30.85	8.63	31	3.2	26.6	11.9	23.45	7.86	24.7	7.3	20.8	6.9	22.2	7.5
MnO	0.51	0.13	0.5	0			0.55	0.16	0.4	0.1			0.6	0.2
MgO	2.35	0.47	0.9	0	0.4	0.4	2.32	0.75	2.2	0.6	4.7	3	2.1	0.7
CaO	8.97	2	9.4	1.8	6.7	3.1	10.18	3.82	10.1	3	10.7	7.5	10.2	3.7
Na_2O	1.58	4.33	0.8	3.1	2.2	2	1.85	2.86	1.3	2.7	1.3	1.6	0.3	0.6
K_2O	1.03	3.68	0.7	3.3	1	2.6	0.42	1.2	1	4.3	0.5	1.3	1.3	4.8
P_2O_5	0.25	0.03	3.5	0.07	1.7	0.3	4.87	0.96	4.8	0.6	3.1	0.4	3.9	0.7
Total	95.94	98.02	97.8	97.67	99.1	96.6	99.15	98.91	98	100.1	98.4	98.7	98.3	97.8
n.*	54	17	15	16			7	7	15	15	6	6	5	5
	$D_{ratio}^{Lfe/LSi}$													
$D_{P2O5/K2O}$	29.8		235.7		14.7		14.5		34.9		20.8		20.2	
$D_{Na2O/K2O}$	1.3		1.2		2.9		1.8		2.2		2.2		2	
$D_{FeO/MgO}$	0.7		-		2.2		1		0.9		2		1	
$D_{MnO/FeO}$	1.1		-		-		1.2		1.2		-		1.1	

*: number of analysis. Lfe: Fe-rich liquid; Lsi: Si-rich liquid. Data sources: 1: homogenized melt inclusions in cumulus apatite; 2: exsolved glasses; 3-7: experimental immiscible pairs.

than in gabbro and wherlites, whereas SiO_2, Al_2O_3 show the opposite behaviour (Fig. 4.3). However, CaO and P_2O_5 concentrations are higher in gabbro than in massive ores, which is in conflict with the experimental results (Fig. 7.2). Mineral modal proportions also control whole rock trace element abundances, e.g. Sc shows strong correlation with clinopyroxene abundances, whereas Cr, Ni, Ga in ores display linear correlation with magnetite modal proportion (Fig. 4.9). The two trends on Fig. 4.5 and Fig. 4.9 are likely a result of fractional style of crystallisation for the Fe-Ti oxides, but equilibrium style of crystallisation for clinopyroxene

and plagioclase.-

P strongly partitions into the Fe-rich liquid (Fig. 7.2, $D_P^{LFe/LSi} \approx 8–10$, Schmidt *et al.*, 2006; Watson, 1976). If massive ore rocks were formed from an Fe-rich liquid, they would have had cumulus apatite. If they formed directly by crystallisation of immiscible liquid to its own composition, they wouldn't be cumulates at all. However, the appearance of apatite marks the base of MZb (Pang *et al.*, 2008b), which is the most leucocratic part of the intrusion. All Panzhihua economic ores were accumulated before the formation of MZb. The absence of coexisting apatite and Fe-Ti oxides indicates liquid immiscibility is not the mechanism for producing oxide layers. In contrast to Panzhihua, co-existence of apatite with Fe-Ti oxides is observed in Bushveld (Ashwal *et al.*, 2005; Eales & Cawthorn, 1996), Skaergaard (Jakobsen *et al.*, 2005; McBirney, 1996), Bjerkreim-Sokndal (Duchesne & Charlier, 2005; Wilson *et al.*, 1996), and Sept Iles layered intrusion (Higgins, 2005; Namur *et al.*, 2010).

Unlike P, K concentrates in the Si-rich liquid during immiscibility (i.e., $D_{K_2O}^{LFe/LSi} = 0.08 – 0.5$) (Fig. 7.2). Thus, P_2O_5/K_2O ratio between Fe-rich and Si-rich liquids (expressed as

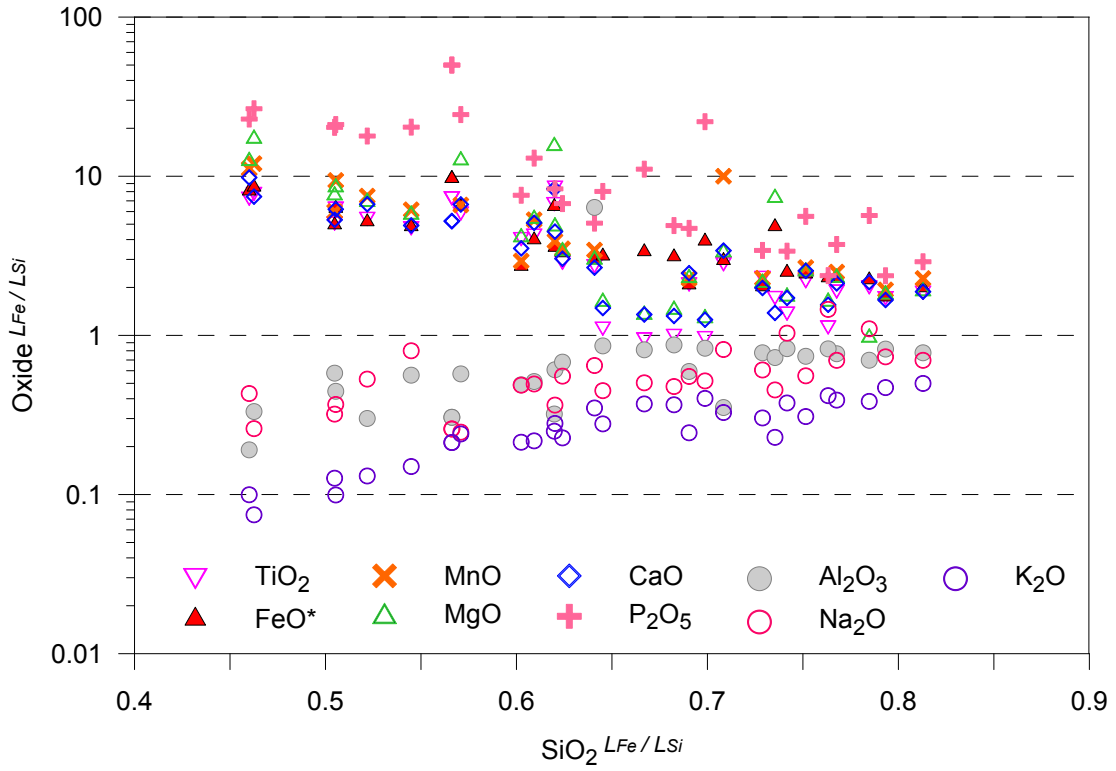

Fig. 7.2 Relative enrichment and depletion of immiscible liquids derived from experiments, melt inclusions and natural basaltic glasses (Charlier & Grove, 2012; Dixon & Rutherford, 1979; Jakobsen *et al.*, 2005; McBirney & Nakamura, 1974; Philpotts, 1982; Veksler *et al.*, 2007). $SiO_2^{LFe/LSi}$ represents the ratio of SiO_2 in Fe-rich liquid to Si-rich liquid. Note K_2O and P_2O_5 are the most enriched oxide in Si-rich liquid and Fe-rich liquid respectively.

$D_{P_2O_5/K_2O}$) is an effective indicator of liquid immiscibility (Veksler, 2009). The $D_{P_2O_5/K_2O}^{LFe/LSi}$ of immiscible pairs in the literature varies from 14.5 to 235.7, with an average of ~53 (Table 7.1) (Charlier & Grove, 2012; Dixon & Rutherford, 1979; Jakobsen *et al.*, 2005; McBirney & Nakamura, 1974; Philpotts, 1982; Veksler *et al.*, 2007,). If liquid immiscibility were responsible for the petrogenesis of Panzhihua intrusion, the P_2O_5/K_2O ratio of various rocks should be distinct and comparable to experimental data.

Before apatite occurs as a cumulus mineral in MZb of the Panzhihua intrusion, the range of whole rock P_2O_5/K_2O ratio is 0.1 to 0.8 for ores, with an average value of 0.4; whereas it varies from 0.1 to 0.3 for gabbro and oxide-gabbro (averaged at 0.2, not including the anorthositic leucogabbro PZ-23 with P_2O_5/K_2O ratio of 5.5). In the bulk gabbro, P_2O_5/K_2O ratio is ~ 2.2 (Zhou *et al.*, 2005), higher than P_2O_5/K_2O ratio of ores (~ 0.18). This is another clear indication that the layered gabbro and massive ores in Panzhihua could not form from two immiscible liquids.

Based on limited literature data on Panzhihua syenite and granite (Shellnutt & Jahn, 2010), their average P_2O_5/K_2O ratios are 0.04 and 0.01, respectively. Thus, the difference in P_2O_5/K_2O between the bulk Panzhihua intrusion and syenite is ~ 55 times, and with granite is ~ 220 times. These values are within the range of literature data of two-liquid pairs (e.g. $D_{P_2O_5/K_2O}$=54.8, C-109, Veksler *et al.*, 2007; $D_{P_2O_5/K_2O}$=230-236, Charlier & Grove, 2012; Philpotts, 1982). However, the bulk composition of Panzhihua is not consistent with being representative of the high-Fe liquid formed during liquid immiscibility.

REE abundances is another indicator of liquid immiscibility. Experiments on elemental partitioning between two immiscible liquids have shown that REEs have the highest partition coefficient between Fe-rich liquid and Si-rich liquid (e.g. $D_{REEs} \approx 10$, Schmidt *et al.*, 2006; Watson, 1976). Hence, if the Panzhihua gabbro and ore represented two immiscible liquids, as suggested by Zhou *et al.* (2005), gabbros should display a strong depletion in REEs. However Panzhihua gabbro have REE contents that are several times higher than the massive ores. If the bulk Panzhihua gabbroic intrusion (including Fe-Ti oxide ores) represents the Fe-rich liquid, whereas syenite or syenite and A-type granite represents the Si-rich liquid (Shellnutt & Jahn, 2010; Zhou *et al.*, 2008, 2013), the mineralized Panzhihua intrusion should be more enriched in REEs than the evolved part. However, the bulk Panzhihua intrusion contains 44 to 55 ppm REEs (Pang, 2008; Song *et al.*, 2013; Zhou *et al.*, 2005,), whereas Panzhihua syenite and A-type granite have ~ 436 ppm and 442 ppm REEs (Shellnutt & Jahn, 2010). Taihe

gabbro and ore have REEs concentrations and distribution patterns similar to the Panzhihua intrusion. Increasing REEs concentrations from massive ore, to layered gabbro, to syenite and granite, reflects partition behaviour during normal magma differentiation, rather than liquid immiscibility.

7.5.2 Early Saturation of Fe-Ti oxide

Evidences for early saturation of Fe-Ti oxide in Panzhihua-type layered intrusion include: (1) Fe-Ti ore bodies concentrate at the lower part of gabbroic intrusions (Li, 1992; Ma *et al.*, 2003; Wang, 1982; Zhou *et al.*, 2005); (2) Fe-Ti oxide inclusions are common in relatively primitive olivine (Pang *et al.*, 2008a); (3) lower concentrations of REE and other incompatible elements in ores than gabbro (Fig. 4.11 and 4.14); (4) less evolved silicate minerals coexist with cumulus low-Ti magnetite (e.g. $An_{Plag}72$, $Mg\#_{Cpx}81$, $Fo_{Ol}73$), compared with Skaerggard, the Upper Zone of Bushveld, and Kiglapait (Table 7.2); (5) Magnetite and ilmenite in ores contain higher MgO and Ni contents than in gabbro (Fig. 4.28 and 4.45); (6) crystallization modelling has shown that magnetite may crystallize early during differentiation of Fe-Ti rich basaltic magma.

The time and relative crystallization sequence of Fe-Ti oxides are controlled by Fe^{3+}/Fe^{2+} ratio of the liquid and thus strongly determine fO_2 (Botcharnikov *et al.*, 2008; Toplis & Carroll, 1995). Mantle-derived magma may be oxidized during ascent through the crust. Processes such as fractionation of Fe^{2+}-bearing minerals, magma mixing and contamination by crustal country rocks may increase the oxidation state of the magma. Our modelling has suggested that the sharp decrease in Cr contents in Emeishan high-Ti basalts at 7.2 to 7.5 wt% MgO may be due to onset of spinel crystallisation caused by an oxidation event. This makes it plausible that the Panzhihua parental magma had been oxidized before intrusion. A second-stage of oxidation may have occurred during emplacement into the Panzhihua intrusion, as a result of interaction with the country rocks (Ganino *et al.*, 2008). These authors suggested that CO_2-rich fluid phase fluxing through the magma could increase its oxidation state from QFM to QFM+1 to 1.5.

Our modelling suggests that TiO_2 content of the melt plays a key role determining the onset of ilmenite crystallisation relative to magnetite. Even at relatively oxidized conditions (NNO+0.3), the high TiO_2 content of basalt EM-82 (2.89 wt% TiO_2) results in magnetite appearing on the liquidus after ~ 2 wt% of ilmenite has already formed. This is inconsistent

with the field observations at Panzhihua. When TiO_2 content is reduced to 2.5 wt%, the melt crystallizes magnetite before ilmenite, and the proportion of magnetite/ilmenite is comparable to the observed. Thus the parental magma of Panzhihua intrusion may have TiO_2 content similar to the boundary value between high-Ti and low-Ti basalts (e.g. TiO_2=2.5 wt%, Xu *et al.*, 2001).

In summary, Panzhihua Fe-Ti oxides may have saturated at an early stage of magma differentiation. The magma may have undergone an oxidation event at deeper levels, when the MgO content was between 7.2 to 7.5 wt%. Decarbonization of the dolomitic country rocks may have also contributed to oxidising conditions.

Table 7.2 Comparison of mineral compositions at the time of Fe-Ti oxides and apatite saturation in Panzhihua and some layered intrusions.

	Panzhihua		Skaergaard	Bushveld MZ&UZ	Kiglapait	Sept Iles MCU I	Bjerkreim Sokndal	Newark	Grader
Ref.	**1**	**2**	**3**	**4**	**5**	**6**	**7**	**8**	**9**
				Fe-Ti oxides saturation					
Ol (Fo)	73	71	56	-	56	66	-	55	-
Cpx (Mg#)	76	79	65	67	70	-	75	64	-
Plag (An)	64	69	53	64	45	61	50	47	45
F*	-	-	55	61	10	-	-	38	-
				Apatite saturation					
Ol (Fo)	64	65	31	34	39	51	-	26	-
Cpx (Mg#)	73	76	44	57	56	71	72	43	-
Plag (An)	52	53	39	49	41	60	46	40	48
F*	-	-	<23	54	5	-	47	-	-

Data sources: 1. data in this study. For Fe-Ti oxide saturation, Cpx and Plag compositions are from a medium-grained melanogabbro (PZ-9) at the base of LZ ,Ol composition from a Hbl-Ol-bearing microgabbro in MGZ. For apatite saturation, Ol, Cpx and Plag compositions are from an apatite-gabbro (PZ-44) from MZb. 2-Pang *et al.*, (2009); 3-McBirney, 1996; Toplis & Carroll, 1995; 4-Tegner *et al.*, 2006; 5-Morse, 1979; 6-Namur *et al.*, 2010; 7-Duchesne & Charlier, 2005; Wilson *et al.*, 2006; 8-Snyder *et al.*, 1993; Weibe, 1988; 9-Charlier *et al.*, 2008.

7.5.3 Fe-Ti oxide ore concentration process

Three major models have been proposed for the Panzhihua-type Fe-Ti-V oxide deposit: (1) Fe-Ti oxides layers formed by direct crystallization and accumulation from immiscible Fe-Ti oxide melts (Zhou *et al.*, 2005, 2013); (2) Fe-Ti oxide layers represent oxide liquid that segregated by double-diffusive convection at depths and intruded as liquid (Hou *et al.*, 2012b); (3) Coupled crystal settling, sorting and multiple magma replenishments (Bai *et al.*, 2012; Pang *et al.*, 2008b, 2009; Song *et al.*, 2013; Zhang *et al.*, 2012). Fluctuation of intensive parameters (fO_2 and pressure) may have also contributed to Fe-Ti oxide ore formation, as sug-

gested for magnetite layers in the Upper Zone of Bushveld Complex (Cawthorn & Ashwal, 2009; Klemm *et al*., 1985).

A field observation that the base of oxide layers is typically gabbro, rather than anorthosite as is common in Bushveld (Cawthorn & Ashwal, 2009), is a strong argument against liquid immiscibility at Panzhihua. The lower boundaries are usually sharp and planar, without dendritic growth, or veins of oxides, as expected when dense Fe-rich liquid pools above lighter Si-rich liquid or crystal mush. The most Fe-Ti oxide rich rock (PZ-13) is composed of approximately 85% magnetite, 10 % ilmenite and 3% spinel. The total $Fe_2O_3^*$ and TiO_2 contents of this ore are 71.8 wt% and 15.1 wt% respectively, much higher than experimentally observed extreme enrichment of iron in Fe-rich liquid (FeO^*<28 wt%, TiO_2<5 wt%, Veksler *et al*., 2007).

The Panzhihua Fe-Ti-V oxide deposit has been suggested to form by crystal settling and sorting after early saturation of Fe-Ti oxides (Pang *et al*., 2008b; Song *et al*., 2013). Song *et al*. (2013) suggested periodic replenishment of more primitive magma along the intrusion floor resulted in the formation of 11 cyclic units observed in the whole rock compositions and Cr content of magnetite from the Zhujiabaobao mine. However, since the whole rock compositions are largely controlled by the mineral modes, and the post-cumulus re-equilibration process are common (see Chapters 4 and 5), the whole rock chemistry of the cumulates cannot reflect the composition of the parental magma. Unlike Song *et al*. (2013), Pang *et al*. (2009) suggested that two replenishments occurred in the Panzhihua magma chamber, based on silicate mineral chemistry. As discussed above, this is inconsistent with the results of this study.

PETROLOG3 modelling suggests melt density of ~ 2.73 g/cm^3 for the parental magma. This density is similar to typical anorthosite (e.g. 2.7 g/cm^3, Cawthorn and Ashwal, 2009), but different to most liquidus phases (ρ_{Mgt}=5.2; ρ_{Ilm}=4.7; ρ_{Fo75}=3.2; $\rho_{Mg\#_{Cpx}75}$=2.8; ρ_{An60}=2.55, Charlier *et al*., 2009; Scoates, 2000). After Fe-Ti oxide saturation, the density of the residual melt decreases rapidly to ~2.64 after 55% crystallization. During this crystallization interval, plagioclase (An_{72-55}) is lighter than the melt, whereas Fe-Ti oxides and other phases are denser.

On the basis of our modelling, a new ore-formation process is proposed here. In our model, the Panzhihua intrusion acts as an open plumbing system, where crystal-rich magmas continuously intrude and flow through. Magmas intruding during the ore forming stage (below MZb level) had similar compositions, resulting in gabbros with nearly constant mineral compositions. The silicate minerals accumulated both at the floor and roof, whereas the Fe-Ti

oxides preferentially accumulate at the bottom. The magmatic system closed after accumulation of ~ 1100 m thick cumulates at the bottom, and ~ 800 m at the roof. After that the trapped melt differentiated in-situ in a closed system. Therefore, an alternative hypothesis is proposed, where Fe-Ti oxides accumulated from crystal-rich magma that flowing though the Panzhihua plumbing system. The details of the new genetic model in introduced below.

7.6 A New Petrogenetic Model

The new petrogenetic model is developed based on the arguments presented above for the Panzhihua gabbroic layered intrusion and associated Fe-Ti-V oxide deposits, and may

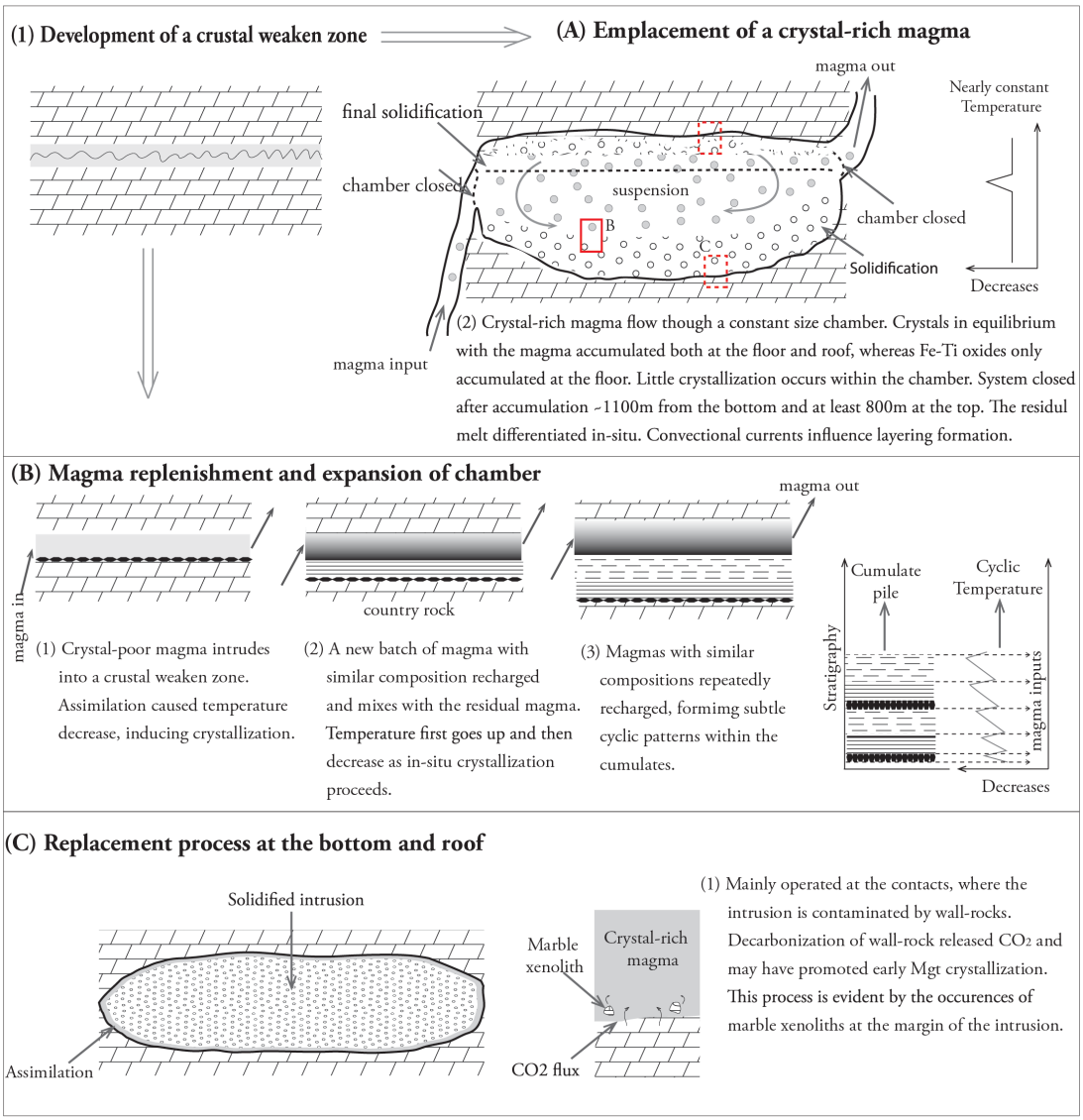

Fig. 7.3 A new petrogenetic model is proposed for the Panzhihua-type gabbroic layered intrusions and associated Fe-Ti-V oxide deposits. See text for details.

appropriately applied to explain the formation of similar Panzhihua-type deposits. The main processes of the new model are summarized as follows (Fig. 7.3).

1. a weakened zone has developed at an upper crustal depth, either due to tectonic processes associated with the formation of the ELIP, or an earlier event.
2. a crystal-rich magma intruded into the weakened zone, initially replacing some of the wall-rock and then gradually increasing the size of the chamber to current scale of the Panzhihua Intrusion by pushing apart the country rocks. The crystals in equilibrium with magma precipitated from the magma due to slower velocity within the chamber. Silicate minerals accumulated both at the floor and at the roof, whereas Fe-Ti oxides accumulated only at the floor due to their much higher density. The chamber closed after accumulation of ~ 1100m-thick cumulates from the bottom, and at least 800m-thick from the top. The residual melt differentiated *in-situ* under closed-system conditions, as inferred from the abruptly upward decreasing in An, Fo and $Mg\#_{Cpx}$. The temperature of magmas flowing through the intrusion was nearly constant, and little crystallization occurred.
3. An increasing size magma replenishment process. After first crystal-rich magma entered the intrusion, more extensive crystallisation and assimilation occurred, as the temperature decreased due to interaction with the cold wall-rocks. New pulses of crystal-rich magma with similar compositions were mixing with the residual melts, leading to crystallisation of minerals with slightly more primitive compositions than what crystallised from the residual melt just before it was leaving the magma chamber. As new pulses of magmas repeatedly recharged the system, continuous minor variations in mineral chemistry may have formed the observed subtle cyclic patterns within cumulates.
4. A replacement process at the contact with the country rocks. At the contacts, the intrusion is contaminated by the surrounding country rocks. CO_2 released from decarbonization of the wall-rock may have contributed to an increase in fO_2, promoting early magnetite crystallization. Some marble xenoliths are found at the margins of the intrusion as evidence for incomplete assimilation of the wall-rock.

7.7 Implications for Sulphide Saturation History

Many processes may induce sulphide saturation, either by incorporating external S to reach sulphide saturation, or decreasing sulphide solubility (the sulfur content at sulphide saturation- SCSS). Disputed in some cases, but not in most (Lehmann *et al.*, 2007; Seat *et*

al., 2011), crustal contamination has been widely considered as an important mechanism for the genesis of many world-class Ni-Cu-PGE sulphide deposits in mafic-ultramafic intrusions, e.g. Noril'sk, Jinchuan, Stillwater, Voisey's Bay (Arndt *et al.*, 2003, 2005; Barnes & Lightfoot, 2005; Brügmann *et al.*, 1993; Keays *et al.*, 2012; Keays & Lightfoot, 2010; Lightfoot *et al.*, 1990, 2012; Naldrett, 1992, 1997; Ripley & Li, 2013; Song *et al.*, 2006a). Mixing of two magmas with distinct compositions can also reduce the SCSS and promote sulphide saturation (Li & Ripley, 2005; Ripley & Li, 2013). Ripley and Li (2013) have discussed the effects of silicate fractional crystallization on sulphide solubility. Mavrogenes and O'Neill (1999) suggested that sulphide solubility increases with decreasing pressure, and concluded that, without addition of external S, mafic magmas that intruded into shallow depths are unlikely to reach sulphide saturation.

The following mechanisms of sulphide saturation unlikely occurred at Panzhihua. First, geochemical and isotopic studies have shown that crustal contamination has played an important role in the generation and evolution of low-Ti basalts, whereas it was insignificant in high-Ti basalts that in genetic relationship with Fe-Ti oxide deposits (Qi and Zhou, 2008; Song *et al.*, 2001; Wang *et al.*, 2007; Xu *et al.*, 2001). Low initial $^{87}Sr/^{86}Sr$ ratio and positive εNd of the Panzhihua rocks suggest weak crustal contamination, except for some microgabbro in the MGZ (Howarth & Prevec, 2013b; Pang *et al.*, 2013; Song *et al.*, 2013). Pang (2008) analysed $\delta^{34}S$ in Panzhihua rocks and suggested a mantle-derived source for sulphur. Hence,

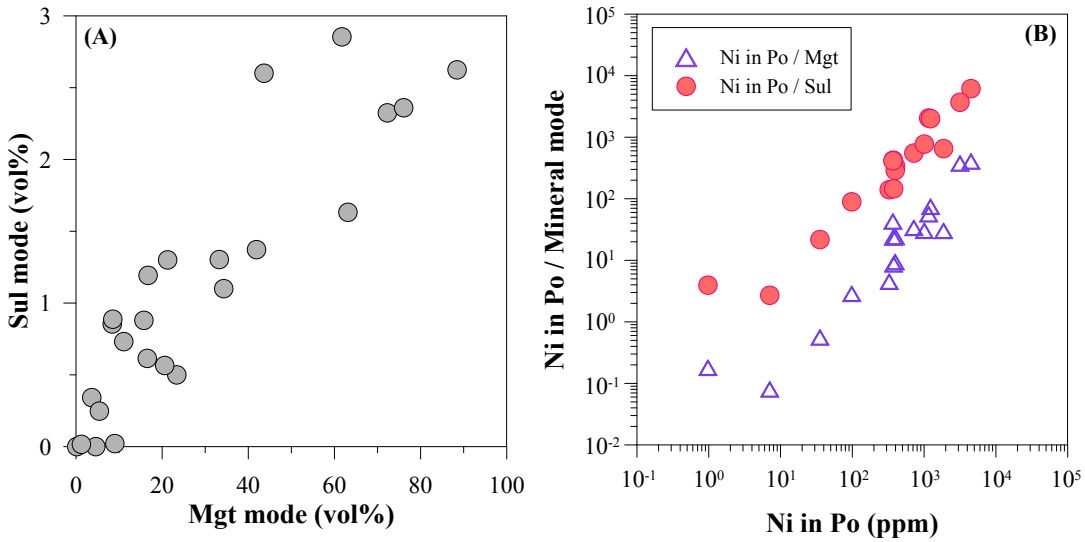

Fig. 7.4 (A) Plot of sulphide modal proportion against magnetite modal proportions for the Panzhihua rocks. All data are measured by Mineral Liberation Analysis (MLA). The positive correlation between modal proportions of sulphide and magnetite is consistent with field observations. (B) Correlations between the content of Ni in Po and ratios of Ni in Po/Mgt mode and Ni in Po/Sul mode.

crustal contamination is not the cause of sulfide saturation in the Panzhihua. Second, since we suggest that parental magmas flowing through the Panzhihua plumbing system had similar compositions, mixing of chemically distinct magmas is not a viable mechanism for sulphide saturation in Panzhihua. The near constant clinopyroxene across the stratigraphy is against with magma mixing hypotheses.

Appearance of sulphides in the Panzhihua intrusion is likely related to crystallization processes. Crystallization of silicate minerals leads to an increases of sulfur content in the magma (Ripley & Li, 2013), whereas magnetite crystallization significantly decreases total iron content in the melt, leading to sulphide saturation (Jenner *et al.*, 2010; Maier *et al.*, 2003; Prendergasr, 2000). The immiscible sulphide is an Fe-rich monosulphide liquid which also contained Ni and Cu. Enrichment of Cu relative to Ni in Panzhihua sulfude is consistent with a relatively late appearance of immiscible sulphide liquid, after crystallisation of olivine has depleted melt in Ni. There is a positive correlation between modal proportions of sulphide and magnetite (Fig. 7.4 A), which are also correlated with Ni contents in pyrrhotite (Po) (Fig. 7.4 B). A strong correlation between magnetite and sulphide abundances is a further evidence for the origin of magnetite ores by fractionation processes, as both magnetite and sulphide are dense and would settle together.

PGE data on Panzhihua rocks show that the intrusion is PGE-depleted relative to ELIP high-Ti basalts (Howarth & Prevec, 2013b; Pang *et al.*, 2013). Pang *et al.* (2013) found the absolute PGE concentrations decrease in the sequence of microgabbro, Fe-Ti oxide ores, layered gabbro, and isotropic gabbros. However, this correlation is not observed from the data of Howarth and Prevec (2013b). Most PGE data plot within S-saturated field (Vogel & Keays, 1997), whereas some ore rocks show slightly less depleted Pd content, which may be related to post-magmatic Pd mobility in high-temperature fluids (Boudreau, 1999a). Isotropic gabbros are characterised by high Cu/Pd ratios but low Pd contents (Fig. 7.5). This indicates the parental magma is PGE-depleted. Howarth and Prevec (2013b) proposed two PGE depletion processes during evolution of Panzhihua magmas: one is triggered by fractionation of Ol, Chr and Pt-rich PGMs at a moderate depth beneath the Panzhihua intrusion, whereas the other is trigged by minor crustal contamination at depth. Song *et al.* (2009) have suggested that fractionation of mafic minerals and IPGE- and Pt-rich PGM may be responsible for the generation of PGE-depleted magmas.

Early-stage sulphide saturation may be excluded based on observations of magnetite

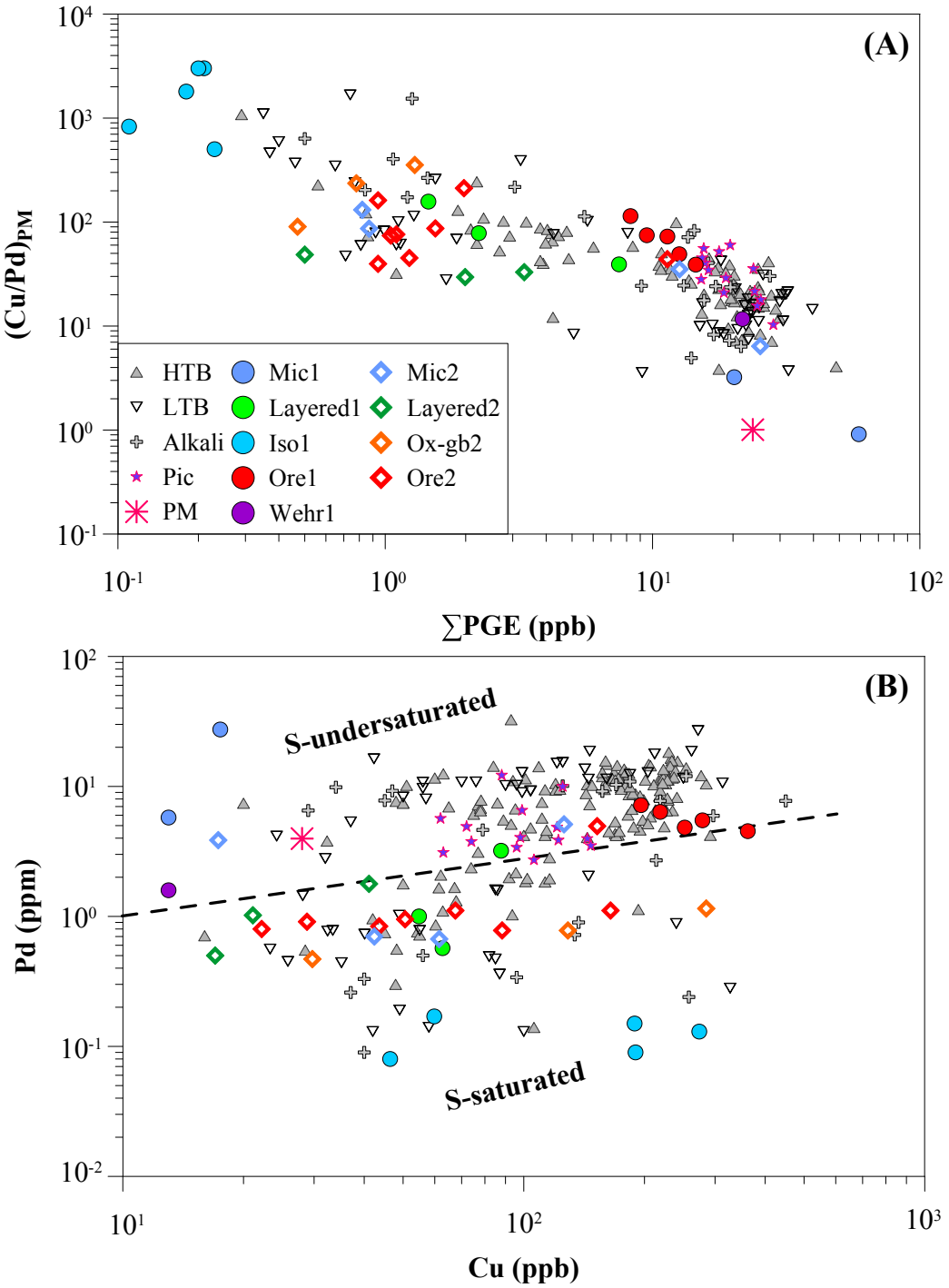

Fig. 7.5 Plots of primitive mantle normalized (Cu/Pd) versus ∑PGE (A) and Pd versus Cu (B) for Emeishan basalts, picrites, and Panzhihua rocks. HTB: high-Ti basalt, LTB: low-Ti basalt, Alkali: alkali basalt, Pic: picrite. Lava data sources: Li *et al.* (2012); Qi *et al* (2008); Qi and Zhou (2008); Song *et al.* (2006, 2009); Wang *et al.* (2006, 2007, 2011); Zhang *et al.* (2006). Panzhihua PGE data are from Howarth et al (2013); Pang et al(2013). Ore 1 and Ore2 are from the Nalaqing mine (Howarth *et al.*, 2013; Pang *et al.*, 2013). Dashed line in (B) separating S-saturated and undersaturated samples is from Li *et al.* (2012) and Vogel and Keays (1997). The primitive mantle data are from Barnes and Maier (1999).

chemistry. A small amount of sulfide fractionation depletes PGEs very much faster than Ni and Cu because partition coefficient of PGEs are much higher. And partition coefficient is much lower for Ni into sulfide at high temperature than at low temperature, so early saturation only has a small effect on reducing Ni content. If immiscible sulphide liquid segregated early from silicate magma, it would have high Ni contents and Ni/Cu values > 1, as inferred from Ni and Cu partition coefficients between sulphide and silicate liquids (Barnes & Maier, 1999). However, this could not explain up to 6 magnitude enrichment of Cu relative to Ni commonly observed in the Panzhihua sulphide and magnetite (Fig. 4.34). The Cr, Ni and Cu distribution in magnetite suggests that, the PGE-depleted relatively primitive magma have undergone fractionation of large amount of olivine at depths, depleting the residual magma in Cr and Ni, but enriching in Cu, which is incompatible in fractionating minerlals. Cr-spinel fractionation may have little effets on PGEs fractionation, except for Ru (Pagé *et al*., 2012; Sattari *et al*., 2002).

In summary, the Panzhihua parental magma is PGE depleted, which may have been caused by fractionation of olivine, and PGM, rather than early sulphide saturation. The present Panzhihua sulphides represent immiscible monosulphide liquids segregated during massive magnetite crystallization. These sulphide liquids were trapped in cumulate piles and crystallized to form current observed PGE and Ni depleted sulphides.

CHAPTER 8

SUMMARY AND CONCLUSIONS

A model was developed that describes the origin of the Panzhihua gabbroic layered intrusion and associated Fe-Ti-V oxide deposits, based on detailed investigations of geochemical variations within rocks and major cumulus minerals, including Fe-Ti oxides and sulphides from the lower part of the Intrusions, where significant Fe-Ti-V oxide ores are concentrated. New data of whole rock and major cumulus mineral chemistry are provided, including LA-ICP-MS analysis of magnetite, ilmenite, and pyrrhotite, which have not be reported previously. Crystallization modelling was performed using Petrolog3 software.

8.1 Geochemical Investigation

Investigations of whole-rock chemistry show that the Panzhihua and Taihe intrusions are largely cumulate bodies. The major element compositions reflect relative abundances of Fe-Ti oxides (magnetite and ilmenite) and silicate minerals (clinopyroxene and plagioclase). In general, $Fe_2O_3^*$, TiO_2, V_2O_5, MnO are controlled by the Fe-Ti oxides, whereas SiO_2, CaO, Al_2O_3, Na_2O and K_2O are controlled by silicate minerals. Some rock chemistry is affected by the presence of olivine, Hbl and Ap. There is little evidence for significant amounts of intercumulus liquid in the lower parts of the Intrusions. The distributions of trace elements are more complicated due to compatibility in more than one mineral. The abundance of a trace element in a rock depends on its partition coefficients in various minerals and their modal proportions. Compared with high-Ti basalts, these intrusive rocks show lower REE contents and less fractionated LREE. However, comparable highly fractionated HREE and general incompatible element distribution patterns, indicate the Panzhihua and Taihe intrusive rocks have genetic relationships with high-Ti basalts.

Two populations of minerals are identified in the Panzhihua gabbroic layered intrusion. Wehrlites contain more primitive silicate minerals, Cr-Ni-rich Fe-Ti oxides, and PGE-depleted pyrrhotite, whereas other rocks contain Ni-depleted olivine, Cr-depleted clinopyroxene, Cr-Ni-depleted Fe-Ti oxides, PGE and Ni-depleted pyrrhotite. The features indicate wehrlite crystallized from less evolved magmas than the gabbroic intrusion. The magma that formed

wehrlite has undergone removal of PGM and/or immiscible sulphide liquid, whereas the magmas parental to the gabbros and ores have experienced early fractionation of spinel and olivine. Nevertheless, these magmas have a common primitive parent.

Post-cumulus re-equilibrium processes have played a significant role in modification of mineral chemistry. Magnetite-ilmenite re-equilibration led to exsolution of granular hercynite. magnetite-clinopyroxene re-equilibration has affected their Cr contents. Magnetite-olivine re-equilibrium has increased Fo content of olivine. This effect is less prominent for clinopyroxene. Based on mineral compositions in oxide-poor gabbros, equilibrium temperatures calculated using a clinopyroxene-olivine thermometer and also Anorthite content of plagioclase, indicate that Fe-Ti oxide crystallization occurred within a relatively small temperature interval.

Variations in whole rock and mineral chemistry along a vertical profile through the Intrusions are closely related to mineral modal proportions and re-equilibration processes. Overall, the MGZ rocks show a more complex pattern due to variations in mineral modes, wall-rock contamination and rapid cooling. In contrast, the LZ and MZa are characterised by relatively constant compositions. Combining our data with published data for rocks from the MZb and UZ, the relatively constant compositions of Panzhihua rocks extends throughout the intrusion except for the top of MZb. The latter is interpreted as *in-situ* crystallization in a closed system, whereas the system was open for accumulation of most Panzhihua cumulates. The parental magmas were suggested to have similar compositions. The reversal recorded in An of plagioclase in the lower MZa is explained by crystallization at elevated melt H_2O contents.

Wehrlite in the MGZ and MZa were formed by rapid cooling of an olivine and/or clinopyroxene bearing, relatively primitive magma. An abnormally high-An plagioclase at the contact of wherlite with the country rock is interpreted as crystallisation at a rapid cooling rate and from an H_2O-bearing melt.

8.2 Magma Crystallization Modelling

Crystallization modelling has shown that Fe-Ti oxide may reach saturation at an early stage under relatively oxidized conditions. Assimilation of dolomitic country rocks may lead to an increase in fO_2 of the melt, resulting in early fractionation of Cr-spinel, and may explain the abrupt drop in Cr_2O_3 contents during evolution of Emeishan high-Ti magmas. This process is also likely during magma emplacement, trigging Cr-poor magnetite crystallization. Additionally, crystallisation of olivine and plagioclase progressively increase fO_2 of the melt, causing

crystallization of magnetite which was followed by clinopyroxene and ilmenite.

The modelled liquidus silicate mineral compositions matched well mineral compositions in the Intrusion. The Fe-Mg exchange during magnetite-olivine and magnetite-ilmenite re-equilibration has depleted magnetite in MgO, but increased olivine and ilmenite in MgO. This may explain observed higher MgO in modelled magnetite, and lower MgO in modelled ilmenite, compared with measured.

Within a small interval of crystallization temperature (1153 to 1127°C), the parental magma fractionated an assemblage of olivine, plagioclase, clinopyroxene, magnetite and ilmenite, which proportions are similar to those in the average bulk Panzhihua Intrusion. This suggests that Panzhihua cumulus minerals may have formed from crystal-rich magmas passing through the magma chamber.

The parental magma is Fe-rich, with Ti content close to the values in high-Ti basalts with the lowest Ti contents. Early crystallisation of olivine and plagioclase leads to $Fe_2O_3^*$ and TiO_2 enrichment in the residual magma. The Mg# of Panzhihua magma is estimated to be 0.49, within the range of 0.46 - 0.61 from previous studies.

8.3 Petrogenetic Model

We proposed a new petrogenetic model for the Panzhihua Intrusion, which may be applicable in other gabbroic layered intrusions and associated Fe-Ti-V oxide deposits. In this model, the Panzhihua Intrusion acts as an open magmatic plumbing system. Moderately evolved crystal-loaded Fe-Ti rich basaltic magmas continuously flow through the plumbing system, leaving crystals cumulates both on the floor and the top, while the residual melt rises to the surface, forming high-Ti basalts. The density differences between minerals may be responsible for crystal settling, sorting, and layering formation. After accumulation of approximately 1100m-thick cumulates at the bottom, and at least 800m-thick cumulates at the top, plumbing system had closed, leading to *in-situ* crystallisation of the trapped magma under closed system conditions, forming the evolved section at the top of the MZb zone.

When a new pulse of the crystal-rich magma recharges and mixes with the residual melt above the cumulate pile, minerals having slightly more primitive compositions form. This effect is minor, as only minor fractionation occurs within the chamber, resulting in the residual liquids being similar to the recharging melt. Within the MGZ, high temperature gradients between the magma and the wall rock resulted in extensive assimilation, forming hornblende-

rich gabbros.

Early fractionation of olivine, Cr-spinel and PGM may be responsible for PGE and Cr, Ni depletions in the Panzhihua parental magma. Sulphides present in the Panzhihua Intrusion are the result of sulphide saturation triggered by massive magnetite crystallization. These sulphides precipitated with Fe-Ti oxides and are often trapped as inclusions by the silicate and oxide minerals.

8.4 Future work

The central part of the proposed petrogenetic model is the direct deposition of crystals suspended in magmas flowing through the chamber, all of which had fairly similar compositions. If correct, this implies that any variations in plagioclase composition within the intrusion should reflect crystallisation of the interstitial liquid. Identification of interstitial plagioclase in samples with the highest levels of incompatible elements (e.g., Zr), which should have the largest amounts of trapped interstitial melt, would allow an insight into the cooling processes through mapping of fine zoning within interstitial plagioclase.

Secondly, this model is developed for the Panzhihua and Taihe Intrusions and associated deposits. Although the other contemporaneous intrusions and deposits in the Pan-Xi district (e.g. Baima, Xinjie, Hongge) have shown similarities to the Panzhihua deposit in some aspects, the applicability of this model to these other deposits needs further investigation. More mineral composition data from the other Panzhihua-type deposits are necessary to make comparison and assess the validity of the model.

Thirdly, a wide variety of Fe-Ti-P oxide deposits has been described in the literature. These deposits have variable ore mineral assemblages, such as magnetite-dominated, magnetite+ilmenite, ilmenite-dominated, and nelsonite. Except for nelsonite, which is widely regarded as being formed as a result of liquid immiscibility, the origin of other deposit types remains controversial. Whether this variety is related to differences in parental magma compositions, fractional crystallization process, crystallization conditions, or liquid immiscibility requires further investigation.

References

Aigner-Torres, M., Blundy, J., Ulmer, P. & Pettke, T. (2007). Laser Ablation ICPMS study of trace element partitioning between plagioclase and basaltic melts: an experimental approach. *Contributions to Mineralogy and Petrology* **153**, 647-667.

Ali, J. R., Thompson, G. M., Zhou, M. F. & Song, X. Y. (2005). Emeishan large igneous province, SW china. *Lithos* **79**, 475-489.

Almeev, R. R., Holtz, F., Koepke, J., Parat, F. & Botcharnikov, R. E. (2007). The effect of H_2O on olivine crystallization in MORB: Experimental calibration at 200 MPa. *American Mineralogist* **92**, 670.

Almeev, R. R., Holtz, F., Koepke, J. & Parat, F. (2012). Experimental calibration of the effect of H_2O on plagioclase crystallization in basaltic melt at 200 MPa. *American Mineralogist* **97**, 1234-1240.

Anderson, A. & Morin, M. (1969). Two types of massif anorthosites and their implications regarding the thermal history of the crust. Origin of Anorthosite and Related Rocks. *New York State Museum and Science Service Memoir* **18**, 57-69.

Andersen, D. J., Lindsley, D. H. & Davidson, P. M. (1993). QUILF: A pascal program to assess equilibria among Fe-Mg-Mn-Ti oxides, pyroxenes, olivine, and quartz. *Computers & Geosciences* **19**, 1333-1350

Anderson, D. L. (1994). The sublithospheric mantle as the source of continental flood basalts; the case against the continental lithosphere and plume head reservoirs. *Earth and Planetary Science Letters* **123**, 269-280.

Ariskin, A. A. & Barmina, G. S. (1999). An empirical model for the calculation of spinel-melt equilibria in mafic igneous systems at atmospheric pressure: 2. Fe-Ti oxides. *Contributions to Mineralogy and Petrology* **134**, 251-263.

Ariskin, A. A. & Barmina, G. S. (2004). COMAGMAT: Development of a magma crystallization model and its petrological Applications. *Geochemistry International* **42**, S1-S157.

Ariskin, A. A., Frenkel, M. Y., Barmina, G. S. & Nielsen, R. L. (1993). COMAGMAT - A fortran program to model magma differentiation processes. *Computers & Geosciences* **19**, 1155-1170.

Ariskin, A. A. & Nikolaev, G. S. (1996). An empirical model for the calculation of spinel melt equilibria in mafic igneous systems at atmospheric pressure .1. Chromian spinels. *Contributions to Mineralogy and Petrology* **123**, 282-292.

Arndt, N. (2012). The formation of massif anorthosite: Petrology in reverse. *Geoscience Frontiers* **4**, 195-198.

Arndt, N. T., Lesher, C. M. & Czamanske, G. K. (2005). Mantle-derived magmas and magmatic Ni-Cu-(PGE) deposits. *Economic Geology*, **100**, 5-23.

Arndt, N. T., Czamanske, G. K., Walker, R. J., Chauvel, C. & Fedorenko, V. A. (2003). Geochemistry and origin of the intrusive hosts of the Noril'sk-Talnakh Cu-Ni-PGE sulfide deposits. *Economic Geology* **98**, 495-515.

Ashwal, L. D. (1993). *Anorthosites*. Berlin: Springer-Verlag, 422 p.

Ashwal, L. D., Webb, S. J. & Knoper, M. W. (2005). Magmatic stratigraphy in the Bushveld Northern Lobe: continuous geophysical and mineralogical data from the 2950 m Bellevue drillcore. *South African Journal of Geology* **108**, 199-232.

Bai, Z. J., Zhong, H., Naldrett, A. J., Zhu, W. G. & Xu, G. W. (2012). Whole-Rock and Mineral Composition Constraints on the Genesis of the Giant Hongge Fe-Ti-V Oxide Deposit in the Emeishan Large Igneous Province, Southwest China. *Economic Geology* **107**, 507-524.

Ballhaus, C. & Sylvester, P. (2000). Noble metal enrichment processes in the Merensky Reef, Bushveld Complex. *Journal of Petrology* **41**, 545-561.

Barnes, S. J. (1986). The effect of trapped liquid crystallization on cumulus mineral compositions in layered intrusions. *Contributions to Mineralogy and Petrology* **93**, 524-531.

Barnes, S.-J., Cox, R. A. & Zientek, M. L. (2006). Platinum-group element, gold, silver and base metal distribution in compositionally zoned sulfide droplets from the Medvezky Creek Mine, Noril'sk, Russia. *Contributions to Mineralogy and Petrology* **152**, 187-200.

Barnes, S.-J. & Kunilov, V. Y. (2000). Spinels and Mg ilmenites from the Noril'sk 1 and Talnakh intrusions and other mafic rocks of the Siberian flood basalt province. *Economic Geology* **95**, 1701-1717.

Barnes, S.-J. & Lightfoot, P. C. (2005). Formation of magmatic nickel sulfide ore deposits and processes affecting their copper and platinum group element contents. In: Hedenquist, J. W., Thompson, J. F. H., Goldfarb, R. J. & Richards, J. P. (eds.) *Economic Geology 100th Anniversary Volume*, pp. 179-214.

Barnes, S.-J. & Maier, W. D. (1999). The fractionation of Ni, Cu, and the noble metals in silicate and sulphide liquids. In: Keays, R. R., Lesher, C. M., Lightfoot, P. C. & Farrow, C. E. G. (eds.) *Dynamic processes in magmatic ore deposits and their application to mineral exploration: Geological Association of Canada, Short Course Notes*, pp. 69-106.

Barnes, S. J. & Maier, W. D. (2002). Platinum-group elements and microstructures of normal Merensky Reef from Impala Platinum Mines, Bushveld Complex. *Journal of Petrology* **43**, 103-128.

Barnichon, J. D., Havenith, H., Hoffer, B., Charlier, R., Jongmans, D. & Duchesne, J. C. (1999). The deformation of the Egersund-Ogna anorthosite massif, south Norway: finite-element modelling of diapirism. *Tectonophysics* **303**, 109-130.

Beattie, P. (1994). Systematics and energetics of trace-element partitioning between olivine and silicate melts: implications for the nature of mineral/melt partitioning. *Chemical Geology* **117**, 57-71.

Berndt, J. (2005). An Experimental Investigation of the Influence of Water and Oxygen Fugacity on Differentiation of MORB at 200 MPa. *Journal of Petrology* **46**, 135-167.

Bindeman, I. N., Davis, A. M. & Drake, M. J. (1998). Ion microprobe study of plagioclase-basalt partition experiments at natural concentration levels of trace elements. *Geochimica Et Cosmochimica Acta* **62**, 1175-1193.

Bindeman, I. N. & Davis, A. M. (2000). Trace element partitioning between plagioclase and melt: investigation of dopant influence on partition behavior. *Geochimica Et Cosmochimica Acta* **64**, 2863-2878.

Bindeman, I. N., Brooks, C. K., McBirney, A. R. & Taylor, H. P. (2008). The low-$\delta^{18}O$ late-stage ferrodiorite magmas in the Skaergaard Intrusion: result of liquid immiscibility, thermal metamorphism, or meteoric water incorporation into magma? *The Journal of Geology* **116**, 571-586.

Blundy, J. & Cashman, K. (2008). Petrologic Reconstruction of Magmatic System Variables and Processes. In: Putirka, K. D. & Tepley, F. J. (eds.) *Reviews in Mineralogy and Geochemistry* **69**, 179-239.

Bogaerts, M. & Schmidt, M. (2006). Experiments on silicate melt immiscibility in the system Fe_2SiO_4–$KAlSi_3O_8$–SiO_2–CaO–MgO–TiO_2–P_2O_5 and implications for natural magmas. *Contributions to Mineralogy and Petrology* **152**, 257-274.

Bolle, O. & Duchesne, J. C. (2007). The Apophysis of the Bjerkreim–Sokndal layered intrusion (Rogaland anorthosite province, SW Norway): A composite pluton build up by tectonically-driven emplacement of magmas along the margin of an AMC igneous complex. *Lithos* **98**, 292-312.

Bookstrom, A. A. (1995). Magmatic features of iron ores of the Kiruna type in Chile and Sweden; ore textures and magnetite geochemistry; discussion. *Economic Geology* **90**, 469-473.

Bordage, A., Balan, E., Villiers, J. P. R., Cromarty, R., Juhin, A., Carvallo, C., Calas, G., Sunder Raju, P. V. & Glatzel, P. (2011). V oxidation state in Fe–Ti oxides by high-energy resolution fluorescence-detected X-ray absorption spectroscopy. *Physics and Chemistry of Minerals* **38**, 449-458.

Borisov, A. & Shapkin, A. (1990). A new empirical equation rating Fe^{3+}/Fe^{2+} in magmas to their composition, oxygen fugacity, and temperature. *Geochem. Int* **27**, 111-116.

Botcharnikov, R. E., Almeev, R. R., Koepke, J. & Holtz, F. (2008). Phase relations and liquid lines of descent in hydrous ferrobasalt--implications for the skaergaard intrusion and columbia river flood basalts. *Journal of Petrology* **49**, 1687-1727.

Bottinga, Y. & Weill, D. F. (1972). The viscosity of magmatic silicate liquids; a model calculation. *American Journal of Science* **272**, 438-475.

Boudreau, A. (1999a). Fluid fluxing of cumulates: The J-M reef and associated rocks of the Stillwater complex, Montana. *Journal of Petrology* **40**, 755-772.

Boudreau, A. (1999b). PELE—a version of the MELTS software program for the PC platform. *Computers & Geosciences* **25**, 201-203.

Bougault, H. & Hekinian, R. (1974). Rift valley in the Atlantic Ocean near 36 50′ N: Petrology and geochemistry of basaltic rocks. *Earth and Planetary Science Letters* **24**, 249-261.

Brügmann, G. E., Naldrett, A. J., Asif, M., Lightfoot, P. C., Gorbachev, N. S. & Fedorenko, V. A. (1993). Siderophile and chalcophile metals as tracers of the evolution of the Siberian Trap in the Noril'sk region, Russia. *Geochimica Et Cosmochimica Acta* **57**, 2001-2018.

Buddington, A. F. & Lindsley, D. H. (1964). Iron-Titanium Oxide Minerals and Synthetic Equivalents. *Journal of Petrology* **5**, 310-357.

Burchfiel, B.C., Chen, Z.L., Liu, Y.P. & Royden, L.H. (1995). Tectonics of the Longmen Shan and adjacent regions, Central China. *International Geology Review* **37**:661-735.

Cawthorn, R. G. (1996). *Layered intrusions*. Amsterdam: Elsevier, 530 p.

Cawthorn, R. G. (2005). Pressure fluctuations and the formation of the PGE-rich Merensky and chromitite reefs, Bushveld Complex. *Mineralium Deposita* **40**, 231-235.

Cawthorn, R. G. (2010). The platinum group element deposits of the Bushveld Complex in South Africa. *Platinum Metals Review* **54**, 205-215.

Cawthorn, R. G. & Ashwal, L. D. (2009). Origin of Anorthosite and Magnetitite Layers in the Bushveld Complex, Constrained by Major Element Compositions of Plagioclase. *Journal of Petrology* **50**, 1607-1637.

Cawthorn, R. G., Barnes, S., G., Ballhaus, C. & Malitch, K. N. (2005). Platinum-group element, chromium, and vanadium deposits in mafic and ultramafic rocks. *Economic Geology* **100**, 215-249.

Cawthorn, R. G. & McCarthy, T. S. (1980). Variations in Cr content of magnetite from the upper zone of the Bushveld Complex -- evidence for heterogeneity and convection currents in magma chambers. *Earth and Planetary Science Letters* **46**, 335-343.

Cawthorn, R. G. & McCarthy, T. S. (1981). Bottom crystallization and diffusion control in layered complexes: evidence from Cr distribution in magnetite from the Bushveld Complex. *Trans. Geol. Soc. S. Afr*, **84**, 41-50.

Charlier, B. (2007). Petrogenesis of magmatic iron-titanium deposits associated with Proterozoic massif-type anorthosites. PhD, FS - Département de géologie, 165 p.

Charlier, B., Duchesne, J. C. & Vander Auwera, J. (2006). Magma chamber processes in the Tellnes ilmenite deposit (Rogaland Anorthosite Province, SW Norway) and the formation of Fe–Ti ores in massif-type anorthosites. *Chemical Geology* **234**, 264-290.

Charlier, B. & Grove, T. L. (2012). Experiments on liquid immiscibility along tholeiitic liquid lines of descent. *Contributions to Mineralogy and Petrology* **164**, 27-44.

Charlier, B., Namur, O., Duchesne, J. C., Wiszniewska, J., Parecki, A. & Vander Auwera, J. (2009). Cumulate origin and polybaric crystallization of fe-ti oxide ores in the suwalki anorthosite, northeastern poland. *Economic Geology* **104**, 205-221.

Charlier, B., Namur, O. & Grove, T. L. (2013). Compositional and kinetic controls on liquid immiscibility in ferrobasalt–rhyolite volcanic and plutonic series. *Geochimica Et Cosmochimica Acta* **113**, 79-93.

Charlier, B., Namur, O., Malpas, S., de Marneffe, C., Duchesne, J. C., Auwera, J. V. & Bolle, O. (2010). Origin of the giant Allard Lake ilmenite ore deposit (Canada) by fractional crystallization, multiple magma pulses and mixing. *Lithos* **117**, 119-134.

Charlier, B., Namur, O., Toplis, M. J., Schiano, P., Cluzel, N., Higgins, M. D. & Vander Auwera, J. (2011). Large-scale silicate liquid immiscibility during differentiation of tholeiitic basalt to granite and the origin of the Daly gap. *Geology* **39**, 907-910.

Charlier, B., Sakoma, E., Sauv, M., Stanaway, K., Auwera, J. V. & Duchesne, J.-C. (2008). The Grader layered intrusion (Havre-Saint-Pierre Anorthosite, Quebec) and genesis of nelsonite and other Fe-Ti-P ores. *Lithos* **101**, 359-378.

Charlier, B., Skår, Ø., Korneliussen, A., Duchesne, J. C. & Vander Auwera, J. (2007). Ilmenite composition in the Tellnes Fe–Ti deposit, SW Norway: fractional crystallization, postcumulus evolution and ilmenite–zircon relation. *Contributions to Mineralogy and Petrology* **154**, 119-134.

Chen, W. T., Zhou, M. F. & Zhao, T. P. (2013). Differentiation of nelsonitic magmas in the formation of the ~1.74 Ga Damiao Fe–Ti–P ore deposit, North China. *Contributions to Mineralogy and Petrology* **165**, 1341-1362.

Choukroune, P., Bouhallier, H. & Arndt, N. (1995). Soft lithosphere during periods of Archaean crustal growth or crustal reworking. *Geological Society, London, Special Publications* **95**, 67-86.

Choukroune, P., Ludden, J., Chardon, D., Calvert, A. & Bouhallier, H. (1997). Archaean crustal growth and tectonic processes: a comparison of the Superior Province, Canada and the Dharwar Craton, India. *Geological Society, London, Special Publications* **121**, 63-98.

Chung, S. L. & Jahn, B. M. (1995). Plume-Lithosphere Interaction in Generation of the Emeishan Flood Basalts at the Permian-Triassic Boundary. *Geology* **23**, 889-892.

Clark, A. H. & Kontak, D. J. (2004). Fe-Ti-P oxide melts generated through magma mixing in the Antauta Subvolcanic Center, Peru: Implications for the origin of nelsonite and iron oxide-dominated hydrothermal deposits. *Economic Geology* **99**, 377-395.

Cliff, R. A. & Rickard, D. (1992). Isotope systematics of the Kiruna magnetite ores, Sweden; Part 2, Evidence for a secondary event 400 m.y. after ore formation. *Economic Geology* **87**, 1121-1129.

Corrigan, D. & Breemen, O. V. (1997). U-Pb age constraints for the lithotectonic evolution of the Grenville Province along the Mauricie transect, Quebec. *Canadian Journal of Earth Sciences* **34**, 299-316.

Courtillot, V., Jaupart, C., Manighetti, I., Tapponnier, P. & Besse, J. (1999). On causal links between flood basalts and continental breakup. *Earth and Planetary Science Letters* **166**, 177-195.

Czamanske, G. K., Kunilov, V. E., Zientek, M. L., Cabri, L. J., Likhachev, A. P., Calk, L. C. & Oscarson, R. L. (1992). A proton-microprobe study of magmatic sulfide ores from the norilsk-talnakh district, Siberia. *Canadian Mineralogist* **30**, 249-287.

Darling, R. S. & Florence, F. P. (1995). Apatite light rare earth element chemistry of the Port Leyden nelsonite, Adirondack Highlands, New York; implications for the origin of nelsonite in anorthosite suite rocks. *Economic Geology* **90**, 964-968.

Danyushevsky, L. V. (2001). The effect of small amounts of H_2O crystallisation of mid-ocean ridge and backarc basin magmas. *Journal of Volcanology and Geothermal Research* **110**, 265-280.

Danyushevsky, L. V., Falloon, T. J., Sobolev, A. V., Crawford, A. J., Carroll, M. & Price, R. C. (1993). The H_2O content of basalt glasses from southwest pacific back-arc basins. *Earth and Planetary Science Letters* **117**, 347-362.

Danyushevsky, L. V. & Plechov, P. (2011). Petrolog3: Integrated software for modeling crystallization processes. *Geochemistry Geophysics Geosystems* **12**, Q07021, doi:10.1029/2011GC003516.

Danyushevsky, L., Robinson, P., Gilbert, S., Norman, M., Large, R., McGoldrick, P. & Shelley, M. (2011). Routine quantitative multi-element analysis of sulphide minerals by laser ablation ICP-MS: Standard development and consideration of matrix effects. *Geochemistry: Exploration, Environment, Analysis* **11**, 51-60.

Danyushevsky, L. V. & Sobolev, A. V. (1996). Ferric-ferrous ratio and oxygen fugacity calculations for primitive mantle-derived melts: Calibration of an empirical technique. *Mineralogy and Petrology* **57**, 229-241.

De, A. (1974). Silicate liquid immiscibility in the deccan traps and its petrogenetic significance. *Geological Society of America Bulletin* **85**, 471-474.

Dick, H. J., Natland, J. H., Alt, J. C., Bach, W., Bideau, D., Gee, J. S., Haggas, S., Hertogen, J. G., Hirth, G. & Holm, P. M. (2000). A long in situ section of the lower ocean crust: results of ODP Leg 176 drilling at the Southwest Indian Ridge. *Earth and Planetary Science Letters* **179**, 31-51.

Dixon, J. E. & Clague, D. A. (2001). Volatiles in basaltic glasses from Loihi seamount, Hawaii: Evidence for a relatively dry plume component. *Journal of Petrology* **42**, 627-654.

Dixon, J. E., Leist, L., Langmuir, C. & Schilling, J. G. (2002). Recycled dehydrated lithosphere observed in plume-influenced mid-ocean-ridge basalt. *Nature* **420**, 385-389.

Dixon, S. & Rutherford, M. (1979). Plagiogranites as late-stage immiscible liquids in ophiolite and mid-ocean ridge suites: an experimental study. *Earth and Planetary Science Letters* **45**, 45-60.

Drake, M. J. (1975). The oxidation state of europium as an indicator of oxygen fugacity. *Geochimica Et Cosmochimica Acta* **39**, 55-64.

Duchesne, J. C. (1999). Fe-Ti deposits in Rogaland anorthosites (south Norway): geochemical characteristics and problems of interpretation. *Mineralium Deposita* **34**, 182-198.

Duchesne, J. C. & Charlier, B. (2005). Geochemistry of cumulates from the Bjerkreim-Sokndal layered intrusion (S. Norway). Part I: Constraints from major elements on the mechanism of cumulate formation and on the jotunite liquid line of descent. *Lithos* **83**, 229-254.

Duchesne, J. C., Shumlyanskyy, L. & Charlier, B. (2006). The Fedorivka layered intrusion (Korosten Pluton, Ukraine): An example of highly differentiated ferrobasaltic evolution. *Lithos* **89**, 353-376.

Duke, J. M. (1976). Distribution of the period four transition elements among olivine, calcic clinopyroxene and mafic silicate liquid: Experimental results. *Journal of Petrology* **17**, 499-521.

Dunn, T. (1987). Partitioning of Hf, Lu, Ti, and Mn between olivine, clinopyroxene and basaltic liquid. *Contributions to Mineralogy and Petrology* **96**, 476-484.

Dymek, R. F. & Owens, B. E. (2001). Petrogenesis of apatite-rich rocks (nelsonites and oxide-apatite gabbronorites) associated with massif anorthosites. *Economic Geology and the Bulletin of the Society of Economic Geologists* **96**, 797-815.

Eales, H. & Cawthorn, R. (1996). The Bushveld Complex. *Developments in Petrology* **15**, 181-229.

Emslie, R. (1978). Anorthosite massifs, rapakivi granites, and late Proterozoic rifting of North America. *Precambrian Research* **7**, 61-98.

Emslie, R., Hamilton, M. & Thériault, R. (1994). Petrogenesis of a mid-Proterozoic anorthosite-mangerite-charnockite-granite (AMCG) complex: Isotopic and chemical evidence from the Nain Plutonic Suite. *The Journal of Geology* **5**, 539-558.

Enkelmann, E., Weislogel, A., Ratschbacher, L., Eide, E., Renno, A. & Wooden, J. (2007). How was the Triassic Songpan-Ganzi basin filled? A provenance study. *Tectonics* **26**, 1-24.

Enkin, R. J., Yang, Z., Chen, Y. & Courtillot, V. (1992). Paleomagnetic constraints on the geodynamic history of the major blocks of china from the Permian to the present. *J. Geophys. Res.* **97**, 13953-13989.

Esperança, S., Carlson, R. W., Shirey, S. B. & Smith, D. (1997). Dating crust-mantle separation: Re-Os isotopic study of mafic xenoliths from central Arizona. *Geology* **25**, 651-654.

Evans, B., Scaillet, B. & Kuehner, S. (2006). Experimental determination of coexisting iron–titanium oxides in the systems FeTiAlO, FeTiAlMgO, FeTiAlMnO, and FeTiAlMgMnO at 800 and 900°C, 1–4 kbar, and relatively high oxygen fugacity. *Contributions to Mineralogy and Petrology* **152**, 149-167.

Fan, W. M., Wang, Y. J., Peng, T. P., Miao, L. C. & Guo, F. (2004). Ar-Ar and U-Pb geochronology of Late Paleozoic basalts in western Guangxi and its constraints on the eruption age of Emeishan basalt magmatism. *Chinese Science Bulletin* **49**, 2318-2327.

Fan, W. M., Zhang, C. H., Wang, Y. J., Guo, F. & Peng, T. P. (2008). Geochronology and geochemistry of Permian basalts in western Guangxi Province, Southwest China: Evidence for plume-litho sphere interaction. *Lithos* **102**, 218-236.

Feig, S., Koepke, J. & Snow, J. (2006). Effect of water on tholeiitic basalt phase equilibria: an experimental study under oxidizing conditions. *Contributions to Mineralogy and Petrology* **152**, 611-638.

Feig, S. T., Koepke, J. & Snow, J. E. (2010). Effect of oxygen fugacity and water on phase equilibria of a hydrous tholeiitic basalt. *Contributions to Mineralogy and Petrology* **160**, 551-568.

Filiberto, J., Jackson, C., Le, L. & Treiman, A. H. (2009). Partitioning of Ni between olivine and an iron-rich basalt: Experiments, partition models, and planetary implications. *American Mineralogist* **94**, 256-261.

Foley, S. F., Barth, M. G. & Jenner, G. A. (2000). Rutile/melt partition coefficients for trace elements and an assessment of the influence of rutile on the trace element characteristics of subduction zone magmas. *Geochimica Et Cosmochimica Acta* **64**, 933-938.

Frietsch, R. (1978). On the magmatic origin of iron ores of the Kiruna type. *Economic Geology* **73**, 478-485.

Frietsch, R. & Perdahl, J.-A. (1995). Rare earth elements in apatite and magnetite in Kiruna-type iron ores and some other iron ore types. *Ore Geology Reviews* **9**, 489-510.

Ganino, C., Arndt, N. T., Zhou, M. F., Gaillard, F. & Chauvel, C. (2008). Interaction of magma with sedimentary wall rock and magnetite ore genesis in the Panzhihua mafic intrusion, SW China. *Mineralium Deposita* **43**, 677-694.

Ganino, C., Harris, C., Arndt, N. T., Prevec, S. A. & Howarth, G. H. (2013). Assimilation of carbonate country rock by the parent magma of the Panzhihua Fe-Ti-V deposit (SW China): Evidence from stable isotopes. *Geoscience Frontiers* **4**, 547-554.

Ghiorso, M. S. & Sack, O. (1991). Fe-Ti oxide geothermometry: thermodynamic formulation and the estimation of intensive variables in silicic magmas. *Contributions to Mineralogy and Petrology* **108**, 485-510.

Ghiorso, M. S. & Sack, R. O. (1995). Chemical mass-transfer in magmatic processes .4. A revised and internally consistent thermodynamic model for the interpolation and extrapolation of liquid-solid equilibria in magmatic systems at elevated-temperatures and pressures. *Contributions to Mineralogy and Petrology* **119**, 197-212.

Gibson, S. A., Thompson, R. N. & Dickin, A. P. (2000). Ferropicrites: geochemical evidence for Fe-rich streaks in upwelling mantle plumes. *Earth and Planetary Science Letters* **174**, 355-374.

Gilbert, S. & Danyushevsky, L. (2009). Laser Ablation ICPMS Methodology for Sulphide Analyses. *Unpublished manuscript*. 1-9.

Godel, B., Barnes, S. J. & Maier, W. D. (2007). Platinum-group elements in sulphide minerals, platinum-group minerals, and whole-rocks of the Merensky Reef (Bushveld Complex, South Africa): Implications for the formation of the reef. *Journal of Petrology* **48**, 1569-1604.

Green, T., Blundy, J., Adam, J. & Yaxley, G. (2000). SIMS determination of trace element partition coefficients between garnet, clinopyroxene and hydrous basaltic liquids at 2-7.5 GPa and 1080-1200 C. *Lithos* **53**, 165-187.

Gu, Y. (2003). Automated scanning electron microscope based mineral liberation analysis. *Journal of Minerals and Materials Characterization and Engineering* **2**, 33-41.

Guo, F., Fan, W. M., Wang, Y. J. & Li, C. W. (2004). When did the emeishan mantle plume activity start? Geochronological and geochemical evidence from ultramafic-mafic dikes in southwestern China. *International Geology Review* **46**, 226-234.

Haggerty, S. (1976). *Opaque mineral oxides in terrestrial igneous rocks. Oxide minerals* **3**, 101-301.

Haggerty, S. E. (1991). Oxide textures; a mini-atlas. *Reviews in Mineralogy and Geochemistry* **25**, 129-219.

Hammer, J. E. (2006). Influence of fO_2 and cooling rate on the kinetics and energetics of Fe-rich basalt crystallization. *Earth and Planetary Science Letters* **248**, 618-637.

Hanski, E., Kamenetsky, V. S., Luo, Z. Y., Xu, Y. G. & Kuzmin, D. V. (2010). Primitive magmas in the Emeishan Large Igneous Province, southwestern China and northern Vietnam. *Lithos* **119**, 75-90.

Hanski, E. & Smolkin, V. (1989). Pechenga ferropicrites and other early Proterozoic picrites in the eastern part of the Baltic Shield. *Precambrian Research* **45**, 63-82.

Hanski, E. & Smolkin, V. (1995). Iron-and LREE-enriched mantle source for early Proterozoic intraplate magmatism as exemplified by the Pechenga ferropicrites, Kola Peninsula, Russia. *Lithos* **34**, 107-125.

Hanski, E., Walker, R. J., Huhma, H., Polyakov, G. V., Balykin, P. A., Hoa, T. T. & Phuong, N. T. (2004). Origin of the Permian-Triassic komatiites, northwestern Vietnam. *Contributions to Mineralogy and Petrology* **147**, 453-469.

Hao, Y. L., Zhng, Z. C., Wang, F. S. & Mahoney, J. J. (2004). Petrogenesis of High-Ti and Low-Ti Basalts from the Emeishan Large Igneous Province. *Geological Review* **50**, 587-592. (in Chinese).

Harlov, D. E., Andersson, U. B., Förster, H. J., Nyström, J. O., Dulski, P. & Broman, C. (2002). Apatite-monazite relations in the Kiirunavaara magnetite-apatite ore, northern Sweden. *Chemical Geology* **191**, 47-72.

Harney, D. M. W., Gruenewaldt, G. & Merkle, R. K. W. (1996). The use of plagioclase composition as an indicator of magmatic processes in the upper zone of the bushveld complex. *Mineralogy and Petrology* **56**, 91-103.

Harney, D. M. W., Merkle, R. K. W. & Vongruenewaldt, G. (1990). Platinum-Group Element behavior in the lower part of the Upper Zone, Eastern Bushveld Complex - Implications for the formation of the Main Magnetite Layer. *Economic Geology and the Bulletin of the Society of Economic Geologists* **85**, 1777-1789.

Hart, S. R. & Dunn, T. (1993). Experimental Cpx/melt partitioning of 24 trace elements. *Contributions to Mineralogy and Petrology* **113**, 1-8.

Hauri, E. H., Wagner, T. P. & Grove, T. L. (1994). Experimental and natural partitioning of Th, U, Pb and other trace-elements between garnet, clinopyroxene and basaltic melts. *Chemical Geology* **117**, 149-166.

He, J., Chen, G., Yang, T. & Min, J. 1988. *The Kandian Grey Gneisses*. Chongqing, Chongqing Publishing House (in Chinese).

He, B., Xu, Y. G., Huang, X. L., Luo, Z. Y., Shi, Y. R., Yang, Q. J. & Yu, S. Y. (2007). Age and duration of the Emeishan flood volcanism, SW China: Geochemistry and SHRIMP zircon U-Pb dating of silicic ignimbrites, post-volcanic Xuanwei Formation and clay tuff at the Chaotian section. *Earth and Planetary Science Letters* **255**, 306-323.

He, Q., Xiao, L., Balta, B., Gao, R. & Chen, J. Y. (2010). Variety and complexity of the Late-Permian Emeishan basalts: Reappraisal of plume-lithosphere interaction processes. *Lithos* **119**, 91-107.

Higgins, M. D. (2005). A new interpretation of the structure of the Sept Iles Intrusive suite, Canada. *Lithos* **83**, 199-213.

Higgins, M. D. & van Breemen, O. (1996). Three generations of anorthosite-mangerite-charnockite-granite (AMCG) magmatism, contact metamorphism and tectonism in the Saguenay-Lac-Saint-Jean region of the Grenville Province, Canada. *Precambrian Research* **79**, 327-346.

Higuchi, H. & Nagasawa, H. (1969). Partition of trace elements between rock-forming minerals and the host volcanic rocks. *Earth and Planetary Science Letters* **7**, 281-287.

Hildebrand, R. S. (1986). Kiruna-type deposits; their origin and relationship to intermediate subvolcanic plutons in the Great Bear magmatic zone, Northwest Canada. *Economic Geology* **81**, 640-659.

Holness, M. B., Stripp, G., Humphreys, M. C. S., Veksler, I. V., Nielsen, T. F. D. & Tegner, C. (2011). Silicate liquid immiscibility within the crystal mush: Late-stage magmatic microstructures in the Skaergaard Intrusion, East Greenland. *Journal of Petrology* **52**, 175-222.

Hou, T., Zhang, Z., Encarnacion, J. & Santosh, M. (2012a). Petrogenesis and metallogenesis of the Taihe gabbroic intrusion associated with Fe–Ti-oxide ores in the Panxi district, Emeishan Large Igneous Province, southwest China. *Ore Geology Reviews* **49***,* 109-127.

Hou, T., Zhang, Z. & Pirajno, F. (2012b). A new metallogenic model of the Panzhihua giant V–Ti–iron oxide deposit (Emeishan Large Igneous Province) based on high-Mg olivine-bearing wehrlite and new field evidence. *International Geology Review*, 1721-1745.

Hou, Z. Q., Chen, W. & Lu, J. R. (2006). Eruption of the continental flood basalts at similar to 259 Ma in the Emeishan large igneous province, SW China: Evidence from laser microprobe Ar-40/Ar-39 dating. *Acta Geologica Sinica-English Edition* **80**, 514-521.

HousH, T. B. & Luhr, J. F. (1991). Plagioclase-melt equilibria in hydrous systems. *American Mineralogist* **76**, 477-492.

Howarth, G. H. & Prevec, S. A. (2013b). Hydration versus oxidation: Modelling implications for Fe-Ti oxide crystallisation in mafic intrusions, with specific reference to the Panzhihua intrusion, SW China. *Geoscience Frontiers* **4**, 555–569.

Howarth, G. H. & Prevec, S. A. (2013c). Trace Element, PGE, and Sr-Nd isotope geochemistry of the Panzhihua mafic layered intrusion, SW China: Constraints on ore-forming processes and evolution of parent magma at depth in a plumbing-system. *Geochimica Et Cosmochimica Acta* **120**, 459–478.

Howarth, G. H., Prevec, S. A. & Zhou, M. F. (2013a). Timing of Ti-magnetite crystallisation and silicate disequilibrium in the Panzhihua mafic layered intrusion: Implications for ore-forming processes. *Lithos* **170-171**, 73-89.

Hu, R. Z., Tao, Y., Zhong, H., Huang, Z. L. & Zhang, C., J. (2005). Mineralization systems of a mantle plume: A case study from the Emeishan igneous province, southwest China. *Earth Science Frontiers* **12**, 042-054. (in Chinese).

Huang, X. L., Xu, Y. G., Li, X. H., Li, W. X., Lan, J. B., Zhang, H. H., Liu, Y. S., Wang, Y. B., Li, H. Y., Luo, Z. Y. & Yang, Q. J. (2008). Petrogenesis and tectonic implications of Neoproterozoic, highly fractionated A-type granites from Mianning, South China. *Precambrian Research* **165**, 190-204.

Humphreys, M. C. S. (2011). Silicate liquid immiscibility within the crystal mush: Evidence from Ti in plagioclase from the Skaergaard Intrusion. *Journal of Petrology* **52**, 147-174.

Hurai, V., Simon, K., Wiechert, U., Hoefs, J., Konečný, P., Huraiová, M., Pironon, J. & Lipka, J. (1998). Immiscible separation of metalliferous Fe/Ti-oxide melts from fractionating alkali basalt: P-T-fO_2 conditions and two-liquid elemental partitioning. *Contributions to Mineralogy and Petrology* **133**, 12-29.

Irvine, T. N. (1982). Terminology for Layered Intrusions. *Journal of Petrology* **23**, 127-162.

Jakobsen, J. K., Veksler, I. V., Tegner, C. & Brooks, C. K. (2005). Immiscible iron- and silica-rich melts in basalt petrogenesis documented in the Skaergaard intrusion. *Geology* **33**, 885-888.

Jakobsen, J. K., Veksler, I. V., Tegner, C. & Brooks, C. K. (2011). Crystallization of the Skaergaard Intrusion from an emulsion of immiscible iron- and silica-rich liquids: Evidence from melt inclusions in plagioclase. *Journal of Petrology* **52**, 345-373.

Jang, Y. D. & Naslund, H. R. (2003). Major and trace element variation in ilmenite in the Skaergaard Intrusion: petrologic implications. *Chemical Geology* **193**, 109-125.

Jarosewich, E., Nelen, J. & NORBERG, J. A. (1980). Reference Samples for Electron Microprobe Analysis*. *Geostandards Newsletter* **4**, 43-47.

Jenner, G. A., Foley, S. F., Jackson, S. E., Green, T. H., Fryer, B. J. & Longerich, H. P. (1993). Determination of partition-coefficients for trace-elements in high-pressure temperature experimental run products by Laser-Ablation Microprobe Inductively-Coupled Plasma-Mass Spectrometry (LAM-ICP-MS). *Geochimica Et Cosmochimica Acta* **57**, 5099-5103.

Jenner, F. E., O'Neill, H. S. C., Arculus, R. J. & Mavrigenes, J. A. 2010. The Magnetite Crisis in the Evolution of Arc-related Magmas and the Initial Concentration of Au, Ag and Cu. *Journal of Petrology*, **51**, 2445-2464.

Jiang, N., Chu, X., Mizuta, T., Ishiyama, D. & Mi, J. (2004). A magnetite-apatite deposit in the Fanshan alkaline ultramafic complex, Northern China. *Economic Geology* **99**, 397-408.

Jochum, K. P., Nohl, U., Herwig, K., Lammel, E., Stoll, B. & Hofmann, A. W. (2005). GeoReM: a new geochemical database for reference materials and isotopic standards. *Geostandards and Geoanalytical Research* **29**, 333-338.

Jolliff, B., Floss, C., McCallum, I. & Schwartz, J. (1999). Geochemistry, petrology, and cooling history of 14161, 7373: A plutonic lunar sample with textural evidence of granitic-fraction separation by silicate-liquid immiscibility. *American Mineralogist* **84**, 821-837.

Jones, M. P. (1987). *Applied mineralogy: a quantitative approach*. Springer.

Kamenetsky, V. S., Chung, S.-L., Kamenetsky, M. B. & Kuzmin, D. V. (2012). Picrites from the Emeishan Large Igneous Province, SW China: a Compositional Continuum in Primitive Magmas and their Respective Mantle Sources. *Journal of Petrology* **53**, 2095-2113.

Keays, R. R. & Lightfoot, P. C. (2010). Crustal sulfur is required to form magmatic Ni-Cu sulfide deposits: evidence from chalcophile element signatures of Siberian and Deccan Trap basalts. *Mineralium Deposita* **45**, 241-257.

Keays, R. R., Lightfoot, P. C. & Hamlyn, P. R. (2012). Sulfide saturation history of the Stillwater Complex, Montana: chemostratigraphic variation in platinum group elements. *Mineralium Deposita* **47**, 151-173.

Kelemen, P. B., Shimizu, N. & Dunn, T. (1993). Relative depletion of niobium in some arc magmas and the continental crust: partitioning of K, Nb, La and Ce during melt/rock reaction in the upper mantle. *Earth and Planetary Science Letters* **120**, 111-134.

Klemm, D. D., Henckel, J., Dehm, R. & Vongruenewaldt, G. (1985). The geochemistry of titanomagnetite in magnetite layers and their host rocks of the Eastern Bushveld Complex. *Economic Geology* **80**, 1075-1088.

Kloeck, W. & Palme, H. (1988). Partitioning of siderophile and chalcophile elements between sulfide, olivine, and glass in a naturally reduced basalt from Disko Island, Greenland. In: Ryder, G. (ed.) *Proceedings of the Lunar and Planetary Science Conference*, 471-483.

Kolker, A. (1982). Mineralogy and geochemistry of Fe-Ti oxide and apatite (nelsonite) deposits and evaluation of the liquid immiscibility hypothesis. *Economic Geology* **77**, 1146-1158.

Kress, V. & Carmichael, I. (1991). The compressibility of silicate liquids containing Fe_2O_3 and the effect of composition, temperature, oxygen fugacity and pressure on their redox states. *Contributions to Mineralogy and Petrology* **108**, 82-92.

LAC, D. (2009). Using the oxidation state of iron in plagioclase to evaluate magma oxygen fugacity: A micro-xanes study. MSc, University of Massachusetts Amherst, 90 p.

Lange, R. A. & Carmichael, I. S. E. (1987). Densities of Na_2O-K_2O-CaO-MgO-FeO-Fe_2O_3-Al_2O_3-TiO_2-SiO_2 liquids: New measurements and derived partial molar properties. *Geochim. Cosmochim. Acta* **51**, 2931-2946.

Langmuir, C. H., Klein, E. M. & Plank, T. (1992). Petrological systematics of mid-ocean ridge basalts: Constraints on melt generation beneath ocean ridges. *Geophysical Monograph Series* **71**, 183-280.

Lattard, D., Sauerzapf, U. & Käsemann, M. (2005). New calibration data for the Fe–Ti oxide thermo-oxybarometers from experiments in the Fe–Ti–O system at 1 bar, 1,000–1,300°C and a large range of oxygen fugacities. *Contributions to Mineralogy and Petrology* **149**, 735-754.

Lee, C. (1996). A review of mineralization in the Bushveld Complex and some other layered intrusions. *Developments in Petrology* **15**, 103-145.

Leeman, W. P., Ma, M. S., Murali, A. V. & Schmitt, R. A. (1978). Empirical estimation of magnetite/liquid distribution coefficients for some transition elements. *Contributions to Mineralogy and Petrology* **65**, 269-272.

Lehmann, J., Arndt, N., Windley, B., Zhou, M.-F., Wang, C. Y. & Harris, C. (2007). Field relationships and geochemical constraints on the emplacement of the Jinchuan intrusion and its Ni-Cu-PGE sulfide deposit, Gansu, China. *Economic Geology* **102**, 75-94.

Lemarchand, F., Villemant, B. & Calas, G. (1987). Trace element distribution coefficients in alkaline series. *Geochimica Et Cosmochimica Acta* **51**, 1071-1081.

Lester, G. W., Clark, A. H., Kyser, T. K. & Naslund, H. R. (2013). Experiments on liquid immiscibility in silicate melts with H_2O, P, S, F and Cl: implications for natural magmas. *Contributions to Mineralogy and Petrology* **166**, 329-349.

Li, C. & Ripley, E. M. (2005). Empirical equations to predict the sulfur content of mafic magmas at sulfide saturation and applications to magmatic sulfide deposits. *Mineralium Deposita* **40**, 218-230.

Li, C. S., Tao, Y., Qi, L. & Ripley, E. M. (2012). Controls on PGE fractionation in the Emeishan picrites and basalts: Constraints from integrated lithophile-siderophile elements and Sr-Nd isotopes. *Geochimica Et Cosmochimica Acta* **90**, 12-32.

Li, D. H. & Mao, Y. S. (1982). V-Ti magnetite-bearing layered intrusions and the formation mechanism of the rhythmic layering, Sichuan, Panxi area. *Journal of Mineralogy and Petrology* **1**, 29-43. (in Chinese).

Li, W. C. (1992). The geological characteristic and geneisis of Panzhihua V-Ti magnetite deposit. *Geology and Prospecting* **10**, 18-21. (in Chinese).

Li, X. H., Li, Z. X., Ge, W., Zhou, H., Li, W., Liu, Y. & Wingate, M. T. D. (2003). Neoproterozoic granitoids in South China: crustal melting above a mantle plume at ca. 825 Ma? *Precambrian Research* **122**, 45-83.

Li, Z. X., Li, X. H., Kinny, P. D. & Wang, J. (1999). The breakup of Rodinia: did it start with a mantle plume beneath South China? *Earth and Planetary Science Letters* **173**, 171-181.

Lightfoot, P. C. & Keays, R. R. (2005). Siderophile and chalcophile metal variations in flood basalts from the Siberian Trap, Noril'sk Region: Implications for the origin of the Ni-Cu-PGE sulfide ores. *Economic Geology* **100**, 439-462.

Lightfoot, P. C., Keays, R. R., Evans-Lamswood, D. & Wheeler, R. (2012). S saturation history of Nain Plutonic Suite mafic intrusions: origin of the Voisey's Bay Ni-Cu-Co sulfide deposit, Labrador, Canada. *Mineralium Deposita* **47**, 23-50.

Lightfoot, P. C., Naldrett, A. J., Gorbachev, N. S., Doherty, W. & Fedorenko, V. A. (1990). Geochemistry of the Siberian Trap of the Noril'sk area, USSR, with implications for the relative contributions of crust and mantle to flood basalt magmatism. *Contributions to Mineralogy and Petrology* **104**, 631-644.

Lin, J. L., Fuller, M. & Zhang, W. Y. (1985). Preliminary Phanerozoic polar wander paths for the North and South China blocks. *Nature* **313**, 444-449.

Lindsley, D. H. (1983). Pyroxene Thermometry. *American Mineralogist* **68**, 477-493.

Lindsley, D. H. (2003). Do Fe–Ti oxide magmas exist? Geology: Yes; Experiments: No!. *Abstracts–GEODE field workshop*, 34-35.

Liu, S. W., Yan, Q. R., Li, Q. G. & Wang, Z. Q. (2009). Petrogenesis of granitoid rocks in the Kangdian Complex, western margin of the Yangtze Craton and its tectonic significance. *Acta Petrologica Sinica* **25**, 1883-1896. (in Chinese).

Longhi, J. (1990). Silicate liquid immiscibility in isothermal crystallization experiments. *Proceedings of the Lunar and Planetary Science Conference* **20**, 13-24.

Longhi, J. & Walker, D. (2006). Fickle nickel: Compositional systematics of lunar rocks appear to be a magma ocean signature. *Annual Lunar and Planetary Science Conference* **37**, 2452.

Loucks, R. R. (1996). A precise olivine-augite Mg-Fe-exchange geothermometer. *Contributions to Mineralogy and Petrology* **125**, 140-150.

Lu, J. R., Zhang, G.D., Zhang, C.X., Gu, G.X., Liu, Y. S. & Huang, Y. (1989). A genetic model for the Layered Intrusions and related V-Ti-magnetite deposits in Panzhihua-Xichang region, Southwest China. *Chinese Journal of Geochemistry* **8**, 126-134. (in Chinese).

Lundberg, B. & Smellie, J. A. T. (1979). Painirova and Mertainen Iron-Ores - 2 deposits of the Kiruna Iron-Ore type in Northern Sweden. *Economic Geology* **74**, 1131-1152.

Luo, X. J. (2003). The rhythmic feature of Panzhihua vanadic titano-magnetite deposit and its research significance. MSc: *Chengdu University of Technology*.

Luo, Z.L., Jin, Y. Z. & Zhao, X. K. (1990). The Emei taphrogenesis of the upper Yangtze Platform in South China. *Geological Magazine* **127**, 393-405.

Ma, Y. X., Ji, X. T., Li, J. C., Huang, M. & Yan, Z. Z. (2003). Mineral resources of Panzhihua, Sichuan Province, SW China. *Chengdu: Sichuan Science and Technology Press*.

Maier, W. D., Barnes, S. J., Gartz, V. & Andrews, G. 2003. Pt-Pd reefs in magnetitites of the Stella layered intrusion, South Africa: A world of new exploration opportunities for platinum group elements. *Geology*, **31**, 885-888.

Marsh, B. (1981). On the crystallinity, probability of occurrence, and rheology of lava and magma. *Contributions to Mineralogy and Petrology* **78**, 85-98.

Marsh, B. D. (1989). Magma Chambers. *Annual Review of Earth and Planetary Sciences* **17**, 439-472.

Mavrogenes, J. A. & O'Neill, H. S. C. (1999). The relative effects of pressure, temperature and oxygen fugacity on the solubility of sulfide in mafic magmas. *Geochimica Et Cosmochimica Acta* **63**, 1173-1180.

Mcbirney, A. R. (1975). Differentiation of Skaergaard Intrusion. *Nature* **253**, 691-694.

McBirney, A. R. (1996). The Skaergaard Intrusion. *Developments in Petrology* **15**, 147-180.

McBirney, A. R. (2008). Comments on: Liquid Immiscibility and the Evolution of Basaltic Magma Journal of Petrology 48, 2187-2210. *Journal of Petrology* **49**, 2169-2170.

McBirney, A. R. & Nakamura, Y. (1974). Immiscibility in late-stage magmas of the Skaergaard intrusion. *Carnegie Inst Washington Yearb* **73**, 348-352.

McCallum, I. & Charette, M. (1978). Zr and Nb partition coefficients: implications for the genesis of mare basalts, KREEP and sea floor basalts. *Geochimica Et Cosmochimica Acta* **42**, 859-869.

McCarthy, T. S. & Cawthorn, R. G. (1983). The geochemistry of vanadiferous magnetite in the Bushveld Complex - Implications for crystallization mechanisms in Layered Complexes. *Mineralium Deposita* **18**, 505-518.

McDonough, W. F. & Sun, S. S. (1995). The composition of the Earth. *Chemical Geology* **120**, 223-253.

Mckenzie, D. & Onions, R. K. (1991). Partial melt distributions from inversion of rare-earth element concentrations. *Journal of Petrology* **32**, 1021-1091.

Miller, J. D. J. & Weiblen, P. W. (1990). Anorthositic rocks of the Duluth Complex: Examples of rocks formed from plagioclase crystal mush. *Journal of Petrology* **31**, 295-339.

Mirmohammadi, M., Kananian, A. & Tarkian, M. (2007). The nature and origin of Fe-Ti-P-rich rocks in the Qareaghaj mafic-ultramafic intrusion, NW Iran. *Mineralogy and Petrology* **91**, 71-100.

Mitsis, I. & Economou-Eliopoulos, M. (2001). Occurrence of apatite associated with magnetite in an ophiolite complex (Othrys), Greece. *American Mineralogist* **86**, 1143-1150.

Mollo, S., Putirka, K., Iezzi, G., Del Gaudio, P. & Scarlato, P. (2011). Plagioclase-melt (dis) equilibrium due to cooling dynamics: Implications for thermometry, barometry and hygrometry. *Lithos* **125**, 221-235.

Morisset, C. E., Scoates, J. S., Weis, D., Sauvé, M. & Stanaway, K. J. (2010). Rutile-bearing ilmenite deposits associated with the proterozoic saint-urbain and lac allard anorthosite massifs, grenville province, Quebec. *Canadian Mineralogist* **48**, 821-849.

Morisset, C. M. (2008). Origin of rutile-bearing ilmenite Fe-Ti deposits in Proterozoic anorthosite massifs of the Grenville Province. **The Faculty of Graduate Studies: University of British Columbia.**

Morse, S. A. (2008). Compositional convection trumps silicate liquid immisciblity in Layered Intrusions: a discussion of Liquid immiscibility and the evolution of basaltic magma by Veksler et al., Journal of Petrology 48, 2187-2210. *Journal of Petrology* **49**, 2157-2168.

Müller, B., Axelsson, M. D. & Öhlander, B. (2003). Trace elements in magnetite from Kiruna, northern Sweden, as determined by LA-ICP-MS. *Gff* **125**, 1 - 5.

Munteanu, M., Wilson, A. H., Yao, Y., Chunnett, G. & Luo, Y. (2010). Sequence of magma emplacement and sulfide saturation in the Gaojiacun–Lengshuiqing intrusive complex (SW China). *Mineralium Deposita* **45**, 517-529.

Mysen, B. O. (1978). Experimental determination of nickel partition coefficients between liquid, pargasite, and garnet peridotite minerals and concentration limits of behavior according to Henry's law at high pressure and temperature. *American Journal of Science* **278**, 217-243.

Naldrett, A. J. (1992). A model for the Ni-Cu-PGE ores of the Noril'sk region and its application to other areas of flood basalt. *Economic Geology* **87**, 1945-1962.

Naldrett, A. J. (1997). Key factors in the genesis of Noril'sk,Sudbury,Jinchuan,Voisey's Bay and other world-class Ni-Cu-PGE deposits:implications for explorration. Australian *Journal of Earth Sciences* **44**, 283-315.

Naldrett, A.J. 2004. Magmatic sulfide deposits: Geology, geochemistry and exploration [M]. *Springer,*

Naldrett, A. J., Wilson, A., Kinnaird, J. & Chunnett, G. (2009). PGE tenor and metal ratios within and below the Merensky Reef, Bushveld Complex: Implications for its genesis. *Journal of Petrology* **50**, 625-659.

Naldrett, A. J., Wilson, A., Kinnaird, J., Yudovskaya, M. & Chunnett, G. (2012). The origin of chromitites and related PGE mineralization in the Bushveld Complex: new mineralogical and petrological constraints. *Mineralium Deposita* **47**, 209-232.

Namur, O., Charlier, B. & Holness, M. B. (2012). Dual origin of Fe-Ti-P gabbros by immiscibility and fractional crystallization of evolved tholeiitic basalts in the Sept Iles layered intrusion. *Lithos* **154**, 100-114.

Namur, O., Charlier, B., Pirard, C., Hermann, J., Liégeois, J.-P. & Auwera, J. V. (2011). Anorthosite formation by plagioclase flotation in ferrobasalt and implications for the lunar crust. *Geochimica Et Cosmochimica Acta* **75**, 4998-5018.

Namur, O., Charlier, B., Toplis, M. J., Higgins, M. D., Liegeois, J. P. & Vander Auwera, J. (2010). Crystallization sequence and magma chamber processes in the ferrobasaltic Sept Iles layered intrusion, Canada. *Journal of Petrology* **51**, 1203-1236.

Nielsen, R. L. (1992). BIGD.FOR - a fortran program to calculate trace-element partition-coefficients for natural mafic and intermediate composition magmas. *Computers & Geosciences* **18**, 773-788.

Nielsen, R. L. & Beard, J. S. (2000). Magnetite-melt HFSE partitioning. *Chemical Geology* **164**, 21-34.

Nystroem, J. O. & Henriquez, F. (1994). Magmatic features of iron ores of the Kiruna type in Chile and Sweden; ore textures and magnetite geochemistry. *Economic Geology* **89**, 820-839.

Nystrom, J. O., Billstrom, K., Henriquez, F., Fallick, A. E. & Naslund, H. R. (2008). Oxygen isotope composition of magnetite in iron ores of the Kiruna type in Chile and Sweden. *Gff* **130**, 177-188.

Nystrom, J. O. & Henriquez, F. (1995). Magmatic features of iron-ores of the Kiruna type in chile and Sweden - ore textures and magnetite geochemistry - a reply. *Economic Geology and the Bulletin of the Society of Economic Geologists* **90**, 473-475.

Ohtake, M., Matsunaga, T., Haruyama, J., Yokota, Y., Morota, T., Honda, C., Ogawa, Y., Torii, M., Miyamoto, H., Arai, T., Hirata, N., Iwasaki, A., Nakamura, R., Hiroi, T., Sugihara, T., Takeda, H., Otake, H., Pieters, C. M., Saiki, K., Kitazato, K., Abe, M., Asada, N., Demura, H., Yamaguchi, Y., Sasaki, S., Kodama, S., Terazono, J., Shirao, M., Yamaji, A., Minami, S., Akiyama, H. & Josset, J. L. (2009). The global distribution of pure anorthosite on the Moon. *Nature* **461**, 236-240.

Ou, X. G. & Jin, S. Y. (2000). Layered Intrusions and its origine of rhythmic layering. *Earth Science Frontiers* **7**, 79-86. (in Chinese).

Owens, B. E. & Dymek, R. F. (1992). Fe-Ti-P-rich rocks and massif anorthosite; problems of interpretation illustrated from the Labrieville and St-Urbain plutons, Quebec. *Canadian Mineralogist* **30**, 163-190.

Pagé, P., Barnes, S.-J., Bédard, J. H. & Zientek, M. L. (2012). In situ determination of Os, Ir, and Ru in chromites formed from komatiite, tholeiite and boninite magmas: Implications for chromite control of Os, Ir and Ru during partial melting and crystal fractionation. *Chemical Geology* **302–303**, 3-15.

Paludan, J., Hansen, U. & Olesen, N. Ø. (1994). Structural evolution of the Precambrian Bjerkreim-Sokndal intrusion, south Norway. *Norsk Geologisk Tidsskrift* **74**, 185-198.

Pang, K. N. (2008). Origin Of The Permian Panzhihua Layered Gabbroic Intrusion And The Hosted Fe-Ti-V Oxide Deposit, Sichuan Province, Sw China. PhD, The University of Hong Kong, 285 p.

Pang, K. N., Li, C., Zhou, M. F. & Ripley, E. M. (2008a). Abundant Fe–Ti oxide inclusions in olivine from the Panzhihua and Hongge layered intrusions, SW China: evidence for early saturation of Fe–Ti oxides in ferrobasaltic magma. *Contributions to Mineralogy and Petrology* **156**, 307-321.

Pang, K. N., Zhou, M. F., Lindsley, D., Zhao, D. & Malpas, J. (2008b). Origin of Fe-Ti oxide ores in mafic intrusions: Evidence from the Panzhihua intrusion, SW China. *Journal of Petrology* **49**, 295-313.

Pang, K. N., Li, C., Zhou, M. F. & Ripley, E. M. (2009). Mineral compositional constraints on petrogenesis and oxide ore genesis of the late Permian Panzhihua layered gabbroic intrusion, SW China. *Lithos* **110**, 199-214.

Pang, K. N., Zhou, M. F., Qi, L., Shellnutt, G., Wang, C. Y. & Zhao, D. (2010). Flood basalt-related Fe–Ti oxide deposits in the Emeishan large igneous province, SW China. *Lithos* **119**, 123-136.

Pang, K. N., Zhou, M. F., Qi, L., Chung, S. L., Chu, C. H. & Lee, H.-Y. (2013). Petrology and geochemistry at the Lower zone-Middle zone transition of the Panzhihua intrusion, SW China: Implications for differentiation and oxide ore genesis. *Geoscience Frontiers* **4**, 517-533.

Panjasawatwong, Y., Danyushevsky, L., Crawford, A. & Harris, K. (1995). An experimental study of the effects of melt composition on plagioclase-melt equilibria at 5 and 10 kbar: implications for the origin of magmatic high-An plagioclase. *Contributions to Mineralogy and Petrology* **118**, 420-432.

Parak, T. (1975). Kiruna iron ores are not "intrusive-magmatic ores of the Kiruna type". *Economic Geology* **70**, 1242-1258.

Paster, T. P., Schauwecker, D. S. & Haskin, L. A. (1974). The behavior of some trace elements during solidification of the Skaergaard layered series. *Geochimica Et Cosmochimica Acta* **38**, 1549-1577.

Pedersen, A. K. (1979). Basaltic glass with high-temperature equilibrated immiscible sulphide bodies with native iron from Disko, central West Greenland. *Contributions to Mineralogy and Petrology* **69**, 397-407.

Prendergast, M. D. 2000. Layering and Precious Metals mineralization in the Rincon del Tigre Complex, eastern Bolivia. *Economic Geology and the Bulletin of the Society of Economic Geologists*, **95**, 113-130.

Philpotts, A. R. (1967). Origin of certain iron-titanium oxide and apatite rocks. *Economic Geology* **62**, 303-315.

Philpotts, A. R. (1979). Silicate Liquid Immiscibility in Tholeiitic Basalts. *Journal of Petrology* **20**, 99-118.

Philpotts, A. R. (1982). Compositions of immiscible liquids in volcanic rocks. *Contributions to Mineralogy and Petrology* **80**, 201-218.

Philpotts, A. R. (2008). Comments on: Liquid immiscibility and the evolution of basaltic magma. *Journal of Petrology* **49**, 2171-2175.

Philpotts, A. R. & Doyle, C. D. (1983). Effect of magma oxidation state on the extent of silicate liquid immiscibility in a tholeiitic basalt. *American Journal of Science* **283**, 967-986.

Phinney, W. C. (1992). Partition-coefficients for iron between plagioclase and basalt as a function of oxygen fugacity - Implications for Archean and Lunar anorthosites. *Geochimica Et Cosmochimica Acta* **56**, 1885-1895.

Putirka, K. D. (2008). Thermometers and barometers for volcanic systems. *Reviews in Mineralogy and Geochemistry* **69**, 61.

PXGT (Pan-Xi Geological Team of the Bureau of Geology and Mineral Resources) (1981). Geological survey report on the Xinjie V-Ti-Magnetite ore district in the Miyi country, Sichuan Province. *Unpublished mannuscript*. pp. 15-35. (in Chinese).

PXGT (Pan-Xi Geological Team of the Bureau of Geology and Mineral Resources) (1987). Metallogenetic conditions and geologic characters of the Hongge vanadic titanomagnetite deposit, Sichuan. *Beijing: Geological Press.* 220 p. (in Chinese).

Qi, L., Wang, C. Y. & Zhou, M. F. (2008). Controls on the PGE distribution of Permian Emeishan alkaline and peralkaline volcanic rocks in Longzhoushan, Sichuan Province, SW China. *Lithos* 106, 222-236.

Qi, L. & Zhou, M. F. (2008). Platinum-group elemental and Sr–Nd–Os isotopic geochemistry of Permian Emeishan flood basalts in Guizhou Province, SW China. *Chemical Geology* **248**, 83-103.

Rajamani, V. & Naldrett, A. J. (1978). Partitioning of Fe, Co, Ni, and Cu between sulfide liquid and basaltic melts and the composition of Ni-Cu sulfide deposits. *Economic Geology* **73**, 82-93.

Reynolds, I. M. (1985a). Contrasted mineralogy and textural relationships in the uppermost titaniferous magnetite layers of the Bushveld Complex in the Bierkraal Area North of Rustenburg. *Economic Geology* **80**, 1027-1048.

Reynolds, I. M. (1985b). The nature and origin of titaniferous magnetite-rich layers in the upper zone of the Bushveld Complex; a review and synthesis. *Economic Geology* **80**, 1089-1108.

Righter, K., Leeman, W. P. & Hervig, R. L. (2006). Partitioning of Ni, Co and V between spinel-structured oxides and silicate melts: Importance of spinel composition. *Chemical Geology* **227**, 1-25.

Ripley, E. M. & Li, C. S. (2013). Sulfide saturation in mafic magmas: Is external sulfur required for magmatic Ni-Cu-(PGE) ore genesis? *Economic Geology* **108**, 45-58.

Ripley, E. M., Severson, M. J. & Hauck, S. A. (1998). Evidence for sulfide and Fe-Ti-P-rich liquid immiscibility in the Duluth Complex, Minnesota. *Economic Geology and the Bulletin of the Society of Economic Geologists* **93**, 1052-1062.

Robinson, P., Townsend, A. T., Yu, Z. & Münker, C. (1999). Determination of scandium, yttrium and rare earth elements in rocks by high resolution inductively coupled plasma-mass spectrometry. *Geostandards Newsletter* **23**, 31-46.

Robinson, P. (2003). XRF analysis of flux-fused discs. *The 5th International Conference on the Analysis of Geological and Environmental Materials: Geoanalysis*, **90**.

Roedder, E. & Weiblen, P. W. (1970). Silicate liquid immiscibility in lunar magmas, evidenced by melt inclusions in lunar rocks. *Science* **167**, 641-644.

Roeder, P. L. & Emslie, R. F. (1970). Olivine-liquid equilibrium. *Contributions to Mineralogy and Petrology* **29**, 275-289.

Roger, F., Jolivet, M. & Malavieille, J. (2010). The tectonic evolution of the Songpan-Garzê (North Tibet) and adjacent areas from Proterozoic to Present: A synthesis. *Journal of Asian Earth Sciences* **39**, 254-269.

Rollinson, H. R. 1993. Using geochemical data: evaluation, presentation, interpretation. 384 pp.

Ryabchikov, I. D. & Kogarko, L. N. (2006). Magnetite compositions and oxygen fugacities of the Khibina magmatic system. *Lithos* **91**, 35-45.

Ryan, B. (2000). The Nain-Churchill boundary and the Nain plutonic suite: A regional perspective on the geologic setting of the Voisey's Bay Ni-Cu-Co deposit. *Economic Geology and the Bulletin of the Society of Economic Geologists* **95**, 703-724.

Sang, Z. N. & Jin, Z. M. (2001). Formation of the rhythmic layering of layered intrusions. *Geological Science and Technology Information* **20**, 20-24. (in Chinese).

Sattari, P., Brenan, J. M., Horn, I. & McDonough, W. F. (2002). Experimental constraints on the sulfide- and chromite-silicate melt partitioning behavior of rhenium and platinum-group elements. *Economic Geology and the Bulletin of the Society of Economic Geologists* **97**, 385-398.

Sauerzapf, U., Lattard, D., Burchard, M. & Engelmann, R. (2008). The titanomagnetite-ilmenite equilibrium: New experimental data and thermo-oxybarometric application to the crystallization of basic to intermediate rocks. *Journal of Petrology* **49**, 1161-1185.

SBGMR (Sichuan Bureau of Geology and Mineral Resources) (1991). *Regional Geology of Sichuan Province*. Beijing: Geological Publishing House. 680 p. (in Chinese).

Schärer, U., Wilmart, E. & Duchesne, J. C. (1996). The short duration and anorogenic character of anorthosite magmatism: U-Pb dating of the Rogaland complex, Norway. *Earth and Planetary Science Letters* **139**, 335-350.

Schmidt, M. W., Connolly, J. A. D., Gunther, D. & Bogaerts, M. (2006). Element partitioning: The role of melt structure and composition. *Science* **312**, 1646-1650.

Scoates, J. S. (2000). The plagioclase-magma density paradox re-examined and the crystallization of proterozoic anorthosites. *Journal of Petrology* **41**, 627-649.

Scoon, R. N. & Mitchell, A. A. (1994). Discordant iron-rich ultramafic pegmatites in the Bushveld Complex and their relationship to iron-rich intercumulus and residual liquids. *Journal of Petrology* **35**, 881-917.

Seat, Z., Gee, M. A. M., Grguric, B. A., Beresford, S. W. & Grassineau, N. V. (2011). The Nebo-Babel Ni-Cu-PGE sulfide deposit (West Musgrave, Australia): Pt. 1. U/Pb zircon ages, whole-rock and mineral chemistry, and O-Sr-Nd isotope compositions of the intrusion, with constraints on petrogenesis. *Economic Geology* **106**, 527-556.

Sensarma, S. & Palme, H. (2013). Silicate liquid immiscibility in the ~ 2.5 Ga Fe-rich andesite at the top of the Dongargarh large igneous province (India). *Lithos* **170-171**, 239-251.

Shearer, C. K., Papike, J. J. & Spilde, M. N. (2001). Trace-element partitioning between immiscible lunar melts: An example from naturally occurring lunar melt inclusions. *American Mineralogist* **86**, 238-246.

Shellnutt, J. G. & Jahn, B. M. (2010). Formation of the Late Permian Panzhihua plutonic-hypabyssal-volcanic igneous complex: Implications for the genesis of Fe–Ti oxide deposits and A-type granites of SW China. *Earth and Planetary Science Letters* **289**, 509-519.

Shellnutt, J. G. & Jahn, B. M. (2011). Origin of Late Permian Emeishan basaltic rocks from the Panxi region (SW China): Implications for the Ti-classification and spatial–compositional distribution of the Emeishan flood basalts. J*ournal of Volcanology and Geothermal Research* **199**, 85-95.

Shellnutt, J. G. & Pang, K. N. (2012). Petrogenetic implications of mineral chemical data for the Permian Baima Igneous Complex, SW China. *Mineralogy and Petrology* **106**, 75-88.

Shellnutt, J. G., Wang, C. Y., Zhou, M. F. & Yang, Y. (2009). Zircon Lu-Hf isotopic compositions of metaluminous and peralkaline A-type granitic plutons of the Emeishan Large Igneous Province (SW China): Constraints on the mantle source. *Journal of Asian Earth Sciences* **35**, 45-55.

Shellnutt, J. G. & Zhou, M. F. (2007). Permian peralkaline, peraluminous and metaluminous A-type granites in the Panxi district, SW China: Their relationship to the Emeishan mantle plume. *Chemical Geology* **243**, 286-316.

Skulski, T., Minarik, W. & Watson, E. B. (1994). High-Pressure Experimental Trace-Element Partitioning between Clinopyroxene and Basaltic Melts. *Chemical Geology* **117**, 127-147

Snyder, D., Carmichael, I. S. E. & Wiebe, R. A. (1993). Experimental study of liquid evolution in an Fe-rich, layered mafic intrusion: constraints of Fe-Ti oxide precipitation on the T-fO_2 and T-*e* paths of tholeiitic magmas. *Contributions to Mineralogy and Petrology* **113**, 73-86.

Sobolev, A. V. & Chaussidon, M. (1996). H_2O concentrations in primary melts from supra-subduction zones and mid-ocean ridges: Implications for H_2O storage and recycling in the mantle. *Earth and Planetary Science Letters* **137**, 45-55.

Sobolev, A. V., Migdisov, A. A. & Portnyagin, M. V. (1996). Incompatible element partitioning between clinopyroxene and basalt liquid revealed by the study of melt inclusions in minerals from Troodos lavas, Cyprus. *Petrology* **4**, 307-317.

Song, X. Y., Ma, R. Z., Wang, Y. L. & Zhang, Z. J. (1994). The characteristics of layering and magma evolution of Panzhihua layered intrusion. *Journal of Mineralogy and Petrology* **14**, 37-45 (in Chinese).

Song, X. Y., Wang, Y. L., Zhang, Z. J. & Ma, R. Z. (1997). Critical factors of the formation of the rhythmic layering of layered intrusion. *Journal of Chendu University of Technology* **24**, 61-64

Song, X. Y., Wang, Y. L., Zhang, C., J & Ma, R. Z. (1999). Quantitative simulation of formation of the rhythmic layering in layered intrusions-A case study of the Panzhihua layered intrusion, Sichuan. *Acta Geologica Sinica* **73**, 37-46. (in Chinese).

Song, X. Y., Zhou, M. F., Hou, Z. Q., Cao, Z. M., Wang, Y. L. & Li, Y. G. (2001). Geochemical constraints on the mantle source of the upper permian Emeishan continental flood basalts, southwestern China. *International Geology Review* **43**, 213-225.

Song, X. Y., Zhou, M. F., Cao, Z. M., Sun, M. & Wang, Y. L. (2003). Ni-Cu-(PGE) magmatic sulfide deposits in the Yangliuping area, Permian Emeishan Igneous province, SW China. *Mineralium Deposita* **38**, 831-843.

Song, X. Y., Zhou, M. F., Cao, Z. M. & Robinson, P. T. (2004). Late permian rifting of the South China Craton caused by the Emeishan mantle plume? *Journal of the Geological Society London* **161**, 773-781.

Song, X. Y., Zhang, C. J., Hu, R., Zhong, H., Zhou, M. F., Ma, R. Z. & Li, Y. G. (2005). Genetic links of magmatic deposit in the Emeishan Large Igneous Province with dynamics of mantle plume. *Journal of Mineralogy and Petrology* **25**, 35-44. (in Chinese).

Song, X. Y., Zhou, M. F., Wang, C. Y., Qi, L. & Zhang, C. J. (2006a). Role of crustal contamination in formation of the Jinchuan intrusion and its world-class Ni-Cu-(PGE) sulfide deposit, Northwest China. *International Geology Review* **48**, 1113-1132.

Song, X. Y., Zhou, M. F., Keays, R. R., Cao, Z. M., Sun, M. & Qi, L. (2006b). Geochemistry of the Emeishan flood basalts at Yangliuping, Sichuan, SW China: implications for sulfide segregation. *Contributions to Mineralogy and Petrology* **152**, 53-74.

Song, X. Y., Qi, H. W., Robinson, P. T., Zhou, M. F., Cao, Z. M. & Chen, L. M. (2008). Melting of the subcontinental lithospheric mantle by the Emeishan mantle plume; evidence from the basal alkaline basalts in Dongchuan, Yunnan, Southwestern China. *Lithos* **100**, 93-111.

Song, X. Y., Keays, R. R., Xiao, L., Qi, H. W. & Ihlenfeld, C. (2009). Platinum-group element geochemistry of the continental flood basalts in the central Emeisihan Large Igneous Province, SW China. *Chemical Geology* **262**, 246-261.

Song, X. Y., Qi, H. W., Hu, R. Z., Chen, L. M., Yu, S. Y. & Zhang, J. F. (2013). Formation of thick stratiform Fe-Ti oxide layers in layered intrusion and frequent replenishment of fractionated mafic magma: evidence from the Panzhihua intrusion, SW China. *Geochemistry, Geophysics, Geosystems* **14**, 712-732.

Sugawara, T. (2001). Ferric iron partitioning between plagioclase and silicate liquid: thermodynamics and petrological applications. *Contributions to Mineralogy and Petrology* **141**, 659-686.

Sun, S. S. & McDonough, W. F. (1989). Chemical and isotopic systematics of oceanic basalts: implications for mantle composition and processes. *Geological Society, London, Special Publications* **42**, 313-345.

Tao, Y., Li, C. S., Hu, R. Z., Ripley, E. M., Du, A. D. & Zhong, H. (2007). Petrogenesis of the Pt-Pd mineralized Jinbaoshan ultramafic intrusion in the Permian Emeishan Large Igneous Province, SW China. *Contributions to Mineralogy and Petrology* **153**, 321-337.

Tao, Y., Li, C., Song, X. Y. & Ripley, E. M. (2008). Mineralogical, petrological, and geochemical studies of the Limahe mafic-ultramatic intrusion and associated Ni-Cu sulfide ores, SW China. *Mineralium Deposita* **43**, 849-872.

Tao, Y., Ma, Y. S., Miao, L. C. & Zhu, F. L. (2009). SHRIMP U-Pb zircon age of the Jinbaoshan ultramafic intrusion, Yunnan Province, SW China. *Chinese Science Bulletin* **54**, 168-172.

Tegner, C. (1997). Iron in plagioclase as a monitor of the differentiation of the Skaergaard intrusion. *Contributions to Mineralogy and Petrology* **128**, 45-51.

Tegner, C. & Cawthorn, R. G. (2010). Iron in plagioclase in the Bushveld and Skaergaard intrusions: implications for iron contents in evolving basic magmas. *Contributions to Mineralogy and Petrology* **159**, 719-730.

Tegner, C., Cawthorn, R. G. & Kruger, F. J. (2006). Cyclicity in the Main and Upper Zones of the Bushveld Complex, South Africa: Crystallization from a zoned magma sheet. *Journal of Petrology* **47**, 2257-2279.

Tollari, N., Barnes, S. J., Cox, R. A. & Nabil, H. (2008). Trace element concentrations in apatites from the Sept-Iles Intrusive Suite, Canada - Implications for the genesis of nelsonites. *Chemical Geology* **252**, 180-190.

Tollari, N., Toplis, M. J. & Barnes, S. J. (2006). Predicting phosphate saturation in silicate magmas: An experimental study of the effects of melt composition and temperature. *Geochimica Et Cosmochimica Acta* **70**, 1518-1536.

Toplis, M. J. & Carroll, M. R. (1995). An experimental-study of the influence of oxygen fugacity on Fe-Ti oxide stability, phase-relations, and mineral-melt equilibria in ferrobasaltic systems. *Journal of Petrology* **36**, 1137-1170.

Toplis, M. J., Dingwell, D. B. & Libourel, G. (1994). The effect of phosphorus on the iron redox ratio, viscosity, and density of an evolved ferro-basalt. *Contributions to Mineralogy and Petrology* **117**, 293-304.

Toulmin Iii, P. & Barton Jr, P. B. (1964). A thermodynamic study of pyrite and pyrrhotite. *Geochimica Et Cosmochimica Acta* **28**, 641-671.

Tuff, J., Takahashi, E. & Gibson, S. (2005). Experimental constraints on the role of garnet pyroxenite in the genesis of high-Fe mantle plume derived melts. *Journal of Petrology* **46**, 2023-2058.

van Westrenen, W., Blundy, J. D. & Wood, B. J. (2001). High field strength element/rare earth element fractionation during partial melting in the presence of garnet: Implications for identification of mantle heterogeneities. *Geochem. Geophys. Geosyst* **2**, 1039, doi: 10.1029/2000GC000133.

Vannucci, R., Bottazzi, P., Wulff-Pedersen, E. & Neumann, E. R. (1998). Partitioning of REE, Y, Sr, Zr and Ti between clinopyroxene and silicate melts in the mantle under La Palma (Canary Islands): implications for the nature of the metasomatic agents. *Earth and Planetary Science Letters* **158**, 39-51.

VanTongeren, J. A. & Mathez, E. A. (2012). Large-scale liquid immiscibility at the top of the Bushveld Complex, South Africa. *Geology* **40**, 491-494.

Veksler, I. V. (2009). Extreme iron enrichment and liquid immiscibility in mafic intrusions: Experimental evidence revisited. *Lithos* **111**, 72-82.

Veksler, I. V., Dorfman, A. M., Borisov, A. A., Wirth, R. & Dingwell, D. B. (2007). Liquid immiscibility and the evolution of basaltic magma. *Journal of Petrology* **48**, 2187-2210.

Veksler, I. V., Dorfman, A. M., Borisov, A. A., Wirth, R. & Dingwell, D. B. (2008). Liquid immiscibility and evolution of basaltic magma: Reply to S. A. Morse, A. R. McBirney and A. R. Philpotts. *Journal of Petrology* **49**, 2177-2186.

Veksler, I. V., Dorfman, A. M., Danyushevsky, L. V., Jakobsen, J. K. & Dingwell, D. B. (2006). Immiscible silicate liquid partition coefficients: implications for crystal-melt element partitioning and basalt petrogenesis. *Contributions to Mineralogy and Petrology* **152**, 685-702.

Vogel, D. C. & Keays, R. R. (1997). The petrogenesis and platinum-group element geochemistry of the Newer Volcanic Province, Victoria, Australia. *Chemical Geology* **136**, 181-204.

Von Gruenewaldt, G. (1993). Ilmenite-apatite enrichments in the Upper Zone of the Bushveld Complex: a major titanium-rock phosphate resource. *International Geology Review* **35**, 987 - 1000.

Wager, L. R. & Brown, G. M. (1968). Layered igneous rocks. *Edinburgh and London (Oliver and Boyd)*. 588 p.

Wager, L. R., Brown, G. M. & Wadsworth, W. J. (1960). Types of Igneous Cumulates. *Journal of Petrology* **1**, 73-85.

Walker, R. J., Morgan, J. W., Hanski, E. J. & Smolkin, V. F. (1997). Re-Os systematics of Early Proterozoic ferropicrites, Pechenga Complex, northwestern Russia: Evidence for ancient Os-187-enriched plumes. *Geochimica Et Cosmochimica Acta* **61**, 3145-3160.

Wallace, P. J. (1998). Water and partial melting in mantle plumes: Inferences from the dissolved H2O concentrations of Hawaiian basaltic magmas. *Geophysical Research Letters* **25**, 3639-3642.

Wang, C. & Zhou, M. F. (2006). Genesis of the Permian Baimazhai magmatic Ni–Cu–(PGE) sulfide deposit, Yunnan, SW China. *Mineralium Deposita* **41**, 771-783.

Wang, C., Zhou, M. F. & Keays, R. (2006). Geochemical constraints on the origin of the Permian Baimazhai mafic–ultramafic intrusion, SW China. *Contributions to Mineralogy and Petrology* **152**, 309-321.

Wang, C. Y., Zhou, M. F. & Qi, L. (2007a). Permian flood basalts and mafic intrusions in the Jinping (SW China) Song Da (northern Vietnam) district: Mantle sources, crustal contamination and sulfide segregation. *Chemical Geology* **243**, 317-343.

Wang, X. C., Li, X. H., Li, W. X. & Li, Z. X. (2007b). Ca. 825 Ma komatiitic basalts in South China: First evidence for >1500 °C mantle melts by a Rodinian mantle plume. *Geology* **35**, 1103-1106.

Wang, C. Y., Prichard, H. M., Zhou, M. F. & Fisher, P. C. (2008a). Platinum-group minerals from the Jinbaoshan Pd-Pt deposit, SW China: evidence for magmatic origin and hydrothermal alteration. *Mineralium Deposita* **43**, 791-803.

Wang, C. Y., Zhou, M. F. & Zhao, D. (2008b). Fe–Ti–Cr oxides from the Permian Xinjie mafic–ultramafic layered intrusion in the Emeishan large igneous province, SW China: Crystallization from Fe- and Ti-rich basaltic magmas. *Lithos* **102**, 198-217.

Wang, C. Y., Zhou, M. F. & Qi, L. (2010). Origin of extremely PGE-rich mafic magma system: An example from the Jinbaoshan ultramafic sill, Emeishan large igneous province, SW China. *Lithos* **119**, 147-161.

Wang, C., Zhou, M. F. & Qi, L. (2011). Chalcophile element geochemistry and petrogenesis of high-Ti and low-Ti magmas in the Permian Emeishan large igneous province, SW China. *Contributions to Mineralogy and Petrology* **161**, 237-254.

Wang, C. Y. & Zhou, M. F. (2013). New textural and mineralogical constraints on the origin of the Hongge Fe-Ti-V oxide deposit, SW China. *Mineralium Deposita*, **48**, 787-798.

Wang, Z. Y. (1982). The petrological characteristics and preliminary genesis study of Panzhihua V-Ti-Fe magnetite ore-hosting layered gabbroci intrusion. *Journal of Mineralogy and Petrology* **1**, 49-64. (in Chinese).

Watson, E. B. (1976). Two-liquid partition coefficients: experimental data and geochemical implications. *Contributions to Mineralogy and Petrology* **56**, 119-134.

Watson, E. B. (1979). Apatite saturation in basic to intermediate magmas. *Geophysical Research Letters* **6**, 937-940.

Watson, J. S. (1996). Fast, Simple Method of Powder Pellet Preparation for X-Ray Fluorescence Analysis. *X-Ray Spectrometry* **25**, 173-174.

Weihed, P. (2010). Metallogenetic evolution of the Fennoscandian Shield. *Smart Science for Exploration and Mining*, **1-2**, 966-968.

Whitaker, M. L., Nekvasil, H., Lindsley, D. H. & Difrancesco, N. J. (2007). The role of pressure in producing compositional diversity in intraplate basaltic magmas. *Journal of Petrology* **48**, 365-393.

Wignall, P. B., Sun, Y., Bond, D. P., Izon, G., Newton, R. J., Vedrine, S., Widdowson, M., Ali, J. R., Lai, X., Jiang, H., Cope, H. & Bottrell, S. H. (2009). Volcanism, mass extinction, and carbon isotope fluctuations in the Middle Permian of China. *Science* **324**, 1179-1182.

Wilson, A. & Chunnett, G. (2006). Trace element and platinum group element distributions and the genesis of the Merensky Reef, western Bushveld Complex, South Africa. *Journal of Petrology* **47**, 2369-2403.

Wilson, J. R., Robins, B., Nielsen, F. M., Duchesne, J. C. & Vander Auwera, J. (1996). The Bjerkreim-Sokndal layered intrusion, Southwest Norway. In: Cawthorn, R. G. (ed.) *Layered intrusions*. Amsterdam: Elsevier, pp. 231-255.

Xiao, L., Xu, Y. G., Chung, S. L., He, B. & Mei, H. J. (2003). Chemostratigraphic correlation of upper permian lavas from Yunnan province, China: Extent of the Emeishan large igneous province. *International Geology Review* 45, 753-766.

Xiao, L., Xu, Y. G., Mei, H. J., Zheng, Y. F., He, B. & Pirajno, F. (2004a). Distinct mantle sources of low-Ti and high-Ti basalts from the western Emeishan large igneous province, SW China: implications for plume–lithosphere interaction. *Earth and Planetary Science Letters* **228**, 525-546.

Xiao, L., Xu, Y. G., Xu, J. F., He, B. & Franco, P. (2004b). Chemostratigraphy of flood basalts in the Garze-Litang region and Zongza Block: Implications for western extension of the Emeishan Large Igneous Province, SW China. *Acta Geologica Sinica-English Edition* **78**, 61-67.

Xu, J. F., Suzuki, K., Xu, Y. G., Mei, H. J. & Li, J. (2007a). Os, Pb, and Nd isotope geochemistry of the Permian Emeishan continental flood basalts: Insights into the source of a large igneous province. *Geochimica Et Cosmochimica Acta* **71**, 2104-2119.

Xu, Y. G., Chung, S. L., Jahn, B. M. & Wu, G. (2001). Petrologic and geochemical constraints on the petrogenesis of Permian–Triassic Emeishan flood basalts in southwestern China. *Lithos* **58**, 145-168.

Xu, Y. G., He, B., Huang, X. L., Luo, Z. Y., Chung, S. L., Xiao, L., Zhu, D., Shao, H., Fan, W. M., Xu, J. F. & Wang, Y. J. (2007b). Identification of mantle plumes in the Emeishan Large Igneous Province. *Episodes* **30**, 32-42.

Xu, Y. G., Luo, Z. Y., Huang, X. L., He, B., Xiao, L., Xie, L. W. & Shi, Y. R. (2008). Zircon U-Pb and Hf isotope constraints on crustal melting associated with the Emeishan mantle plume. *Geochimica Et Cosmochimica Acta* **72**, 3084-3104.

Yang, J.S., Robinson, P.T., Jiang, C.F. & Xu, Z.Q. (1996). Ophiolites of the Kunlun Mountains, China and their tectonic implications. *Tectonophysics* **258**, 215-231.

Yang, Z., Sun, Z., Yang, T. & Pei, J. (2004). A long connection (750–380 Ma) between South China and Australia: paleomagnetic constraints. *Earth and Planetary Science Letters* **220**, 423-434.

Yao, P. H., Wang, K. N., Du, C. L., Lin, A. T. & Song, X. (1993). *Records of China's iron ore deposits*. Beijing: Metallurgic Industry Press. p. 638-641. (in Chinese).

Yin, A. & Harrison, T.M. (2000). Geological evolution of the Himalayan-Tibetan orogen. *Annual Review of Earth and Planetary Sciences* **28**, 211-280.

Yu, Z. S., Robinson, P., Townsend, A. T., Münker, C. & Crawford, A. J. (2000). Determination of high field strength elements, Rb, Sr, Mo, Sb, Cs, Tl and Bi at ng g^{-1} levels in geological reference materials by magnetic sector ICP-MS after HF/$HClO_4$ high pressure digestion. *Geostandards Newsletter-the Journal of Geostandards and Geoanalysis* **24**, 39-50.

Zhang, S. B., Zheng, Y. F., Wu, Y. B., Zhao, Z. F., Gao, S. & Wu, F. Y. (2006). Zircon U–Pb age and Hf isotope evidence for 3.8 Ga crustal remnant and episodic reworking of Archean crust in South China. *Earth and Planetary Science Letters* **252**, 56-71.

Zhang, X. Q., Song, X. Y., Chen, L. M., Xie, W., Yu, S. Y., Zheng, W. Q., Deng, Y. F., Zhang, J. F. & Gui, S. G. (2012). Fractional crystallization and the formation of thick Fe–Ti–V oxide layers in the Baima layered intrusion, SW China. *Ore Geology Reviews* **49**, 96-108.

Zhang, X. Q., Zhang, J. F., Song, X. Y., Deng, Y. F., Guan, J. X. & Zheng, W. Q. (2011). Implications of compositions of plagioclase and olivine on the formation of the Panzhihua V-Ti magnetite deposit, Sichuan Province. *Acta Petrologica Sinica* **27**, 3675-3688.

Zhang, Z. C. & Wang, F. S. (2002). Geochemistry of two types of basalts in the Emeishan basaltic province: Evidence for mantle plume-lithosphere interaction. *Acta Geologica Sinica-English Edition* **76**, 229-237.

Zhang, Z.C., Mahoney, J. J., Mao, J. & Wang, F. (2006a). Geochemistry of picritic and associated basalt flows of the western Emeishan flood basalt province, China. *Journal of Petrology* **47**, 1997-2019.

Zhang, Z. C., Mahoney, J. J., Mao, J. W. & Wang, F. S. (2006b). Geochemistry of picritic and associated basalt flows of the western Emeishan flood basalt province, China. *Journal of Petrology* **47**, 1997-2019.

Zhang, Z. C., Mao, J. W., Wang, F. S. & Pirajno, F. (2006c). Native gold and native copper grains enclosed by olivine phenocrysts in a picrite lava of the Emeishan large igneous province, SW China. *American Mineralogist* **91**, 1178-1183.

Zhang, Z. C., Zhi, X. C., Chen, L., Saunders, A. D. & Reichow, M. K. (2008). Re-Os isotopic compositions of picrites from the Emeishan flood basalt province, China. *Earth and Planetary Science Letters* **276**, 30-39.

Zhang, Z. C., Mao, J. W., Saunders, A. D., Ai, Y., Li, Y. & Zhao, L. (2009). Petrogenetic modeling of three mafic-ultramafic layered intrusions in the Emeishan large igneous province, SW China, based on isotopic and bulk chemical constraints. *Lithos* **113**, 369-392.

Zhang, Z.M., Liou, J.G. & Coleman, R.G. (1984). An outline of the plate tectonics of China. *Geological Society of America* **95**, 295-312.

Zhao, T. P., Chen, W. & Zhou, M. F. (2009). Geochemical and Nd-Hf isotopic constraints on the origin of the ~ 1.74-Ga Damiao anorthosite complex, North China Craton. *Lithos* **113**, 673-690.

Zhong, H., Hu, R. Z., Wilson, A. H. & Zhu, W. G. (2005). Review of the link between the Hongge layered intrusion and Emeishan flood basalts, Southwest China. *International Geology Review* **47**, 971-985.

Zhong, H., Zhou, X. H., Zhou, M. F., Sun, M. & Liu, B. G. (2002). Platinum-group element geochemistry of the Hongge Fe-V-Ti deposit in the Pan-Xi area, southwestern China. *Mineralium Deposita* **37**, 226-239.

Zhong, H., Yao, Y., Hu, S., Zhou, X., Liu, B., Sun, M., Zhou, M. & Viljoen, M. (2003). Trace-Element and Sr-Nd isotopic geochemistry of the PGE-Bearing Hongge layered intrusion, Southwestern China. *International Geology Review* **45**, 371-382.

Zhong, H., Yao, Y., Prevec, S. A., Wilson, A. H., Viljoen, M. J., Viljoen, R. P., Liu, B. G. & Luo, Y.-N. (2004). Trace-element and Sr-Nd isotopic geochemistry of the PGE-bearing Xinjie layered intrusion in SW China. *Chemical Geology* **203**, 237-252.

Zhong, H. & Zhu, W.-G. (2006a). Geochronology of layered mafic intrusions from the Pan–Xi area in the Emeishan large igneous province, SW China. *Mineralium Deposita* **41**, 599-606.

Zhong, H. & Zhu, W. G. (2006b). Geochronology of layered mafic intrusions from the Pan-Xi area in the Emeishan large igneous province, SW China. *Mineralium Deposita* **41**, 599-606.

Zhong, H., Zhu, W., Chu, Z., He, D. & Song, X. (2007a). Shrimp U–Pb zircon geochronology, geochemistry, and Nd–Sr isotopic study of contrasting granites in the Emeishan large igneous province, SW China. *Chemical Geology* **236**, 112-133.

Zhong, H., Zhu, W. G., Chu, Z. Y., He, D. F. & Song, X. Y. (2007b). Shrimp U-Pb zircon geochronology, geochemistry, and Nd-Sr isotopic study of contrasting granites in the Emeishan large igneous province, SW China. *Chemical Geology* **236**, 112-133.

Zhong, H., Zhu, W. G., Hu, R. Z., Xie, L. W., He, D. F., Liu, F. & Chu, Z. Y. (2009). Zircon U-Pb age and Sr-Nd-Hf isotope geochemistry of the Panzhihua A-type syenitic intrusion in the Emeishan large igneous province, southwest China and implications for growth of juvenile crust. *Lithos* **110**, 109-128.

Zhong, H., Qi, L. A., Hu, R. Z., Zhou, M. F., Gou, T. Z., Zhu, W. G., Liu, B. G. & Chu, Z. Y. (2011). Rhenium-osmium isotope and platinum-group elements in the Xinjie layered intrusion, SW China: Implications for source mantle composition, mantle evolution, PGE fractionation and mineralization. *Geochimica Et Cosmochimica Acta* **75**, 1621-1641.

Zhou, M. F., Malpas, J., Song, X. Y., Robinson, P. T., Sun, M., Kennedy, A. K., Lesher, C. M. & Keays, R. R. (2002a). A temporal link between the Emeishan large igneous province (SW China) and the end-Guadalupian mass extinction. *Earth and Planetary Science Letters* **196**, 113-122.

Zhou, M. F., Yan, D. P., Kennedy, A. K., Li, Y. & Ding, J. (2002b). SHRIMP U-Pb zircon geochronological and geochemical evidence for Neoproterozoic arc-magmatism along the western margin of the Yangtze Block, South China. *Earth and Planetary Science Letters* **196**, 51-67.

Zhou, M. F., Robinson, P. T., Lesher, C. M., Keays, R. R., Zhang, C. J. & Malpas, J. (2005). Geochemistry, Petrogenesis and Metallogenesis of the Panzhihua Gabbroic Layered Intrusion and Associated Fe-Ti-V Oxide Deposits, Sichuan Province, SW China. *Journal of Petrology* **46**, 2253-2280.

Zhou, M. F., Ma, Y., Yan, D. P., Xia, X., Zhao, J. H. & Sun, M. (2006a). The Yanbian Terrane (Southern Sichuan Province, SW China): A Neoproterozoic arc assemblage in the western margin of the Yangtze Block. *Precambrian Research* **144**, 19-38.

Zhou, M. F., Yan, D. P., Wang, C. L., Qi, L. & Kennedy, A. (2006b). Subduction-related origin of the 750 Ma Xuelongbao adakitic complex (Sichuan Province, China): Implications for the tectonic setting of the giant Neoproterozoic magmatic event in South China. *Earth and Planetary Science Letters* **248**, 286-300.

Zhou, M. F., Zhao, J. H., Qi, L., Su, W. C. & Hu, R. Z. (2006c). Zircon U-Pb geochronology and elemental and Sr-Nd isotope geochemistry of Permian mafic rocks in the Funing area, SW China. *Contributions to Mineralogy and Petrology* **151**, 1-19.

Zhou, M. F., Arndt, N. T., Malpas, J., Wang, C. Y. & Kennedy, A. K. (2008). Two magma series and associated ore deposit types in the Permian Emeishan large igneous province, SW China. *Lithos* **103**, 352-368.

Zhou, M. F., Chen, W. T., Wang, C. Y., Prevec, S. A., Liu, Patricia P. & Howarth, G. H. (2013). Two stages of immiscible liquid separation in the formation of Panzhihua-type Fe-Ti-V oxide deposits, SW China. Geoscience Frontiers.

Zhu, W. G., Zhong, H., Li, X. H., Liu, B. G., Deng, H. L. & Qin, Y. (2007). ^{40}Ar–^{39}Ar age, geochemistry and Sr–Nd–Pb isotopes of the Neoproterozoic Lengshuiqing Cu–Ni sulfide-bearing mafic–ultramafic complex, SW China. *Precambrian Research* **155**, 98-124.

Zhu, W. G., Zhong, H., Deng, H. L., Wilson, A. H., Liu, B. G., Li, C. Y. & Qin, Y. (2006). SHRIMP zircon U-Pb age, geochemistry, and Nd-Sr isotopes of the Gaojiacun mafic-ultramafic intrusive complex, Southwest China. *International Geology Review* **48**, 650-668.

APPENDIX I

METHODOLOGY

A.1 Mineral Liberation Analysis (MLA)

Mineral modal proportions were obtained from carbon-coated polished thin sections, using an SEM (scanning electron microscope)-based MLA method at the Central Sciences Laboratory, University of Tasmania. A total of 2000 locations were counted on a grid of 1 × 4 cm area of thin sections.

A high quality BSE (back-scattered electron) image of the selected area was first obtained using the SEM. The MLA software package automatically identifies different mineral phases based on BSE intensity. For a point overlapping several phases, an image segmentation step was performed to identify mineral phases and delineate grain boundaries within the area. X-ray analysis function of the SEM was used to define minerals compositions for phases that cannot be confidently identified on the basis of BSE intensity. Images were processes off-line to generate mineral liberation data, using an extended BSE Liberation Analysis. For more details on the MLA method see Gu. (2003).

A.2 Whole-rock XRF and Solution ICP-MS Analyses

Samples were first cut to produce fresh cubes (~3 × 3 x 3 cm) in the lapidary at CODES, the University of Tasmania. A hydraulic crusher was used to crush the dried cubes into small chips, which were then milled to rock powder using a tungsten-carbide ring-mill.

A Philips PW1480 X-Ray Spectrometer was applied to analysis of whole rock major and trace element compositions on fused glass discs and pressed pellets, respectively. The glasses were prepared by fusing a mixture of ~ 0.500 g rock powder diluted in 4.500g lithium tetraborate-metaborate mix and 1 ml of 60.6% lithium nitrate (LiNO3) at 1100˚C. The loss on ignition (LOI) was determined by heating 1~2 g rock powder at 1000˚C for 12 h and reweighting. The pellets were made by pressing (3.5 tonnes cm^{-2}) 10g of rock powder bind with PVP-MC (Polyvinylpyrrolidone-Methylcellulose). Details of sample preparation and XRF analysis procedures can be found in Robinson. (2003) and Watson. (1996).

Solution ICP-MS analysis was performed to determine low-level trace elements and rare earth elements (REE) of selected representative samples. 100 mg rock powder was dissolved using PicroTrace® high pressure acid (HF/H_2SO_4) digestion. The solution was then evaporated at 180˚C for four days. After that, the residue was dissolved with 1 ml of $HClO_4$, dried, and re-dissolved with 2 ml HNO_3 and 1 ml HCl again. The solution was diluted to 100 ml before analysis using an Agilent 7700 ICP-MS at CODES, University of Tasmania. See Robinson *et al*. (1999) and Yu *et al*. (2000) for more details.

A.3 Electron Microprobe Analysis (EMPA)

Major and minor elements in silicates (olivine, clinopyroxene, plagioclase), oxides (magnetite, ilmenite, spinel), and sulphides (pyrrhotite) were analysed on carbon-coated polished thin sections using a Cameca SX100 electron microprobe housed at the Central Science Laboratory (CSL), University of Tasmania. Measurements were taken from the centre of each grain. On average, 4 olivines, 5 plagioclases, 6 clinopyroxenes, ilmenites and pyrrotites, and 7 magnetites were analysed in each sample. Quantification was performed using a range of natural mineral standards (Jarosewich *et al*., 1980). For silicates and oxides Si and Ca were calibrated on Delegate Cpx; Mg on San Carlos olivine; Zn on Gahnite; Na on plagioclase; K on Microcline; Cr on New Caledonia Chromite; Al on plagioclase; Fe on hematite; Ni on NiSi; Mn on Rhodonite; Ti on Rutile, V on V metal; Cl on Tugtupit; P on Durango apatite. For sulphides: Fe and S on marcasite, Co on cobaltite, Ni pentlandite, Cu on cuprite.

The operating conditions were 15 kV accelerating voltage and 20 nA beam current for silicates and oxides; 15 kV and 30 nA for sulfides. Counting times were usually 10s for major elements, i.e. Si, Al, Fe, Ca, Na and K. The analyses were performed with a beam diameter of 2 μm for silicates and oxides and < 1 μm for sulfides.

Detection limits were 0.03 wt% SiO_2, 0.06 wt% TiO_2, 0.06 wt% Al_2O_3, 0.07 wt% Cr_2O_3, 0.01 wt% FeO, 0.08 wt% MnO, 0.07 wt% MgO, 0.04 wt% CaO, 0.04 wt% Na_2O and 0.03 wt% K_2O.

A.4 Laser Ablation Inductively Coupled Plasma Mass Spectrometry (LA-ICPMS)

A new wave UP-213 laser ablation system equipped with the MEOLaser 214 software and an Agilent 7500cs Quadrapole ICP-MS based at CODES, University of Tasmania, was

used to determine trace element concentrations of magnetite, ilmenite and pyrrhotite. Analyses were done on polished rock chips mounted in 25 mm round epoxy mounts. On average, 9 grains were analysed for magnetite and ilmenite, and 8 grains for pyrrhotite.

The in-house calibration standard STDGL2b-2 (Danyushevsky *et al.*, 2011) and an international reference material GSD-1G (Jochum *et al.*, 2005) were used for sulfide and oxide minerals analyses, respectively. The standards were analysed every 1 - 1.5 hours to calculate the concentrations of unknowns and to correct for the instrument drift.

Laser pulse rate was set at 10 HZ for standards and 5 HZ for samples. Standard analyses were performed with a fixed spot size of 100 μm. Larger spot sizes (50 to 100μm) were used in analysing magnetite and ilmenite than sulphides (25 to 50 μm), in order to eliminate or minimize the effects of extensive oxy-exsolution which is common in oxide minerals. Analysis started with a pre-ablation at a low pulse rate (1 HZ) for a few seconds to remove any contamination on the surface. The whole data acquisition lasted for a total of 90 seconds with the initial 30 seconds of gas background analysis and subsequently 60 seconds of sample ablation.

Data quantification was performed with an in-house Excel-based spreadsheet. FeO wt% concentrations obtained from EMPA were used as the internal standard for both oxides and sulphides. Detail data reduction method sees Gilbert and Danyushevsky (2009).

APPENDIX II List of Samples and Analyses

A2.1 List of all Panzhihua samples analyzed during this study.

Intrusion	Zone	Orebody	Sample	RockName	XRF	ICPMS	MLA	EMPA						LA-ICP-MS		
								Ol	Cpx	Plag	Mgt	Ilm	Po	Mgt	Ilm	Po
Lanshan (Panzhihua)	MGZ		PZ-1	wehr	1	1	1	1	1	1	1	1		1	1	
			PZ-2	gb	1	1	1		1	1	1	1	1	1	1	1
			PZ-3	gb	1	1	1	1	1	1	1	1		1	1	
			PZ-4	ore	1	1	1				1	1	1	1	1	1
			PZ-5	hb-gb	1	1	1		1	1	1	1		1	1	
			PZ-6	wehr	1	1	1	1	1		1		1	1		1
			PZ-7	hb-gb	1	1	1	1	1							
			PZ-8	hb-gb	1	1	1		1			1			1	1
	LZ	Body 9	PZ-9	gb	1	1	1		1	1	1	1	1	1	1	1
			PZ-10	ox-gb	1	1	1		1	1	1	1	1	1	1	
			PZ-11	ore	1		1	1	1	1	1	1	1	1	1	1
	MZa	Body 8	PZ-12	ore	1		1	1	1		1	1	1	1	1	1
			PZ-13	ore	1	1	1	1	1	1	1	1	1	1	1	
			PZ-14	ore	1		1	1	1	1	1	1	1	1	1	
			PZ-15	ore	1		1	1	1		1	1	1	1	1	1
		Body 6	PZ-16	gb	1	1	1		1	1	1	1	1			
			PZ-17	wehr	1	1	1	1	1	1	1	1		1	1	
			PZ-18	ore	1		1	1	1		1	1	1	1	1	
			PZ-19	gb	1	1	1		1	1	1	1	1	1	1	1
			PZ-20	ox-gb	1	1	1	1	1		1	1	1	1	1	1
		Body 5	PZ-21	ox-gb	1		1	1	1	1	1	1	1	1	1	1
			PZ-22	ox-gb	1		1	1	1	1	1	1	1	1	1	1
			PZ-23	leucogb	1	1	1								1	
Zhujiaabaobao (Panzhihua)	LZ	Body 9	PZ-24	ore	1	1	1		1	1	1	1		1	1	1
			PZ-25	ox-gb	1		1		1	1	1	1		1	1	1
			PZ-26	ore	1		1	1	1	1	1	1		1	1	1
	MZa	Body 8	PZ-27	ore	1		1		1	1	1	1	1	1	1	1
			PZ-28	leucogb	1	1	1			1	1	1	1	1	1	1
			PZ-29	ox-gb	1	1	1		1		1	1	1	1	1	1
			PZ-30	ore	1		1	1	1	1	1	1	1	1	1	1
		Body 6	PZ-31	ore	1		1	1	1	1	1	1	1	1	1	1
			PZ-32	leucogb	1	1	1			1		1			1	
			PZ-33	ore	1	1	1		1		1	1	1	1	1	1
		Body 5	PZ-35	ox-gb	1		1		1		1	1	1	1	1	1
			PZ-36	ox-gb	1		1		1	1	1	1	1		1	1
			PZ-37	cpx-rich ore	1	1	1	1	1		1	1	1	1	1	
			PZ-38	ox-gb	1		1	1	1	1	1	1	1	1	1	1
		Body 4	PZ-39	gb	1	1	1		1	1	1	1	1	1	1	1
			PZ-40	gb	1	1	1	1	1	1	1	1	1	1	1	1
			PZ-41	ox-gb	1	1	1	1	1	1	1	1	1	1	1	1
			PZ-42	ox-gb	1		1	1	1	1	1	1	1	1	1	1
			PZ-43	gb	1	1	1		1	1	1	1			1	
	MZb		PZ-44	ap-gb	1	1	1	1	1	1	1	1	1	1	1	
			PZ-45	ap-gb	1	1	1		1	1	1	1		1	1	1

A2.2 List of all Taihe samples and analyzed during this study.

Intrusion	Ore body	Sample	RockName	XRF	ICP-MS	MLA	EMPA						LA-ICP-MS		
							Ol	Cpx	Plag	Mgt	Ilm	Po	Mgt	Ilm	Po
Taihe		TH-1	ore	1	1					1	1		1	1	
		TH-2	ore	1						1	1		1	1	
		TH-3	ore	1	1					1	1		1	1	
		TH-4	ore	1	1					1	1		1	1	
		TH-5	ox-gb	1						1	1		1	1	
		TH-6	ore	1	1					1	1		1	1	
		TH-7	ore	1	1					1	1		1	1	
		TH-8	ore	1						1	1		1	1	
		TH-9	gb	1	1					1	1		1	1	
		TH-10	gb	1	1					1	1			1	
		TH-11	gb	1	1										